Bak.-Mag. Andriy Smolyanyuk

Predicting novel phases of bismuthates and iridates

DOCTORAL THESIS

For obtaining the academic degree of
Doktor der technischen Wissenschaften

Doctoral Programme in Technical Sciences
Technical Physics

Graz University of Technology

Supervisor:
Ass. Prof. Dr. Lilia Boeri

Institute of Theoretical and Computational Physics

Graz, December 2018

AFFIDAVIT

I declare that I have authored this thesis independently, that I have not used other than the declared sources/resources, and that I have explicitly indicated all material which has been quoted either literally or by content from the sources used. The text document uploaded to TUGRAZonline is identical to the present doctoral thesis.

Date

Signature

Abstract

The general motivation behind this thesis is to use novel computer simulation methods to predict new materials and study their properties. In principle, computer simulation methods allow us to describe properties of real materials knowing only its chemical composition. To do this the first step is to determine the crystal structure of a given chemical composition and this can be done either by experiment or using computational methods of crystal structure prediction. The use of computational methods gives an opportunity to predict a crystal structure for conditions under which performing experiments is problematic, too expensive or even impossible: extremely high pressure, toxic or radioactive materials etc. When the crystal structure of the material of interest is known, band structure theory is employed to study its properties.

The aim of this thesis is to predict and analyze the properties of two classes of oxides, bismuthates and iridates, in regimes which are not easily accessible, or have not been accessed yet, by experiment. This is possible thanks to the combination of novel *ab initio* methods for crystal structure prediction and electronic structure, which permit to predict the properties of materials on a computer, with an accuracy which is nowadays often comparable to experiments.

The original work presented in this thesis is divided in two parts. In the first part, we study the high-pressure behaviour of alkaline-earth bismuthates $ABiO_3$ (A=Ba, Sr, Ca), up to the megabar range [1, 2]. At ambient pressure the three compounds are charge-ordered insulators. The insulating behaviour is associated to a breathing and tilting distortion of their perovskite structure. Hole doping suppresses charge ordering and induces a transition to a metallic superconducting state [3–5]. The high-pressure behavior of these compounds was unknown at the time we started our work. In two subsequent publications, we applied two different methods, i.e. group-theoretical analysis and evolutionary algorithms, to predict the structural evolution of all $ABiO_3$ compounds under pressure. We showed that all compounds exhibit several transitions under pressure to very distorted (non-perovskite) structures, which preserve charge disproportionation and insulating behavior. We show that distorted phases are an efficient way to obtain a densely packed lattice, which preserves the tendency of bismuth to charge disproportionation. Our findings for $BaBiO_3$ were confirmed by an independent theoretical and experimental work [6].

The second part presents preliminary results, in which we apply crystal structure prediction methods to explore the phase diagram of sodium iridates. The interest in these systems is motivated by the rich variety of their physical properties which results from the interplay between crystal field, spin-orbit coupling and strong local electronic interactions. Our aim is to search for thermodynamically stable structures of possible ternary compounds, containing sodium,

iridium and oxygen, which have not been synthesized yet. This phase diagram contains very interesting compounds, such as pentavalent post-perovskite $NaIrO_3$, hexagonal Na_2IrO_3, which is a candidate for *quantum spin liquid* state, Na_4IrO_4 with square-planar coordinated Ir and hyperkagome $Na_3Ir_3O_8$ and $Na_4Ir_3O_8$; the latter is *quantum spin liquid* candidate too. For this task we employ the evolutionary algorithms extended to the case of variable-composition crystal structure prediction. We determined four possible thermodynamically stable ternary compounds, which have not been synthesized experimentally, which we will investigate further. During the search we also identified a novel 2D phase of IrO_2, which may be a triangular Kitaev system.

Kurzfassung

Die allgemeine Motivation hinter dieser Arbeit ist die Verwendung neuartiger Computersimulationsmethoden, um neue Materialien vorherzusagen und ihre Eigenschaften zu untersuchen. Grundsätzlich erlauben Computersimulationsmethoden die Beschreibung von Eigenschaften realer Materialien, wobei nur die chemische Zusammensetzung bekannt ist. Um dies zu tun, besteht der erste Schritt darin, die Kristallstruktur einer gegebenen chemischen Zusammensetzung zu bestimmen, und dies kann entweder durch Experiment oder unter Verwendung numerischer Verfahren zur Vorhersage der Kristallstruktur erfolgen. Die Verwendung von Berechnungsmethoden bietet die Möglichkeit, eine Kristallstruktur für Bedingungen vorherzusagen, die für die Durchführung von Experimenten problematisch, zu teuer oder sogar unmöglich sind: extrem hoher Druck, toxische oder radioaktive Materialien usw. Wenn die Kristallstruktur des interessierenden Materials bekannt ist, werden Bandstrukturmethoden verwendet, um deren Eigenschaften zu untersuchen.

Das Ziel dieser Arbeit ist die Vorhersage und Analyse der Eigenschaften von zwei Klassen von Oxiden, Bismutaten und Iridaten, in Bereichen, die experimentell nicht oder nur schwer zugänglich sind. Dies ist möglich dank der Kombination neuartiger ab-initio-Verfahren zur Vorhersage der Kristallstruktur und der elektronischen Struktur, die es ermöglichen, die Eigenschaften von Materialien am Computer mit einer Genauigkeit zu bestimmen, die heutzutage oft mit Experimenten vergleichbar ist.

Die in dieser Arbeit vorgestellte Originalarbeit ist in zwei Teile gegliedert. Im ersten Teil untersuchen wir das Hochdruckverhalten von Erdalkalibismutaten $ABiO_3$ (A = Ba, Sr, Ca) bis in den Megabar-Bereich [1, 2]. Bei Umgebungsdruck sind die drei Verbindungen ladungsgeordnete Isolatoren. Das isolierende Verhalten ist mit einer breathing und Kippverzerrung der Perowskitstruktur verbunden. Lochdotierung unterdrückt die Ladungsordnung und induziert den Übergang in einen metallischen supraleitenden Zustand [3–5]. Das Hochdruckverhalten dieser Verbindungen war zum Zeitpunkt des Beginns unserer Arbeit unbekannt. In zwei aufeinanderfolgenden Publikationen haben wir zwei unterschiedliche Methoden angewandt, d.h. eine gruppentheoretische Analyse und evolutionäre Algorithmen, um die strukturelle Entwicklung aller $ABiO_3$ Verbindungen unter Druck vorherzusagen. Wir haben gezeigt, dass alle Verbindungen unter Druck mehrere Übergänge zu sehr verzerrten (Nicht-Perowskit) Strukturen aufweisen, wodurch die Ladungsordnung und das isolierende Verhalten erhalten bleiben. Wir zeigen, dass verzerrte Phasen ein effizientes Mittel sind, um ein dicht gepacktes Gitter zu erhalten, das die Tendenz von Wismut zu einer Ladungsordnung aufrechterhält. Unsere Ergebnisse für $BaBiO_3$ wurden durch eine unabhängige theoretische und

experimentelle Arbeit bestätigt [6].

Der zweite Teil präsentiert vorläufige Ergebnisse, in denen wir Kristallstrukturvorhersageverfahren anwenden, um das Phasendiagramm von Natriumiridaten zu untersuchen. Das Interesse an diesen Systemen ist auf die vielfältigen physikalischen Eigenschaften zurückzuführen, die sich aus dem Zusammenspiel von Kristallfeld, Spin-Orbit-Kopplung und starken lokalen elektronischen Wechselwirkungen ergeben. Unser Ziel ist die Suche nach thermodynamisch stabilen Strukturen von möglichen ternären Verbindungen, die Natrium, Iridium und Sauerstoff enthalten, die noch nicht synthetisiert wurden. Dieses Phasendiagramm enthält sehr interessante Verbindungen, wie etwa fünfwertiges Post-Perowskit $NaIrO_3$, hexagonales Na_2IrO_3, das ein Kandidat für eine *Quantenspinflüssigkeit* ist, Na_4IrO_4 mit quadratisch-planar koordiniertem Ir und Hyperkagom $Na_3Ir_3O_8$ und $Na_4Ir_3O_8$; Letzteres ist auch ein Kandidat für eine *Quantenspinflüssigkeit*. Für diese Aufgabe verwenden wir die evolutionären Algorithmen, die für den Fall der Kristallstrukturvorhersage mit variabler Zusammensetzung erweitert wurden. Wir haben vier mögliche thermodynamisch stabile ternäre Verbindungen ermittelt, die nicht experimentell synthetisiert wurden, die wir weiter untersuchen werden. Bei der Suche haben wir auch eine neue 2D-Phase von IrO_2 identifiziert, bei der es sich um ein dreieckiges Kitaev-System handeln kann.

Contents

Acknowledgments

I would like to thank very much my supervisor, *Lilia Boeri*, for the opportunity to do my PhD in her group, all her help, lessons and fruitful discussions I had during my PhD time. And a separate thanks for the acquaintance with the fascinating city of Rome and for the chance to participate in all the schools and conferences.

Thank you, *Markus Aichhorn*, who became a project manager of my project, for all the discussions and knowledge I gained from you. My gratitude to *Cesare Franchini* for the collaboration in $BaBiO_3$ and $ABiO_3$ projects, and the knowledge you gave to me. I am grateful to *Igor Mazin* for the collaboration in IrO_2 project, the valuable ideas and knowledge you gave to me, and for introducing me to `Wolfram Mathematica`.

I want to thank all my ITPCP colleagues for all the discussions and friendly atmosphere in the institute I had during this time. A special thanks to the team of *Welcome Center* for the help in resolving life-abroad-related issues and all the events you organized.

Thank you, *Andreas Hirczy* for a perfect maintenance of ITPCP computer infrastructure and *Brigitte Schwarz* for all the help with bureaucratic work.

Thanks to the *ZID* of TU Graz and the *Vienna Scientific Cluster* for providing the computational resources for this work.

A big thanks for my family for their support during my PhD study. Many thanks to my wife, *Yulia*, for all your inspiration, support and love.

List of symbols and abbreviations

In this list, the meaning of most of the mathematical symbols and abbreviations is given together with a reference to the page where they first appear.

μSR	muon spin spectroscopy → p. 57
erf(x)	error function, $\frac{2}{\sqrt{\pi}} \int_0^x e^{-t^2} dt$ → p. 69
CDW	charge density wave → p. 8
CFS	crystal field splitting → p. 6
cRPA	constrained random phase approximation → p. 55
CSM	continuous symmetry measure → p. 71
DFT	density functional theory → p. 3
EA	evolutionary algorithm → p. 77
GGA	generalized gradient approximation → p. 67
HF	Hartree-Fock method → p. 69
HSE	Heyd, Scuseria and Ernzerhof hybrid functional → p. 69
IR	irreducible representation → p. 75
LDA	local density approximation → p. 67
NMR	nuclear magnetic resonance → p. 57
PES	potential energy surface → p. 3
QMO	quasimolecular orbital → p. 60
QSL	quantum spin liquid → p. 57
RVB	resonating valence bond → p. 43
TB	tight-binding model → p. 17
TM	transition metal → p. 11
TMO	transition metal oxide → p. 6

VB	valence bond → p. 43

Part I.

Introduction

Introduction

The aim of this thesis is to predict novel materials and study their properties using computational methods, based on Density Functional Theory (DFT) and beyond. Our research concerns two families of oxides: bismuthates, containing bismuth, and iridates, containing iridium. In the case of bismuthates we focus on their high pressure behaviour, while in the case of iridates our aim is to search for thermodynamically stable structures of possible ternary compounds, containing sodium, iridium and oxygen. In both cases, the ranges of pressures and chemical compositions we explore are not easily accessible by experiments. Nevertheless, the methods for ab initio crystal structure prediction employed in this thesis will allow us to explore the material phase space with an accuracy sufficient to make reliable computational predictions.

Motivation: The development of quantum mechanics permitted to obtain a successful description of nature on the scale of atoms and subatomic particles. Nowadays's material science can count on powerful tool to model the properties of real materials through quantum mechanical simulations. These allow to describe the properties of the material of interest knowing only its chemical composition. By means of band structure theory it is possible to determine if the material is a metal or insulator, determine its equilibrium crystal structure, calculate its optical properties and much more.

The main ingredient needed for the quantum mechanical simulation of a given material is the set of chemical species and their coordinates, defining its crystal structure. Up to recent times, the only way to determine this essential information was by experiment. To emphasize the limitation of theoretical methods, in 1988 John Maddox wrote: *"One of the continuing scandals in the physical sciences is that it remains impossible to predict the structure of even the simplest crystalline solids from a knowledge of their composition" [7].* The situation changed in the last 10-15 years, with the development of *ab initio* methods for crystal structure prediction.

The basic principle underlying crystal structure prediction methods is quite simple. In fact, the total energy of a given structure, defined by the atomic positions of all its constituents, can be easily obtained by quantum mechanical methods. The crystal structure itself is defined by the positions of all atoms that it contains. A specific crystal structure is a point in the phase space defined by all possible atomic positions. A naive approach to crystal structure prediction would thus amount to sample the entire phase space to obtain the total energy corresponding to each point, thus constructing an (infinite) *potential energy surface* (PES). Finding the ground-state

structure would then amount to finding global minimum on the potential energy surface, while the local minima correspond to metastable structures that can be realized under specific conditions.

However, the problem is intractable in this direct approach due to the large number of degrees of freedom involved, which makes it impossible to sample the entire phase space. Indeed, even in the simplest case of a monoatomic crystal, considering the translational invariance, in the most general case we would need six continuous parameters to describe the lattice (three lattice vectors and three angles between them). If we tried to map the continuous variables to a discrete grid, and imagined using a very coarse mesh of 10 points for each variable, we would need 10^6 calculations and this is already very demanding computationally. In general, for a unit cell with N atoms, the number of parameters is $d = 3N + 3$, where $3N - 3$ degrees of freedom are the internal coordinates of the atom in the unit cell and the remaining six parameters are the three lattice constants and the three angles between them; this makes a direct approach computationally unfeasible. However, the recent progress in computational technologies and the development of new methods to efficiently sample the PES, such as random sampling, evolutionary algorithms, molecular dynamics, metadynamics, data mining etc. (see Refs. [8, 9] for reviews of different methods), in the last few years allowed considerable progress in the field: using a regular computer it is now possible to predict the crystal structure for a given chemical composition for unit cells of 4-8 atoms; even larger systems can be treated on a supercomputer and, combining several such calculations, phase diagrams in the pressure and composition space can be accurately predicted. These developments made it possible to predict structures for conditions under which performing experiments is problematic or even impossible: extremely high pressure, toxic or radioactive materials etc. This means that nowadays quantum mechanical simulations offer the possibility not only to explain the properties of existing materials, but also to design new ones.

The motivation of this thesis is to apply these tools to study properties of representatives of two material families: bismuthates and iridates, where the main properties of the materials are dictated by Bi and Ir atoms respectively. The systems under the interest exhibit a wide variety of physical properties, whose description requires methods beyond the standard DFT, specifically designed to treat systems in the strongly correlated regimes. Thus, the successful application of crystal structure prediction methods together with the post-DFT electronic structure methods is a strong demonstration of the predictive power of nowadays's *ab initio* methods.

In the following, for brevity we will refer collectively to bismuthates and iridates as transition metal oxides (TMO). This definition is not entirely correct because, while Ir belongs to the class of *transition metals* with incompletely filled *d*-shell, Bi is not. However, the physical properties of bismuthates, and the computational methods used to describe them, are similar. Therefore, we will describe these two oxide families on equal footing.

In general, the peculiar properties of TMO arise due to the strong local interaction between electrons, and hence they are classified as a *strongly correlated materials*. This term includes a wide class of materials whose physical properties arise from the collective behavior of electrons, and cannot be described by the methods based on the single-particle approximation. Over the

last twenty years, many methods have been developed to investigate this regime, and as we shall see their use is essential to describe the physical properties of our systems.

The thesis is based on the following publications:

1. *Ab initio* prediction of the high-pressure phase diagram of $BaBiO_3$ [1].
2. *Ab initio* study of $ABiO_3$ (A=Ba, Sr, Ca) under high pressure [2].
3. *Ab initio* prediction of the Na-Ir-O ternary diagram *(in preparation).*
4. *Ab initio* prediction of a new triangular Kitaev system: IrO_2 *(in preparation).*

In the first two publications we explore the possibility of suppressing charge disproportionation in $BaBiO_3$ and related compounds using high pressure. $BaBiO_3$ is a charge-ordered insulator which becomes superconducting upon hole doping [3, 10]; other alkali-earths bismuthates exhibit similar physics. The insulating behavior in $BaBiO_3$ is associated to a breathing and tilting distortion of the ideal cubic perovskite structure [11, 12], which is suppressed by doping. The initial motivation of our work was to investigate whether high pressure could be used to suppress the structural distortion in the undoped compound, and possibly induce a superconducting state. To check this hypothesis we used crystal structure prediction methods to construct an enthalpy-pressure phase diagram for $BaBiO_3$ and the results are described in the first publication; the second publication generalizes our investigation to the case of $SrBiO_3$ and $CaBiO_3$. Each compound exhibits several structural phase transitions and all compounds show a transition from a low-pressure perovskite to a high-pressure distorted structure. Charge disproportionation is not suppressed by a pressure and all compounds remain insulating up to 100 GPa.

The aim of the second set of publications, based on preliminary results presented in this thesis, is to make a broad search of the ternary phase diagram of sodium (Na), iridium (Ir) and oxygen (O) to determine possible stable compounds that have not been synthesized by experiments yet. The interest in iridates is motivated by their rich variety of physical properties which results from the interplay between the crystal field, spin orbit coupling (SOC) and strong electronic correlations. This field of study has emerged relatively recently and only a few prominent compounds have been identified. A new type of insulator, termed a relativistic $J_{eff} = \frac{1}{2}$ Mott insulator, was discovered in Sr_2IrO_4 while other structures have been predicted to be candidates for interesting magnetic phase: *quantum spin liquid*, which shows short-range magnetic order, but no long-range orders. Two ternary Na-Ir-O compositions, namely Na_2IrO_3 and $Na_4Ir_3O_8$, were proposed as candidates to host a quantum spin liquid state. The possibility that many Na-Ir-O compositions have not yet been explored raised our motivation to study these systems. In our preliminary variable-composition evolutionary search we determined five possibly thermodynamically stable structures, which we will investigate further. On the other hand, during the search over possible binary Ir_xO_{1-x} compositions we identified 2D phase of IrO_2, which may be a triangular Kitaev system.

The tools discussed in this thesis could guide the synthesis of new compounds since they are

capable of predicting specific compositions exhibiting promising crystal structures and describe their properties.

Structure and extended summary of the thesis

The thesis is organized in two parts: **Part I** (chapters 1, 2 and 3) give an introduction to the original work presented in **Part II** (chapters 4 and 5).

Part I: Introductory chapters

The discussion in this thesis will start describing the main physical properties that are observed in bismuthates and iridates and the models used to study them (**Chapter 1**).

We will start our description by rationalizing the typical crystal structures that are known to occur in transition metal oxides in **Sec. 1.1**.

Even when the full information about the crystal structure is missing, it is possible to explore crystal structure trends by considerations based on the local geometry and on the physical properties of the single ions. The most famous in this respect are Pauling's rules [13], published in 1929. They permit to predict the crystal structure of ionic compounds, based on the ratio of ionic radii of ions forming a solid, their electrostatic bond strength, the connectivity of polyhedrons formed by ions etc.

A similar geometrical interpretation, described in **Sec. 1.1**, is valid for the transition metal oxides (TMO): oxygen is much bigger than most transition metal ions and the crystal structure construction starts considering a close packing of oxygen ions that forms a layer. These close packed oxygen layers can occur in different types of stacking, with the smaller TM ions occupying the interstices. Together the type of stacking and the arrangement of the occupied interstices determine the crystal structure. In general, two types of coordination environments for the TM ion are favored in this procedure: octahedral and tetrahedral. The coordination environment determines some aspects of the electronic and magnetic structure of the solid. For example, the local symmetry of the coordination environment dictates the order and degeneracy of the energy levels of the electrons associated with TM, called *the crystal field splitting* (CFS), discussed in **Sec. 1.2.2**.

The crystal structure of a material determines its **electronic structure**. Before going into the details of *ab initio* calculations, we will describe model approaches to describe the electronic structure of TMOs. We will start with a simple *tight-binding* model, described in **Sec. 1.2.1**. In this model the total electronic wave function of the crystal is approximated with a superposition of electronic wave functions located at each lattice site. Although the model works reasonably well for many crystalline insulators, it fails for TMOs, in which strong electronic correlations make the single-particle picture invalid. The textbook example of strongly correlated electron

systems are Mott insulators, i.e. systems which are described as metals in the single-particle picture, but behave as insulators. The simplest model to consider the interacting particles on the lattice is the Hubbard model [14], described in **Sec. 1.2.3**. This model is able to describe the Mott metal-insulator transition.

The last important ingredient we need to correctly describe the electronic structure of the compounds under interest is the spin-orbit coupling (described in **Sec. 1.2.4**): the mixing between spin and orbital motion of the electron due to the relativistic effects. For the light atoms the effect is negligible, but it becomes important for the compounds that contain heavy atoms since the strength of the SOC increases with the atomic number as Z^2 [15]. Thus, the effect of SOC is pronounced for Ir atom. The main effect of SOC on an atom is a splitting of its atomic energy levels which in a solid translates into a splitting of the bands. In iridates, the interplay of SOC and crystal field splitting leads to peculiar physical properties. The prominent example is a new type of Mott insulator: relativistic $J_{eff} = \frac{1}{2}$ Mott insulator, observed in Sr_2IrO_4 [16], which exhibits K_2NiF_4 crystal structure. In this compound Ir has 5 valence electrons and the combined effect of SOC and crystal field splitting leads to an energy level splitting in which there is only one half-filled band; it has $J_{eff} = \frac{1}{2}$ character. By varying values of the Coulomb interaction U it is possible to induce a metal-insulator transition which happens for moderate values of $U \sim 2$ eV.

The interplay between SOC, CFS and electronic correlations in general leads to a high variety of physical properties, which are observed for example, in other iridates. For some specific situations a special type of bond-directional interactions emerges (see **Sec. 1.3**), where the spin-spin magnetic interaction depends on the spatial orientation of the bond that connects sites of the interacting spins. This leads to a new type of magnetic materials: *Kitaev materials*. The Kitaev interaction itself leads to a frustration on the triangular lattice giving rise to complicated magnetic orders. The simplest model, used to describe this interaction is the Kitaev model [17]. When it is realized on the honeycomb lattice it has a very peculiar magnetic *quantum spin liquid* ground state. A possible way to realize this model in real materials was proposed by Jackeli and Khaliullin [18, 19] for A_2BO_3 compounds with a hexagonal arrangement of B ions (where the B ion is situated in an octahedral O cage) and is described in **Sec. 1.3.1**. The system should be an insulator with strong SOC. The key ingredient is that the BO_6 octahedra are arranged in the way they share an edge. In the ideal case this leads to the suppression of the Heisenberg exchange interaction due to the destructive interference of hoppings between the neighboring Ir atoms, so the only remaining interaction between the nearest neighbors is the Kitaev interaction [19].

After the discussion of the theoretical background, in **Chapter 2** we will review some relevant experimental and theoretical results available in literature. The discussion will start with **bismuthates** concentrating mostly on $BaBiO_3$ as a representative of the whole class (**Sec. 2.1**). $BaBiO_3$ is a charge-ordered insulator, but doping induces an insulator-metal transition, leading to a superconducting state with the relatively high $T_c \sim 34$ K [3]. $BaBiO_3$ was synthesized in 1963 [20] and the charge-ordering in $BaBiO_3$ was reported in 1976 [11]. For the fist time superconductivity with a T_c of 13 K was reported in 1975 for $BaPb_{1-x}Bi_xO_3$ [10] and a superconductivity with a T_c of 34 K was reported in 1988 for $Ba_{0.6}K_{0.4}BiO_3$. Bismuthates form a class of non-cuprate oxide

superconductors and until the discovery of MgB_2 in 2001 [21] it was one of the superconductors with the highest T_c's except the cuprates (the first cuprate superconductor was discovered in 1986 in the Ba-La-Cu-O system [22]).

After a discussion of the main experimental finding, we will move on to describe theoretical models of charge density wave (CDW) and superconductivity. Due to sizable self-interaction contained in semilocal functionals [23, 24], standard DFT calculations cannot reproduce the charge-ordered insulating state, since they underestimate the lattice distortion and the corresponding gap. The problem was solved only recently in Ref. [25], using hybrid density functional theory/Hartree Fock approach HSE functional (Heyd, Scuseria and Ernzerhof) [26]. A related issue is the suppression of the charge density wave distortion by doping. In standard DFT, the CDW distortion is suppressed at a much lower doping ($x = 0.25$) [25] than in experiments ($0.37 < x < 0.53$) [3]. HSE calculation solved this issue, showing that at a moderate values of doping the bipolarons are formed, and they are able to trap two holes [25], resulting in an insulating state.

While the description of the normal-state phase diagram is solved, the origin and nature of superconductivity in $BaBiO_3$ remains an open issue. *Ab initio* calculations report values of the electron-phonon coupling parameters much smaller than observed in experiments [27–29]. Different alternative explanations of superconductivity were also proposed. Among them the attractive Hubbard model [30] with a negative U, and a superconducting mechanism due to the condensation of bipolarons [31].

We start the discussion of **iridates** in **Sec. 2.2** describing the peculiar case of the relativistic $J_{eff} = \frac{1}{2}$ Mott insulator, discovered in Sr_2IrO_4 [16]. We first explain how the general mechanism of relativistic MIT works, and then explore how the MIT can be tuned in actual compounds through doping and dimensionality control.

After this, we highlight another intriguing class of iridates, in which Ir is pentavalent [32, 33]. Under special circumstances, that depend mostly on the relative strength of the SOC and CFS, a nonmagnetic $J_{eff} = 0$ state can emerge, where a low spin $S = 1$ state would be expected, when the SOC is not strong enough [34]. The discussion of iridates finishes highlighting the possible candidates for quantum spin liquid, focusing mainly on Na_2IrO_3 and α-Li_2IrO_3.

After giving an overview on the available experimental and theoretical literature on bismuthates and iridates, in **Chapter 3** we will discuss the **methods** used in this work to investigate these systems. We start with a short introduction in **Sec. 3.1** to the approaches to solve the quantum mechanical problem, namely the Hartree-Fock method, which is a wave function-based approach, and Density Functional Theory (DFT), where the electronic density serves as the main variable. Density Functional Theory is in principle an exact theory. In its current implementations, it captures the main features of the electronic structures of most existing compounds remarkably well. However, it fails for a wide class of systems, i.e. strongly correlated systems, in which the local correlations between electrons cannot be approximated at the mean-field level. A straightforward way to improve the standard DFT is to combine it with the Hartree-Fock theory: the latter offers a better description of the exchange energy (the expression of exchange energy

of a Slater determinant is indeed exact). Various schemes how to couple the two theories were proposed. We will highlight the functional, proposed by Heyd, Scuseria and Ernzerhof [26], that we will later used to get a correct description of the electronic structure of $BaBiO_3$.

After describing the standard quantum mechanical simulations, which assume that the crystal structure of a compound is known, we will describe tools that are able to predict, manipulate and analyze crystal structures. We need these tools to predict new materials or the behavior of materials in conditions which are not easily accessible in experiment.

In **Sec. 3.3** we describe a method to obtain the coordination environment as implemented in the `CHEMENV` module of `PYMATGEN` package [35, 36]. This tool permits to automatically determine the local coordination environment of an atom for a given structure, using a three-steps procedure: first a list of neighbors of all sites in a unit cell is determined by portioning space using Voronoi diagrams [37]. After that, *unreasonable* neighbors are discarded (for example, atoms that are too far from a given site). The final stage is to find a model polyhedron that can be related to the real polyhedron. The concept of the Continuous Symmetry Measure is introduced to quantify the similarity between the model and the real polyhedron [38].

The next topic discussed in **Sec. 3.4** is the classification of distortions by means of *isotropy* subgroups [39]. This group-theoretical method permits to describe all possible distortions of a given crystal which give rise to a lowering of its symmetry. The method can be used, for example, to describe the distortions in the perovskite structure, such as the breathing and tilting distortion [40, 41]. Another application is to predict the crystal structure of the phase resulting from a second-order phase transition of a parent phase.

We conclude the chapter with a discussion in **Sec. 3.5** of the evolutionary crystal structure prediction method as implemented in the `USPEX` package [42–44], which is the main computational tool that we used to predict the crystal structures. The idea of the method is to apply the ideas of biological evolution to solve the optimization problem at the heart of crystal structure prediction. In this approach, a set of crystal structures for a given pressure and composition represent a *population*, which is evolved using operations inspired by biological evolution (crossover, mutation, selection), to find individuals that minimize the enthalpy (fitness) of the population.

Part II: Original results

In the second part of this thesis we present our original results of investigation of specific compounds from the bismuthate and iridate families.

Chapter 4 is based on two published papers:

1. *Ab initio* prediction of the high-pressure phase diagram of $BaBiO_3$[1].
2. *Ab initio* study of $ABiO_3$ (A=Ba, Sr, Ca) under high pressure[2].

In the first paper, we investigated the possibility to suppress the charge density wave (CDW) in $BaBiO_3$ and induce the insulator-metal transition by applying an external pressure up to 100 GPa. We show that $BaBiO_3$ undergoes three structural phase transition: from monoclinic to triclinic at about 20 GPa, from triclinic to *clustered* monoclinic at 28 GPa and, finally, to highly distorted structure at about 87 GPa. None of these phases is a metal, thus contradicting our original hypothesis that pressure could be used to induce superconductivity in $BaBiO_3$. After our publication, a similar study appeared, where joint theoretical and experimental results are present [6]. The measured resistivity data confirm our prediction that $BaBiO_3$ is insulator up to 80 GPa and the theoretical calculations confirm this is due to the formation of distorted structures similar to ours.

In the second paper we extend our investigations for $BaBiO_3$ to two other alkaline-earth bismuthates, $SrBiO_3$ and $CaBiO_3$. We compute the relative phase diagrams and find that in each case there are several structural phase transitions. However, we also identify a common trend: all structures exhibit a transition to a highly distorted structure, which is different for each compound. The shift of the transition pressure w.r.t the cation radius is explained by means of the chemical pressure with the only exception for $BaBiO_3$: the *clustered* phase of $BaBiO_3$, which is stable between 28 and 87 GPa, shifts the transition to a higher pressure. We find an explanation for the formation of distorted structures, showing that it is energetically favorable increase of the number of the nearest neighbors. In addition, charge disproportionation is robust in all compounds and with a strong tendency to charge disproportionate it is not possible to have a highly symmetric structure; thus all high pressure phases are highly distorted.

In the next chapter (**Chapter 5**) we focus on iridates. We start our discussion with preliminary results of the prediction of the ternary sodium (Na), iridium (Ir), oxygen (O) phase diagram obtained with evolutionary crystal structure prediction. Compounds in this family show a rich variety of physical properties due to the interplay between the SOC, CFS and strong electronic correlations. Several structures, such as Na_2IrO_3 and $Na_4Ir_3O_8$, were synthesized and proposed as candidates for a quantum spin liquid state [45, 46]. However, these are only a few structures, and it is very likely that more compounds, with different stoichiometry, may be synthesized in the future. The aim of our study is to make a broad search of possible stable and metastable compounds at unknown compositions and, analyzing their crystal structures with the automated methods discussed in Sec. 3.3, identify compositions that could host phases with interesting physics, based on electron count and lattice geometry.

During this preliminary search, an unexpected group of metastable 2D phases of IrO_2 emerged during the search for possible binary Ir_xO_{1-x} chemical compositions. The structure lowest in energy is a 1T polytype of the same type that appears in TM dichalcogenides. Under real conditions, when SOC and magnetic order are taken into account, the structure is dynamically stable and this is a strong indication that this phase may be stabilized in experiment under appropriate conditions. The structure may be an attractive platform to realize a triangular Kitaev material.

1. Physical properties of the systems of interest

This chapter describes physical concepts, which are relevant to the original material contained in Part II of this thesis. Is starts from describing the mechanism of formation of typical crystal structures in TMO compounds, continuing with the explanation of relevant microscopical phenomena, such as strong correlations, spin-orbit coupling and exchange interactions, following with description of important macroscopic phenomena: charge ordering, metal-to-insulator transitions and frustrated magnetism.

1.1. Crystal structure

1.1.1. Typical crystal structures of transition metal oxides

In this section we will review the most common structures of transition metal oxides (TMO) and briefly explain the main geometrical mechanisms responsible for their formation. For this task we will mostly follow the Ref. [47].

For TMO the most important type of bonding between atoms is ionic bonding, so to a first approximation for a given compound ionic bonding together with the sizes of the corresponding ions determines the resulting crystal structure. The ionic radius of an atom depends on its species, valence, spin state and is different for different coordination state.

The main building block in TMO is oxygen, which is much bigger than most transition metal (TM) ions: the typical ionic radius of O^{2-} is $\sim 1.35 - 1.42$ Å, 3d TM is $\sim 0.5 - 0.7$ Å; the radius of Ir^{4+} is ~ 0.625 Å [48]. Thus, the description of the crystal structure formation should start from oxygen, that plays the most important role. This construction can be understood as a close packing of large ions, namely oxygens, while smaller atoms occupy the interstices.

The construction starts with forming a close packing of O atoms. For a single plane the closest packing is hexagonal (see Fig. 1.1c and in Fig. 1.1a each oxygen of such layer is depicted as an empty circle). For the next layer there are two possibilities: atoms can lie either on top of the center of the "up-triangles" of Fig. 1.1a (marked by squares) or "down-triangles" (marked by triangles). We will denote the positions of atoms of the first layer with A, the positions of the atoms on the layer of squares with B, and the layer of triangles with C.

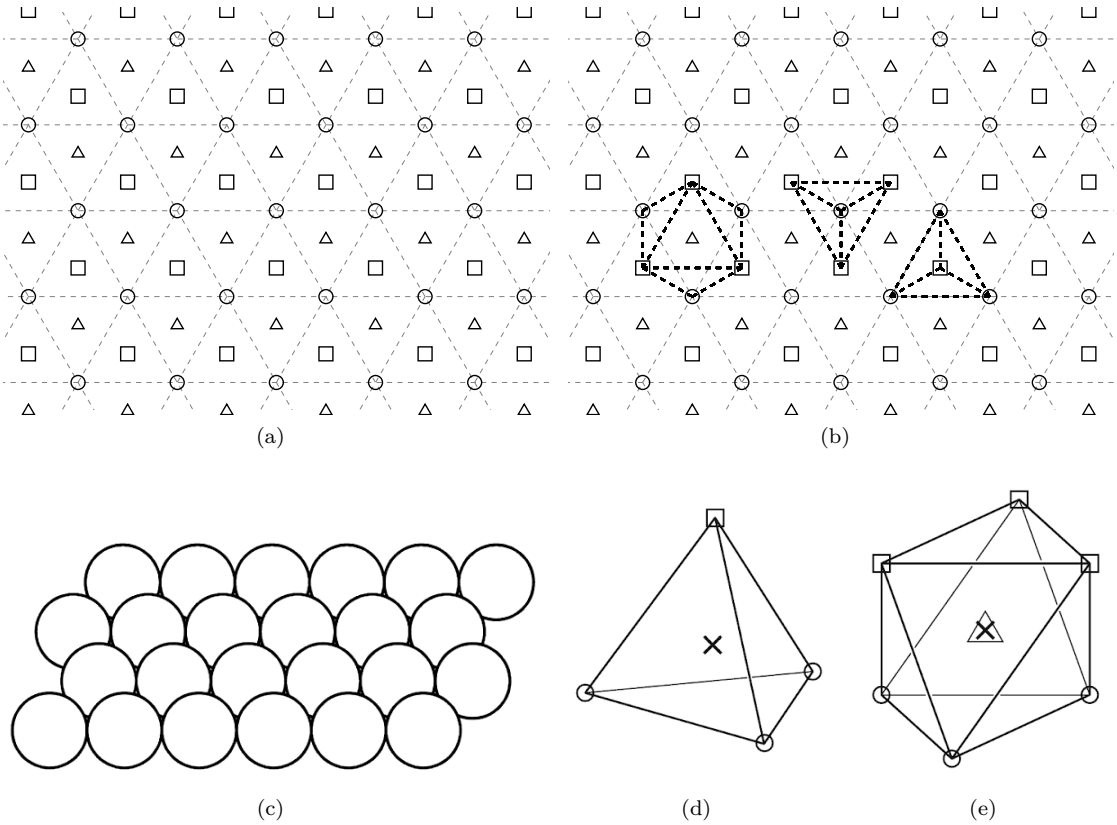

Figure 1.1.: (a) Possible locations of ions in the next close-packed layer of such ions (squares or small triangles); (b) same picture indicating typical TM coordination environments: octahedral and tetrahedral (dashed lines); (c) close packing of layer of large anions; typical location of small TM ion (crosses) in (d) tetrahedral and (e) octahedral interstices formed by large anions. Figs. 3.38 and 3.39 are adapted from *Transition Metal Compounds* (p. 81), by D. Khomskii, 2014, Cambridge: Cambridge Univ. Press [47]. Copyright 2014 by Cambridge Univ. Press. Adapted with permission.

Using these considerations it is possible to motivate the construction of a tetrahedral or octahedral coordination environment for the TM ion, which are typical for the TM ions. Consider two layers of O atoms with atoms at positions A and B (circles and squares in Fig. 1.1a). There are two types of interstices between these layers: tetrahedral positions below each square or above each circle, as indicated by dashed lines on the central and right side of Fig. 1.1b, and octahedral positions with TM ion occupying positions marked with triangles (left side of Fig. 1.1b). The actual tetrahedron and octahedron are depicted on the Fig. 1.1d and Fig. 1.1e respectively.

Close-packed oxygens can have different stacking, for example $ABAB\ldots$, $ABCABC\ldots$, etc. Different stacking will result in different packing of TM-O polyhedra. For example, $ABAB\ldots$ stacking will form empty triangles on top of each other and if they are occupied by a TM ion this gives columns of face sharing MO_6 octahedra. If the TM ion M only occupies the octahedral hole

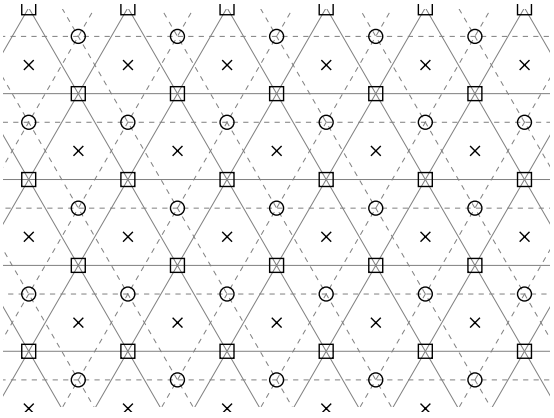

Figure 1.2.: (AMB) stacking pattern of 1T-IrO_2 crystal structure. A- and B-stacking of oxygen are depicted with open circles and squares respectively. Ir ions are depicted with crosses. B-layer is situated on top of A-layer and Ir layer is in between.

in every second layer, i.e. $(AMB)(AMB)\ldots$, we have the CdI_2 structure, where TM ions form two-dimensional triangular layers of edge-sharing MO_6 octahedra, similarly as in our predicted IrO_2 monolayer as depicted in Fig. 1.2 (see Sec. 5.2).

Some of the most common TMO structures are constructed as follows: the NaCl-type structure is formed when the sequence is $ABCABC\ldots$, in which TM ions occupy all octahedral interstices. The *rutile* structure (TiO_2, IrO_2 etc.) can be formed by "even" M' rows of edge-shared octahedra (the top horizontal line of triangles in Fig. 1.1a) in the first layer and "odd" M'' rows in the second layer (the second from top horizontal line of triangles in Fig. 1.1a), $AM'BM''AM'BM''\ldots$ The *spinel* AB_2O_4 structure may be visualized as $ABCABC\ldots$ close packing with A occupying tetrahedral interstices and B octahedral. The α-Li_2IrO_3 structure can be described as $ABCABC\ldots$ oxygen stacking with Li and Ir atoms occupying octahedral positions: one layer is fully occupied by Li atoms and the other layer has $\frac{1}{3}$ concentration of Li and $\frac{2}{3}$ concentration of Ir. In the latter layer Li is situated in the middle of the hexagons formed by Ir atoms.

1.1.2. Perovskite structure

The perovskite structure, together with some of its variants, is one of the most common structures for TMOs, found in compounds such as $SrTiO_3$, $BaTiO_3$, $SrIrO_3$ and many other.

The *perovskite* structure, found in ABO_3 compounds, is constructed by close packing of oxygens with $ABCABC\ldots$ stacking, where A cations, that usually have comparable to O sizes, occupy some of the positions of oxygen in every other row. We can imagine rows, where A forms a sublattice, and in this sublattice the A and O sites form a chessboard pattern, see Fig. 1.3, where the A cation is 12-times coordinated by oxygens. The B cation occupies all available octahedral positions.

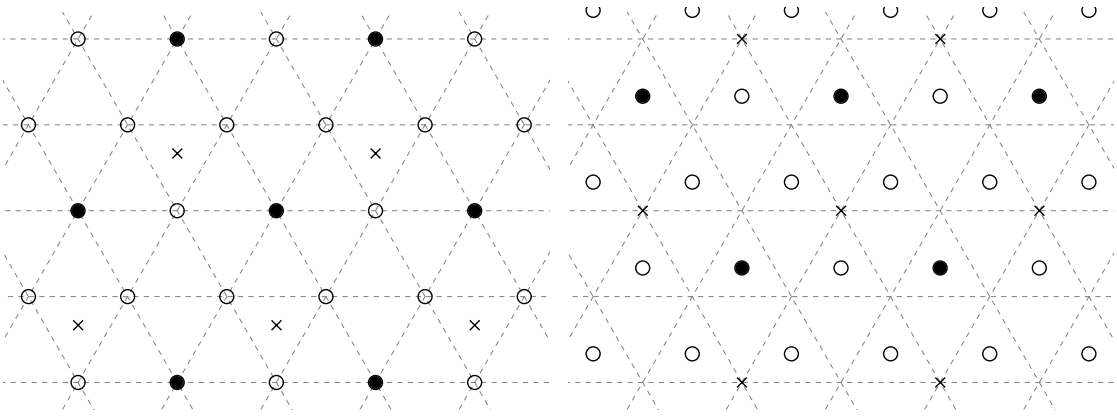

(a) A-layer (b) B-layer

Figure 1.3.: ABO_3 perovskite close packing with $ABCABC\ldots$ stacking. Only (a) A-layer and (b) B-layer are depicted. A – filled circles, B – crosses and O – empty circles.

However, the most common way to represent the *perovskite* structure is using a cubic lattice. There are two such representations: A-type, see Fig. 1.4a, where the A ions occupy the center of the cube, B ions occupy its corners and O are in the middle of each edge and B-type, see Fig. 1.4b, where A ions occupy the corners of a cube, B are at the center of the cube and O are in the middle of each face.

Actually, only a few compounds form an ideal cubic perovskite structure; usually we deal with distorted perovskite structures. There are three types of possible distortions [50]: distortions of the octahedra, cation displacements within the octahedra and tilting of the octahedra. The first two types are driven by electronic instabilities: for example, Jahn-Teller distortion is a mechanism of distortions of the octahedra (like in $KCuF_3$ [51]), and the ferroelectric displacement is a mechanism of cation displacements, like in $BaTiO_3$.

The most common is the third type (tilting), and we will give more attention to it in the following. Octahedral tilting can be realized by tilting rigid MO_6 octahedra while maintaining their corner-sharing connectivity. Usually, it happens when the A cation is too small to fit in octahedral network and the energy is gained by shortening the A-O distances.

These distortions depend on the relative sizes of corresponding ions. The ideal close packing in ABO_3 perovskites corresponds to the situation when $2(R_B + R_O) = a$ and $2(R_A + R_O) = \sqrt{2}a$, where a is the lattice parameter of the cubic lattice, R_A, R_B and R_O are radii of A cation, B cation and oxygen respectively. An indicator of structural stability and distortions of crystal structure can be derived by taking the ratio between these two quantities, called *Goldschmidt's tolerance factor* [52]:

$$t = \frac{R_A + R_O}{\sqrt{2}(R_B + R_O)}. \tag{1.1}$$

In the ideal case $t = 1$.

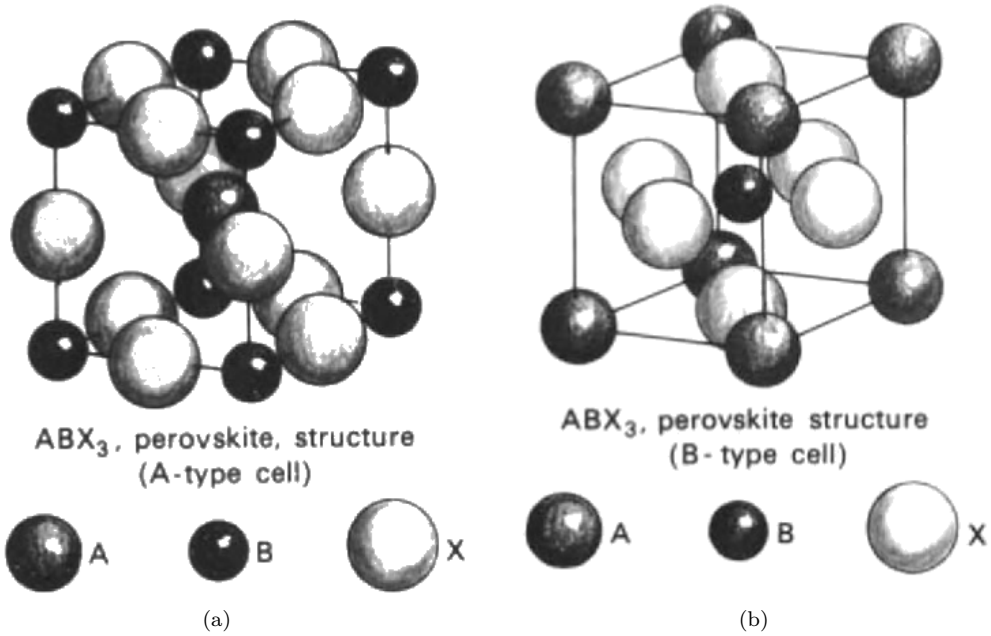

Figure 1.4.: Two types of *perovskite* structure representation: (a) A-type centered on the B ion and (b) B-type centered on the A ion. A ions are depicted by big dark gray spheres, B ions are depicted by small black spheres and X ions are depicted by big white spheres. Adapted from *Structure and Properties of Inorganic Solids* (pp. 169,170), by F. Galasso, N. Kurti, and R. Smoluchowski. 2016, Elsevier Science [49]. Copyright 2016 by Elsevier Science. Adapted with permission.

Empirically, the perovskite structure is stable in the range $0.71 \leq t \leq 1$. For $t > 1$ hexagonal structures tend to form, in the range $0.9 - 1$ — cubic or tetragonal, in the range $0.7 - 0.8$ –0 orthorhombic or rhombohedral (the A ions are too small to fit into the B ion interstices), where octahedra rotations appear. They usually lead to a decrease in the B-O-B angle, leading to a reduction of the effective B-O-B hopping and, thus of the bandwidth. This can strongly influence the physical properties of compounds; for example it is possible to induce a metal-to-insulator transition by substitution of the A ion with a smaller one.

A powerful tool to classify rigid octahedral rotations is provided by the *Glazer notation* [53]. Glazer analyzed and classified all possible tilting patterns, and arrived to 23 tilt's systems. Octahedral rotations can be obtained as consecutive rotations around the cubic axes, a, b and c respectively. Octahedra are connected and if one is rotated around c axis clockwise, its inplane neighbors should rotate anti-clockwise to favor the connectivity. But the octahedron in the next plane is free to rotate in any direction. If it is rotated clockwise, then rotation is referred as the "in phase" rotation and is denoted c^+; if anti-clockwise – "out of phase" and is denoted c^-. It is assumed that the octahedra in the next neighbor plane will rotate in the same way as the first octahedra; hence the periodicity in the c direction can only be doubled. Rotations can also occur

around the a and b axes, and they are denoted in the same manner.

The notation $(a^+b^-c^+)$ classifies all possible rotations, where the position of the symbol represents the rotation axis. The symbol itself corresponds to the amplitude of rotation. If there is no rotation around some axis "0" is used instead of "+" or "-". For example, the notation $(a^0b^+b^+)$ will describe no rotation around the a axis, and two in-phase rotations with the same amplitude around the b and c axes.

It is possible to have a more complex perovskite structure, *double* perovskite, with chemical composition $AA'BB'O_6$. Since in this case the ions on the same crystallographic position can have different sizes, another type of distortion appears: a *breathing* distortion, corresponding to an alternating size of octahedra. Usually, it is coupled to tilting distortion and such a combination can lead to a big variety of possible structures. All possible structures can be constructed by means of group theory, namely *isotropy* subgroups; this method will be described later, in Section 3.4.

1.2. Models to describe electronic structure

The previous section gave a brief description on how crystal structure of typical TMO is formed. Now we want to describe models used to investigate an electronic structure of TMO and corresponding energy scales.

In TMO compounds the relevant atomic orbitals to describe the low-energy electronic excitations are the d-orbitals of the TM ion and the p-orbitals of O. In an isolated atom, the p-orbitals are triply degenerate (the orbital quantum number l can take values $-1, 0, 1$) and d-orbitals are fivefold degenerate ($l = -2, -1, 0, 1, 2$) for each spin.

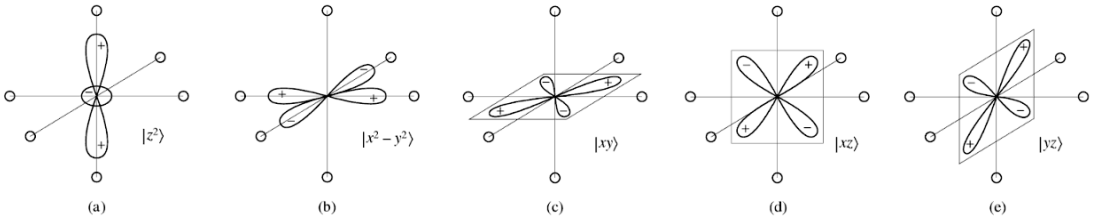

Figure 1.5.: Typical shapes (electron densities) of orbitals: (a, b) e_g orbitals; (c, d, e) t_{2g} orbitals. Fig. 3.3 is adapted from *Transition Metal Compounds* (p. 41), by D. Khomskii, 2014, Cambridge: Cambridge Univ. Press [47]. Copyright 2014 by Cambridge Univ. Press. Adapted with permission.

Atomic p-orbitals can be represented using *cubic harmonics* in the following way:

$$\begin{aligned} p_x =& \frac{1}{\sqrt{2}}\left(Y_1^{-1} - Y_1^1\right), \\ p_y =& \frac{i}{\sqrt{2}}\left(Y_1^{-1} + Y_1^1\right), \\ p_z =& Y_1^0, \end{aligned} \tag{1.2}$$

where Y_l^m are spherical harmonics, with orbital quantum number l and magnetic quantum number m ($-l \leq m \leq l$). They are dumb-bell shaped pointing towards corresponding Cartesian axis.

The representation of d-orbitals in terms of cubic harmonics is following:

$$\begin{aligned} d_{xy} =& \frac{i}{\sqrt{2}}\left(Y_2^{-2} - Y_2^2\right), \\ d_{yz} =& \frac{i}{\sqrt{2}}\left(Y_2^{-1} + Y_2^1\right), \\ d_{xz} =& \frac{1}{\sqrt{2}}\left(Y_2^{-1} - Y_2^1\right), \\ d_{x^2-y^2} =& \frac{1}{\sqrt{2}}\left(Y_2^{-2} + Y_2^2\right), \\ d_{z^2} =& Y_2^0. \end{aligned} \tag{1.3}$$

The typical shape of d-orbitals is presented in Fig. 1.5.

The minimal Hamiltonian that describes the electronic structure of TMO crystals

$$H = H_{TB} + H_{int} + H_{SOC}. \tag{1.4}$$

comprises three terms: a kinetic term (H_{TB}) describing the hopping of electrons between lattice sites; an interaction term (H_{int}), describing strong local correlations beyond the mean-field single particle approximation, and a spin-orbit coupling term (H_{SOC}), which describes the interaction between orbital and spin degrees of freedom - for reasons which will become clearer in the following, we have decided to treat the SOC separately. The meaning of each of these terms, and their relevance for the electronic structure of TMO, is briefly described below.

1.2.1. Kinetic term

The first term, H_{TB}, is a tight-binding model (TB) and includes contributions from the kinetic energy of electrons and the atomic potentials (onsite energies):

$$H_{TB} = -\sum_{\substack{i,j \\ \nu,\mu,\sigma}} t_{ij}^{\nu\mu}\left(c_{i\sigma\nu}^\dagger c_{j\sigma\mu} + h.c.\right), \tag{1.5}$$

where $c^{\dagger}_{i\sigma\nu}$ and $c_{i\sigma\nu}$ are creation and annihilation operators that add or remove an electron with spin σ to ν-orbital at site i. The summation over i and j runs over all atomic sites in the crystal. Exploiting the periodicity of the crystal, the sum (1.5) is usually rearranged so that the index i runs on all lattice sites, while j runs only on selected shells of neighbors. ν and μ are orbital indices, which indicate a specific orbital at a given site. Thus, in TMOs, $\nu, \mu = \{p_x, p_y, p_z\}$ if the site is occupied by an oxygen atom, and $\nu, \mu = \{d_{xy}, d_{xz}, d_{yz}, d_{x^2-y^2}, d_{z^2}\}$ for a TM ion. Finally, the sum over σ runs over the two possible spin states.

$t^{\nu\mu}_{ij}$ is a *hopping* matrix element between ν orbital at site i and μ orbital at site j, corresponding to their overlap, if $i \neq j$ or $\nu \neq \mu$. For two atomic orbitals, $\varphi_{i\sigma\nu}(\vec{r})$ at site i and $\varphi_{j\sigma\mu}(\vec{r})$ at site j, it can be expressed as:

$$t^{\nu\mu}_{ij} = \int d\vec{r} \varphi^{*}_{i\sigma\nu}(\vec{r}) \frac{\hbar^2}{2m_e} \nabla^2 \varphi_{j\sigma\mu}(\vec{r}), \tag{1.6}$$

where m_e is the mass of an electron and $\hbar$ is the reduced Plank constant. If $i = j$ and $\nu = \mu$, it is called an *onsite energy* $\varepsilon_{i\nu} = t^{\nu\nu}_{ii}$ corresponding to the energy level of orbital ν situated at site i.

Using Bloch's Theorem, in a periodic solid the TB Hamiltonian (1.5) can be transformed to reciprocal space and reduced to the diagonal form:

$$H^{k}_{TB} = \sum_{\vec{k},i,\sigma} \epsilon_{\sigma i}(\vec{k}) c^{\dagger}_{\vec{k}\sigma i} c_{\vec{k}\sigma i} \ , \tag{1.7}$$

where $\epsilon_{\sigma i}(\vec{k})$ is a dispersion relation for i-th band with spin character σ. $c^{\dagger}_{\vec{k}\sigma i}$ and $c_{\vec{k}\sigma i}$ are creation and annihilation operators for a Bloch wave at momentum $\vec{k}$ in band i associated with spin σ. Summation over $\vec{k}$ runs over $\vec{k}$-vectors in the 1st Brillouin zone.

1.2.2. Crystal field splitting

The overlap between the d orbitals of the TM ion and the p orbitals of O leads to their *hybridization*. The result of this hybridization strongly depends on the type of the TM ion environment. In this section the interplay between them is described.

In a crystal the spherical symmetry of an atom is violated and the resulting point symmetry is dictated by the symmetry of the crystal, lifting the degeneracy of d orbitals: the energy levels split in a way which is dictated by the point symmetry of the coordination environment of the TM ion. This splitting is called *crystal field splitting* (CFS). The new degeneracies are determined from the degeneracies of the corresponding irreducible representations of the point group associated with this point symmetry.

For example, in a cubic field the atomic d orbitals split into two-fold degenerate e_g orbitals, of d_{z^2} and $d_{x^2-y^2}$, and three-fold degenerate t_{2g} orbitals, of d_{xy}, d_{yz} and d_{xz}. The splitting between the onsite energies of the e_g and t_{2g} orbitals is denoted as Δ_{CF}.

As mentioned in Sec. 1.1.1, the typical coordination environments for the TM ion in TMO

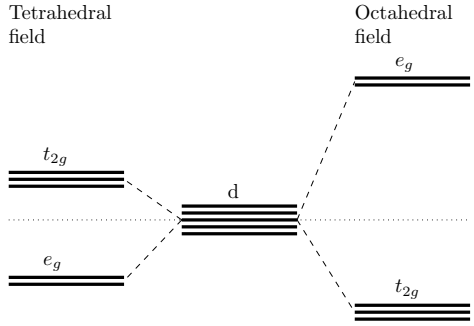

Figure 1.6.: The energy splitting due to the crystal field splitting in tetrahedral (left panel) and octahedral (right panel) environment.

compounds are octahedral and tetrahedral. The energy level diagrams corresponding to these two coordination environments are plotted in Fig. 1.6. The important difference between the two is that in the octahedral environment CFS t_{2g} levels are below e_g while in the tetrahedral one the order of CFS is inverted. The reason is that in octahedral environment the overlap between the p orbitals of O with the e_g orbitals of the TM ion is stronger than that with the t_{2g} orbitals. In case of tetrahedral splitting the situation is opposite. The value of the tetrahedral splitting is smaller than the value of the octahedral splitting: $\Delta_{CF}^{tetrahedral} = 0.44\Delta_{CF}^{octahedral}$.

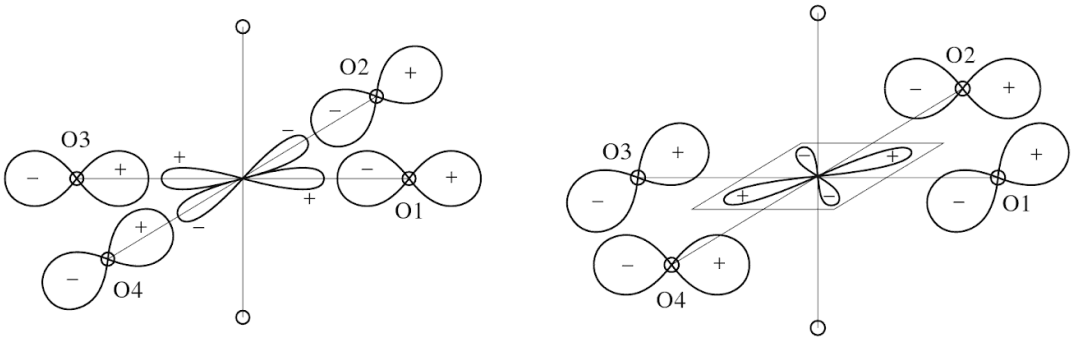

Figure 1.7.: Illustration of the covalency contribution to the crystal field splitting for e_g electrons (left panel) and t_{2g} electrons (right panel) due to p-d hybridization. Figs. 3.5 and 3.7 are reprinted from *Transition Metal Compounds* (pp. 43,45), by D. Khomskii, 2014, Cambridge: Cambridge Univ. Press [47]. Copyright 2014 by Cambridge Univ. Press. Reprinted with permission.

We will now describe how CFS can be derived from the tight-binding model using octahedral coordination environment as an example, where TM ion has six O nearest neighbors. For this example, we will neglect neighbor shells farther than the first. This situation is depicted in Fig. 1.7, where TM ion is situated in the middle and six oxygens are depicted as empty circles. For this example, we will use a simplified notation: in particular, we will omit site indices in

hopping matrix element using only orbital indices, i.e $t_{\nu\mu}$, since we have only nearest neighbor hopping, and omit site indices for onsite energies: the onsite energy of the d orbitals of the TM ion is ε_d and the onsite energy of the p orbitals of oxygens is ε_p.

A crucial concept to understand the following discussion is that of orbital hybridization; this is very easily understood considering a model with only two sites: one with d orbital of TM ion and one with p orbital of oxygen with the orientation such that they have a finite overlap (the actual type of orbital is not important now). The hopping between p and d orbitals is described by a single matrix element t_{pd}. For this case, the hopping between p orbitals of O and d orbitals of TM ion describes a strength of hybridization between these orbitals and we will use a short notation t_{pd} for hopping between these two sites.

As a result of p-d hybridization, a bonding (ε_b) and an antibonding (ε_a) levels form, with energies:

$$\varepsilon_b = \varepsilon_p - \frac{t_{pd}^2}{\varepsilon_d - \varepsilon_p}, \tag{1.8}$$

$$\varepsilon_a = \varepsilon_d + \frac{t_{pd}^2}{\varepsilon_d - \varepsilon_p} \tag{1.9}$$

if $\varepsilon_d > \varepsilon_p$ and $t_{pd} \ll \varepsilon_d - \varepsilon_p$. Bonding orbital has the most contribution from p orbital, while the most contribution to antibonding orbital is from d orbital.

Coming back to the problem of CFS in octahedral environment, we now discuss the CFS for e_g ($d_{x^2-y^2}$ and d_{z^2}) and t_{2g} (xz, xy, yz) orbitals in terms of p-d hybridization.

As a representative of e_g orbitals we will use $d_{x^2-y^2}$ (similar considerations apply for d_{z^2} orbital). Also in this case we consider a single site.

For symmetry reasons, only the four p orbitals of oxygens, that lie in xy plane and point towards the lobes of the $d_{x^2-y^2}$ orbital have a finite overlap (see left panel in Fig. 1.7). This type of hybridization is the strongest possible and is usually called σ-hybridization; we will denote the corresponding matrix element as t_{pd}^{σ}, where the superscript σ emphasizes the type of overlap.

The corresponding term of the Hamiltonian in TB notation can be written as

$$H_{TB}^{x^2-y^2} = t_{pd}^{\sigma}\left[d_{x^2-y^2}^{\dagger}(p_{1x} - p_{2y} - p_{3x} + p_{4y} + h.c.)\right], \tag{1.10}$$

For creation and annihilation operators instead of orbital index we will use the orbital character itself, so $d^{\dagger}$, d and $p^{\dagger}$, p are creation and annihilation operators for the electron to be added/removed to a d and p orbital respectively. Index accounts for a specific type of orbital and distinguishes between different sites, i.e. p_{ix} refers to the p_x orbital at i site. The site numbering is the same as in Fig. 1.7. For d orbital the site index is omitted and only the orbital type is written.

For the d_{z^2} the situation is analogous, but one needs to also account for the p_z orbitals of oxygens situated above and below the xy-plane (upper and lower empty circles in Fig.1.7). Again, the

hybridization is of σ-type, but two different hopping processes with different amplitude are involved: hopping between oxygens situated in the xy plane and the ones situated out of the xy plane. However, the shapes of d_{z^2} and $d_{x^2-y^2}$ orbitals are represented by the functions that belong to the same irreducible representation of the O_h point group and the resulting energy splitting for the electron in the d_{z^2} orbital is the same as for the $d_{x^2-y^2}$ case. The same result is obtained diagonalizing the TB Hamiltonian written for the d_{z^2} and $d_{x^2-y^2}$ orbitals using the appropriate values for the hopping amplitudes. For brevity we skip this derivation here; for example, the derivation can be found in Ref. [54].

To describe the case of the t_{2g} orbitals we will discuss only the case of d_{xy} orbital, since the same considerations apply to d_{xz} and d_{yz} orbitals, which are equivalent by symmetry. Also in this case, due to symmetry reasons, only four p orbitals of oxygens, that lie in the xy plane will have a finite overlap with d_{xy} orbital, but in this case they are perpendicular to TM-O bond (see right panel of Fig. 1.7). This kind of hybridization is called *π-hybridization* and to denote the corresponding hopping matrix element we will use t_{pd}^{π} notation. A TB model can be derived also in this case:

$$H_{TB}^{xy} = t_{pd}^{\pi}\left[d_{xy}^{\dagger}(-p_{1y} - p_{2x} + p_{3y} + p_{4x} + h.c.)\right]. \tag{1.11}$$

It is crucial that the strength of π-hybridization is smaller than that of σ-hybridization (typically $t_{pd\pi} \sim \frac{1}{2}t_{pd\sigma}$). For this reason bonding-antibonding splitting (similar as described by eq. (1.8)) will be smaller for the t_{2g} orbitals than for the e_g ones. The resulting picture is shown schematically in Fig. 1.8. The resulting antibonding orbitals are mostly of d character and the e_g and the t_{2g} orbitals are split. Bonding and antibonding orbitals form orbitals for each of the two symmetries considered: two antibonding orbitals with e_g symmetry and three with t_{2g}; same considerations hold for bonding orbitals. Antibonding e_g orbitals are shifted higher in energy than t_{2g} orbitals and the energy difference between them is Δ_{CF}.

It is worth noting, that in general two mechanisms contribute to CFS effect: the one mentioned before, i.e. covalent bonding, and the Coulomb potential generated by the surrounding ions. In fact, for the case $\varepsilon_d > \varepsilon_p$, that was assumed in the derivation before, the effect of two contributions are qualitatively the same. We discussed only covalent bonding mechanism since it is relevant to the description of kinetic term of the Hamiltonian and discussion of the other mechanism gives no contribution to the qualitative description of CFS.

We want to note that degeneracy can be lifted further, if distortion of the coordination environment is applied. For example, tetragonal distortion of octahedra, as depicted on Fig. 1.9, splits e_g levels into nondegenerate d_{z^2} and $d_{x^2-y^2}$, and splits t_{2g} into d_{xy} and degenerate d_{xz}, d_{yz} pair. The order of resulting levels depends on whenever octahedra was elongated or contracted.

In a solid the discrete atomic energy spectrum is transformed into energy bands, that describe the range of energies that an electron in a solid may have. The wave function that represents a single band depends on the wave vector $\vec{k}$. The degeneracy of the band can be lifted by the CFS. However, now the energy splitting is determined not from the irreducible representations

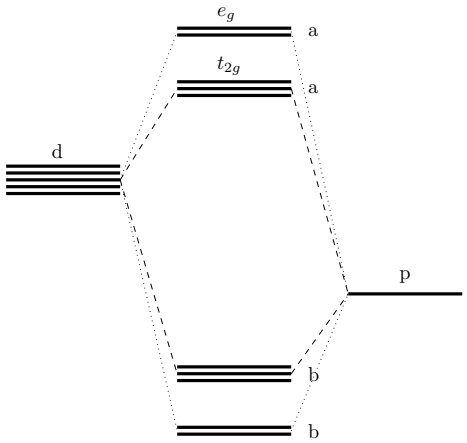

Figure 1.8.: The process of formation of bonding (b) and antibonding (a) p-d orbitals. Different splitting for e_g and t_{2g} is due to the different hybridization strength between respective d and p orbitals.

of the point group associated with the CFS, but from a subgroup that leaves a given $\vec{k}$-vector invariant. The discussed before energy splitting of the energy levels for an electron at a single site is the same as the splitting of the band at the Γ point, since the subgroup that leaves $\vec{k} = (0, 0, 0)$ invariant is the entire point group itself.

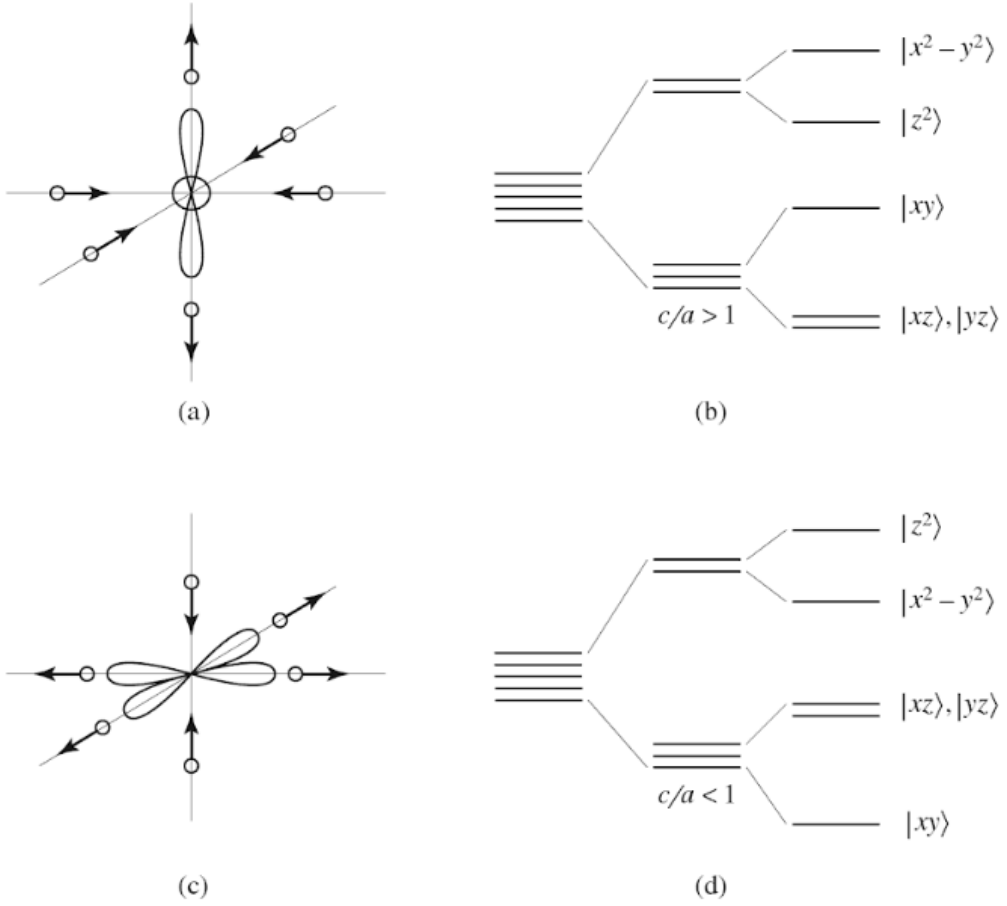

Figure 1.9.: Tetragonal elongation (a) and compression (c) of octahedron environment. The corresponding crystal field splitting energy levels are depicted in (b) and (d) respectively for tetragonal elongation and compression. Fig. 3.9 is reprinted from *Transition Metal Compounds* (p. 47), by D. Khomskii, 2014, Cambridge: Cambridge Univ. Press [47]. Copyright 2014 by Cambridge Univ. Press. Reprinted with permission.

1.2.3. Interaction Hamiltonian

In the single-particle TB Hamiltonian described so far, the electronic interaction are not considered. Independent particle approximation leads to a wrong description of strongly correlated materials: the system with odd number of electrons per unit cell will always be described as a metal, while most of strongly correlated materials are insulators even with odd number of electrons per unit cell.

To treat this problem and to be able to describe the metal-insulator transition, that is driven by the strength of electron-electron interactions (Mott MIT), we need to adapt Hamiltonian to include the term that describes electronic interactions H_{int}. The expression of interaction Hamiltonian H_{int} is following:

$$H_{int} = H_U + H_V + H_J. \tag{1.12}$$

The first term, H_U, describes the intrasite ($i = j$) Coulomb repulsion (Hubbard term):

$$H_U = \sum_{i,\nu} U_{\nu\nu} n_{i\uparrow\nu} n_{i\downarrow\nu}, \tag{1.13}$$

where the particle number operator is $n_{j\sigma\nu} = c^{\dagger}_{j\sigma\nu} c_{i\sigma\nu}$, that describes the number of electrons with spin σ at orbital ν on site i. Only sites with localized d orbitals are considered ($U_{\nu\nu} = U_{dd}$). $U_{\nu\nu}$ is a Coulomb repulsion of two electrons at the same site:

$$U_{\nu\nu} = \int d\vec{r} d\vec{r}' |\varphi_{i\sigma\nu}(\vec{r})|^2 \frac{e^2}{|\vec{r} - \vec{r}'|} |\varphi_{i,-\sigma\nu}(\vec{r}')|^2. \tag{1.14}$$

The second term is the intersite ($i \neq j$) Coulomb repulsion $V^{ij}_{\mu\nu}$:

$$H_V = \sum_{\substack{i \neq j \\ \nu\mu}} \sum_{\sigma\sigma'} V^{ij}_{\nu\mu} n_{i\sigma\nu} n_{j\sigma'\mu}, \tag{1.15}$$

where

$$V^{ij}_{\nu\mu} = \int d\vec{r} d\vec{r}' |\varphi_{i\sigma\nu}(\vec{r})|^2 \frac{e^2}{|\vec{r} - \vec{r}'|} |\varphi_{j\sigma'\mu}(\vec{r}')|^2. \tag{1.16}$$

This term is needed in order to account for charge-ordering effect.

Finally, the third term is the intrasite exchange term that is responsible for Hund's rule coupling for the site i:

$$H_J = - \sum_{\substack{\nu \neq \mu \\ \sigma \neq \sigma'}} J_{\nu\mu} \left(c^{\dagger}_{i\sigma\nu} c_{i\sigma'\nu} c^{\dagger}_{i\sigma'\mu} c_{i\sigma\mu} - c^{\dagger}_{i\sigma'\mu} c^{\dagger}_{i\sigma\mu} c_{i\sigma\nu} c_{i\sigma'\nu} \right), \tag{1.17}$$

where for real orbitals φ the exchange interaction is:

$$J_{\nu\mu} = \int d\vec{r}d\vec{r}'\varphi_{i\nu}(\vec{r})\varphi_{i\mu}(\vec{r})\frac{e^2}{|\vec{r}-\vec{r}'|}\varphi_{i\nu}(\vec{r}')\varphi_{i\mu}(\vec{r}'). \tag{1.18}$$

We will continue this section with the simplest model, namely the single-band Hubbard model [14], that can give a basic understanding of the Mott MIT transition. For real materials the model corresponds to the case, when only one band, that corresponds to the localized orbital, is close to the Fermi level and is well-separated from other bands:

$$H_H = -t\sum_{\langle i,j\rangle,\sigma}\left(c^\dagger_{i\sigma}c_{j\sigma} + c^\dagger_{j\sigma}c_{i\sigma}\right) + U\sum_i n_{i\uparrow}n_{i\downarrow}. \tag{1.19}$$

This model is a partial limit of (1.4), where only one localized orbital at each site is considered, so we omit any orbital indices. We are interested only in hopping between nearest neighbor sites, denoted by $\langle i,j\rangle$, thus we omit any indices for hopping matrix element and denote it simply as t. For simplicity, the intrasite Coulomb interaction is denoted as U. Intersite Coulomb interactions are neglected $V^{ij}_{\mu\nu} = 0$, since the local screening is usually big and $V^{ij}_{\mu\nu}$ decays exponentially with the distance between sites. In a single-band model $J_{\mu\nu} = 0$.

Despite its simplicity, the single band Hubbard model cannot be solved exactly, except for the 1D case [55]. Indeed, while the TB part can be diagonalized in reciprocal space:

$$H_{TB} = \sum_{\vec{k},\sigma}\varepsilon(\vec{k})c^\dagger_{\vec{k},\sigma}c_{\vec{k},\sigma}\ , \tag{1.20}$$

where the summation runs over $\vec{k}$ vectors in the 1st Brillouin zone. $\varepsilon(\vec{k})$ is a k-dependent band dispersion with bandwidth $W = 2zt$, where z is the site coordination number. $c^\dagger_{\vec{k},\sigma}$ and $c_{\vec{k},\sigma}$ are creation and annihilation operators that create/destroy an electron with spin σ in the Bloch state $|\vec{k}\rangle$.

The interaction part is diagonal in real space, and there is no transformation that can diagonalize the two terms simultaneously.

The first approximate solution of this model was given by Hubbard, using Green's function decoupling method [57, 58]. He introduced the idea of Hubbard subbands: the original density of states of the noninteracting system is split into two subbands: lower band and an upper Hubbard band (see Fig. 1.10), when the interaction is taken into account. For large U the subbands are separated by a gap, and the system becomes insulating. There is a critical value of U, $U_c \sim W$, where the two bands touch and the system is a zero-gap semiconductor. For $U < U_c$ the system is metallic and two bands overlap. We can say that this picture approaches the MIT from the insulating side. However, this explanation fails to provide a description of metallic phase with Fermi-Liquid properties [56]: there is no mass renormalization of an electron when the system is metallic and the description of the coherent quasiparticle peak at the Fermi level and spectral

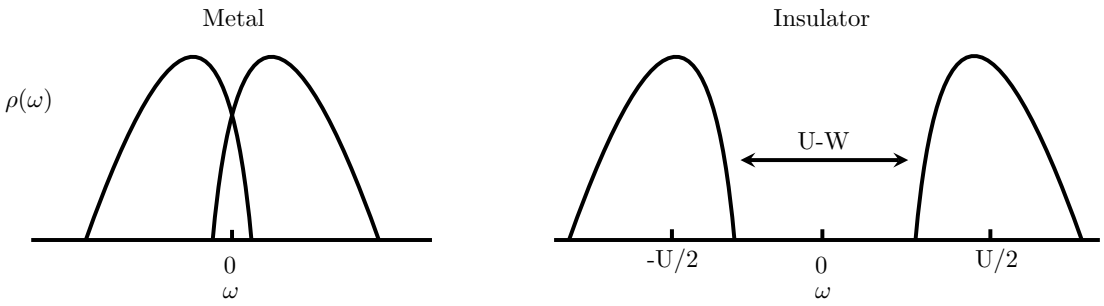

Figure 1.10.: Schematic evolution of the density of states with U in the Hubbard picture: two Hubbard subbands overlap in metallic phase (left panel) and are separated in insulating phase (right panel) with the middle of bands situated at positions $\pm U/2$. Fig. 25 is adapted with permission from A. Georges, G. Kotliar, W. Krauth, and M. J. Rozenberg. "Dynamical mean-field theory of strongly correlated fermion systems and the limit of infinite dimensions". Rev. Mod. Phys. 68, 13 (1996) [56]. Copyright 1996 by the American Physical Society.

weight redistribution is missing.

Another view is to approach the transition point from the metallic side as done using Gutzwiller variational method [59]. Brinkman and Rice [60] pointed out that Gutzwiller method allows one to describe MIT. In this picture the quasiparticle effective mass is $m^* = m/Z$, where the quasiparticle weight $Z \propto (U_c - U)$. The MIT is driven by the localization of the Fermi liquid quasiparticles and their disappearance in the insulator, since $\frac{m^*}{m} \propto \frac{1}{U_c - U} \to \infty$ quasiparticles become too heavy and their movement is substantially reduced. However, this approach does not account for the formation of Hubbard bands in the metallic state and gives an oversimplified picture of insulator with no DOS [56, 58].

Significant advances in understanding of strong correlations were lead by the development of Dynamical Mean-Field Theory (DMFT) [56, 61]. In this approach, the lattice problem is mapped onto a single-site effective problem, where the dynamics at a given site can be represented as the interaction of local degrees of freedom at this site with an external bath, that collects all other degrees of freedom on other sites [62]. The DMFT equations can be solved using different numerical methods, such as iterated perturbation theory (IPT), exact diagonalization (ED), quantum Monte Carlo etc. For a review, see Ref. [62, 63].

DMFT was able to reconcile the two pictures mentioned before: in real material both effects are present simultaneously [62]. As shown in Fig. 1.11, the spectral function of a strongly correlated metal displays a three-peaks structure: a central (coherent) peak of quasi-particles, correctly described by the Gutzwiller picture, and incoherent peaks at $\pm U$, describing atomic-like transitions that corresponds to the addition or removal of one electron on an atomic site (Hubbard picture). In a solid the latter are responsible for a formation of Hubbard bands. When U is increased the spectral weight from quasiparticle peak is transferred to the Hubbard bands and at

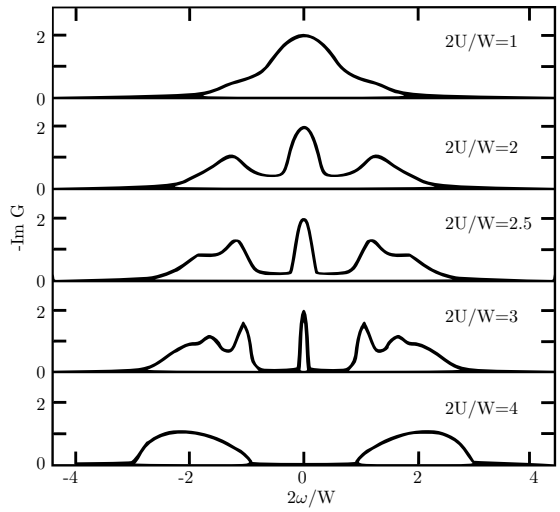

Figure 1.11.: Local spectral function for several values of the interaction strength in DMFT. These results have been obtained using the IPT approximation, for the half-filled Hubbard model with a semi-circular d.o.s. Fig. 30 is adapted with permission from A. Georges, G. Kotliar, W. Krauth, and M. J. Rozenberg. "Dynamical mean-field theory of strongly correlated fermion systems and the limit of infinite dimensions". Rev. Mod. Phys. 68, 13 (1996) [56]. Copyright 1996 by the American Physical Society.

critical U ($U_c = 2W$) the quasiparticle peak disappears.

The DMFT method can be easily extended to treat multiband models; however, the cost increases rapidly with the number of correlated orbitals (n_c), and in practice most studies focus on cases with $n_c \leq 5$. Many different examples can be found in literature, where DMFT is combined with DFT downfolding or projection methods to describe the electronic structure of strongly correlated materials. A review can be found in Ref. [63].

Here, we will focus on purely model studies, which aim at identifying the main features of multiband behaviour. In particular, we will focus on models with two degenerate bands, aiming at describing the doubly-degenerate e_g bands, and with three degenerate bands for t_{2g} systems.

With respect to the single-band case, a complication arises with the fact that in multiband systems one needs to account for Hund's coupling J_H (eq. (1.18)). It was shown that in a N-band degenerate systems when $J_H = 0$, the critical interaction strength U_c/W grows with the degeneracy N and is maximal at half-filling [64, 65]. However, introducing J_H reduces the critical value U_c/W for the Mott-transition at half-filling and thus enhances correlations [66–68].

A recent systematic studies of two-band and three-band models [69, 70] show that for all integer fillings, except half-filling, the Hund's coupling actually increases the critical U needed to drive Mott insulator transition as depicted in Fig. 1.12. In the left panel a quasiparticle weight Z is plotted as a function of the interaction strength U and the number of electrons with indication

of corresponding specific materials. The black bars indicate the Mott MIT. The right panel describes the change of critical U_c w.r.t the strength of Hund's coupling J_H for the cases of two and three orbitals with various fillings.

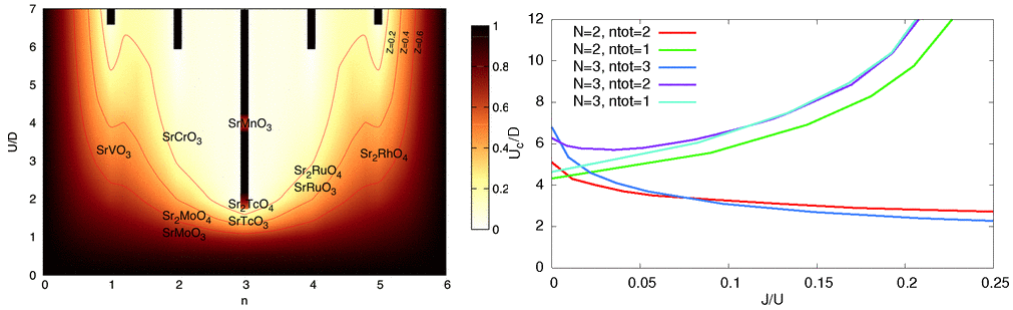

(a) (b)

Figure 1.12.: (a) Quasiparticle weight Z in a model with 3 orbitals, for $J/U = 0.15$, as a function of the interaction strength U and the number of electrons — from empty (0) to full (6). Darker regions correspond to good metals and lighter regions to bad metals. The black bars signal the Mott-insulating phases. One notes that, among integer fillings, the case of 2 electrons (2 holes) displays bad-metal behavior in an extended range of coupling. Specific materials are schematically placed on the diagram. (b) Metal-Mott insulator critical coupling U_c for the N-band degenerate Hubbard model as a function of the ratio J/U. Only fillings such that $n < N$ are shown here. The ones for $n > N$ give identical results due to particle-hole symmetry. For half-filled cases (two electrons in two bands and three electrons in three bands) the Hund's coupling correlates the system and reduces the critical U_c/D. For all other fillings, on the contrary, U_c/D is strongly increased (D is a half of a bandwidth $W = 2D$). Fig. 1 is reprinted with permission from L. de'Medici. "Hund's coupling and its key role in tuning multiorbital correlations". Phys. Rev. B 83, 205112 (2011) [69]. Copyright 2011 by the American Physical Society. Fig. 2 is reprinted with permission from L. de'Medici, J. Mravlje, and A. Georges. "Janus-Faced Influence of Hund's Rule Coupling in Strongly Correlated Materials". Phys. Rev. Lett. 107, 256401 (2011) [70]. Copyright 2011 by the American Physical Society.

The recent boom of relativistic transition metal oxides, such as iridates and ruthenates, has motivated the extension of the study of strongly correlated systems with the inclusion of SOC. A few specific examples are discussed in [71–73] and briefly described in Chapter 2 of the present thesis. Here, we just summarize the main results of a model study of a three band system when strong correlations, Hund's rule coupling and spin-orbit coupling (λ) or a tetragonal crystal field is taken into account [74] by solving the Hubbard-Kanamori Hamiltonian H_{HK} using DMFT.

$$H_{HK} = H_{TB} + \sum_i H^i_{loc}, \tag{1.21}$$

where i is a site index and the local Hamiltonian on each site i is given by (we omit index i for

simplicity)

$$H_{loc} = U \sum_{\nu} n_{\nu\uparrow} n_{\nu\downarrow} + V \sum_{\nu \neq \mu} n_{\nu\uparrow} n_{\mu\downarrow} + (V - J_H) \sum_{\nu<\mu,\sigma} n_{\nu\sigma} n_{\mu\sigma} + \\ + J_H \sum_{\nu \neq \mu} \left(c^{\dagger}_{\nu\uparrow} c^{\dagger}_{\mu\downarrow} c_{\nu\downarrow} c_{\mu\uparrow} + c^{\dagger}_{\nu\uparrow} c^{\dagger}_{\nu\downarrow} c_{\mu\downarrow} c_{\mu\uparrow} \right), \tag{1.22}$$

where ν and μ are orbital indices, $c^{\dagger}_{\mu\sigma}$ and $c_{\mu\sigma}$ are creation and annihilation operators as described before, $n_{\mu\sigma}$ is the particle number operator. U and V are intraorbital and interorbital Coulomb interactions respectively. J_H is the coefficient of the Hund's coupling. The conventional choice of parameters, $V = U - 2J_H$, is adopted to make the Hamiltonian rotationally invariant in orbital space.

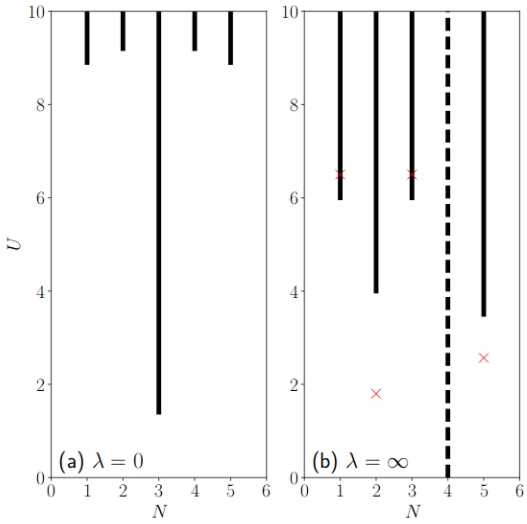

Figure 1.13.: The Mott insulator occurs for values of U indicated by bars for a Hund's coupling of $J_H = 0.2U$. The left picture shows the case without SOC, the right with an infinite SOC. Note that in the latter case no Mott insulator occurs for $N = 4$ since this case is a band insulator. Fig. 6 is reprinted with permission from R. Triebl, G. J. Kraberger, J. Mravlje, and M. Aichhorn. "Spin-orbit coupling and correlations in three-orbital systems". arXiv:1807.05106v1, 2018 [74].

The critical U_c values for Mott transition for Hund's coupling of $J_H = 0.2\ U$ for cases of various fillings are plotted in Fig. 1.13 for $\lambda = \infty$ (right panel; black bars indicate Mott insulator region). Study shows that the SOC increases correlation strength for $N = 1, 5$ cases, with a higher impact for $N = 5$ case. For $N = 3$ the influence of SOC is opposite. A peculiar result is found for $N = 4$, where the system turns out to be a band insulator. The case $N = 2$ is the Hund's metal phase, which is a phase in which Hund's coupling influences crucially the metallic properties and have the following three main features (citation from Ref. [75] follows):

- Enhanced electron correlations and masses.

- High local spin configurations dominating the paramagnetic fluctuations.
- Selectivity of the electron correlation strength depending on the orbital character.

In this case two regimes are found depending on the value of U: for small U the SOC increases the quasiparticle weight Z, but for large U the SOC decreases Z, but in turn critical interaction U_c decreases too [74].

1.2.4. Spin-orbit coupling

We will now discuss the last term, H_{SOC}, of the full Hamiltonian (1.4):

$$H_{SOC} = \lambda \vec{L}\vec{S}, \tag{1.23}$$

where λ is a strength of the SOC, $\vec{L}$ is the total angular momentum operator and $\vec{S}$ is the spin operator; here H_{SOC} is written in case of many-electron atom. In this section we adopt the first quantization notation for H_{SOC} and in following we will at first discuss the effect of the SOC in the single particle description; the generalization for the many-electron atom will be discussed in the end of the section.

The SOC Hamiltonian describes the mixing between orbital and spin degrees of freedom, due to relativistic effects. These effects are negligible in most systems, but they become important in compounds that contain heavy atoms, as the strength of the SOC increases with atomic number Z as Z^2 [15] (another estimate is Z^4, but Z^2 estimate is in a better agreement with experiments [76]). In TMO, these effects are relevant for 4d and 5d TM ions. For example, for Ir the effective SOC constant is $\lambda \sim 0.5$ eV. The main effect of SOC on an atom is a splitting of atomic energy levels; in a solid, this translates into a splitting of bands which would otherwise be degenerate.

To highlight the main effect of SOC on the energy level structure, it is enough to describe the effect of SOC for one electron that moves in atomic potential. SOC is a relativistic effect and the relativistic treatment of the problem is possible using the Dirac equation (written here for an electron in an electromagnetic field with an electric potential V and magnetic vector potential $\vec{A}$):

$$\left(\beta mc^2 + eV + c\left(\sum_{n=1}^{3} \alpha_n \left(p_n - \frac{e}{c}A_n\right)\right)\right)\phi(x,t) = i\hbar\frac{\partial\phi(x,t)}{\partial t}, \tag{1.24}$$

where $\phi(x,t)$ is a wave function for an electron of the rest mass m with space-time coordinates x and t; e is the electron's charge. p_n are the components of the momentum operator and A_n are components of magnetic vector potential. c is speed of light and $\hbar$ is the reduced Plank constant.

α_n and β are 4×4 matrices with the following properties ($i \neq j$):

$$\alpha_i^2 = \beta^2 = \hat{I}, \tag{1.25}$$

$$\alpha_i \alpha_j + \alpha_j \alpha_i = 0, \tag{1.26}$$

$$\alpha_i \beta + \beta \alpha_i = 0, \tag{1.27}$$

where $\hat{I}$ is the unity matrix. The indexes i, j are used to distinguish the three α matrices.

Expanding the Dirac equation in roots of $\frac{1}{c}$ (for brevity we omit the derivation here) one obtains the following Hamiltonian:

$$H = \frac{1}{2m}\left(\frac{\hbar}{i}\nabla - e\vec{A}(\vec{r})\right)^2 + V(\vec{r}) + mc^2 - \frac{e\hbar}{2m}\vec{\sigma}\vec{B} - \frac{1}{8m^3c^2}(\vec{p} - e\vec{A})^4 + \frac{\hbar^2 e}{8m^2c^2}\nabla^2 V(\vec{r}) - \\ - \frac{e\hbar}{4m^2c^2}\vec{\sigma}[\vec{E} \times (\vec{p} - e\vec{A})], \tag{1.28}$$

where vector $\vec{\sigma}$ has Pauli matrices as its components and $\vec{E}$ is an electric field. The last term is the spin-orbit coupling term and it can be separated in two components: the spin-orbit coupling H_{SOC} component and the angular magneto-electric H_{AME} component:

$$-\frac{e\hbar}{4m^2c^2}\vec{\sigma}[\vec{E} \times (\vec{p} - e\vec{A})] = -\frac{e\hbar}{4m^2c^2}\vec{\sigma}[\vec{E} \times \vec{p}] + \frac{e\hbar}{4m^2c^2}\vec{\sigma}[\vec{E} \times e\vec{A}] = H_{SOC} + H_{AME}. \tag{1.29}$$

H_{SOC} term in case of the spherical potential $V(\vec{r}) = V(r)$ is expressed as:

$$H_{SOC} = \frac{\hbar}{4m^2c^2}\frac{1}{r}\frac{dV}{dr}\vec{\sigma}(\vec{r} \times \vec{p}) = \frac{1}{2m^2c^2}\frac{1}{r}\frac{dV}{dr}\vec{s} \cdot \vec{l} \tag{1.30}$$

or in the final simplified form:

$$H_{SOC} = \zeta \vec{l} \cdot \vec{s} \tag{1.31}$$

with ζ is the so-called SOC constant, which is positive. $\vec{s} = \frac{\hbar}{2}\vec{\sigma}$ and $\vec{l} = \vec{r} \times \vec{p}$ are the operators for the spin and orbital momentum of an electron respectively.

The single-electron SOC Hamiltonian can be further expressed as:

$$H_{SOC} = \zeta \vec{l} \cdot \vec{s} = \zeta \left[l_z s_z + \frac{1}{2}(l_+ s_- + l_- s_+) \right], \tag{1.32}$$

where $l_\pm$, $s_\pm$ are *ladder operators*: $l_\pm = l_x \pm i l_y$ and $s_\pm = s_x \pm i s_y$.

If we denote the spherical harmonics as $|l, m_l\rangle = Y_l^{m_l}$, the l-operators act on them as follows:

$$l_z |l, m_l\rangle = m_l |l, m_l\rangle, \tag{1.33}$$

$$l_\pm |l, m_l\rangle = \sqrt{(l \mp m_l)(l \pm m_l + 1)}\, |l, m_l \pm 1\rangle, \tag{1.34}$$

provided that $l_\pm$ operators are bounded: $l_+ |l, l\rangle = 0$ and $l_- |l, -l\rangle = 0$.

If we denote the single-particle spin states as $|s, m_s\rangle$, $(-s \leq m_s \leq s)$, s-operators give:

$$s_z |s, m_s\rangle = m_s |s, m_s\rangle , \tag{1.35}$$

$$s_\pm |s, m_s\rangle = \sqrt{s(s+1) - m_s(m_s \pm 1)}\, |s, m_s \pm 1\rangle , \tag{1.36}$$

provided that $s_\pm$ operators are bounded too: $s_+ |s, s\rangle = 0$ and $s_- |s, -s\rangle = 0$. Here we used atomic units ($\hbar = 1$).

The states of a single electron in terms of l, m_l and s, m_s quantum numbers are the direct tensor product of $|l, m_l\rangle$ and $|s, m_s\rangle$ states: $|l, m_l\rangle \otimes |s, m_s\rangle$ and for brevity we will denote them as $|m_l, m_s\rangle = |l, m_l\rangle \otimes |s, m_s\rangle$.

The SOC interaction couples $\vec{l}$ and $\vec{s}$, yielding a total angular momentum $\vec{j} = \vec{l} + \vec{s}$. The operators $\vec{j}^2 = j(j+1)\,|j, m_j\rangle$ and $\vec{j}_z = m_j\,|j, m_j\rangle$ have common eigenvectors $|j, m_j\rangle$, where $j \in \{|l-s|, |l-s|+1, \ldots, l+s\}$ and $m_j \in \{-j, -j+1, \ldots, j\}$. They commute with the single-electron SOC Hamiltonian and thus its basis states can be labeled as $|j, m_j\rangle$. The relation between $|j, m_j\rangle$ and $|m_l, m_s\rangle$ states is straightforward:

$$|j, m_j\rangle = \sum_{m_l=-l}^{l} \sum_{m_s=-s}^{s} \langle l, m_l, s, m_s | j, m_j\rangle\, |m_l, m_s\rangle , \tag{1.37}$$

where the coefficients $\langle l, m_l, s, m_s | j, m_j\rangle$ are known as the Clebsch-Gordan coefficients.

Now, we want to to demonstrate the effect of SOC for a single electron in a state which corresponds to the occupation of a p orbital. We use cubic harmonics representation ((1.2)) as a basis set to describe p orbitals. In this case the single-electron Hamiltonian (1.32) is represented by the following matrix:

$$H^p_{SOC} = \frac{\zeta}{2} \begin{array}{c} \\ p_{x\uparrow} \\ p_{y\uparrow} \\ p_{z\uparrow} \\ p_{x\downarrow} \\ p_{y\downarrow} \\ p_{z\downarrow} \end{array} \begin{array}{c} \begin{array}{cccccc} p_{x\uparrow} & p_{y\uparrow} & p_{z\uparrow} & p_{x\downarrow} & p_{y\downarrow} & p_{z\downarrow} \end{array} \\ \begin{bmatrix} 0 & -i & 0 & 0 & 0 & 1 \\ i & 0 & 0 & 0 & 0 & -1 \\ 0 & 0 & 0 & -1 & i & 0 \\ 0 & 0 & -1 & 0 & i & 0 \\ 0 & 0 & -1 & -i & 0 & 0 \\ 1 & i & 0 & 0 & 0 & 0 \end{bmatrix} \end{array} . \tag{1.38}$$

The sixfold degeneracy of the p states (including spin) is lifted by SOC and diagonalizing H^p_{SOC} gives two-fold degenerate states with $j = \frac{1}{2}$ and four-fold degenerate states with $j = \frac{3}{2}$ with eigenvalues $E_1 = -\zeta$ and $E_2 = \frac{\zeta}{2}$ respectively. The importance of this result will be emphasized later, when we will discuss the effect of SOC on t_{2g} states.

Now we want to apply the same procedure for a single electron in a d state. Again, as a basis set the cubic harmonics are used (as defined in eq. (1.3)). The matrix representation of the SOC

Hamiltonian for this case is following:

$$H^d_{SOC} = \frac{\zeta}{2}\begin{bmatrix} & z^2_\uparrow & x^2-y^2_\uparrow & xy_\uparrow & yz_\uparrow & xz_\uparrow & z^2_\downarrow & x^2-y^2_\downarrow & xy_\downarrow & yz_\downarrow & xz_\downarrow \\ z^2_\uparrow & 0 & 0 & 0 & 0 & 0 & 0 & 0 & 0 & i\sqrt{3} & -\sqrt{3} \\ x^2-y^2_\uparrow & 0 & 0 & -2i & 0 & 0 & 0 & 0 & 0 & i & 1 \\ xy_\uparrow & 0 & 2i & 0 & 0 & 0 & 0 & 0 & 0 & 1 & -i \\ yz_\uparrow & 0 & 0 & 0 & 0 & i & -i\sqrt{3} & -i & -1 & 0 & 0 \\ xz_\uparrow & 0 & 0 & 0 & -i & 0 & \sqrt{3} & -1 & i & 0 & 0 \\ z^2_\downarrow & 0 & 0 & 0 & i\sqrt{3} & \sqrt{3} & 0 & 0 & 0 & 0 & 0 \\ x^2-y^2_\downarrow & 0 & 0 & 0 & i & -1 & 0 & 0 & 2i & 0 & 0 \\ xy_\downarrow & 0 & 0 & 0 & -1 & -i & 0 & -2i & 0 & 0 & 0 \\ yz_\downarrow & -i\sqrt{3} & -i & 1 & 0 & 0 & 0 & 0 & 0 & 0 & -i \\ xz_\downarrow & -\sqrt{3} & 1 & i & 0 & 0 & 0 & 0 & 0 & i & 0 \end{bmatrix}. \tag{1.39}$$

Diagonalizing the Hamiltonian, the tenfold degenerate d states are split into a quartet with energy $E_1 = -\frac{1}{2}\zeta$ with $j = \frac{3}{2}$ and a sextet with energy $E_2 = \zeta$ with $j = \frac{5}{2}$, see Fig. 1.14.

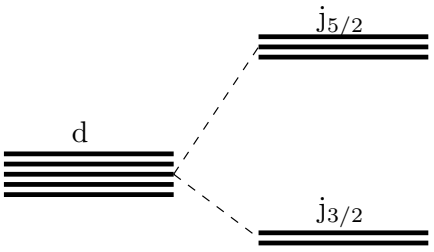

Figure 1.14.: Under the SOC d levels are split into a quartet with $j = \frac{3}{2}$ and a sextet with $j = \frac{5}{2}$.

Interplay between spin-orbit coupling and crystal field splitting To have a proper description of real materials, the interplay of CFS and SOC should be considered. To do this, we will have to adapt our description of CFS in terms of hybridization of p and d orbitals, given before in Sec. 1.2.2, to the case of a single electron in an atomic potential.

Recalling results of Sec. 1.2.2, d and p orbitals form bonding and antibonding states, where the latter are mostly of d character. Antibonding and bonding states are split into states with e_g and t_{2g} symmetry separated by an onsite energy difference Δ_{CF}.

In order to recover the splitting of atomic d states into an e_g and a t_{2g} manifold, the full rotational symmetry of atomic potential should be lifted, that the effect of CFS can effectively be described in our single electron problem introducing a fictitious potential with an appropriate symmetry. With this in mind, we introduce an effective CFS Hamiltonian, that is diagonal in the cubic d

basis, that shifts the e_g states up in energy. The splitting between the e_g and t_{2g} states is Δ_{CF}.

$$H_{CFS} = \begin{bmatrix} & e_{g\uparrow} & t_{2g\uparrow} & e_{g\downarrow} & t_{2g\downarrow} \\ e_{g\uparrow} & \Delta_{CF} & 0 & 0 & 0 \\ t_{2g\uparrow} & 0 & 0 & 0 & 0 \\ e_{g\downarrow} & 0 & 0 & \Delta_{CF} & 0 \\ t_{2g\downarrow} & 0 & 0 & 0 & 0 \end{bmatrix}. \tag{1.40}$$

To shorten our notation we assume that e_g "unfolds" into d_{z^2}, $d_{x^2-y^2}$ and t_{2g} "unfolds" into d_{xy}, d_{xz}, d_{yz} with the corresponding spin, and the "unfolded" H_{CFS} Hamiltonian has the same structure as H^d_{SOC} in (1.39). As a result of the operation of this Hamiltonian onto d states, e_g orbitals are shifted up in the energy. Here and in the following we assume Δ_{CF} is positive. In this simple example we neglect the effect of hopping and consider only onsite interactions.

Thus the Hamiltonian, describing the interplay of SOC and CFS is:

$$H = H^d_{SOC} + H_{CFS} \tag{1.41}$$

with eigenvalues:

$$E_1 = \frac{1}{4}\left(-\zeta + 2\Delta_{CF} + \sqrt{25\zeta^2 + 4\zeta\Delta_{CF} + 4\Delta^2_{CF}}\right), \tag{1.42}$$

$$E_2 = \zeta, \tag{1.43}$$

$$E_3 = \frac{1}{4}\left(-\zeta + 2\Delta_{CF} - \sqrt{25\zeta^2 + 4\zeta\Delta_{CF} + 4\Delta^2_{CF}}\right), \tag{1.44}$$

For a finite Δ_{CF}, E_2 corresponds to a doublet state and E_1, E_3 are quartet states, as depicted in the middle of Fig. 1.15. When $\Delta_{CF} = 0$, the first two form $j = 5/2$ sextet state and the last quartet is $j = 3/2$ quartet, as it was described before (see Fig. 1.14).

For $\Delta_{CF} \gg \zeta$ the orbital momentum of the e_g states is quenched and they are not mixed with t_{2g} by SOC (in the first approximation). In this case the effect of SOC is only considered for t_{2g} states. t_{2g} states form a triplet with $\langle l^z \rangle = 0, \pm 1$ [47]. To show this we will express the t_{2g} states as the following linear combination of cubic harmonics (1.3):

$$\begin{aligned} |t^0_{2g}\rangle &= -\frac{i}{\sqrt{2}}(Y^2_2 - Y^{-2}_2) = d_{xy}, \\ |t^1_{2g}\rangle &= Y^1_2 = -\frac{1}{\sqrt{2}}(d_{xz} + id_{yz}), \\ |t^{-1}_{2g}\rangle &= Y^{-1}_2 = \frac{1}{\sqrt{2}}(d_{xz} - id_{yz}) \end{aligned} \tag{1.45}$$

with new basis state $|t^{l_z}_{2g}\rangle$. It is possible to map this triplet onto the triplet of states with an effective orbital momentum $l_{eff} = 1$, where the matrix elements of the orbital momentum of this triplet coincide with those for $l = 1$ of p states and differ only by a minus sign. This situation is

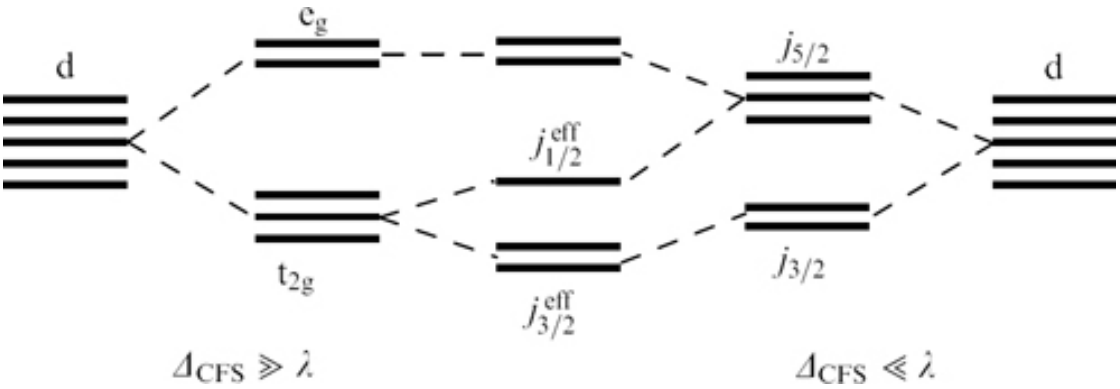

Figure 1.15.: The splitting of d levels due to the interplay of the CFS and the SOC. Fig. 9 is reprinted with permission S. V. Streltsov and D. I. Khomskii. "Orbital physics in transition metal compounds: new trends". Physics-Uspekhi 60, 1121 (2017) [76]. Copyright 2017 by the IOP Publishing.

called *T-P correspondence* [77]. Thus, the multiplet structure of t_{2g}-orbitals will be the inverted multiplet structure of the p-orbitals, that was derived before. As a result, the t_{2g} states are split into twofold degenerate $j_{eff} = \frac{1}{2}$ states and fourfold degenerate $j_{eff} = \frac{3}{2}$ states as depicted in the middle of Fig. 1.15. This situation is realized in compounds with Ir^{4+} ions in an octahedral oxygen coordination environment and will be discussed later in more details.

Now we will make a few additional comments, following the considerations described in Ref. [47]. The effect of SOC in solids depends on its strength in comparison to the strength of the crystal field splitting Δ_{CF}: if the CFS is smaller that the SOC, than one can treat CFS as a perturbation of the atomic picture — the level splitting corresponding to this situation is shown in the right part of Fig. 1.15. In the opposite limit, when the CFS is bigger that the SOC, which is usually the case for 3d and most 4d compounds, at first one should look at the crystal field levels and then account for an action of SOC on them (level splitting as depicted in the left part of Fig. 1.15).

***LS* and *jj*-coupling** The treatment of SOC in many-electron atoms is a complicated problem and generally there are two approximations [76].

The first approximation, called LS or Russell-Saunders approximation, is used to treat many-electron atoms with a relatively weak SOC, weaker than the Hund's rule interatomic exchange J_H: according to Hund's first rule, first the total spin of electrons is determined $\vec{S} = \sum_i \vec{s}_i$ and then the total angular momentum $\vec{L} = \sum_i \vec{l}_i$ (i labels electrons). Finally, SOC couples $\vec{S}$ and $\vec{L}$, and produces the total angular momentum $\vec{J} = \vec{L} + \vec{S}$. The quantum number J can than assume values $J = L + S, L + S - 1, \ldots, |L - S|$. The full SOC for an atom in LS scheme is written in the form:

$$H_{SOC}^{LS} = \lambda \vec{L}\vec{S}, \tag{1.46}$$

where the coupling constant λ is composed of the partial SOC coupling constants ζ_i of all the

relevant electrons, denoted by index i. In case of electrons occupying the same shell, all ζ_i are the same ($\zeta_i = \zeta$) and λ is expressed as:

$$\lambda = \pm\frac{\zeta}{2S}, \tag{1.47}$$

where the "+" sign is used for less-than-half-filled shells and the "-" sign for more-than-half-filled shells. This leads to Hund's third rule: for $\lambda > 0$ we have a normal multiplet order (terms with smaller J have lower energy) and an "inverted" multiplet order for $\lambda < 0$ (terms with higher J have lower energy), since $E_{SOC} = \frac{\lambda}{2}(J(J+1) - L(L+1) - S(S+1))$. The coupling constant λ depends on the valence and spin state of corresponding ion [47].

In the opposite limit of strong SOC, $\lambda > J_H$, another approximation is used, called the jj-coupling scheme: one first couples the spin and total angular momentum of each electron i to yield the total angular momentum of each electron $\vec{j}_i = \vec{l}_i + \vec{s}_i$. Then the total momentum is given by the sum of total momenta of individual electrons:

$$\vec{J} = \sum_i \vec{j}_i. \tag{1.48}$$

In this scheme, for a strong SOC the one-electron states are split into j-components (for example d states split into $j = \frac{5}{2}$ and $j = \frac{3}{2}$) and then other interactions may remove this degeneracy. By doing this, the first Hund's rule is violated.

The LS coupling scheme can be used to describe 3d and 4d TM ions. The jj-coupling scheme is appropriate for rear earth elements or actinides. In 5d TM ions the situation is typically more complicated, as they are often in an intermediate regime between LS and jj coupling [76].

1.3. Bond-directional interactions

To describe magnetic properties of the solid it is convenient to derive a model magnetic Hamiltonian, $H_{magnetic}$, that describes the interaction between magnetic moments. This section will cover only the specific topic of magnetic interactions, namely the bond-directional interactions (anisotropic magnetic interactions).

Interplay between electronic correlations, SOC and CFS leads to a high variety of physical properties of 4d and 5d TMO compounds. The variety of phases as an interplay between electronic correlations and SOC is plotted in Fig. 1.16. A special type of magnetic materials, *Kitaev materials*, emerges. *Kitaev materials* are systems, where bond-directional exchange interactions are present and they lead to unconventional forms of magnetism, such as *spin liquids* or the formation of non-trivial spin textures [78]. In this section we will discuss the origin of this interaction and models used to describe it.

Bond-directional interactions are Ising-like interactions, where the exchange easy axis depends on

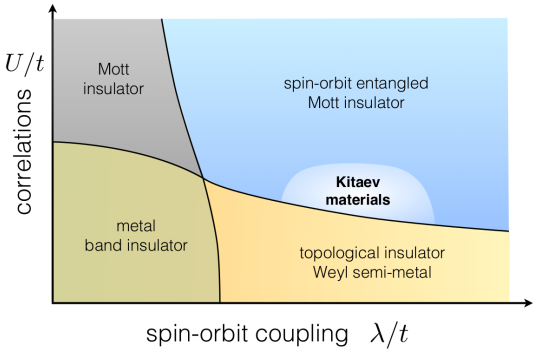

Figure 1.16.: General form of the phase diagram in the presence of electronic correlations and spin-orbit coupling. Fig. 1 is reprinted with permission S. Trebst. "Kitaev Materials". arXiv:1701.07056v1, 2017 [78].

the spatial orientation of an exchange bond [78]. The simplest model describing bond-directional interactions is *Kitaev model* [17]:

$$H_{Kitaev} = -\sum_{\gamma\text{-bonds}} K S_i^{\gamma} S_j^{\gamma}. \tag{1.49}$$

The summation goes over all bonds. The bond between i and j sites belong to one of three possible types $\gamma = \{x, y, z\}$. Bond type is defined by the direction of the corresponding exchange

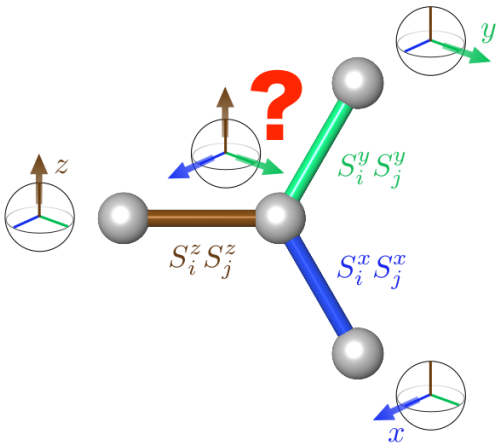

Figure 1.17.: Exchange frustration arising from spin-orbit induced bond-directional interactions, i.e. Ising-like couplings where the exchange easy axis depends on the spatial orientation of an exchange bond. Spins subject to these bond-directional interactions cannot simultaneously minimize all couplings, which holds both for quantum and classical moments. Fig. 4 is reprinted with permission S. Trebst. "Kitaev Materials". arXiv:1701.07056v1, 2017 [78].

easy axis for spins on sites i and j (this axis is in direction γ). Accordingly, we denote the bond between i and j sites as γ-bond (see Fig. 1.17). Figure also indicates an arise of exchange frustration since no choice of spin direction on the middle site is able to satisfy interactions on all bonds. S_i^γ stands for a γ component of $S = \frac{1}{2}$ operator. K is a strength of the Kitaev interaction.

1.3.1. Jackeli-Khaliullin mechanism

Mechanism to realize Kitaev model [17] in real materials was proposed by Jackeli and Khaliullin [18, 19] and in this section we will follow their derivation.

t_{2g} and e_g electronic states are separated in O_h octahedral crystal field splitting, when a crystal field is strong, leading to a low spin state with one hole in t_{2g} manifold for a system with 5 d-electrons, i.e. Ir^{4+}. One can form a basis of three t_{2g} orbitals (we are keeping the notation used in [19]):

$$|l_z = 0\rangle = |xy\rangle\,, \tag{1.50}$$

$$|l_z = -1\rangle = -\frac{1}{\sqrt{2}}(i\,|xz\rangle - |yz\rangle), \tag{1.51}$$

$$|l_z = 1\rangle = -\frac{1}{\sqrt{2}}(i\,|xz\rangle + |yz\rangle), \tag{1.52}$$

that has an effective angular momentum $l_{eff} = 1$. $|xy\rangle$, $|xz\rangle$ and $|yz\rangle$ represent t_{2g} manifold of d orbitals.

The single ion Hamiltonian in case of spin-orbit coupling (λ) and additional tetragonal crystal field splitting (Δ, while $\Delta > 0$ for an oxygen octahedron elongated along $z \parallel c$-axis) has the following form:

$$H_0 = \lambda \vec{l} \cdot \vec{s} + \Delta l_z^2, \tag{1.53}$$

with the lowest state being a Kramers doublet:

$$|\widetilde{\uparrow}\rangle = \sin\theta\,|l_z = 0, \uparrow\rangle - \cos\theta\,|l_z = +1, \downarrow\rangle\,, \tag{1.54}$$

$$|\widetilde{\downarrow}\rangle = \sin\theta\,|l_z = 0, \downarrow\rangle - \cos\theta\,|l_z = -1, \uparrow\rangle\,, \tag{1.55}$$

where θ is a parameter giving correspondence between a strength of SOC and tetragonal splitting: $\tan 2\theta = \frac{2\sqrt{2}\lambda}{\lambda - 2\Delta}$. Kramers doublet wave functions are formed by a mixture of different orbital and spin states, that will have a great impact on the symmetry of interatomic interaction.

In the limit of a large λ, the λ is larger than exchange interaction between states of Kramers doublet. In this case, the model exchange Hamiltonian is obtained from the corresponding superexchange model. There are two ways to connect octahedra: corner sharing with 180° TM-O-TM bond and edge sharing with 90° bond (see Fig. 1.18). We define the coordinate frame in the way that axes are pointing towards oxygens, see the upper panel of Fig. 1.18. z-axis points out of the plane.

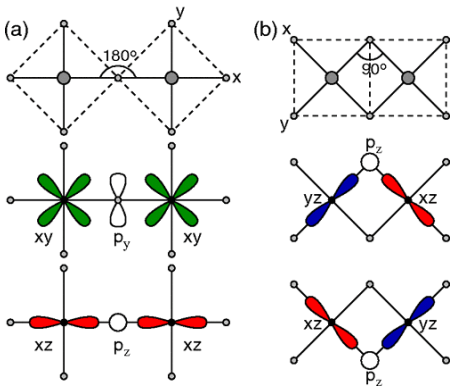

Figure 1.18.: Two possible geometries of a TM-O-TM bond with corresponding orbitals active along these bonds. The large (small) dots stand for the transition metal (oxygen) ions. (a) A 180°-bond formed by corner-shared octahedra, and (b) a 90°-bond formed by edge-shared octahedra. Fig. 2 is reprinted with permission from G. Jackeli and G. Khaliullin. "Mott Insulators in the Strong Spin-Orbit Coupling Limit: From Heisenberg to a Quantum Compass and Kitaev Models". Phys. Rev. Lett. 102, 017205 (2009) [19]. Copyright 2009 by the American Physical Society.

In the first case, for a bond in a given direction α={x, y, z}, the hopping happens via oxygen p states, perpendicular to this direction, p_β and p_γ, with $\{\alpha, \beta, \gamma\} = \{x, y, z\}, \{y, z, x\}$ or $\{z, x, y\}$. The case of x-bond is depicted in Fig. 1.18(a). Hopping matrix is diagonal and hopping happens via $|\alpha\beta\rangle$-$|\alpha\beta\rangle$ and $|\alpha\gamma\rangle$-$|\alpha\gamma\rangle$ orbitals. The exchange Hamiltonian between sites i and j has the following form [18]:

$$H_{ij} = J_1 \vec{S}_i \vec{S}_j + J_2 (\vec{S}_i \cdot \vec{r}_{ij})(\vec{r}_{ij} \cdot \vec{S}_j), \tag{1.56}$$

where the first part is Heisenberg exchange of strength J_1 and the second is pseudodipolar interaction of strength J_2. $\vec{r}_{ij}$ is a direction-vector between sites i and j. $\vec{S}_i$ is the $S = \frac{1}{2}$ operator. The interaction is mostly isotropic with a weak anisotropy, coming from Hund's coupling, despite strong λ.

In the situation of a 90° bond, hopping matrix has only non-diagonal elements: hopping is via $|\gamma\alpha\rangle$-$|\gamma\beta\rangle$ and symmetrical $|\gamma\beta\rangle$-$|\gamma\alpha\rangle$ paths. The hopping path is along the γ-bond in $\alpha\beta$ plaquette, thus via p_γ oxygen orbital. In the Fig. 1.18(b) xy plaquette is depicted describing z-bond. Isotropic part of the Hamiltonian vanishes due to the destructive interference of hoppings via two oxygens. Anisotropic interaction is present due to the Hund's coupling. It is important, that interaction depends on the bond orientation. The Hamiltonian for a hopping via γ-directed oxygen p-orbital is (i.e. γ-bond between i and j sites):

$$H_{ij}^{\gamma} = -K S_i^{\gamma} S_j^{\gamma}, \tag{1.57}$$

where K is the strength of Kitaev interaction. Summed over all bonds it gives the Hamiltonian mentioned in eq. (1.49).

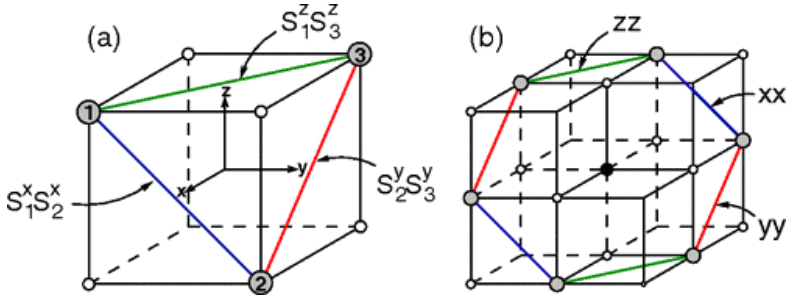

Figure 1.19.: Examples of the structural units formed by 90° TM-O-TM bonds and corresponding spin-coupling patterns. Gray circles stand for magnetic ions, and small open circles denote oxygen sites. (a) Triangular unit cell of ABO2-type layered compounds, periodic sequence of this unit forms a triangular lattice of magnetic ions. The model (1.49) on this structure is a realization of a quantum compass model on a triangular lattice: e.g., on a bond 1-2, laying perpendicular to x-axis, the interaction is $S_1^xS_x^2$. (b) Hexagonal unit cell of A_2BO_3-type layered compound, in which magnetic ions (B-sites) form a honeycomb lattice. (Black dot: nonmagnetic A-site). On an xx-bond, the interaction is $S_x^iS_x^j$, etc. For this structure, the model (1.57) is identical to the Kitaev model. Fig. 3 is reprinted with permission from G. Jackeli and G. Khaliullin. "Mott Insulators in the Strong Spin-Orbit Coupling Limit: From Heisenberg to a Quantum Compass and Kitaev Models". Phys. Rev. Lett. 102, 017205 (2009) [19]. Copyright 2009 by the American Physical Society.

Jackeli and Khaliullin proposed two structural motifs to "engineer" the Kitaev model (see Fig. 1.19): triangular system, with TM sitting in an equilateral triangle, that is common for ABO_2 layered compounds (usually A – alkali ion, B – TM ion) and hexagonal, with TM sitting in hexagons, common for A_2BO_3 compounds (like Na_2IrO_3 or α-Li_2IrO_3). In each case there are three bonds and for each corresponding Kitaev-like Hamiltonian is used to describe an interaction on this bond.

1.3.2. $JK\Gamma$ model

However, in real materials the situation is more complex: the Heisenberg interaction can emerge due to distortion of octahedra and direct overlap of d-orbitals. Also the local symmetry of the TM ion coordination environment can allow interactions other than Kitaev and Heisenberg. The generic Hamiltonian describing the magnetic interaction between the two sites of edge-connected octahedra is following [78]:

$$H_{JK\Gamma} = -\sum_{\gamma-bonds} J\vec{S}_i\vec{S}_j + KS_i^\gamma K_j^\gamma + \Gamma\left(S_i^\alpha S_j^\beta + S_i^\beta S_j^\alpha\right), \tag{1.58}$$

where the sum goes over the nearest-neighbor spins at sites, coupled by the bond ij along γ direction. The first term is an isotropic Heisenberg exchange with the coupling strength J. The second term is Kitaev term of strength K, which was discussed before. The third term is a

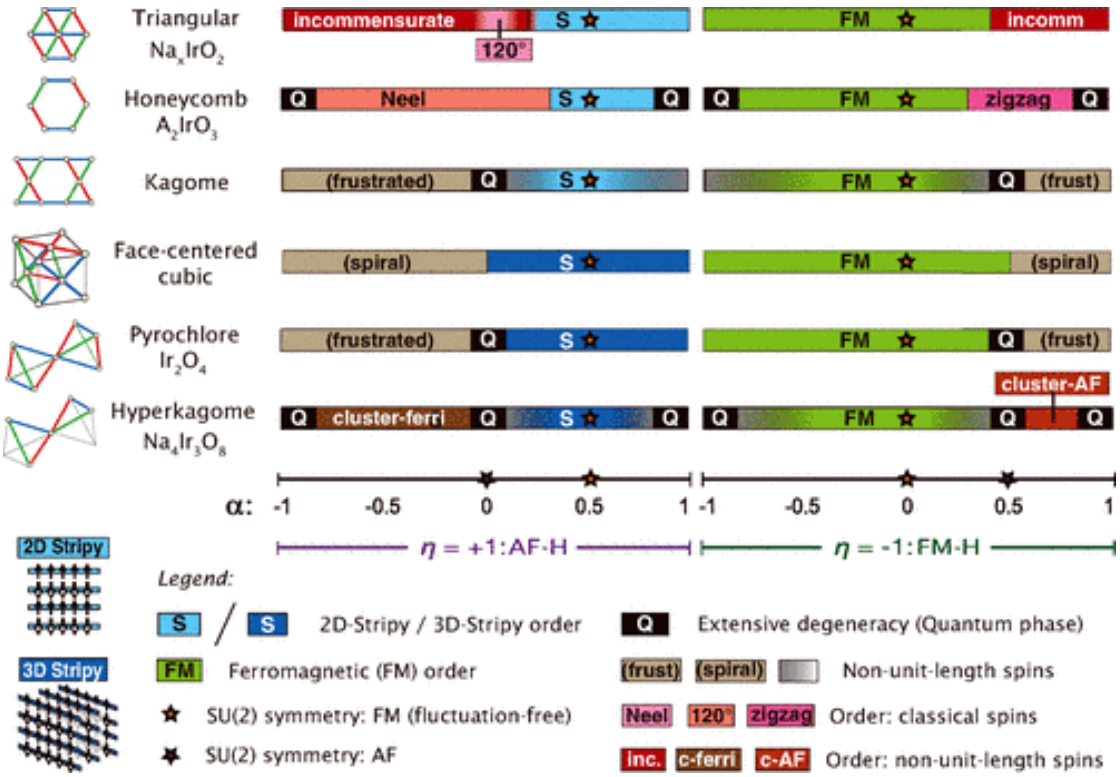

Figure 1.20.: Phase diagrams for the Kitaev-Heisenberg Hamiltonian $H_{KH} = \eta(1 - |\alpha|)\vec{S}_i \cdot \vec{S}_j - 2\eta\alpha S_i^\gamma S_j^\gamma$ with $\eta = \pm 1$ on the various lattices. The parameter space is a ring: the endpoints should be identified. Fig. 1 is reprinted with permission from I. Kimchi and A. Vishwanath. "Kitaev-Heisenberg models for iridates on the triangular, hyperkagome, kagome, fcc, and pyrochlore lattices". Phys. Rev. B 89, 014414 (2014) [79]. Copyright 2014 by the American Physical Society.

symmetric off-diagonal exchange Γ that couples the two orthogonal spin components $\alpha, \beta \perp \gamma$. The strength of J, K and Γ strongly depends on the material.

The model is often simplified to the *Heisenberg-Kitaev* model, where $\Gamma = 0$. Originally, this model was proposed for the honeycomb lattice. However, it can be applied for the triangular, hyperkagome, kagome, fcc and pyrochlore lattices too [79]. The corresponding to each lattice phase diagram is plotted in Fig. 1.20. Depending on the ratio of J and K parameters, and the type of lattice various magnetic phases can emerge.

As for the triangular lattice, we expect the following phases: incommensurate non-unit length spins wave, 120° Neel order (in the vicinity of K=0), 2D-Stripy AFM order and FM order.

1.4. Frustrated magnetism

In this section we will give a brief overview of the topic of frustrated magnetism and its connection to the quantum spin liquid state.

Frustrated magnets is a very special and peculiar class of magnets. The word "frustration" means a situation when a spin (or a number of spins) cannot find an orientation to fully satisfy all the interactions with its neighboring spins [80]. Frustration can be caused by competing interactions or by lattice geometry, for example triangular, face-centered cubic and hexagonal-close-packed lattices are *frustrated* if the only interaction is antiferomagnetic nearest-neighbor interaction.

The simplest example to illustrate this idea is of triangular lattice with antiferromagnetic nearest-neighbor interaction of the Ising type, where spins can be either in the same direction or in opposite directions. Consider only one triangle with a, b, c corners as depicted in Fig. 1.21. If one now puts spins on sites a and b in opposite direction, antiferromagnetic interaction between them will be satisfied, however there is no way to choose the direction of spin on c site to make spins on a, c and b, c sites to be simultaneously in opposite directions: if you satisfy a-c bond then b-c bond will be unsatisfied and vice versa.

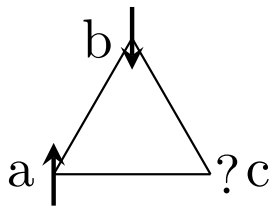

Figure 1.21.: Frustration on triangular lattice with anitiferromagnetic nearest-neighbor interaction of the Ising type: if the AFM interaction between a-b is satisfied there is no way to satisfy both a-c and b-c interactions for the collinear spin directions. For brevity only a single triangle is drawn.

We need to recall, that frustration arises because of geometry and type of interactions. For example, frustration on triangular lattice may be lifted if there is another competing interaction, like second nearest neighbor interaction.

The most revealing property of frustrated magnet is temperature dependence of its magnetic susceptibility. By Currie-Weiss law we know, that susceptibility can be expressed as:

$$\chi = \frac{1}{T - \Theta}, \tag{1.59}$$

with T being a temperature and Θ is the Curie–Weiss constant, that characterize the sign and strength of underlying magnetic interactions: $\Theta > 0$ for ferromagnetic interactions and $\Theta < 0$ for antiferromagnetic. In nonfrustrated antiferromagnetic magnets there is a cusp in susceptibility below Néel temperature $T_N \sim \Theta$, that describe a temperature at which long-range magnetic order forms [81]. However, in frustrated systems an ordered state will gain only a small fraction of exchange energy, so $T_N \ll \Theta$ [47]. The ratio $\frac{\Theta}{T_N}$ quantify the amount of frustration in the system [82]. In the region $T_N < T < \Theta$ there exists short-range magnetic correlation, but with no long-range order.

Quantum fluctuation together with frustration can prevent magnetic ordering at $T = 0$, while non-zero local magnetization will exist. These factors lead to a large variety of "spin liquid" phases and we will briefly introduce the topic following [83].

Quantum effects may generate a *valence bond* (VB) state, which is a singlet state that connects two $S = \frac{1}{2}$ spins at neighboring sites. This state minimizes the energy of antiferromagnetic coupling between spins. Two types of systems with this states may arise: *valence-bond crystals*, that have long-range order in the VB arrangements and *spin liquids*, that do not develop long-range order in any local parameter at any temperature [83]. It is worth noting that VB can be formed not only within neighbor sites but on distant sites.

There are different arrangements of VB states and they can mix, reducing the energy. For example, for 1D chain we can have a state $(12)(34)(56)\ldots$, where formation of VB state between sites is denoted by brackets, or we can connect other pairs $\ldots(23)(45)\ldots$. The mixture of such states is called *resonance* and the final state is created from all of these configurations, the *resonating valence bond* (RVB) state.

A key difference between valence-bond crystals and RVB liquids is that the former has integer excitations, while excitations for RVB liquids are fractionalized.

2. Review on bismuthates and iridates

In this chapter we will briefly review the recent experimental and theoretical investigations of bismuthates and iridates. For the bismuthates we focus on $BaBiO_3$ as a representative compound to discuss its electronic properties, the insulator-metal transition and emergence of superconductivity emphasizing difficulties in the ab initio description of experimental results. As for iridates, we will describe the novel $J_{eff} = \frac{1}{2}$ Mott insulator state, insulator-metal transitions in iridates, the peculiar case of pentavalent Ir and, finally, talk about the prominent candidates for realization of quantum spin liquid.

2.1. Bismuthates

The interest in $ABiO_3$ bismuthates emerged due to their superconducting properties, since these compounds exhibit relatively high T_c's (∼30–40 K), and are oxides and non-cuprate superconductors. The first member of the family to attract attention was $BaBiO_3$, which was synthesized in 1963 [20]. The parent compound is an insulator, but an insulator-metal transition can be induced by the hole doping, leading to a superconducting state with T_c = 13 K for $BaPb_{1-x}Bi_xO_3$ and T_c = 34 K for $Ba_{1-x}K_xBiO_3$ [3]. Later superconductivity was also reported for doped isovalent $SrBiO_3$ [4], with T_c values of ∼12 K for $Sr_{1-x}K_xBiO_3$ (x = 0.45–0.6), ∼13 K for $Sr_{1-x}Rb_xBiO_3$ (x = 0.5) and ∼12 K, ∼5 K and ∼9 K for $K_{1-x}A_xBiO_3$, A=La, Bi and Ca respectively [5]. Recently, a superconductor with A-site ordered double-perovskite structure, $(Na_{0.25}K_{0.45})Ba_3Bi_4O_{12}$, was synthesized with T_c of ∼27 K.

Among all these compounds, $BaBiO_3$ is the most investigated one; since its properties are representative of the whole class, we will concentrate our review mostly on $BaBiO_3$.

$BaBiO_3$ has a monoclinic structure (see Fig. 2.1a), which is a distortion of the cubic perovskite structure. Because of charge disproportionation this structure can be effectively described as a double perovskite, $AB'B''O_3$. Two distortions of the BiO_6 octahedra are present: tilting and breathing distortion, as depicted in Fig. 2.1c. The tilting distortion corresponds to a rigid rotation of the octahedra (the angle of rotation is denoted by φ on the figure) while the breathing distortion is associated with an alternating size of BiO_6 octahedra (the white arrows on the figure show the direction of the O displacements, caused by this distortion). The breathing distortion is coupled to the charge disproportionation in $BaBiO_3$, originating from the fact that Bi is a multivalence element, i.e., it skips the +4 valence, which is less energetically favorable [84]. Valence skipping

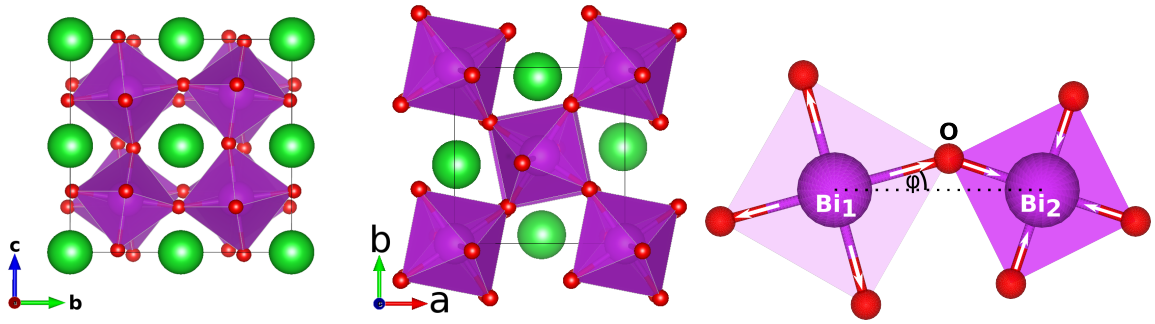

(a) (b) (c)

Figure 2.1.: (a) $BaBiO_3$ and (b) $SrBiO_3$ crystal structure (c) tilting and breathing distortions. The tilting angle is φ. The breathing distortion is denoted by white arrows.

can be synthesized by the formula:

$$2Bi^{4+} \rightarrow Bi^{5+} + Bi^{3+}.$$

The breathing distortion is caused by the fact that the Bi^{5+}-O distance is shorter than the Bi^{3+}-O since the electrons feel a stronger attraction from oxygen (see Fig. 2.1c, where Bi_1 is Bi^{3+}, and Bi_2 is Bi^{5+}) and this, together with a periodic alternating charge distribution (charge density wave, CDW) leads to a breathing distortion. $SrBiO_3$ exhibit similar properties, however the crystal structure is different, P121n1, due to different type of tilting distortion (see the structure on the Fig. 2.1b).

A remarkable feature of $BaBiO_3$ is the possibility to induce an insulator to metal transition by hole doping, for example by substitution of Ba by K (see the phase diagram in Fig. 2.3). Under doping $Ba_{1-x}K_xBiO_3$ undergoes two structural phase transitions: from monoclinic to orthorhombic at $x \sim 0.1$ and at $x \sim 0.37$ from orthorhombic to cubic [87]. In the orthorhombic phase the breathing distortion is suppressed and only the tilting distortion survives. In the cubic phase no distortions of octahedra are present, the CDW is suppressed, and $BaBiO_3$ becomes metallic and superconducting with T_c~34 K, being a high-T_c noncuprate superconductor.

Another possibility to suppress the CDW or tune the structural distortions can be realized in the systems with reduced dimensionality. For example, it was shown that tilting of BiO_6 octahedra can be suppressed in thin films [88], but, it is not enough to induce an insulator-metal transition. Another study shows, that the minimum thickness to have a breathing distortion and CDW in thin films is ~11 unit cells, which gives a way to control $BaBiO_3$ properties via thickness control [89]. Disappearance of lattice distortions may be accompanied by an insulator-to-metal transition. This scenario is supported by the optical conductivity measurements but no reliable measurements of the electronic transport have been obtained.

Remarkably, hole doping induces superconductivity also in reduced dimensions: superconductivity

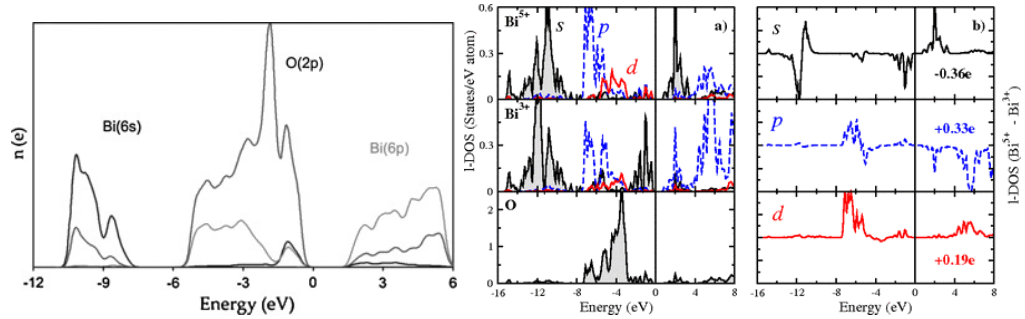

(a) (b)

Figure 2.2.: (a) Partial electron density of states of α-Bi_2O_3, plotted with respect to the highest occupied state. The black lines represent Bi 6*s* states, light gray Bi 6*p* states, and dark gray O 2*p* states. (b) Calculated scQPGWTCTC (left panel) partial DOS decomposed over Bi_1, Bi_2 and O (apical and planar oxygen yield identical DOS) and (right panel) DOS difference between Bi_1 and Bi_2 decomposed into l quantum numbers. Fig. 4 is reprinted with permission from A. Walsh, G. W. Watson, D. J. Payne, R. G. Edgell, J. Guo, P.-A. Glans, T. Learmonth, and K. E. Smith. "Electronic structure of the α and δ phases of Bi_2O_3 : A combined *ab initio* and x-ray spectroscopy study". Phys. Rev. B 73, 235104 (2006) [85]. Copyright 2006 by the American Physical Society. Fig. 3 is reprinted with permission from C. Franchini, A. Sanna, M. Marsman, and G. Kresse. "Structural, vibrational, and quasiparticle properties of the Peierls semiconductor $BaBiO_3$: A hybrid functional and self-consistent GW + vertex-corrections study". Phys. Rev. B 81, 085213 (2010) [86]. Copyright 2010 by the American Physical Society.

was discovered in bilayers of $BaBiO_3$ and $BaPbO_3$ with T_c's as high as $T_c \approx 8$ K [90].

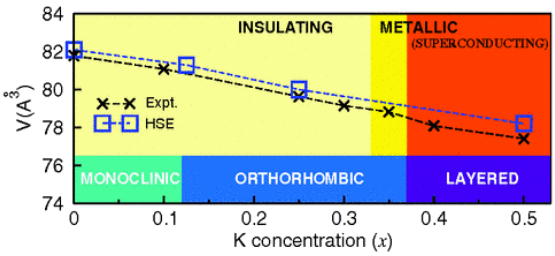

Figure 2.3.: Phase diagram and volume (V) of $Ba_{1-x}K_xBiO_3$ upon doping throughout the insulator-metal transition. The computed volumes are compared to neutron powder diffraction data [87]. Fig. 3a is reprinted with permission from C. Franchini, G. Kresse, and R. Podloucky. "Polaronic Hole Trapping in Doped $BaBiO_3$", Phys. Rev. Lett. 102, 256402 (2009) [25]. Copyright 2009 by the American Physical Society.

2.1.1. Theoretical findings and challenges

CDW in $BaBiO_3$ leads to an insulating state, while an ideal $BaBi^{4+}O_3$ would be a metal and adopt an ideal cubic perovskite structure.

The first DFT studies of $BaBiO_3$ date back to 1983 [91]. These studies, which employed LDA and GGA functionals, correctly predicted a distorted ground state for undoped $BaBiO_3$ but severely underestimated the size of the breathing distortion, and hence predicted a metal instead of an insulator [28, 91–93]. The reason is a sizable self-interactions that are present in semilocal DFT [23, 24]. The first successful *ab intio* description of $BaBiO_3$ is contained in Ref. [25] which employed hybrid functionals (see Section 3.1 for more details on theory of hybrid functionals).

Now, we will describe $BaBiO_3$ electronic structure, but before describing the electronic structure of $BaBiO_3$ we will say a few words about the electronic structure of α-Bi_2O_3, that gives an idea on the impact of Bi-O hybridization: Bi $6s$ states are mostly below O $2p$ states as shown in Fig. 2.2a, but a significant amount of $6s$ states is present at the top of the valence band (Bi-O antibonding state). In $BaBiO_3$ Bi $6s$ states remain below O $2p$ states, but Bi^{3+} $6s$ states in top of the valence band have moved up in the energy relative to the O $2p$ states (see Fig. 2.2b). Two factors contribute to this process: increase of the antibonding interaction between O $2p$ states Bi $6s$ states and the indirect impact from ionic Ba^{2+} cations, that stabilizes O $2p$ states and moves them down in the energy [94]. The empty $6s$ states of Bi^{5+} have moved further up because of the stronger hybridization with O $2p$ due to a shorter Bi^{5+}-O distance in comparison to Bi^{3+}-O distance. As a result, Bi^{3+} states are in the top of the valence band and Bi^{5+} are in the bottom of the conduction band.

HSE hybrid functional correctly predicts an insulating charge disproportionated state in $BaBiO_3$ with a band gap of 0.65 eV [25], while values reported in the literature are in range from 0.2 [10] to 1.1 eV [93]. Structural data is also in a good agreement with experiment: predicted Bi-O length difference is $b = 0.18$ Å, while experimental value is $b = 0.17$ Å [11]; the calculated value of tilting distortion is $t = 11.9°$ and experimental value is $t = 11.2°$ [11].

A recent study reproduces the same result using GGA+U [95] with $U = 0.7$ eV for Wannier functions; the U value for atomic orbitals was estimated to be $U = 2.5$ eV. It was shown, that GGA+U gives $b = 0.15$ Å and $t = 12°$ with a gap of 0.55 eV, that are close to experimental values. It was reported, that charge difference is 0.43 e^-, meaning that charge disproportionation is rather weak and a strong hybridization of Bi(s) and O(p) is present, confirmed by Bi(s) and O(p) contributions to the obtained Wannier functions: the contribution of Bi(s) is around 20-23% and the contribution of O(p) is around 80-77%.

We want to point out that charge disproportionation is never strong in $BaBiO_3$, meaning that it is never one electron, that is transferred from Bi^{4+}, so the notation of +3 and +5 valence states is rather formal. The reason is a strong hybridization of Bi(s) and ligand O(p) states. Motivated by strong hybridization and a possibility of O to host charge holes, another mechanism of charge

transfer was proposed [96, 97]: condensation of holes on ligands L with the following mechanism:

$$2(\mathrm{Bi}^{3+}L) \rightarrow \mathrm{Bi}^{3+}L^2 + \mathrm{Bi}^{3+}.$$

These two pictures are consistent with each other and it is the most probably that both processes contribute to a formation of CDW in $BaBiO_3$.

When $BaBiO_3$ is doped by K, $Ba_{1-x}K_xBiO_3$ undergoes a phase transition to an orthorhombic perovskite-like semiconducting phase at $x \approx 0.12$ [87]. The compound becomes superconducting with no measurable distortions for a larger K concentrations ($0.37 < x < 0.53$) [3]. It was a challenge for *ab initio* methods to describe the insulating state of orthorhombic structure of hole doped $BaBiO_3$ [87, 98, 99] in $0.1 < x < 0.37$ region and why transition to the metallic state does not happen in this region. Since the electronic state of parent material was described incorrectly by LDA or GGA functionals, the same approach is unreliable for hole-doped $BaBiO_3$ too. However, the problem is tractable by hybrid DFT-Hartree-Fock theory with HSE functional (see Section 3.1 for more details on theory of hybrid functionals) [25]. Hole-doped $BaBiO_3$ remains semiconducting upon moderate hole doping because Bi^{3+} sites can trap two holes from the valence band to form Bi^{5+}.

We will now describe *ab initio* modeling for this case following Ref. [25], where the use of hybrid functionals was employed. The insulator to metal transition is controlled by the coupling between the additional holes, that are trapped on original Bi^{3+} sites and the oxygen polarization fields that surround the BiO_6 octahedra. The quasiparticle that is composed of a hole plus its accompanying polarization field (distortion) is called a *polaron*.

At first, we will describe the hole-doped system without polaronic distortions. For this task, a supercell with 8 perovskite unit cells is used, with initial structure employing the same tilting distortion as in the monoclinic structure. The replacement of 2 or 4 of original 8 Ba atoms with K atoms corresponds to a hole-doping considerations of $x = 0.25$ and $x = 0.5$ respectively. For $x = 0.25$ resulting structure is orthorhombic with K atoms arranged along [001] direction. The relaxed structure is in a good agreement with experimental crystal structure. Fermi-level moves into the Bi^{3+} dominated valence band and the system becomes metallic as depicted in Fig. 2.4(b). At $x = 0.5$ (see Fig. 2.4(c)) the conduction and valence bands overlap and there is no charge disproportion. The effect was simulated by electronic hole doping in the primitive cell ($Ba_2Bi_2O_6$) with similar results indicating that chemical effects do not play a major role. This description describes well the structural properties but, fails to reproduce the insulating state of the system, as observed in experiments [99, 101].

Polarons allow the stabilization of an insulating state. To model the isolated polaron fcc-like supercell with 16 $BaBiO_3$ unit cells was used, where two Ba atoms are replaced by K atoms that corresponds to $x = 0.125$. It was shown that the trapping of the two holes on the former Bi^{3+} lattice site emerges during relaxation and it is strongly linked to the local lattice relaxations. This Bi site is denoted as “bipolaron” since it traps two holes. The final relaxed model is insulating as

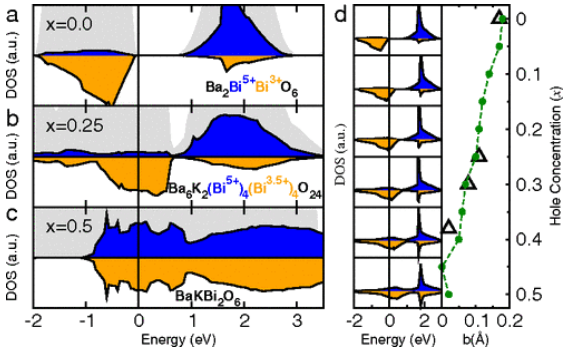

Figure 2.4.: (a–c) Evolution of the density of states (DOS) on Bi^{3+} [gray (orange)] and Bi^{5+} [black (blue)] atoms with K hole doping x for the nonpolaronic solution (superlattice with 8 unit cells). The light-gray shadows indicate the total DOS. (d) Evolution of the DOS of hole-doped $BaBiO_3$ simulated by removing a fraction of an electron (x) leading to a reduction of the gap between the Bi^{3+} [gray (orange)] and Bi^{5+} [black (blue)] subbands, and the simultaneous reduction of the Bi-O bond length difference b between Bi^{3+} and Bi^{5+} sites. The Δ symbols represent the estimated values of the breathing distortion b computed from the Rice and Wang gap equation [100]. Fig. 2 is reprinted with permission from C. Franchini, G. Kresse, and R. Podloucky. "Polaronic Hole Trapping in Doped $BaBiO_3$", Phys. Rev. Lett. 102, 256402 (2009) [25]. Copyright 2009 by the American Physical Society.

depicted in Fig. 2.5(b).

The two holes form a single unoccupied band below the bottom of the conduction band (see Fig. 2.5(e)) which is formed by an antibonding linear combination between Bi(s) states and its surrounding O(p) orbitals. The lattice distortion that accompanies the bipolaron is driven by moving the antibonding Bi-O state above the Fermi level. The spatial charge distribution of the bipolaron is depicted in Fig. 2.5(h), showing that actually only 15% of the charge is localized on the Bi site.

It is worth noting, that it was not possible to stabilize the polaronic solution using LDA+U treatment, since Bi(s) orbitals are too delocalized in this treatment.

In the case of $x = 0.25$ the distance between bipolarons is smaller and a strong interaction between them was reported. The bipolaronic subband is split into two: a lower broad subband and a narrow second subband, as depicted in Fig. 2.5(f). Metallic nondisproportionated state at $x = 0.5$ is caused by an overlap between the valence band and the polaronic band.

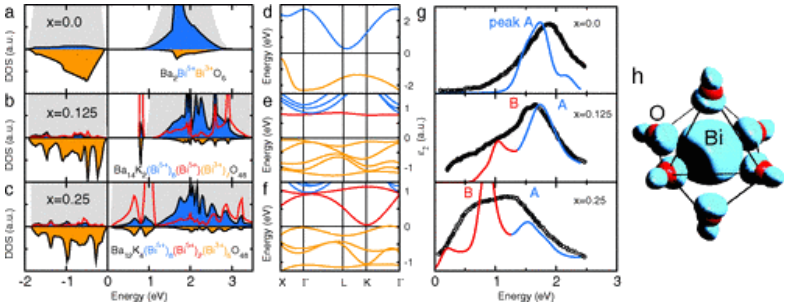

Figure 2.5.: (a–c) Evolution of the DOS and (d–f) corresponding band structure upon K substitution for the polaronic solution. The gray shadows indicate the total density of states, and red curves indicate the bipolaronic states as created by doping. (g) Comparison between the theoretical and measured imaginary part of the dielectric function for x = 0 , 0.125. and 0.25. Peak (A) corresponds to excitations from Bi^{3+} into Bi^{5+} states; peak (B) corresponds to excitations from Bi^{3+} into bipolaronic states [red curves in (b, c, e, f)]. The experimental curves (open circles) are taken from Ref. 22 (x=0) and Ref. 23 (x=0.21). For the calculated curves, the excitation energies have been scaled by a factor of 0.8 to approximately account for excitonic effects otherwise not included in the calculations. (h) Charge density corresponding to the bipolaronic band (red line) of (e) localized around the BiO_6 octahedron at the converted Bi^{3+} $\rightarrow$ Bi^{5+} atom. Fig. 4 is reprinted with permission from C. Franchini, G. Kresse, and R. Podloucky. "Polaronic Hole Trapping in Doped $BaBiO_3$", Phys. Rev. Lett. 102, 256402 (2009) [25]. Copyright 2009 by the American Physical Society.

2.1.2. Attempts to explain superconductivity in $BaBiO_3$

It is also a challenge for *ab initio* methods to explain the origin of superconductivity in $BaBiO_3$. A large value of electron-phonon coupling parameter λ (about 1.0-1.2) in $Ba_{1-x}K_xBiO_3$ was confirmed by experiments [102–104]. Several theoretical studies were attempted to study the origins of superconductivity in $Ba_{1-x}K_xBiO_3$. Much smaller value of λ (around 0.3) was estimated by an early study of the Bi-O breathing mode on the basis of the frozen-phonon approximation [28]. Later, a more detailed study using the virtual crystal approximation was performed including all phonon branches: LDA theory with linear-response approach was employed for $Ba_{0.6}K_{0.4}BiO_3$, but the calculation gave nearly the same $\lambda = 0.3$ [27]. A recent *ab initio* study using GGA with linear-response approach and Wannier interpolation technique pointed out the importance to account for tilting distortion of BiO_6 octahedra and the estimated value of electron-phonon coupling with octahedral distortion taken into account is $\lambda = 0.45$ [29].

The shortcomings of the DFT with semilocal functionals to describe electronic correlations was emphasized [23–25]. A study using GW and screen-hybrid functional DFT approaches to have a proper treatment of electronic correlations was performed [105]. It was reported that the shift of the electronic bands due to Bi-O breathing mode is larger than the one obtained using LDA functional and the rescaling of the LDA electron-phonon coupling parameter, obtained in the virtual crystal application, was performed and yielded $\lambda = 1$. However, the overall agreement of

the experimentally measured Eliashberg spectral function α^2F is not satisfactory: the agreement of λ and T_c with the experiment is achieved by the threefold increase in the electron-phonon coupling of the high-frequency oxygen-breathing mode, while to have a better agreement with experiment the high-frequency part of α^2F should decrease and low-frequency α^2F increase.

Different explanations for superconductivity in bismuthates was proposed. One of the first explanations proposed is based on the attractive Hubbard model [30], where, in contrast to original Hubbard model, the value U is negative. The model correctly captures the valence skipping, as well as able to describe both an insulating charge disproportionated or a superconducting state at half-filling [31, 84]. However, the estimation of Coulomb interaction parameters for the Bi 6*s* orbitals using constrained DFT shows no indication for negative U of the electronic origin [106].

Another possible scenario is based on the condensation of bipolarons. It was shown that electrons (or holes) added to a commensurate charge density wave insulator can bind to form bipolaron states [107]. These bipolaron states can form a Bose condensate, resulting in superconductivity at relatively high temperature [108]. It was shown that this picture can be applied for $BaPb_{1-x}Bi_xO_3$ [31], however no convincing results that this picture is responsible for the superconductivity in $BaBiO_3$ were provided.

The final answer on the origin of superconductivity in $BaBiO_3$ is still to be found.

2.1.3. $BaBiO_3$ under pressure

Naively one would expect that another scenario of the insulator-to-metal transition is also possible: under increasing pressure the bandwidth is continuously increased leading to the band overlap and closing of the gap. For example, this scenario holds for $LaMnO_3$ perovskites [109].

The first experimental studies of $BaBiO_3$ under pressure was limited to pressures as high as 20 GPa [110, 111]. However, no data on the crystal structure was reported due to the low experimental resolution. The only reported structural feature was an anomaly in the bulk modulus at 4 GPa where the bulk modulus decreases. This anomaly was attributed to the change of the tilt system. It was reported that the system remains insulating up to at least 10 GPa.

Regarding the pressure effect on octahedral tiltings in perovskites, several empirical rules were proposed [112, 113]. A recent systematic study of this topic based on *ab initio* calculations [114] predicts that the value of the tilting distortion in perovskite of $BaBiO_3$ type increases with pressure for a moderate pressures.

Recently in our work we showed that $BaBiO_3$ undergoes a transition to a highly distorted phase and remains insulating up to 100 GPa (as will be discussed later in Sec. 4.1). The results were independently confirmed by a combined theoretical and experimental work [6]. However, only transport measurements were done in the experiment, confirming insulating behaviour up to 80 GPa, but no data on crystal structure were reported.

2.2. Iridates

In this section we will describe an important class of $J_{eff} = \frac{1}{2}$ Mott insulators and related systems. At first we will start with a textbook example, Sr_2IrO_4 (its crustal structure is depicted in Fig. 2.6a), which is the first system in which a metal-insulator transition in the $J_{eff} = \frac{1}{2}$ state was discovered for the first time, and then continue with efforts to induce insulator-metal transition in this and related systems. Then we will discuss an exotic pentavalent Ir^{5+}, which in contrast to Ir^{4+} host a $J_{eff} = 0$ state. In the final part we will discuss possible candidates for quantum spin liquid state. The most investigated among the iridates candidates are Na_2IrO_3 and α-Li_2IrO_3 showed in Fig. 2.6b and Fig. 2.6c. β-Li_2IrO_3 and γ-Li_2IrO_3, two interesting allotropes of Li_2IrO_3, are shown in Fig. 2.6d and Fig. 2.6e, respectively. The main structural peculiarity of these two structures is a non-planar honeycomb arrangement of Ir atoms.

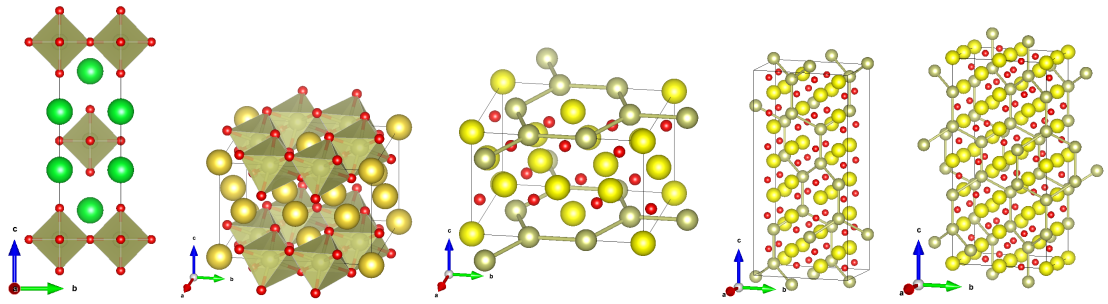

(a) (b) (c) (d) (e)

Figure 2.6.: The crystal structure of (a) Sr_2IrO_4, (b) Na_2IrO_3, (c) α-Li_2IrO_3, (d) β-Li_2IrO_3 and (e) γ-Li_2IrO_3. Lime spheres are Sr, golden spheres are Na, yellow spheres are Li, small red spheres are O and green spheres are Ir.

2.2.1. Relativistic Mott insulator

In late 90s a big interest in iridates has emergent due to the fact that a strong value of spin-orbit coupling in these compounds causes a rich variety of physical phenomena. A milestone example is Sr_2IrO_4, which for the first time was synthesized in 1957 [115] and revisited in 1990s [116, 117]. The interest in Sr_2IrO_4 was motivated by the fact that it has the same structure as superconducting noncuprate Sr_2RuO_4 compound (K_2NiF_4 structure, see Fig. 2.6a). However, although it is a system with an odd number of valence electrons, Sr_2IrO_4 is insulating. This effect cannot be justified only due to the strong correlations: in comparison to 3d elements, U is smaller for Ir and reasonably high U cannot open a gap in Sr_2IrO_4 compound.

It is now understood that the insulating state of Sr_2IrO_4 results from the interplay between SOC and strong correlations. Materials which exhibit this type of physics are now known as relativistic Mott insulators [16].

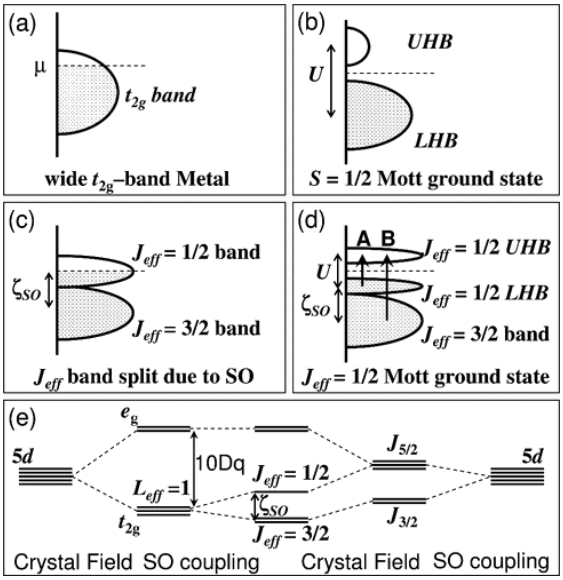

Figure 2.7.: Schematic energy diagrams for the $5d^5$ (t_{2g}^5) configuration (a) without SO and U, (b) with an unrealistically large U but no SO, (c) with SO but no U, and (d) with SO and U. Possible optical transitions A and B are indicated by arrows. (e) 5d level splittings by the crystal field and SO coupling. Fig. 1 is reprinted with permission from B. J. Kim, H. Jin, S. J. Moon, J.-Y. Kim, B.-G. Park, C. S. Leem, J. Yu, T. W. Noh, C. Kim, S.-J. Oh, J.-H. Park, V. Durairaj, G. Cao, and E. Rotenberg. "Novel $J_{eff} = 1/2$ Mott State Induced by Relativistic Spin-Orbit Coupling in Sr_2IrO_4". Phys. Rev. Lett. 101, 076402 (2008) [16]. Copyright 2008 by the American Physical Society.

A strong octahedral crystal field splitting in Sr_2IrO_4 splits d-states into e_g and t_{2g} states favoring a low-spin state: the only occupied states are t_{2g} hosting five valent electrons of Ir^{4+}. In the absence of SOC or strong correlations the t_{2g} states would be partially filled and the system will be a metal as depicted in Fig. 2.7(a). As was mentioned before, a U-driven transition to the conventional Mott insulator is not applicable here, see Fig. 2.7(b), since the value of U needed to open the gap is unrealistically high. As was discussed in Sec. 1.2.4, SOC splits t_{2g} states into the lower lying $J_{eff} = \frac{3}{2}$ state and the higher lying $J_{eff} = \frac{1}{2}$ state; the former is then fully occupied and the latter becomes half occupied, as is shown in Fig. 2.7(c). The former can be easily split with a moderate value of U as depicted in Fig. 2.7(d).

This situation can be described by the three-orbital Hubbard model with a spin-orbit coupling, where intraorbital, interorbital and intrasite exchange terms are taken into account (see Sec. 1.2.3 for the discussion of the Hamiltonian). By using this model it was shown that a large SOC greatly reduces the value of U at which the transition from a paramagnetic metal to an antiferromagnetic insulator [118] takes place; the same result as was pointed out by the model study mentioned in Sec. 1.2.3. The Hund's coupling induces the anisotropic spin exchange and stabilizes the in-plane AFM order.

$J_{eff} = 1/2$ state leads also to unusual magnetic properties: orbital momentum is twice larger than spin magnetic moment [16]. Magnetic state in Sr_2IrO_4 is a canted AFM state, as a consequence of Dzyaloshinskii-Moriya interaction [19], resulting in a weak ferromagnetism.

2.2.2. Insulator-to-metal transition

Once Sr_2IrO_4 had been identified as a relativistic Mott insulator, many authors have explored the possibility of inducing an insulator-to-metal transition, similarly to what is done in ordinary Mott insulators. One possibility is to use dimensionality control. Sr_2IrO_4 belongs to $Sr_{n+1}Ir_nO_{3n+1}$ Ruddlesden-Popper series, which comprises structures made of n layers of $SrIrO_3$ between SrO planes. In this Ruddlesden-Popper series $n = 1$ corresponds to Sr_2IrO_4, $n = 2$ corresponds to $Sr_3Ir_2O_7$ and $n = \infty$ to $SrIrO_3$.

Naively, one expects that the bandwidth of the t_{2g} orbitals would increase with n, and hence the system should become more metallic. This is confirmed by experiments [119]; $Sr_3Ir_2O_7$ is a narrow bandgap AFM insulator [120] and $SrIrO_3$ is a correlated metal [121]. *Ab initio* the result can be reproduced using DMFT theory [122] that allows for a realistic treatment of competing SOC, crystal field and Coulomb interaction. The study also pointed out that the deviation from $J_{eff} = \frac{1}{2}$ state is negligible for $SrIrO_3$ and Sr_2IrO_4, but becomes significant for Sr_3IrO_7.

The tunability of the electronic and magnetic properties of $(SrIrO_3)_m/(SrTiO_3)$ by change of dimensionality in terms of number of layers m and by strain was also showed by means of *ab initio* calculations [123] based on DFT and constrained random phase approximation (cRPA). The estimated effective value of U for Ir changes significantly: from 1.59 eV for $m = 1$ to 0.95 eV for $m = \infty$. The bandwidth W is also controlled by dimensionality: W changes from $W = 1.9$ eV for $m = 1$ to $W = 2.8$ eV for $m = 3$. Both the reduction of U and the increase of W is responsible for the dimensionality controlled insulator-metal transition. Strain is responsible for the change of the structural distortions and the continuous application of compressive strain induces insulator-metal transition by an increment of W.

An alternative way to induce a MIT in iridates is to use doping and this route has been explored by several authors. We focus on a few representative examples. $CaIrO_3$, which has a postperovskite structure, can be doped by Na [124]. In this structure, IrO_6 octahedra from a quasi-2D lattice and $CaIrO_3$ is an insulator with AFM magnetic ordering [124, 125]. The magnetic order is destabilized with increasing doping and $Ca_{1-x}Na_xIrO_3$ becomes a paramagnetic metal in the region $x > 0.3$. If $CaIrO_3$ is doped with Ru, leading to $Ca(Ir_{1-x}Ru_x)O_4$, the transition is at $x \sim 0.3$ from an antiferromagnetic Mott insulating phase to a ferromagnetic metal [126].

However, although the interpretation of the initial experimental results and *ab initio* calculation supported $J_{eff} = \frac{1}{2}$ picture[124, 125, 127], the subsequent *ab initio* calculations pointed out that the splitting of t_{2g} states associated with the tetragonal distortions is large and comparable with the strength of SOC [128, 129]. The result was confirmed by the subsequent RIXS experiments [130] concluding $CaIrO_3$ is not $J_{eff} = \frac{1}{2}$ Mott insulator.

A more complicated situation is observed for Sr_2IrO_4. It can be doped with Rh and the fully-substituted compound, Sr_2RhO_4, is a metal. In the $Sr_2Ir_{1-x}Rh_xO_4$ system the phase diagram is very rich [131, 132], having two insulating and two metallic regions: in the $0 \leq x \leq 0.16$ region magnetic ordering temperature and electric resistivity drops down and system becomes metallic. However, in the region $0.24 < x < 0.85$ it returns to the insulating state due to the presence of the localized states with a complicated magnetic state. Finally, close to $x = 1$ the system becomes a correlated metal.

Doping with Rh was also studied using *ab initio* methods by means of DFT+U+SOC calculations and the results are in reasonable agreement with experimental data [133]. Although Rh is nominally isovalent to Ir, Rh substitution of Ir is accompanied by a substantial hole transfer from the Rh site to the nearest-neighbor Ir sites. This shifts down the chemical potential and a two-dimensional metallic state is formed by conducting Rh planes, that are intercalated by insulating Ir planes. The hole doping causes a flipping of the inplane net ferromagnetic moment on the Rh plane and induces the transition from the AFM-I to the AFM-II ordering.

When doped with Ru, insulator-to-metal transition happens in $Sr_2Ir_{1-x}Ru_xO_4$ system too, but accompanied by a structural transition. The most peculiar result is the transition between two magnetic states in the region of low doping ($x < 0.3$): *ab-plane* and *c-axis* ordering [134].

The $n = 2$ member of the Ruddlesden-Popper system, $Sr_3Ir_2O_7$, has also been doped with electrons via La substitution of Sr. The insulator-metal transition happens for a very small value of doping, $x \sim 0.04$, from the antiferromagnetic insulator to the paramagnetic metal [135].

From the numerous examples discussed so far we see that physics in iridate compounds is very rich and for each specific composition has its specific details.

2.2.3. An exotic pentavalent Ir

Another intriguing class of iridates are the pentavalent iridates, in which Ir is in a Ir^{5+} configuration; in this case, since both the crystal field and SOC are strong, according to the atomic picture Ir should be in a $J_{eff} = 0$ state: four valence electrons fill the lower $J_{eff} = \frac{3}{2}$ states, depicted in the middle panel in Fig. 2.7(e), leading to a singlet $J_{eff} = 0$.

Indeed, this occurs in the post-perovskite $NaIrO_3$, which was synthesized using high-pressure solid state synthesis [32]. $NaIrO_3$ is an insulator, however the first LDA+U+SOC calculations with $U = 1$ eV value[1] performed for the experimental crystal structure were not able to reproduce the insulating ground state [32]. Later, by means of GGA+U+SOC calculations it was shown [136] that the optimized structure gives a nearly insulating state, with a S=0 state driven by crystal field (t_{2g} state are split into three non degenerate levels due to the high distortion of octahedra), rather than driven by the SOC J=0 state, thus being a band insulator.

[1] No estimation of U value was given: it was chosen as an approximate value expected for iridium.

To finally answer the question of the origin of insulating properties of $NaIrO_3$, a phase diagram in terms of Coulomb interaction U and SOC was calculated by LDA+Gutzwiller method [137] for the experimental structure. The use of LDA+Gutzwiller method was motivated by the failure of the LDA+U+SOC calculations to represent an insulating state even with U as large as 7 eV: calculations always converge to nonmagnetic metallic solution (as was the case in the first study mentioned above). To find the point on the phase diagram that corresponds to the real system, the value of SOC was estimated by *ab initio* calculations to be $\lambda = 0.33$ eV. As for the value of U, authors speculate that the reasonable values of U should be around 2.0–3.0 eV and it was chosen to be U=2.0 eV, which is slightly above the metal-insulator transition, which happens at $U_c = 1.8$ eV. With choice of $\lambda = 0.33$ eV and $U = 2.0$ eV (the same holds for $2.0 \leq U \leq 3.0$ eV) the system is a band insulator [137] with renormalized bandwidth induced by the correlation effect (the bandgap is 0.5 eV).

Another allotrope of $NaIrO_3$ exists, which has a hexagonal structure [33]. This structure shows a weak temperature dependent magnetism and semiconducting state. However, it has J=0 state and weak magnetism emerges due to impurities. In contrast to Na_2IrO_3, which we will discuss later, $NaIrO_3$ is stable at ambient conditions.

2.2.4. Realizing a quantum spin liquid

Another branch of investigations in iridates aims at realizing a new state of matter: *quantum spin liquid* (QSL). QSL has a degenerate magnetic ground state with a sizable local magnetic moment; however, the moments do not exhibit a long-range order. This is the reason why the term *liquid* is used. This state is interesting by itself and has also been related to the superconductivity in cuprates [138].

Probing the occurrence of a QSL state is a big challenge for experimentalists: there are no clear indicators of this state. The only possibility to detect QSL is via implicit evidences, mostly related to the absence of effects due to long-range magnetic order at low temperatures, while local magnetic moment is still present. The absence of long-range magnetic order can be measured by nuclear magnetic resonance (NMR) or muon spin spectroscopy (μSR) experiments. The latter technique is also able to measure the local magnetic moment. Specific heat measurements can indicate possible phase transitions happening in the system, i.e. the development of an ordered state. One can use thermal transport measurements to determine if excitations are localized or itinerant.

A big variety of compounds were proposed as a candidates for QSL state and a comprehensive list can be found in Ref. [139]. In following we will only review the prominent QSL candidates among Ir-based compounds.

A possible path to realize QSL in iridates were proposed by Jackeli and Khaliullin [19] (discussed in more detail in Sec. 1.3.1), who introduced a possible mechanism to implement Kitaev model [17] in Mott insulators with a strong SOC. Indeed, the Kitaev model for the honeycomb lattice has a

spin-liquid ground state. The work of Jackeli and Khaliullin motivated several proposals to realize Kitaev interactions, and hence QSL, in actual materials. After this proposal, a high amount of possible candidates were proposed and we will review the most prominent of them in the following text.

One of the most studied candidates is Na_2IrO_3 (see Fig. 2.6b), where IrO_6 octahedra share an edge and form a layered hexagonal structure with Na occupying the position in middle of hexagon, formed by Ir atoms. Na_2IrO_3 shows a 'zig-zag' magnetic order with $T_N = 15\ K$ [140]. The isovalent compound α-Li_2IrO_3, which has a similar crystal structure (Fig. 2.6c), shows a complicated incommensurate magnetic order [141]. The drastic differences in physical properties of two compounds with the same structure imply a high capability to tune them. Indeed, studies of $(Na_{1-x}Li_x)IrO_3$ show that T_N drops to 1.2 K at $x = 0.70$ and rises again to 7 K at $x = 0.90$ [142].

Examples of Na_2IrO_3 and α-Li_2IrO_3 showed a possibility to tune the properties of the system by substitution of A-cation mostly due to the change in the geometry of the honeycomb lattice. While attempts to produce another alkali honeycomb iridate by substitution of K, Rb and Cs have failed due to the large ionic radii, a new metastable a Cu_2IrO_3 compound[2] proposed [143], that provides a nearly perfect geometry with the angle between the edges of the honeycomb closer to 120° than in Na_2IrO_3. A closer to an ideal case geometry should reduce the Heisenberg interaction and make the Kitaev interaction stronger, thus moving the system closer to the Kitaev spin liquid limit. Indeed, the frustration index increases significantly to $f = 40$, while for Na_2IrO_3 $f = 8.2$. Cu_2IrO_3 exhibits a weak magnetic order with T_N=2.7 K, which is is substantially lower than in Na_2IrO_3 (T_N=15 K). However, further investigation is needed to establish the true nature of magnetism in this system.

In these systems CFS splits d-states into higher-lying e_g and lower-lying t_{2g}. The latter are occupied by 5 valent electrons of Ir^{4+}, while e_g states are empty. The usual theoretical treatment of Na_2IrO_3 and α-Li_2IrO_3 is based on the hypothesis that electronic structure in this materials is dominated by the SOC, and hence electrons in the t_{2g} bands are effectively described by atomic orbitals with effective total angular momentum $J_{eff} = \frac{3}{2}$ and $J_{eff} = \frac{1}{2}$. The upper $J_{eff} = \frac{1}{2}$ band is half-filled and Ir atoms can be described as localized magnetic moments. This picture is then treated in the framework for Heisenberg-Kitaev model [144, 145].

There are a lot of experimental and theoretical studies of these two compounds and detailed review can be found for example in Ref. [45]. In the following we will mostly focus on the magnetic properties of Na_2IrO_3 and α-Li_2IrO_3. Experimentally, neither Na_2IrO_3 nor α-Li_2IrO_3 have been found in a QSL state. At low temperatures Na_2IrO_3 exhibits an AFM *zigzag* order and Li_2IrO_3 exhibits a *spiral* AFM order (Ref. [147] and references therein).

The presence of strong FM Kitaev interaction in this materials was shown using *ab initio* many-body electronic-structure calculations [148, 149] and the fitting to the uniform magnetic susceptibility data [150]. However, the simple Heisenberg-Kitaev model (eq. (1.58) with only the

[2] The linking of Ir-honeycomb layers in Cu_2IrO_3 is different than in the parent $NaIrO_3$ structure: they are linked by CuO_2 dumbbells.

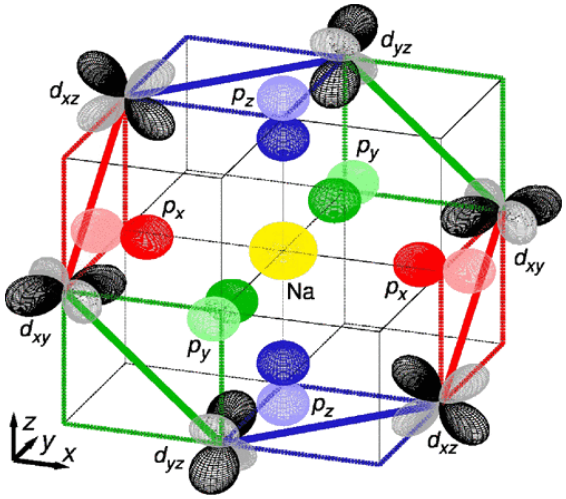

Figure 2.8.: Most relevant O p-assisted hopping paths in idealized Na_2IrO_3 structure. For each of the three Ir-Ir bond types only hopping between two particular t_2g orbitals is possible. The same holds for the second and third nearest neighbor hopping via O p and Na s orbitals. Ir-Ir bonds are color coded as follows: xy bonds are shown by blue lines, xz bonds by green, and yz bonds by red ones. Reuse Permissions Fig. 2 is reprinted with permission from I. I. Mazin, H. O. Jeschke, K. Foyevtsova, R. Valentí, and D. I. Khomskii. "Na_2IrO_3 as a Molecular Orbital Crystal". Phys. Rev. Lett. 109, 197201 (2012) [146]. Copyright 2012 by the American Physical Society.

Heisenberg J and Kitaev K interactions) cannot explain the experimental magnetic ordering of Na_2IrO_3 and α-Li_2IrO_3: none of these phases are present on phase diagram in the region of FM Kitaev coupling (c.f. Fig. 1.20).

A possible way to reconcile theory and experiment is to introduce interactions beyond the first nearest neighbor shell [151, 152]. One possibility is to include the Heisenberg interaction of the second J_2 and third J_3 nearest neighbors [148]: a model study shows that the phase diagram of the model hosts magnetic zigzag order and that positive J_2 and J_3 values of 4-5 meV would be consistent with the experimentally observed Currie-Weiss temperature for Na_2IrO_3. The same model was employed for α-Li_2IrO_3 [149], but the predicted magnetic moment (2.22 μ_B) is larger than the experiment (1.74 μ_B).

On the other hand, by means of *ab initio* calculations it was shown that next-nearest neighbors Kitaev interaction (K_2) is the second largest term in Na_2IrO_3 [153], which is not explicitly accounted in previous models since only the nearest-neighbor Kitaev interaction K_1 was included. Taking this considerations into account, the minimal extension of the nearest-neighbor Kitaev model, the K_1-K_2 model was proposed [154]. The model study shows that K_1-K_2 model is able to describe zigzag ordering without introducing unrealistically large second and third-neighbor Heisenberg interactions J_2 and J_3. However, no estimation of the interaction parameters for the real material was given in this study.

All in all, various models (some also include the off-diagonal interaction between the first nearest-neighbors Γ_1) with estimations of the interaction parameters was proposed and a review of some typical scenarios can be found in Ref. [155]. A big issue here is a difficulty to distinguish between some of these scenarios and any of the various parameter sets in experiments at zero magnetic field: more advanced experiments should be made.

An alternative picture able to explain the electronic and magnetic structure of these compounds was proposed utilizing an unusual concept: *quasimolecular orbitals*, which involve six Ir atoms arranged in a hexagon (QMO) [146, 156]. This picture, being delocalized, is a complete denial of Heisenberg-Kitaev model. What distinguishes the molecular orbital picture from that of usual molecular solids is the absence of spatial clusterization: each Ir atom participates in three different QMO via its three t_{2g} orbitals (see Fig. 2.8 for an example of such QMO). However, the description of actual electronic structure of Na_2IrO_3 lies in an intermediate regime between QMO and relativistic orbitals picture [156]. This concept is more promising in case of Li_2IrO_3: it is best described by $J_{eff} = \frac{1}{2}$ state at ambient pressure, but under the application of small hydrostatic pressure ($\sim$0.1 GPa) it crosses to QMO state [157].

Other interesting systems are the hyper-honeycomb β-Li_2IrO_3 (see Fig. 2.6d) and the stripy-honeycomb γ-Li_2IrO_3 (see Fig. 2.6e), where the honeycomb no longer forms a plane but is rather a complicated three-dimensional object, in which some of neighboring hexagonal cells are rotated with respect to each other. Both systems show magnetic ordering into an incommensurate antiferromagnetic spiral with similar propagation vectors [158–161].

The last candidate, which has an unusual chemical composition and is very promising for the realization of a QSL state, is the hyper-kagome $Na_4Ir_3O_8$. It was reported in 2007 that this compound shows no long-range magnetic order down to 2 K [46], the lowest temperature measured in this experiment. Later the same behaviour was demonstrated to persist down to 75 mK [162]. Finally, μSR experiments showed that short range order appears below T_F=6 K with a state similar to a spin ice [163, 164].

3. Methods

In this chapter we present the description of the methods used to treat the materials of interest. These include both traditional electronic structure theory methods to compute the physical properties of known systems, and more advanced methods to predict and analyze the crystal structure of materials when these are not known from experiment. First we give a brief introduction into Density Functional Theory (DFT) and the idea of hybrid functionals, that are used to improve it. Later, we introduce the reader to the basic concepts of group theory and describe the algorithm to determine the local coordination environment of a given site. The discussion continues with the description of isotropy subgroups, that are used to describe and classify second-order structural phase transitions and predict structures that emerge as a result of such transition. In the end, we describe the evolutionary structure prediction method, used to obtain the crystal structures of the investigated materials.

3.1. Electronic structure in hybrid density functional theory

In this section we will introduce the basic concepts of Density Functional Theory (DFT) following Refs. [165–167]. DFT is accurate enough in most cases, but fails for the systems where the strong local electronic correlations are important. An important example connected to this work is the family of $ABiO_3$ compounds. We use hybrid Hartree Fock/DFT theory with HSE functional (Heyd, Scuseria and Ernzerhof) [26] to account for strong correlations and to have a correct description of the electronic properties, since the method was successfully applied for $BaBiO_3$ [25, 86].

The properties of the system of interacting ions and electrons are described by Schrödinger's equation with the following Hamiltonian:

$$H = -\frac{1}{2}\sum_{I=1}^{M}\nabla_I^2 - \frac{1}{2}\sum_{i=1}^{N}\nabla_i^2 + \sum_{i=1}^{N}\sum_{j>i}^{N}\frac{1}{r_{ij}} + \sum_{I=1}^{M}\sum_{J>I}^{M}\frac{Z_I Z_J}{R_{IJ}} - \sum_{i=1}^{N}\sum_{I=1}^{M}\frac{Z_I}{r_{iI}}, \tag{3.1}$$

written in atomic units, where N is a number of electrons, M — a number of nuclei, I, J indices run over nuclei and i, j describe electrons, Z_I — a charge of I-th nucleus, r_{ij} is a distance between electrons i and j, R_{IJ} is a distance between nuclei I and J and r_{iI} is a distance between electron

i and nucleus I. The first term is a kinetic energy of nuclei motion, the second — a kinetic energy of electrons, the third — an electron-electron repulsion, the fourth — a nucleus-nucleus repulsion and, finally, the fifth — an electron-nucleus attraction.

The wave function that describes a specific state α of this system is the following:

$$\Phi_\alpha(\vec{r}_1, \vec{r}_2, \ldots, \vec{R}_1, \vec{R}_2, \ldots), \tag{3.2}$$

where $\vec{r}_i$ and $\vec{R}_I$ are positions of i-th electron and I-th nucleus respectively.

To proceed with the solution of this Hamiltonian, a Born–Oppenheimer approximation is made: since nuclei are much heavier than electrons, mass of a single proton is ∼1800 times larger than mass of a single electron, their kinetic energy is much smaller. Under these circumstances it is natural to assume that nuclei are frozen and that the electron subsystem instantly adjusts to a nuclear potential field. With this approximation, the total wave function is factored into electronic and nuclear components:

$$\Phi_\alpha = \Phi_\alpha^{elec}\left(\{\vec{r}_i\}; \{\vec{R}_I\}\right) \otimes \Phi_\alpha^{nuc}\left(\{\vec{R}_I\}\right), \tag{3.3}$$

where we used a shorthand notation to note the positions of all electrons $\{\vec{r}_i\}$ and nuclei $\{\vec{R}_I\}$. Nuclear coordinates enter the electronic wave function only parametrically: explicitly it depends only on the electronic coordinates.

This allows us to split the Hamiltonian (3.1) into the electronic and nuclear part:

$$H_{elec}\Phi_\alpha^{elec}\left(\{\vec{r}_i\}; \{\vec{R}_I\}\right) = \varepsilon\left(\{\vec{R}_I\}\right)\Phi_\alpha^{elec}\left(\{\vec{r}_i\}; \{\vec{R}_I\}\right), \tag{3.4}$$

$$H_{nuc}\Phi_\alpha^{nuc}\left(\{\vec{R}_I\}\right) = E\ \Phi_\alpha^{nuc}\left(\{\vec{R}_I\}\right), \tag{3.5}$$

where

$$H_{elec} = -\frac{1}{2}\sum_{i=1}^{N}\nabla_i^2 + \sum_{i=1}^{N}\sum_{j>i}^{N}\frac{1}{r_{ij}} - \sum_{i=1}^{N}\sum_{I=1}^{M}\frac{Z_I}{r_{iI}} + \sum_{I=1}^{M}\sum_{J>I}^{M}\frac{Z_I Z_J}{R_{IJ}}, \tag{3.6}$$

$$H_{nuc} = -\sum_I \nabla_I^2 + \varepsilon\left(\{\vec{R}_I\}\right). \tag{3.7}$$

The electronic eigenvalues $\varepsilon\left(\{\vec{R}_I\}\right)$ act as a potential for the nuclei. The last term in H_{elec}, the nuclei-nuclei potential, can be considered as a constant, since the movement of nuclei is frozen. The nuclear coordinates $\{\vec{R}_I\}$ enter the electronic part of the Hamiltonian H_{elec} only as parameters.

The third term in H_{elec}, the nuclei-electron attraction, is often termed as the external potential V_{ext}. However, V_{ext} is not necessarily limited to the nuclear field but may include an external electric or magnetic fields etc.

In following, we will only consider the electronic part of the Hamiltonian. We will shorten our notation, noting that the wave function depends explicitly only on the coordinates of the electrons and we will denote the electronic wave function as Ψ:

$$\Psi = \Phi_{\alpha}^{elec} = \Psi(\vec{r}_1, \vec{r}_2, ..., \vec{r}_N).$$

Since electrons are fermions, Ψ will have one very important property: when two electrons are exchanged, the wave function should change its sign, being antisymmetric:

$$\Psi(..., \vec{x}_i, \vec{x}_j, ...) = -\Psi(..., \vec{x}_j, \vec{x}_i, ...),$$

and this property is a generalization of a *Pauli exclusion rule*: it is not possible for two electrons to occupy the same state.

One way to find the ground state Ψ_0, the state with the minimum energy, is to use a *variational principle*, that states that the expectation value of the Hamiltonian from any trial wave function Ψ_{trial} will be an upper bond to the true energy of the ground state:

$$\langle \Psi_{trial} | \, H \, | \Psi_{trial} \rangle = E_{trial} \geq E_0 = \langle \Psi_0 | \, H \, | \Psi_0 \rangle \tag{3.8}$$

and the equality holds only when $\Psi_{trial} = \Psi_0$.

Here we deal with the *functional*, i.e. the mapping that assigns a number to a function. Here the expectation value of the Hamiltonian $\langle \Psi_{trial} | \, H \, | \Psi_{trial} \rangle$ is a functional that assigns a number E_{trial} to a function Ψ_{trial}.

To find the ground-state wave function Ψ_0 and its corresponding energy E_0 we need to minimize the functional of the energy by searching over all acceptable N-electron wave functions (quadratic integrable and continuous everywhere; they belong to a Hilbert space):

$$E_0 = \min_{\Psi} E[\Psi] = \min_{\Psi} \langle \Psi | \, H \, | \Psi \rangle. \tag{3.9}$$

Of course, a search over all the eligible wave functions is not possible, but we can apply the variational principle to some subsets of them, which are chosen in the way that minimization is done in some algebraic scheme. For example, if a trial function Ψ_{trial} is chosen to be a linear combination of some set of N orthogonal basis functions Ψ_i with coefficients $\{c_i\}$, i.e. $\Psi_{trial} = \sum_{i=1}^{N} c_i \Psi_i$, than the minimization problem is reduced to a matrix diagonalization.

The best approximation to the exact wave function that can be obtained from the particular subset will be the result of minimization.

Hartree-Fock method A drastic simplification to our problem can be done if it is possible to factor the wave function. This can be done, if we consider a simpler system, that contains the

noninteracting electrons with the Hamiltonian:

$$H_{nonint} = \sum_{i=1}^{N} h(i) \tag{3.10}$$

where $h(i)$ is the operator that describes the kinetic and potential energy of an electron i. Here we neglect the electron-electron repulsion, but one also can choose $h(i)$ to be an effective one-electron Hamiltonian that includes the effects of electron-electron repulsion in some average way.

A wave function of this Hamiltonian is a simple product, called a *Hartree product*, of spin orbital wave functions for each electron:

$$\Psi^{HP}(\vec{r}_1, \vec{r}_2, \ldots) = \chi_1(\vec{r}_1)\chi_2(\vec{r}_2)\ldots\chi_N(\vec{r}_N) \tag{3.11}$$

since $h(i)\chi_j(\vec{r}_i) = \varepsilon_j\chi_j(\vec{r}_i)$. Here, an electron i is described by a *spin orbital* χ_i. Spin orbital χ_i is the one-electron function and is composed of a spacial orbital $\varphi_i(\vec{r})$, that describes spatial distribution of an electron, and one of the two spin functions, $\alpha(s)$ or $\beta(s)$. $\alpha(s)$ is the spin-up wave function and $\beta(s)$ is the spin-down wave function. s is the spin of the electron. Spin functions are orthonormal.

$$\chi_i = \varphi_i(\vec{r})\sigma(s),\ \sigma = \alpha, \beta. \tag{3.12}$$

However, the Hartree product wave function does not account for the indistinguishability of electrons, i.e. is not antisymmetric with respect to the interchange of two electrons.

It is possible to construct an antisymmetric wave function if the appropriate linear combination of the Hartree products is taken, namely it should have a form of the *Slater determinant*:

$$\Psi_{SD} = \frac{1}{\sqrt{N!}} \begin{vmatrix} \chi_1(\vec{r}_1) & \chi_2(\vec{r}_1) & \ldots & \chi_N(\vec{r}_1) \\ \chi_1(\vec{r}_2) & \chi_2(\vec{r}_2) & \ldots & \chi_N(\vec{r}_2) \\ \vdots & \vdots & \ddots & \vdots \\ \chi_1(\vec{r}_N) & \chi_2(\vec{r}_N) & \ldots & \chi_N(\vec{r}_N) \end{vmatrix}. \tag{3.13}$$

The Hartree-Fock energy E_{HF} is given by:

$$E_{HF} = \langle \Psi_{SD} | H | \Psi_{SD} \rangle = \sum_{i}^{N} (i|\hat{h}|i) + \frac{1}{2}\sum_{i}^{N}\sum_{j}^{N} (ii|jj) - (ij|ji), \tag{3.14}$$

where

$$(i|\hat{h}|i) = \int \chi_i^*(\vec{r}_1) \left(-\frac{1}{2}\nabla^2 - \sum_{I}^{M} \frac{Z_I}{r_{1I}} \right) \chi_i(\vec{r}_1) d\vec{r}_1 \tag{3.15}$$

defines the kinetic energy and electron-nucleus attraction contributions.

$$(ii|jj) = \iint |\chi_i(\vec{r}_1)|^2 \frac{1}{r_{12}} |\chi_j(\vec{r}_2)|^2 d\vec{r}_1 d\vec{r}_2 \tag{3.16}$$

defines the *Coulomb* integral and

$$(ij|ji) = \iint \chi_i(\vec{r}_1)\chi_j^*(\vec{r}_1)\frac{1}{r_{12}}\chi_j(\vec{r}_2)\chi_i^*(\vec{r}_2) d\vec{r}_1 d\vec{r}_2 \tag{3.17}$$

defines the *exchange* integral. Both represent the interaction between two electrons.

The next simplification is to assume that electron does not interact with other electrons, but instead interacts with some average field, created by all electrons. For this purpose one-electron *Fock operator*[166] is derived:

$$\hat{f}(i) = -\frac{1}{2}\nabla_i^2 - \sum_{I=1}^{M} \frac{Z_I}{r_{iI}} + V^{HF}(i) \tag{3.18}$$

$V^{HF}(i)$ is a Hartree-Fock potential:

$$V^{HF}(\vec{r}_1) = \sum_{j}^{N} \left(\hat{J}_j(\vec{r}_1) - \hat{K}_j(\vec{r}_1) \right). \tag{3.19}$$

$\hat{J}$ is a Coulomb operator:

$$\hat{J}_j(\vec{r}_1) = \int |\chi_j(\vec{r}_2)|^2 \frac{1}{r_{12}} d\vec{r}_2 \tag{3.20}$$

and represents the potential that an electron at position $\vec{r}_1$ experiences due to the average charge distribution of another electron in spin orbital χ_j.

$\hat{K}$ is an exchange operator:

$$\hat{K}_j(\vec{r}_1)\chi_i(\vec{r}_1) = \int \chi_j^*(\vec{r}_2)\frac{1}{r_{12}}\chi_i(\vec{r}_2)\ d\vec{r}_2\ \chi_j(\vec{r}_1). \tag{3.21}$$

It has no classical interpretation and can be defined through its effect when it is operating on a spin orbital. It leads to an exchange of the variables in the two spin orbitals.

Using Fock operators, the system of *Hartree-Fock* equations is constructed:

$$\hat{f}(i)\chi_i = \epsilon_i \chi_i, i = (\overline{1, N}), \tag{3.22}$$

where ϵ_i are eigenvalues of the Fock operator and physically they represent the orbital energy. They are *Lagrangian multipliers* that are introduced throughout the minimization procedure of E_{HF} in order to satisfy the constraint of orthonormality of $\{\chi_i\}$. To solve these equations one introduces a set of basis functions for expansion of the spin orbitals. These produces matrix equations which one solves.

The ground state function is determined using the *self-consistent field* procedure: at first the trial set of orbitals and the corresponding Hamiltonian are constructed and HF equation are solved. This results in a new set of orbital coefficients, which are used in the next iteration. The procedure repeats until the difference between input and output orbitals in two consecutive steps is less than some predefined threshold.

Density functional theory Another approach, which gained a lot of popularity in quantum chemistry and computational physics, is *density functional theory* (DFT). In this approach the main variable is not a wave function, but an electron *density* ρ, since it has all necessary information to uniquely describe the system. It reduces the number of variables from $3N$ spatial variables to only three spatial variables, that makes the computational treatment easier. The electron density is defined as

$$\rho(\vec{r}) = N \int \dots \int \Psi^*(\vec{r}_1, \dots, \vec{r}_N)\Psi(\vec{r}_1, \dots, \vec{r}_N)d\vec{r}_2 \dots d\vec{r}_N, \tag{3.23}$$

where N is a number of electrons.

The electron density of the ground state Ψ_0 is correspondingly:

$$\rho_0(\vec{r}) = N \int \dots \int \Psi_0^*(\vec{r}_1, \dots, \vec{r}_N)\Psi_0(\vec{r}_1, \dots, \vec{r}_N)d\vec{r}_2 \dots d\vec{r}_N, \tag{3.24}$$

The main idea of DFT was introduced by Hohenberg and Kohn[168] in two theorems (citation from [166] follows).

Theorem 1 The external potential $V_{ext}(\vec{r})$ is (to within a constant) a unique functional of $\rho_0(\vec{r})$; since, in turn $V_{ext}(\vec{r})$ fixes $\hat{H}$ we see that the full many particle ground state is a unique functional of $\rho_0(\vec{r})$.

From the theorem it follows that the ground state density uniquely determines the external potential and thus all properties of the system.

The complete ground state energy is a functional of the ground state electron density:

$$E_0[\rho_0] = T[\rho_0] + E_{ee}[\rho_0] + E_{ext}[\rho_0], \tag{3.25}$$

where T is the kinetic energy functional, E_{ee} — the energy functional due to the electron-electron repulsion and E_{ext} — the energy functional due to the external potential (nuclei-electron attraction, electric and magnetic fields etc.).

It is possible to separate E_0 to the system dependent (E_{ext}) and universal ($T[\rho_0] + E_{ee}[\rho_0]$) parts. The latter is the *Hohenberg-Kohn functional* $F_{HK}[\rho_0] = T[\rho_0] + E_{ee}[\rho_0]$.

Theorem 2 $F_{HK}[\rho]$, the functional that delivers the ground state energy of the system, delivers the lowest energy if and only if the input density is the true ground state density, ρ_0.

The theorem represents the variational principle:

$$E_0 \leq E[\rho] = F_{HK}[\rho] + \int V_{ext}(\vec{r})\rho(\vec{r})d\vec{r}, \tag{3.26}$$

where ρ is a trial electron density. And it targets the way to find the ground state of the system.

However, it also follows that DFT is limited to only describe the ground state electronic density and cannot describe the excited states of the system.

Theses theorems alone do not give a recipe to solve the Schrödinger equation. The solution was presented in a later work by Walter Kohn and Lu Sham [169]: the system of the interacting electrons is mapped to the system of the non-interacting quasiparticles that has the same electronic density as the former interacting system. This construction leads to the so called *Kohn-Sham equations*:

$$\left(-\nabla^2 + v_{eff}(\vec{r})\right)\phi_i(\vec{r}) = \varepsilon_i\phi_i(\vec{r}), \tag{3.27}$$

where v_{eff} is an effective Kohn-Sham potential, ε_i — energy of corresponding Kohn-Sham orbital ϕ_i and the density is $\rho(\vec{r}) = \sum_i^N |\phi_i(\vec{r})|^2$. Kohn-Sham orbitals have no physical interpretation and the only their connection to the real system is that their densities add up to the exact density. However, the eigenvalue of the highest occupied Kohn-Sham orbital is equal to the negative of the exact ionization energy.

The effective Kohn-Sham potential is defined as:

$$v_{eff}(\vec{r}) = v_{ext}(\vec{r}) + \int \frac{\rho(\vec{r}')}{|\vec{r} - \vec{r}'|}d\vec{r}' + \frac{\delta E_{xc}[\rho]}{\delta\rho(\vec{r})}, \tag{3.28}$$

where v_{ext} is external potential, created by nuclei, electric and magnetic fields etc., the second term is the Hartree term, that represents the potential due to the average density distribution, and the third is the local exchange-correlation potential.

In principle, eq. (3.28) is exact. In fact, the exchange-correlation potential contains all many-body interaction effects between electrons beyond the average Coulomb electrostatic repulsion, represented by the Hartree term. However, the exact expression of $v_{xc} = \frac{\delta E_{xc}[\rho]}{\delta\rho(\vec{r})}$ is not known, but several (good) approximations have been developed over the years.

The most popular approximations are the *local density approximation* (LDA) and the *generalized gradient approximation* (GGA).

In the LDA:

$$E_{xc}^{LDA}[\rho] = \int \rho(\vec{r})\epsilon_{xc}(\vec{r})d\vec{r},$$

where $\epsilon_{xc}(\vec{r})$ is the exchange-correlation energy per particle of a homogeneous electron gas of density $\rho(\vec{r})$. The quantity can be further split into exchange and correlation parts: $\epsilon_{xc}(\vec{r}) = \epsilon_x(\vec{r}) + \epsilon_c(\vec{r})$

The exchange energy part is

$$\epsilon_x = -\frac{3}{4}\sqrt{3}\frac{3\rho(\vec{r})}{\pi}.$$

However, no explicit expression for $\epsilon_c(\vec{r})$ exists [166], but there are available different analytical expressions of $\epsilon_c(\vec{r})$ based on interpolation schemes of numerical simulations. One of the most accurate ones was obtained by Perdew and Wang [170].

It is possible to generalize all arguments mentioned above for a spin polarized system. Within this model, one includes two electronic densities: $\rho_\uparrow$ for spin up electrons and $\rho_\downarrow$ for spin down. The total density is $\rho = \rho_\uparrow + \rho_\downarrow$. Now the functional of the density depends on the spin too.

In the GGA the exchange-correlation functional includes not only the density itself but also the gradient of density $\nabla\rho$ in order to account for the non-homogeneity of the true electron density:

$$E_{xc}^{GGA}[\rho_\uparrow, \rho_\downarrow] = \int \epsilon_{xc}(\rho_\uparrow, \rho_\downarrow, \nabla\rho_\uparrow, \nabla\rho_\downarrow)d\vec{r}$$

To describe a solid one needs to take into account its periodicity, which is done by invoking Bloch's theorem to express the Kohn-Sham orbitals as a multiplication of the periodic Bloch functions $u(\vec{r})$ (that has the periodicity of the crystal) and a complex phase factor $e^{i\vec{k}\vec{r}}$, where $\vec{k}$ is the crystal wave vector. New Kohn-Sham orbitals can by labeled by $\vec{k}$-vector and a band index ν:

$$\phi_{\vec{k}\nu}(\vec{r}) = e^{i\vec{k}\vec{r}}u_{\vec{k}\nu}(\vec{r}). \tag{3.29}$$

It is convenient to expand the Bloch functions in terms of a set of the basis functions, for example as a set of plane waves.

Hybrid functionals DFT works rather well for a vast number of systems, however the standard LDA and GGA approximations fail to explain the electronic properties in materials where electrons tend to be localized and are strongly interacting (strongly correlated materials). The main drawback is that the correction for the self-interaction of electron with itself is missing in the LDA and GGA exchange functionals. The errors can be significant, since these terms involve large Coulomb interactions. In Hartree-Fock theory the self-interaction is canceled in the exact treatment of the exchange.

In this thesis, we have employed a class of methods, which are a simple conceptual extension of DFT. The idea to improve DFT is to find the better representation of exchange-functional. On the other hand, Hartree-Fock theory provides an exact expression of the exchange energy of a Slater determinant. Under these circumstances, a possible strategy is to mix the exact exchange from Hartree-Fock theory with the contribution of the correlation effects from DFT:

$$E_{xc} = E_x^{HF} + E_c^{DFT}, \tag{3.30}$$

however, this mixing scheme turn out not to give more accurate results [166].

Later, various mixing schemes were proposed. The most famous in the quantum chemistry community is the B3LYP (Becke, three parameter, Lee-Yang-Parr) [171] functional:

$$E_{xc}^{B} = (1-a)E_x^{LDA} + aE_x^{HF} + bE_x^{B88} + cE_c^{LYP} + (1-c)E_c^{VWN}, \tag{3.31}$$

where the a, b, c coefficients were determined using the fitting to the heats of formation of small molecules ($a = 0.2$, $b = 0.72$ and $c = 0.81$) [171]. E_x^{LDA} is the standard local exchange part from LDA, E_c^{VWM} is the local correlation functional of Vosko, Wilk, and Nusair (VMW) for LDA [172], E_x^{HF} — the exact (Hartree-Fock) exchange, E_x^{B88} — the local exchange functional for GGA, proposed by Becke [173], and E_c^{LYP} is the Lee-Yang-Parr correlation functional for GGA [174].

However, the calculation of the exact HF exchange is computationally expensive, especially for metals. The way to increase the calculation speed is to find an efficient way to calculate the exchange interaction. It was shown, that the range of the exchange interaction decays exponentially as a function of the band gap in insulators [175] and in metallic systems the decay is algebraic [26]. The strategy to decrease the calculation time is to introduce a scheme to truncate the interaction.

The solution was proposed to screen only the long-range part of the exchange interaction, leaving the Coulomb repulsion untouched [26]. The Coulomb operator $\frac{1}{r}$ is split into the short-range (SR) and long-range (LR) components:

$$\frac{1}{r} = \underbrace{\frac{\mathrm{erfc}(\omega r)}{r}}_{\mathrm{SR}} + \underbrace{\frac{\mathrm{erf}(\omega r)}{r}}_{\mathrm{LR}}, \tag{3.32}$$

where $\mathrm{erf}(x)$ is the error function, $\mathrm{erfc}(x) = 1 - \mathrm{erf}(x)$ and ω is an adjustable parameter. For $\omega = 0$ the long-range component becomes zero and the short-range component is equal to a Coulomb operator $\frac{1}{r}$, while for $\omega = \infty$ the situation is opposite. The choice of the error function is arbitrary but it leads to a drastic simplification when Gaussian basis set is used since it can be integrated analytically.

Using this screening and noting that the HF and PBE long-range exchange contribution are rather small and tend to cancel each other, the following hybrid functional (HSE) was proposed [26]:

$$E_{xc}^{\omega} = aE_x^{HF,SR}(\omega) + (1-a)E_x^{PBE,SR}(\omega) + E_x^{PBE,LR}(\omega) + E_c^{PBE}, \tag{3.33}$$

where ω controls the amount of short-range interactions, $\omega = 0.15a_0^{-1}$ is a reasonable value to achieve a good accuracy. $\omega \to \infty$ asymptotically reaches PBE. The value of a controls the mixing between SR part HF and PBE exact exchange and usually is taken $a = \frac{1}{4}$. $E_x^{HF,SR}$ is a short range contribution of the Hartree-Fock exchange, $E_x^{PBE,SR}$ and $E_x^{PBE,LR}$ are the short and long range contributions of the PBE exchange respectively.

3.2. A short introduction into group theory

In this section we introduce the basic group theory terminology and theorems that are needed in order to explain later the isotropy subgroups.

In algebra, a *Group* is a set of *elements* $A, B, C, \ldots$ with a group *multiplication* operation defined on its elements in such a way that the following properties hold:

1. The multiplication operation is *closed*, meaning that applied to any two elements that belong to group, it gives an element that belongs to the same group.
2. *Associative law* holds, meaning that for any elements A, B, C of the group, the relation $A(BC) = (AB)C$ holds.
3. There exists a *unit element* E such as $AE = EA = A$.
4. There is an *inverse* element A^{-1} for each element of the group, so that $A^{-1}A = AA^{-1} = E$.

A very simple example of a group is the set $\{1, -1, i, -i\}$, i being the imaginary unit, with a regular number multiplication "*" as a group multiplication and "1" as a unit element.

If the multiplication operation is commutative, i.e. $AB = BA$ for any A, B, then the group is said to be *Abeliean*. If the group has a finite number of elements it is called a *finite* group and the number of elements is called the *order* of the group.

An important concept in group theory is the *representation* of a group: it is any group, that is composed of concrete mathematical entities and is homomorphic to the original group, i.e. there is a structure-preserving map between two groups. The typical representation of a group consist of elements, which are square matrices and the group multiplication is a matrix multiplication. Thus some matrix $\Gamma(A)$ is associated with each group element A. The number of rows and columns is called the *dimensionality* of the representation [176].

If the matrices of the representation can be transformed into block form by some transformation, then such representation is called *reducible*. This means that the representation can be expressed by the representation of lower dimensionality. If this cannot be done, then representation is called *irreducible*. In quantum mechanics, an irreducible representation describes the transformation properties of a set of degenerate states and the dimensionality of the representation is the number of degenerate states.

3.3. Determination of local environment polyhedra

Local environment of specific site can be used as a descriptor of the crystalline structure of materials [177]. For example, octahedra is a common local environment for a cation in bismuthates and iridates. By *coordination (local) environment* we mean the polyhedra formed by neighbors of the site of interest. Usually, coordination environments are used to visualize the building

blocks of a specific crystal structure, since the coordination environment is also responsible for the chemical and physical properties of the material. In this section we will describe a method to obtain the coordination environment, as implemented in `CHEMENV` [35] module of `PYMATGEN` package [36], which we used to classify the crystal structures of bismuthates (Chapter 4.1). We will first describe the general idea of the method, and then the specific implementation.

The coordination environment identification procedure is done in three steps [177]:

1. At first one needs to obtain a list of neighbors of the atoms. An efficient way to do this is to split the space into separate regions, where each region surrounds one atom and contains the points which are the closest to this atom. This partition scheme is called Voronoi diagram [37] and the regions are Voronoi cells.

2. The next step is to discard some neighbors using reasonable physical arguments. It may be a distance cutoff, i.e. atoms that are at distance larger than αd_{min} are discarded, where d_{min} is a minimum distance between the nearest neighbors of a given atom (typical values are between 1.05 and 2.00); or an angle cutoff $\gamma\Omega_{max}$, depending on a solid angle Ω of the common Voronoi cells, seen from a given atom (reasonable values of γ are between 0.05 and 0.8). In this procedure, it is common to consider only atoms of a specific type and discard all others; a typical example is the case, in which only cation-anion environment is of interest.

3. The final step is to relate the real polyhedron, formed by the set of neighbors, with the set of model polyhedra which are listed in the literature [178, 179]. For this task one needs to define *distance* measure from the real polyhedron to a model one, which defines the measure of similarity of two given polyhedra. This can be done using the concept of Continuous Symmetry Measure (CSM) [38], with the distance between polyhedra defined as:

$$S = \min \frac{\sum_{k=1}^{N} |Q_k - P_k|^2}{\sum_{k=1}^{N} |Q_k - Q_0|^2} \cdot 100, \tag{3.34}$$

   where N is the number of vertices (atoms), Q_k is a coordinate vector of k-th vertex of the real polyhedron, Q_0 is a coordinate vector of the center of mass of the real polyhedron $Q_0 = \frac{1}{N}\sum_{k=1}^{N} Q_k$, P_k is a coordinate vector of k-th vertex of model polyhedron. S measures the similarity between the real polyhedron and the model polyhedron: for a perfect match $S = 0$ and for a completely different structure $S = 100$. Usually, one first reduces the choice of possible model polyhedra selecting those for which $S < 10$. At this point, the coordination environment is chosen among the set of all polyhedra as the one with the lowest CSM.

Since there is the need to use a cutoff on distance and solid angle, some ambiguity may arise. Imagine a distorted octahedron, in which one vertex is shifted from the center as depicted in

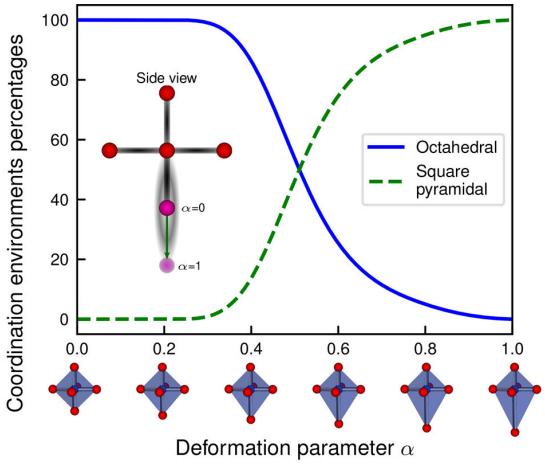

Figure 3.1.: Illustration of the evolution of the percentages of octahedral and square-pyramidal environments for an octahedron that is smoothly distorted (the bottom atom is moved away to a distance equal to twice the initial distance to the central atom as shown by the green arrow in the inset). The deformation is schematically shown in the inset with the initial and final positions respectively given by the values 0 and 1 of the deformation parameter α. Reprinted with permission from D. Waroquiers, X. Gonze and et al. "Statistical Analysis of Coordination Environments in Oxides". Chemistry of Materials 29, 8346 (2017)[177]. Copyright 2017 American Chemical Society.

Fig. 3.1. An instability arises: depending on the cutoff distance the algorithm will find an octahedral or square pyramidal environment. As a workaround, one can scan the grid of distances and angles and, based on the result of this scan, assign the likelihood for the most prominent coordination environments.

The `CHEMENV` approach was used in the $BaBiO_3$ study to perform a *neighbors analysis*, i.e. to analyze the coordination environment of a set of structures and extract the information on the number of the nearest neighbors. This approach should lead to a better accuracy in comparison to the simple determination of the neighbors only counting the sites inside a sphere of a given cutoff radius with the center on the site of interest, since the likelihood of polyhedra and scan over the grid gives more rational information on the physically reasonable neighbors.

The problem of the ambiguity of determination of the coordination environment is illustrated on Fig. 3.2. The number of the nearest neighbors and a label of corresponding to the lowest-S polyhedron are plotted in each cell. The x-axis shows a grid of distance cutoff and the y-axis — angle cutoff. Here the coordination environment of one specific Bi atom is plotted. One can see, that for low-pressure *monoclinic* $BaBiO_3$ (Fig. 3.2a) there is no ambiguity and the reported coordination environment is octahedral for all reasonable values of the cutoff. The situation is drastically different for the high-pressure *distorted* $BaBiO_3$ (Fig. 3.2b): there is no single environment that will describe neighbors of that specific Bi for the entire grid.

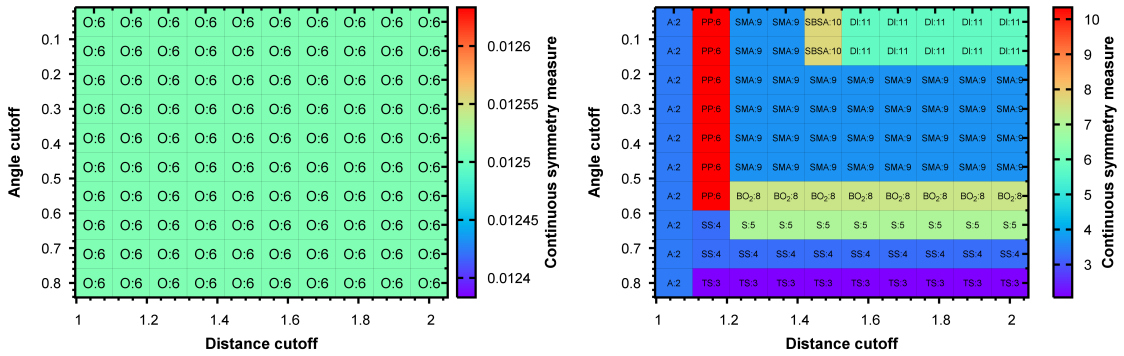

(a) Monoclinic (b) Distorted

Figure 3.2.: The environment analysis for (a) low-pressure *monoclinic* and (b) high-pressure *distorted* $BaBiO_3$ as a function of the distance and angle cutoff. The environment of Bi_1 is shown in each cell indicating the label of the environment and the number of the nearest neighbors. Color indicates the value of the continuous symmetry measure assigned to the corresponding coordination environment.

In order to obtain a final estimate of the number of the nearest neighbors we average the number of the nearest neighbors over the grid, excluding cells were $S > 10$ and the number of the neighbors is less than 5, since this situation is unphysical for $BaBiO_3$. Finally, this data is averaged over all inequivalent Bi atoms; as we shall see in the following, distorted $BaBiO_3$ structures are low-symmetry and host different types of Bi atoms.

3.4. Isotropy subgroups

In this section we describe the *isotropy* subgroups following the unpublished work of Stokes and Hatch [39]. The concept is used to get the description of the displacive structural phase transitions. It allows us to determine all possible distortions of a parent structure that lead to a lowering of its symmetry, like for example the lowering of the symmetry of high-temperature phase when the temperature is decreased and the second-order structural phase transition takes place.

The method may be used to generate all possible phonon modes, for example to do a setup for a frozen phonon calculations [180], it gives a tool to classify tilting octahedral distortions in perovskites: it is possible to recover the Glazer classification of tilting distortions by isotropy subgroup analysis [40]. Actually, Glazer used symmetry consideration in his derivation, but his work flow was not that straightforward. Of course one is not limited to only describe the tilting distortions, any type of distortion can be accounted [41]. Combining the method with the *ab initio* approach it is possible to predict the possible structures if the parent structure is given, for

example to look for a possible structures of perovskite materials [181].

There are two types of structural phase transitions taking place in solids: *reconstructive*, where the first-coordination chemical bonds are broken and reconstructed (first-order phase transition), and *displacive*, where the second-coordination bonds are broken and reconstructed, while the first-coordination bonds are not (second-order phase transition). Here, we discuss only the displacive phase transitions, where the transition occurs because of the smooth displacement of some atoms in the crystal.

Let us first consider a crystal with space-group symmetry G; operators in G have the form $g = \{R|\vec{v}\}$, where R is a point group and $\vec{v}$ is a translation vector. The operator g moves an atom at position $\vec{r}_i$ to position $\vec{r}_j = R\vec{r}_i + \vec{v}$, which must be occupied by an atom of the same type, since G leaves the crystal invariant.

Now, let us introduce an atomic displacement $\vec{u}_i$ — displacement for an atom at position $\vec{r}_i$. When the g operator acts on the atom at position $\vec{r}_i$ we obtain $g(\vec{r}_i + \vec{u}_i) = \vec{r}_j + R\vec{u}_i$. This means that the displacement of the atom at $\vec{r}_j$ after the application of g, $R\vec{u}_i$, may differ from the displacement $\vec{u}_j$ before the application of g, meaning that some displacements may lead to the symmetry lowering. It is useful to denote the displacements of all atoms in the crystal by a vector ϕ, that spans $3N$-dimensional space S, and is a concatenation of all $\vec{u}_i$ vectors: $\phi = \{u_{1x}, u_{1y}, u_{1z}, u_{2x}, \ldots, u_{Nz}\}$.

If we operate with every g in G on the vector ϕ, we obtain a set of vectors $\{g\phi\}$ that spans an n-dimensional subspace S' of S, where n is the rank of the set of vectors $\{g\phi\}$, with all linear combination of these vectors belonging to S'. It is possible to define a set of n basis vectors ψ_i of S'. Since every vector in S' can be written as a linear combination of basis vectors, so can be done for the vector resulting in operation g on the basis vector:

$$g\psi_i = \sum_{j=1}^{n} \psi_i D_{ji}(g), \tag{3.35}$$

where $D(g)$ is the matrix representation of operator g which can be different for different g. It is easy to show that $D(g_i g_j) = D(g_i)D(g_j)$, meaning that these matrices have the same multiplication table as the group G and themselves form a group. They can be used to construct a homomorphic mapping of g to $D(g)$, thus they are a representation of group G.

The S space can be decomposed into subspaces with the sum of dimensions equal $3N$: first we start with the vector ϕ and find the corresponding subspace S' by acting with every operation g on the vector ϕ. It is possible to define another vector χ which is orthogonal to all vectors in the S' subspace. Then, the set of vectors $\{g\chi\}$ spans another subspace S'', with all vectors in S' orthogonal to vectors in S'' and the subspaces S' and S'' do not overlap. This procedure is repeated until all subspaces of S are defined.

Each subspace has a corresponding group representation. It is possible do decompose the subspace itself into subspaces, meaning that this subspace is reducible and the representation is reducible too.

And it is possible to define all irreducible subspaces of S and thus all irreducible representations of the group G. It is possible to choose a set of basis vectors for each subspace in the way that sets belonging to different subspaces are orthogonal to each other. Then a set of basis vectors of the S space is constructed by a concatenation of sets of basis vectors of each subspace. In this context, it is possible to drive an analogy between the eigenvectors of the normal phonon modes with the basis vectors of each subspace.

A displacement ϕ should lead to a lowering of the crystal symmetry from G to G' ($G' \subset G$). If we take all vectors ϕ that belong to a subspace S', we can obtain a set of subgroups $\{G'_i\}$ of a group G, where $g\phi = \phi$ for $g \in G'_i$. Each subgroup G'_i defines some subspace S'' of S' defining vectors invariant under the operations that belong to this subgroup. All in all, this gives a decomposition of the S' subspace into invariant subspaces S'' associated with a set of subgroups, which are called *isotropy* subgroups. They belong to IR associated with the subspace S'.

Considering that each vector in S' can be written as a linear combination of the basis vectors $\phi = \sum_i^n \eta_i \phi_i$ and using the equation (3.35) we get:

$$g\phi = \sum_{j=1}^{n} \left(\sum_{i=1}^{n} D_{ji}(g)\eta_i \right) \phi_j. \tag{3.36}$$

We see, that we can work in the convention where the operator g operates on coefficients η_i instead of basis vectors ϕ_i:

$$g\eta_i = \sum_{j=1}^{n} D_{ij}(g)\eta_j, \tag{3.37}$$

where the coefficients η_i are considered as components of the vector $\vec{\eta}$ in the "representation space".

This leads to a considerable simplification, since instead of decomposition of the S' subspace we can work with a decomposition of the representation space by the isotropy subgroups, where subspaces are defined by satisfying the relation $g\vec{\eta} = \vec{\eta}$ for all $g \in G'$, where G' is an isotropy subgroup.

We should note, that if there are two different subspaces S' and S'' associated with the same IR, than the same vector $\vec{\eta}$ from the representation space results in the same subgroup symmetry, since the representation matrices $D(g)$ are dictated by the IR and thus are the same for S' and S''. This means that a given linear combination of the basis vectors of S' leads to the same resulting symmetry as the same linear combination of the basis vectors of S''. However, the actual atomic distortions will be different.

The procedure to generate the possible atomic distortions that lower the symmetry of the crystal is the following and is illustrated in Fig. 3.3: for a starting space group G we generate all possible IRs using group-theoretical methods. For a given IR we generate vectors $\vec{\eta}$ in the representation space and determine all the possible isotropy subgroups using the relation $g\vec{\eta} = \vec{\eta}$ and probing all $g \in G$. It is worth to note that no information on the atomic position is needed at these steps.

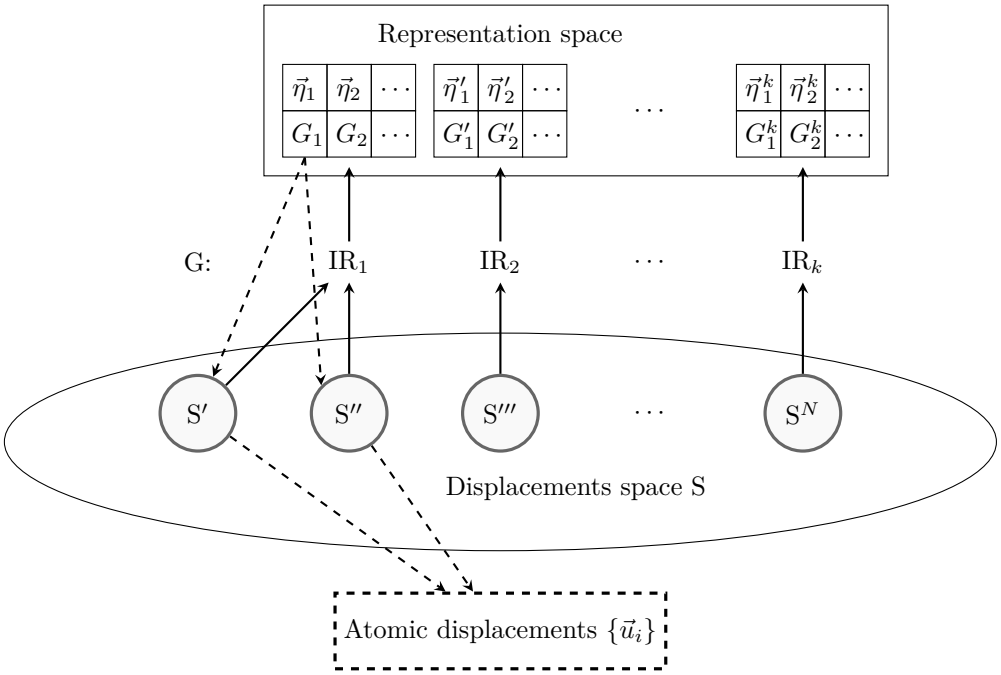

Figure 3.3.: It is possible to determine all irreducible representations (IR) of the parent space group G. Each representation is related to some subspace (denoted by circles) of the space S of displacement vector ϕ as marked by solid arrows and to the subspaces (denoted by rectangular tables) of the corresponding "representation" space, that are described by order parameters $\{\vec{\eta}\}$. The relation between IR and the corresponding representation space is marked by the solid arrows too. Each order parameter $\vec{\eta}_i$ of the "representation" subspace generates a corresponding isotropy subgroup G_i (follow the column in the table). Each subspace of S is related to some isotropy subgroup and this relation is marked by the dashed arrows; for brevity some relations are omitted. Transforming an order parameter $\vec{\eta}$ in the basis of the related subspace of S, it is possible to get the corresponding sets of atomic displacements.

Then we need to specify the atomic positions and generate all subspaces of S that are associated with a given IR. If an IR is not associated with any atomic displacements in the crystal, then we will find no subspaces of S associated with this IR. After that, the atomic displacements are generated using $\vec{\eta}$ and forming a corresponding linear combination of the basis vectors for each subspace. The procedure is repeated for each IR.

3.5. Evolutionary crystal structure prediction

In this section we will describe the evolutionary crystal structure prediction algorithm, which offers an unbiased way to search for the crystal structure of a compound at a given composition at a specific pressure. The only input information needed is the chemical composition itself, therefore

this method is extremely powerful to predict structures at all conditions, for which no experimental data on the crystal structure are available (high pressure, radioactive or rare elements, etc). As for the implementation specific features, their description will be based following the implementation of the `USPEX` code [42–44].

Historically, the first big success was the prediction (in 2004) of the post-perovskite structure of $MgSiO_3$ [182] under the high pressure (the transition to the predicted phase is at 83.7 GPa in the LDA calculations or at 98.7 GPa in the GGA), that was experimentally verified. Another very important result for the search of the high-T_c superconductors, was the prediction of H_3S with T_c=200 K at 200 GPa [183]. Again, experimentally verified [184].

Another very peculiar and interesting prediction was the prediction of a stable helium compound: Na_2He that is stable above 113 GPa[185]. This prediction is remarkable because He is an inert gas and do not tend to create chemical bonds with other elements.

We will now briefly describe the idea of the evolutionary algorithm (EA) in general and then describe its implementation in the `USPEX` code following the Ref. [186].

EA is a population-based optimization algorithm and the underlying idea is inspired by the biological evolution with key concepts such as reproduction, mutation, recombination and selection. A population consists of the candidate solutions to the optimization problem, *individuals*. The quality of each candidate may be determined using a *fitness* function. A wise choice of the fitness function is very important for the evolutionary algorithm performance.

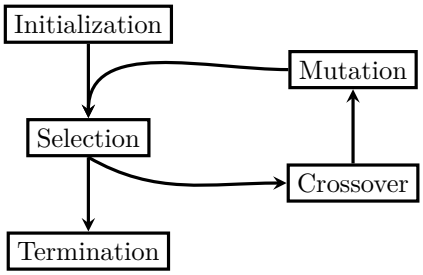

Figure 3.4.: A schematic description of the EA algorithm: the population is initialized, a fitness function is evaluated for each individual and they are ranked accordingly making the selection procedure to be possible, crossover and mutation operators are applied to produce the new offspring and the flow comes back to selection operation. These steps are repeated until a given convergence criteria is reached and the calculation is terminated.

In general EA algorithm works as follows (see Fig. 3.4):

1. An initial population is generated randomly.
2. The fitness function is evaluated for each individual and they are ranked accordingly.
3. *Mutation* and *crossover* operators are applied on individuals to produce the new offspring. The offspring and a specified fraction of the best individuals will be used to generate a new

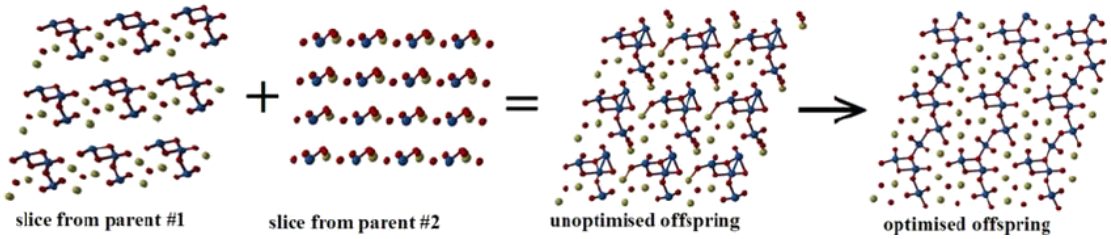

Figure 3.5.: A demonstrations how heredity operator works: it takes slices from two parent structures and combines them to create the offspring that is later subjected to structural optimization. Fig. 1 is reprinted with permission from A. R. Oganov, Y. Ma, A. O. Lyakhov, M. Valle, and C. Gatti. Evolutionary Crystal Structure Prediction and Novel High-Pressure Phases. In High-Pressure Crystallography (eds E. Boldyreva and P. Dera) (Springer Netherlands, Dordrecht, 2010), 293 [187]. Copyright 2010 Springer Nature.

population. Each population is called a *generation*. *Mutation* acts on the individual and randomly changes some of its properties. *Crossover* takes two individuals and generates an offspring combining them.

4. Steps 2 and 3 are repeated until a given convergence criteria is reached.

In the case of **evolutionary crystal structure prediction**, the role of the individual is played by the crystal structure. Each structure is represented by a set of fractional atomic coordinates and lattice vectors, i.e. by the real numbers[42]. The lattice is described by three crystallographic angles, α, β and γ, and three lengths of lattice vectors, a, b and c.

A set of candidate structures forms a population. Usually, the first population is initialized randomly, but structures should satisfy some *hard constraints*.

These *hard constraints* are[186]:

- Minimal interatomic distances, depending on the atom types.
- Minimum/maximum values of crystallographic angles α, β and γ.
- Minimum lattice vector length.

Hard constraints ensure that the minimal interatomic distances are sufficient to ensure the stability of *ab initio* calculations, meaning, for example, that the overlap of atomic core regions is not pathological and allows one to reduce the search space by leaving out unphysical structures.

The fitness function is the energy (enthalpy) of a given structure, derived from the *ab initio* calculations. This function is used to rank structures and defines the probability that a given structure will be selected as a parent for the offspring generation process. The worst structures are discarded and they will not appear in the new generation.

There are tree operators that produce offspring[188]:

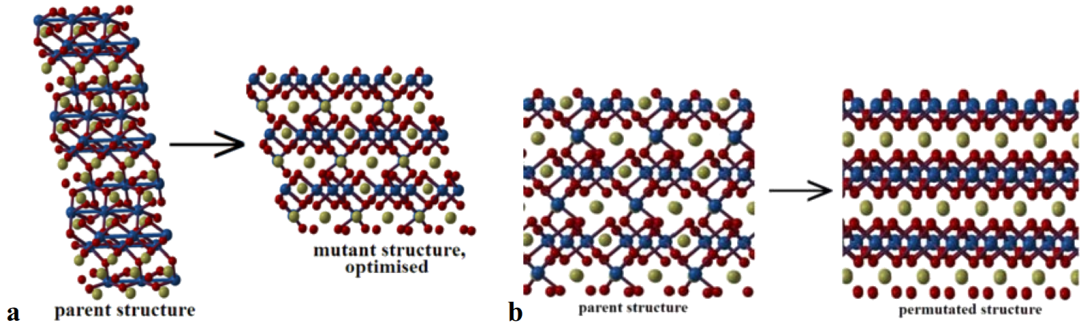

Figure 3.6.: A demonstration of (a) lattice mutation and (b) permutation operators. Lattice mutation distorts the shape of the cell. Permutation swaps the chemical elements of a pair of randomly chosen sites. Fig. 2 is reprinted with permission from A. R. Oganov, Y. Ma, A. O. Lyakhov, M. Valle, and C. Gatti. Evolutionary Crystal Structure Prediction and Novel High-Pressure Phases. In High-Pressure Crystallography (eds E. Boldyreva and P. Dera) (Springer Netherlands, Dordrecht, 2010), 293 [187]. Copyright 2010 Springer Nature.

1. *Heredity* (see Fig. 3.5), which combines spatially coherent slabs of two parent structures. The lattice vectors of the offspring are weighted averages of the lattice vectors of the parents.

2. *Lattice mutation* (see Fig. 3.6(a)), which distorts the shape of the cell by applying a random symmetric stress matrix.

3. *Permutation* (see Fig. 3.6(b)), which swaps the chemical elements of a pair of randomly chosen atoms.

In Fig. 3.4 these three operators correspond to “Crossover” and “Mutation” steps.

After a new population is generated, each structure is relaxed using the *ab initio* methods.

In order to ensure a proper convergence of the algorithm, some care is required to avoid the presence of duplicates, which could bias the algorithm. In fact, the representation of a crystal structure in terms of lattice vectors and atomic coordinates is not unique, i.e. the same structure can be represented in different ways. To handle this problem, the concept of the unique identifier, called the *fingerprint*, is introduced[189].

A fingerprint is a function of a structure, which according to Ref. [189], has the following properties:

- It is derived from the structure itself.
- Invariant with respect to shifts of the coordinate system, rotations and reflections.
- Sensitive to different orderings of the atoms.
- Formally related either to experiment (diffraction patterns) or microscopic energetics.

- Robust against numerical errors.

It is also required that fingerprints of similar structures are similar and their difference should be a meaningful measure of structural similarity.

Of course, different functions exist that can satisfy these conditions. The one used in `USPEX` implementation is the following:

$$\Phi(R) = \frac{N}{\sum_{cell} N_i N_j b_i b_j} \sum_{i,cell} \sum_{j} \frac{b_i b_j}{4\pi R_{ij}^2 \frac{N_j}{V} \Delta} \delta(R - R_{ij}) - 1. \tag{3.38}$$

It involves a sum over all interatomic distances R_{ij}. The term before the sum is a normalization constant, where N is the total number of atoms in the unit cell, N_i and N_j are the number of atoms of each type, b defines their scalar atomic properties: it can be either the atomic number, electronegativity, chemical scale, Mendeleev number or neutron scattering length. The double sum runs over all atoms i in the cell and j within the threshold distance R_{max} of the ith atom. V is the unit cell volume and $\delta(R - R_{ij})$ is a Gaussian-smeared delta function, meant to absorb numerical errors and provide smoothness of $\Phi(R)$. $\Phi(R)$ is discretized over bins of width Δ. Fingerprint function, defined in this way, is short ranged, i.e. $\Phi(\infty) = 0$.

Unresolved issue is that the fingerprint function (3.38) is not very sensitive to ordering of the atoms on a given structure and is dependent on b-parameters. The issue can be overcome if the components of the fingerprint function, that are coming from a different atomic pairs A-B, are separated. The total fingerprint is a matrix, where each element is a function:

$$F_{AB}(R) = \sum_{A_i,cell} \sum_{B_j} \frac{\delta(R - R_{ij})}{4\pi R_{ij}^2 \frac{N_A N_B}{V} \Delta} - 1 = g_{AB}(R) - 1, \tag{3.39}$$

with the double sum running over all i-th atoms of type A within the unit cell and all j-th atoms of type B within the distance R_{max}. N_A and N_B are number of atoms of type A and B respectively. $g_{AB}(R)$ is the pair correlation function.

Since fingerprints (3.38) and (3.39) are quantized, they can be represented as vectors. Values of $F_{AB}(k)$ in each bin k (bin width is Δ) are vector coordinates. Each structure can be uniquely described by a fingerprint vector and dissimilarity between the two structures can be measured as a distance between their fingerprint vectors.

The *cosine distance*:

$$D_{cosine} = \frac{1}{2}(1 - \cos\theta_F) = \frac{1}{2}\left(1 - \frac{\mathbf{F_1} * \mathbf{F_2}}{|\mathbf{F_1}||\mathbf{F_2}|}\right) = \frac{1}{2}\left(1 - \frac{\sum_k F_1(k)F_2(k)}{\sqrt{\sum_k F_1^2(k)}\sqrt{\sum_k F_2^2(k)}}\right) \tag{3.40}$$

is the most suitable choice of distance measure in order to have a robust against numerical errors treatment. The distance is defined as an angle θ_F between two F-vectors and D_{cosine} function is defined in the way that its range is $[0, 1]$. One quantifies the difference between structures by computing the distance between them.

It is straightforward to generalize (3.40) for the case of the multicomponent fingerprints $F_{AB}(k)$:

$$D_{cosine} = \frac{1}{2}\left(1 - \frac{\sum_{AB}\sum_k F_{1,AB}(k)F_{2,AB}(k)w_{AB}}{\sqrt{\sum_{AB}\sum_k F_{1,AB}^2(k)w_{AB}}\sqrt{\sum_{AB}\sum_k F_{2,AB}^2 w_{AB}}}\right), \tag{3.41}$$

where the sums are over all F_{AB} components, where each component is taken only once, since $F_{AB} = F_{BA}$. The weight w_{AB} of each fingerprint component is defined as:

$$w_{AB} = \frac{N_A N_B}{\sum_{cell} N_A N_B}. \tag{3.42}$$

Variable-composition crystal structure prediction It is possible to extend the method described before to predict simultaneously all stable stoichiometries and structures together. Here, we will follow the [190] to describe the basic ideas:

1. The initial population is generated sampling not only the structures at a given composition, but also various compositions.
2. Variation operators are allowed to change the chemical composition: heredity no longer preserves the chemical composition and a *chemical transmutation* operator is introduced. For a randomly chosen atom, the latter changes the associated chemical element.
3. The fitness function is replaced by the (free) energy per atom minus the (free) energy of the most stable isochemical mixture of already sampled compounds, i.e. *formation (free) energy*. Now the fitness function depends on the history of simulation.

The convex hull is determined at each generation step and the sampling and procedure to generate offspring will follow it.

Compositional phase diagrams We want to talk now about how to extend our ability to predict a structure for a given chemical composition to a possibility to determine thermodynamically stable compositions themselves.

The first ingredient we need is a *formation enthalpy*, that shows the energetic gain of forming a specific composition w.r.t pure elements:

$$dF = F(A_xB_y) - (xF(A) + yF(B)), \tag{3.43}$$

where A and B are two chemical elements, $F(A)$ and $F(B)$ are enthalpies of pure elements, x and y concentration of elements A and B respectively, and $F(A_xB_y)$ is an enthalpy of the corresponding structure with composition A_xB_y. The corresponding chemical reaction is $xA + yB = A_xB_y$. The formula is easily generalized to any number of chemical elements in the composition.

The negative formation enthalpy shows that composition is stable against the decomposition into pure elements. The problem here is that calculated in this way formation enthalpy, even

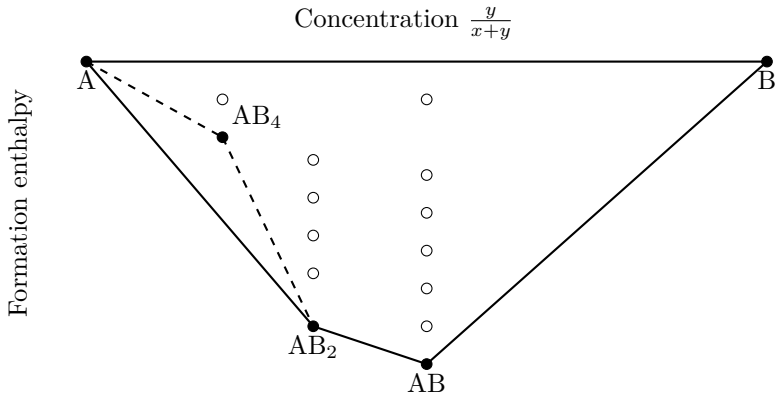

Figure 3.7.: A sketch of the binary phase diagram. The x-axis is the concentration of the element B in the binary compound A_xB_y and the y-axis is a negative part of the formation enthalpy. The ground state structures are denoted by solid circles and the convex hull is denoted by solid lines, note that it is not necessary that a ground state structure for a given composition is lying on the convex hull. The metastable structures are denoted by open circles. An example of the decomposition of $AB_4 \rightarrow A + AB_2$ is marked by the dashed lines.

though negative, does not show that the composition is stable against the decomposition into the combination of other compositions, namely the process $A_xB_y \rightarrow A_lB_m + A_nB_k$, with $x = l + n$ and $y = m + k$.

To handle this problem, it is convenient to work in the composition-formation enthalpy "space". For a binary compound we need only one variable to describe the composition and for convenience a fraction of the second element $\frac{y}{x+y}$ is taken as x-coordinate. The y-coordinate is formation enthalpy (F). The binary phase diagram can be conveniently plotted, as sketched in Fig. 3.7. Now, for each composition and corresponding structures we have a point in this space, depicted as a circle on the plot. The ground state structure of a given composition will have the lowest formation enthalpy (filled circles on the plot). We can also have metastable structures; they are denoted as the open circles.

The structures, which are thermodynamically stable, are the ones that belong to the *convex hull* of the set of all these points. Of course, only the part of space with the negative formation enthalpy is considered. Structures, that are above the convex hull will decompose into the closest structures on the convex hull. As an example, for the phase diagram, depicted on the Fig. 3.7, AB_4 will decompose into $A + AB_2$.

Ternary phase diagrams It is possible to extend the method described above to predict also the *ternary phase diagram* for chemical compositions of compounds comprising 3 different chemical species ($A_xB_yC_{1-x-y}$, with subscripts corresponding to the fraction of each component in the composition) with values of x in the [0,1] range and y in the [0,1-x] range. Now, the

composition-formation enthalpy space will be three dimensional. However, all possible chemical compositions can be conveniently plotted at the same time using two-dimensional triangular graph, as depicted on the Fig. 3.8, where Na, Ir and O atoms are taken as an example.

The ratios of the tree species in the composition can be determined in the following way: each corner represents the pure phase and thus the concentration of each species at the corner is 100%. On the opposite edge of the triangle the concentration is 0% and it linearly depends on the distance from a given point to this edge. By drawing the lines parallel to the edges (dashed lines on the Fig. 3.8) it is possible to introduce the grid, used to determine the concentrations. Each such a line corresponds to a constant concentration of specific species. For example, the horizontal dashed lines represent constant concentration c of Ir, producing binary diagrams $\mathrm{Na}_x\mathrm{Ir}_c\mathrm{O}_{1-c-x}$ with $x \in [0, 1-c]$. If the concentrations of two species (x and y respectively) are known, the concentration of the third is $1-x-y$.

As for the binary case, to get the thermodynamically stable structures one needs to construct a convex hull, now spanning three dimensions. All the structures that belong to the convex hull will be thermodynamically stable.

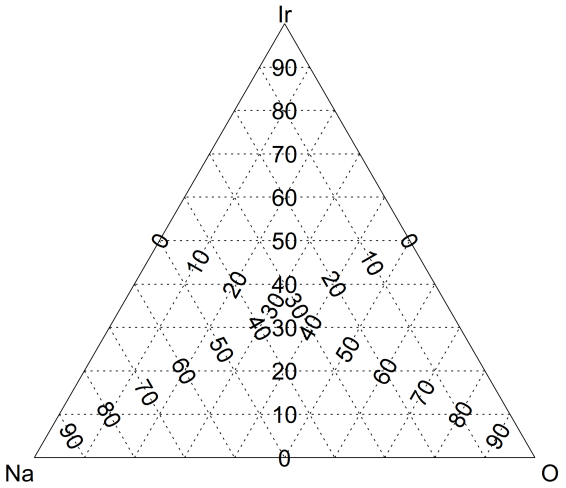

Figure 3.8.: Grid used to describe the ternary phase diagram, where $\mathrm{Na}_x\mathrm{Ir}_y\mathrm{O}_{1-x-y}$ is taken as an example. Corners represent the pure chemical species and the concentrations of each chemical species in the compound decreases when lines parallel to the opposite edge are followed. This is indicated by numbers that show the percentage of the corresponding species.

Part II.

Results

4. *Ab initio* investigation of bismuthates under high pressure

We start this section describing results of our investigation of $BaBiO_3$ under high pressure. The results were presented in Physical Review B [1] and in the following we include the paper in its entirety. The author performed all the computations; the only exception is that the crystal structures obtained by group-theoretical analysis were provided by Cesare Franchini. The author wrote the manuscript with support from his supervisor Lilia Boeri. All authors discussed the results and contributed to the final manuscript.

Later we describe results of our investigation of $ABiO_3$ under high pressure. The results were presented in Physical Review B [2] and in the following we include the paper in its entirety. The author performed all the computations and wrote the manuscript with support from his supervisor Lilia Boeri. All authors discussed the results and contributed to the final manuscript.

4.1. *Ab initio* prediction of the high-pressure phase diagram of $BaBiO_3$

PHYSICAL REVIEW B **96**, 035103 (2017)

Ab initio prediction of the high-pressure phase diagram of $BaBiO_3$

Andriy Smolyanyuk,[1] Lilia Boeri,[1] and Cesare Franchini[2]
[1]*Institute of Theoretical and Computational Physics, Graz University of Technology, NAWI Graz, 8010 Graz, Austria*
[2]*Faculty of Physics, University of Vienna, 1090 Vienna, Austria*
(Received 15 February 2017; revised manuscript received 2 May 2017; published 5 July 2017)

Abstract

$BaBiO_3$ is a well-known example of a 3D charge density wave (CDW) compound, in which the CDW behavior is induced by charge disproportionation at the Bi site. At ambient pressure, this compound is a charge-ordered insulator, but little is known about its high-pressure behavior. In this work, we study from first-principles the high-pressure phase diagram of $BaBiO_3$ using phonon modes analysis and evolutionary crystal structure prediction. We show that charge disproportionation is very robust

in this compound and persists up to 100 GPa. This causes the system to remain insulating up to the highest pressure we studied.

4.1.1. Introduction

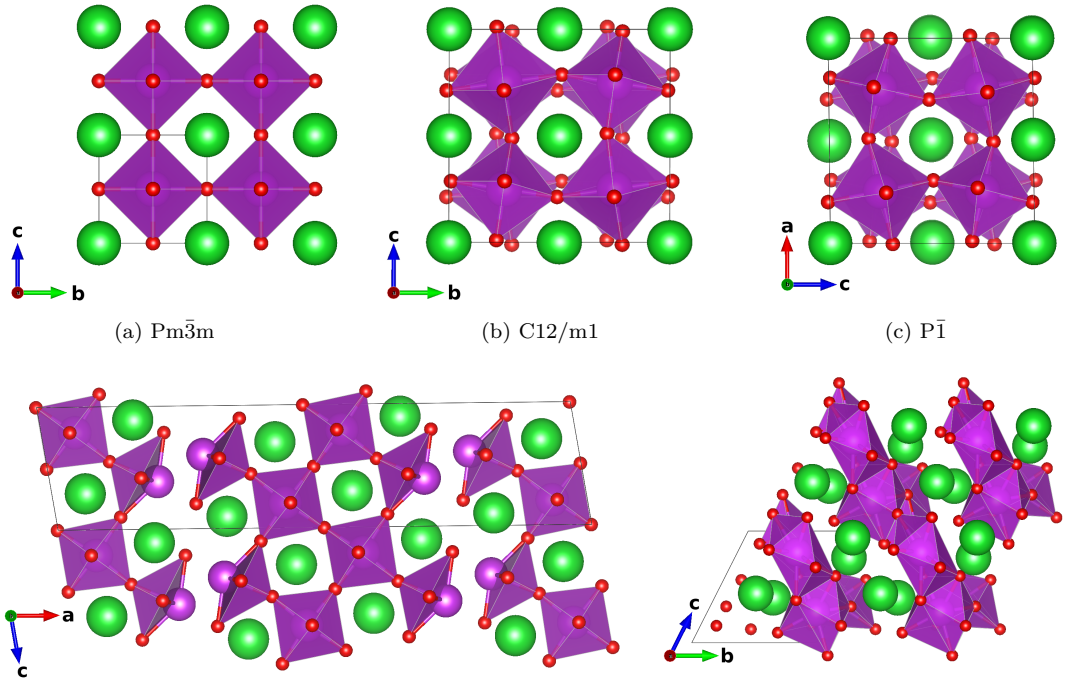

(a) $Pm\bar{3}m$ (b) C12/m1 (c) $P\bar{1}$

(d) $C12/m1^C$ (e) Distorted

Figure 4.1.: (*color online*) $BaBiO_3$ ground-state structures used in this work: (a) ideal perovskite structure; (b) experimental $BaBiO_3$ structure for ambient pressure and room temperature; (c) triclinic structure stable from 20 GPa to 28 GPa pressure; (d) *"clustered"* monoclinic structure stable between 28 GPa and 87 GPa pressure; (e) non-symmetric *distorted* structure stable from 87 GPa pressure. Structures (c), (d) and (e) where obtained using evolutionary crystal structure prediction (EP). Large green spheres are Ba atoms, large purple spheres are Bi atoms, and small red spheres are O atoms.

Transition-metal oxide perovskites are currently a subject of intense study, since they exhibit many interesting properties which makes them attractive for both fundamental and applied research. Ferroelectricity [191], high-T_c superconductivity, charge ordering, and colossal magnetoresistance [192] are some of the most intriguing examples. One of the most distinctive materials of this family is $BaBiO_3$ [11, 94], which is a charge-ordered insulator and becomes superconducting upon doping [3, 193].

Recent studies have shown that also at reduced dimensionality $BaBiO_3$ exhibits several remarkable properties: experimental investigation of suppression of structural distortion in thin films [194] and

suppression of the charge density wave (CDW) in the $BaBiO_3$ films [195], as well as theoretical predictions of topological phases [196] and 2D electron gas at the surface [197] were recently reported in the literature.

In this compound Bi behaves as a mixed-valence element and can occur n either the formal Bi^{3+} or Bi^{5+} oxidation state. The $BaBiO_3$ compound can thus be seen as an $ABB'O$ perovskite where B is Bi^{3+} and B' is Bi^{5+}. Although the Bi^{4+} oxidation state was never observed in any other compounds, a hypothetical $BaBi^{4+}O_3$ should have an ideal perovskite cubic — $Pm\bar{3}m$ — structure (Fig. 4.1(a)) and should be a metal.The mixed valence state of Bi and the periodical arrangement of atoms leads to formation of a CDW state. This has two consequences: the different attraction strength of oxygen to the two types of Bi leads to a chess-pattern breathing distortion of the Bi-O octahedra; in turn, this CDW breathing distortion splits the antibonding Bi(s)-O(p) antibonding state and establishes an insulating ground state [198, 199].

Upon hole doping $BaBiO_3$ undergoes an insulator to metal transition and becomes a superconductor; superconducting T_c's up to 13 K were reported for $BaPb_{1-x}Bi_xO_3$ [193], and up to 34 K for $Ba_{1-x}K_xBiO_3$ [3]. The suppression of the CDW state upon doping, and the occurrence of superconductivity, have been intensely debated in the literature. [27, 93, 198–206]. Only recently, with the adoption of post-DFT techniques, has it been possible to obtain a consistent description of the whole phase diagram.

In many compounds, high pressure is a viable alternative to doping to tune the material properties. In particular, this has recently been exploited in several 2D transition metal dichalchogenides to study the interplay of CDW and superconductivity. For instance, it was demonstrated that in pristine 1T-$TiSe_2$ [207] and 2H-$NbSe_2$ [208] pressure induces a quantum melting of the CDW. It is extremely intriguing to investigate whether a similar behavior could occur in $BaBiO_3$, i.e., whether pressure could be used to suppress the three-dimensional CDW insulating state and promote a metallic, superconducting state. Based on simple theoretical arguments, all insulators should become metallic at high enough pressure (or density), due to increasing hybridization and higher bandwidth. It is reasonable therefore to expect that, under pressure, $BaBiO_3$ should undergo a structural transition to the ideal perovskite structure, becoming metallic by band overlap. However, this picture may be too naive.

In fact, in the last two decades the study of matter at extreme conditions has shown that even simple elements exhibit a physical and chemical behavior, which cannot be explained in these simple terms. For instance, simple free-electron metals such as lithium and sodium become insulating under pressure; [209, 210]; hydrides, which form insulating molecular crystals at ambient pressure, can become metallic, and exhibit superconductivity with T_c's as high as 200 K; [183, 211–220]; even higher T_c's have been predicted for elemental hydrogen, above the Wigner-Huntington transition [221–224]. Explaining the high-pressure behavior of solids thus requires first an accurate understanding of the structural modifications induced by pressure.

The aim of this work is to investigate the possibility of suppressing the CDW state and induce an insulator to metal transition in $BaBiO_3$ under pressure, performing a theoretical study of

its crystal and electronic structure. Since the available experimental information is extremely limited, we are using two structural prediction techniques to determine the possible high-pressure phases. The first is based on group-theoretical analysis of irreducible representations of unstable phonon modes using the `ISOTROPY` software suite [180, 225] and the second is based on using evolutionary algorithms approaches as implemented in the `USPEX` package [42].

The first is a classic, elegant approach which is able to describe the most typical structural distortions occurring in transition-metal perovskites. The basic idea is that continuous phase transitions may be classified using group-subgroup relations where the distorted phase is described by a subgroup of the space group of the parent phase. Subgroups which consist of operations that leave the order parameter invariant are called isotropy subgroups and they may be deduced from irreducible representations of the parent group [39]. The `ISOTROPY` software suite provides a convenient tool for the group theoretical analysis of phase transitions in solids based on the theory of *isotropy* subgroups. In our case, we further refined the sub-set of subgroups of the ideal perovskite structures performing an analysis of the eigenvectors of the phonon modes that become unstable at different pressures, as described in detail in Sec. 4.1.2. The second is a more general approach to the prediction of crystal structures, inspired by biological evolution. The idea is to generate and evolve a *population* of crystal structures, applying various variation operators which are similar to biological mechanisms such as reproduction, mutation, recombination and selection to minimize a fitness function, which is typically the enthalpy of the system, obtained from an accurate *ab initio* calculation. Evolutionary algorithms have been proven very successful at predicting the crystal structure of actual materials in many cases [42]. In contrast to the previous method, in this case the set of possible structures is not limited to a subgroup of the perovskite structure, but is completely general. Further details can be found in Sect. 4.1.2.

Our calculations based on the two approaches above show that charge ordering persists up to 100 GPa and the system remains insulating in this pressure range.

To investigate the electronic properties we are using a hybrid Hartree-Fock/density functional theory (DFT) calculation with the HSE (Heyd-Scuseria-Ernzerhof) exchange-correlation functional [26]. In fact, the role of electronic correlations on the accurate description of the CDW was discussed in many papers and it was shown that it is essential to use post-DFT approaches to obtain a proper description of the electronic structure of this system [198, 203, 204, 206].

This paper is organized as follows. In Sec. 4.1.2 we describe the results of our *ab initio* calculations starting with our prediction for the high-pressure phase diagram (Sec. 4.1.2), followed by the description of the phonon mode analysis in Sec. 4.1.2. We present the results obtained with the *ab initio* evolutionary prediction method in Sec 4.1.2 and electronic properties of the predicted ground-state structures are analyzed in Sec 4.1.2. The main conclusions of this work are summarized in Sec. 4.1.3. Computational details are described at the end of the paper in Sec 4.1.4.

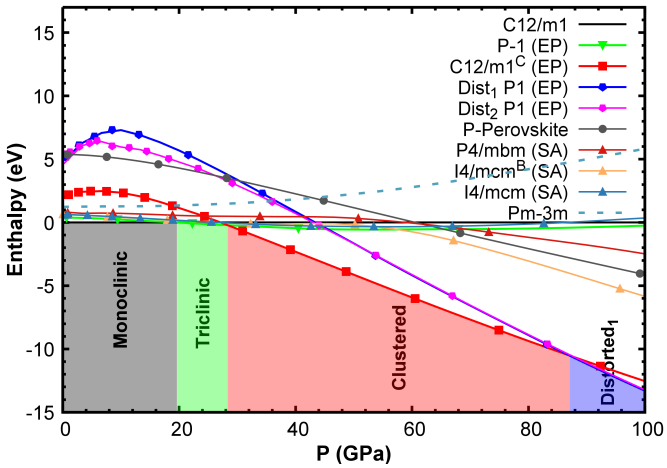

Figure 4.2.: (*color online*) Predicted high-pressure phase diagram of $BaBiO_3$. Up to 100 GPa, we predict three structural phase transitions: monoclinic ($C12\bar{m}1$) to triclinic ($P\bar{1}$) at about 20 GPa, triclinic to clustered ($C12\bar{m}1^C$) at about 28 GPa, and clustered to distorted (P1) at about 87 GPa.

4.1.2. Results

$BaBiO_3$ was synthesized for the first time in 1963 [20] and was identified as a perovskite but it was hard to precisely determine the right structure: rhombohedral, orthorhombic, monoclinic or triclinic symmetries were reported by various groups [11, 226, 227]. It was finally established that at room temperature and ambient pressure the structure is monoclinic ($C12\bar{m}1$), Fig. 4.1(b). This structure can be described as a perovskite with two types of distortions: *breathing* and *tilting* distortions of Bi-O octahedra. In the breathing distortion the octahedra alternate in size, while upon tilting the octahedra are rotated. The role of the breathing and tilting distortions has been widely discussed in the literature. In particular, DFT calculations reported conflicting results [93, 200–202]. Only recently the use of post-DFT methods has permitted us to reproduce the experimental findings correctly [198, 203, 204].

Predicted Phase Diagram

Figure 4.2 shows our predicted high-pressure phase diagram [1] The system undergoes three structural phase transitions and remains insulating up to 100 GPa. Figure 4.1 shows the structures which are most relevant for the discussion (the structures are provided as *cif*-files in the Supplemental Material). An extended version of the phase diagram is provided in Fig. 1 of the Supplemental Material.

[1] To model the effect of pressure on the system we performed a set of fixed volume relaxation for different volume values allowing atomic positions and unit cell shape to vary. The corresponding pressure at each volume was obtained from the stress tensor.

As a reference structure we chose the monoclinic (C12$\bar{m}$1) $BaBiO_3$ structure, which was determined by the experiment at ambient pressure. The structures with *EP* after the title are the best structures obtained using the evolutionary crystal structure prediction method. They become energetically favorable in the high-pressure region. The structures with *SA* are obtained using the group-theoretical approach for crystal structure prediction. At high pressure these structures are energetically more favorable than our reference (C12$\bar{m}$1) structure, but are way behind the structures obtained using the evolutionary method. The *P-Perovskite* is a post-perovskite structure that we added into consideration by chemical intuition. This structure was obtained by Oganov *et al.* for $MgSiO_3$ at extreme pressure and has 20 atoms in the unit cell [182].

Following the lowest enthalpy path in our calculated phase diagram, we find that a first transition from the monoclinic [C12$\bar{m}$1, see Fig. 4.1(b), 10 atoms in the unit cell] to triclinic [P$\bar{1}$, see Fig. 4.1(c), 40 atoms in the unit cell] structure occurs at about 20 GPa. The P$\bar{1}$ structure is a distortion of the C12$\bar{m}$1 structure with one additional tilting axis. A transition from triclinic (P$\bar{1}$) to clustered monoclinic [C12$\bar{m}1^C$, Fig. 4.1(d), 40 atoms in the unit cell] occurs at about 28 GPa. We call this structure clustered because it has "domains" created by shearing parts of the original structure. The last transition is at about 87 GPa, where the clustered monoclinic (C12$\bar{m}1^C$) is transformed to a highly distorted structure with no symmetry [P1, see Fig. 4.1(e), 20 atoms in the unit cell]. We will refer in text to it as *distorted*.

The experimental information about $BaBiO_3$ at high pressure is extremely scarce and limited to $P \leq 20$ GPa [110, 111]. Unfortunately, the experimental resolution was not enough to have a full refinement of the crystal structure. An anomaly at about 4 GPa was reported, at which the bulk modulus decreases and this was attributed to the change of the tilt system (due to additional type of octahedra tilting). Moreover it was reported that the system remains insulating up to at least 10 GPa. Our results are consistent with the measurements that $BaBiO_3$ is an insulator in this pressure range. However, we cannot reproduce the anomaly at 4 GPa.

Before discussing in detail the crystal and electronic structure across the phase diagram, we will illustrate the details of our structural search methods.

Phonon Mode Analysis

The group-theoretical method has been successfully used to identify and predict structural distortions in a variety of perovskites [228, 229]. A powerful extension is to combine this method with the results of a phonon mode analysis of the parent structure [230]. For $BaBiO_3$ the starting point is the ideal cubic perovskite structure, Fig. 4.1(a). It has a P3$\bar{m}$3 (cubic) symmetry with 5 atoms in the unit cell; it is a metal, since no charge disproportionation is possible in this case. The six O nearest neighbors of Bi form a perfect octahedron. This octahedron can be distorted in several ways and there are two kinds of distortions usually present in real perovskite systems: *breathing* and *tilting* (see Fig. 4.3).

A *breathing* distortion means that some O atoms move closer or farther away from the Bi atom,

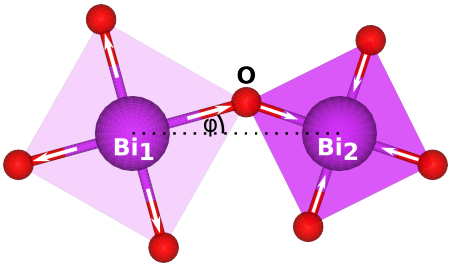

Figure 4.3.: (*color online*) Breathing and tilting distortions applied to an ideal cubic perovskite structure. Breathing is indicated by squares of different size where the white arrows show the direction in which O atoms are displaced. Tilting is shown as a rotation of a square by angle φ around axis normal to the plane of the paper.

Table 4.1.: (*color online*) Irreducible representations associated with unstable phonon eigenvectors of the P3$\bar{m}$3 structure at 0 GPa and 100 GPa pressure. "#" is the mode number.

P=0 GPa			**P=100 GPa**			
#	**M**	**R**	**Γ**	**M**	**R**	**X**
1	**M3+**	**R1+**	**Γ4-**	**M3+**	**R4+**	**X5-**
2				**M5-**		
3		**R4+**				
4			**Γ5-**	M3-		
5						
6						

which is located at the center of the octahedron. Octahedra are coupled to each other and the breathing of one of them creates an opposite breathing on its neighbors. There are different kinds of breathing distortions depending on which and how many pairs of O are distorted. In the monoclinic structure of $BaBiO_3$ all O atoms are involved in the breathing distortion and the overall picture is a 3D chess pattern of octahedra with alternating sizes. A *tilting* distortion is the rotation of an octahedron around a tilting axis. Neighboring octahedra in the plane normal to the tilting axis are coupled and rotate in the opposite direction. Octahedra in adjacent planes may rotate in the same (*in-phase* rotation) or in the opposite direction (*antiphase* rotation). The latter is present in monoclinic $BaBiO_3$.

The ideal cubic perovskite is dynamically unstable at ambient pressure and room temperature, and the analysis of unstable phonon modes gives an insight of which distortions correspond to a lowering of the energy of the system and thus allow us to predict more favorable structures. This can be achieved by computing the phonon dispersion relations and the corresponding eigenvectors. Eigenvectors with imaginary eigenvalues represent the direction of atomic displacements that lead to a decrease in energy. The stable structure can then be obtained following the most favorable

distortion, which may be a linear combination of unstable phonon eigenvectors. The space of possible combinations can be reduced using the group-theoretical method and the unstable phonon modes mapping on the corresponding irreducible representations.

We calculated the phonon dispersion relations and the corresponding phonon eigenvectors for $BaBiO_3$ in the ideal cubic perovskite structure [2] using a finite-difference supercell method, [231, 232] and classified unstable eigenvectors with the corresponding irreducible representations. We first tested our approach at ambient pressure, and the results we obtained are consistent with the experimental structure (see below). After that, the investigation of stability of modes was repeated for several pressures in the range from 0 to 100 GPa (see Fig. 2 in supplemental material); the results for 0 GPa and 100 GPa pressure are summarized in Table 4.1.

At ambient pressure our result is consistent with the experimentally reported structure, namely monoclinic $BaBiO_3$, since this structure can be obtained combining a breathing distortion with irreducible representation R1+ and the R4+ irreducible representation tilting ($a^0b^-b^-$ in Glazer notation [53]) distortion, which are both present in the results of our analysis. The M3+ irreducible representation is an in-plane breathing distortion, which is not present in monoclinic $BaBiO_3$ because the R1+ breathing is more favorable.

Table 4.2.: List of calculated by PBE and HSE values for monoclinic (C12$\bar{m}$1) structure in comparison with experimental data. δ is breathing distortion ($\delta = \frac{1}{2}(\overline{Bi_1O} - \overline{Bi_2O})$, where $\overline{Bi_1O}$ and $\overline{Bi_2O}$ are average Bi_1-O and Bi_2-O bond distances, respectively), φ is the average tilting angle, and V is the volume per one formula unit of $BaBiO_3$.

	δ (Å)	φ (deg)	V_0 (Å^3)
PBE	0.074	11.97	85.92
HSE	0.096	10.95	82.67
PBE [203]	0.07	12.1	85.76
HSE [203]	0.09	11.9	82.10
Experiment [11]	0.09	10.1	82.11

In Table 4.2 we report the values of the breathing distortion (δ), the tilting angle (φ) and equilibrium volume (V_0) for the ambient pressure structure measured by experiment and calculated using both the PBE (Perdew-Burke-Ernzerhof) exchange-correlation functional in the anzatz of the generalized gradient approximation (GGA) and HSE functionals. HSE gives a more accurate description of the structure, and reproduces correctly the electronic properties: monoclinic $BaBiO_3$ is a charge-ordered insulator with a bandgap of about 0.8 eV, while in GGA it is a zero-gap semiconductor. Although our calculations predict a transition from the monoclinic to the triclinic structure already at around 20 GPa, we followed the evolution of the monoclinic structure to high pressure to see whether the monoclinic distortions are suppressed. We find that the distortions are preserved under pressure and the tilting angle φ is proportional to pressure. Thus, the CDW is very robust in this compound and is not suppressed under pressure. Up to about 85 GPa the band gap increases but afterwards its value decreases and the structure becomes a semimetal

[2] Results are available in the supplemental material

(the related information is provided in Fig. 3 of the Supplemental Material).

There are two regions were a substantial change in stability of the phonon modes takes place: at about 30 GPa the R1+ mode become stable and at about 70 GPa the M3- and M5- modes become unstable (for details see Fig. 2 of the Supplemental Material). Based on the eigenvector analysis at 100 GPa, we constructed a pool of candidate high-pressure structures. This pool is valid also at lower pressures, since unstable modes at lower pressures are a subset of the 100 GPa ones. In particular, we have used the M3+, M5-, and R4+ irreducible representations. In total, we investigated 17 structures with 10, 20 and 40 atoms in the unit cell (see Table V of the Supplemental Material for irreducible representations and order parameters used to obtain these structures). The structures P4$\bar{m}$bm, I4$\bar{m}$bm and I4$\bar{m}$bm^B (see Fig. 4.2) are the best obtained by this method followed by `DFT` relaxations. P4$\bar{m}$bm is obtained from the ideal perovskite structure by applying in-phase tilting ($a^0a^0c^+$ in Glazer notation [53]) and I4$\bar{m}$bm by antiphase tilting ($a^0a^0c^-$). I4$\bar{m}$bm^B is equivalent to I4$\bar{m}$bm with an additional in-plane breathing distortion. These three structures are metals, but they are around 7 to 13.5 eV higher in enthalpy with respect to the ground state at 100 GPa, and thus very unlikely to be observed in experiments.

Ab initio evolutionary prediction

We performed *ab initio* evolutionary algorithm calculations at fixed composition for structures with 10, 20, and 40 atoms in the unit cell corresponding to 2, 4, and 8 formula units (f.u.) respectively. The 10-atom 0 GPa calculation was used to test the reliability of the method. The structure we obtained for this run is consistent with the experiment. Calculations with 10, 20, and 40 atoms were made at 50 and 100 GPa. Up to 5-10 best structures from each run were chosen for more accurate relaxations to obtain the final ranking of the energies and were relaxed for various pressures in the pressure range from 0 to 100 GPa using fixed-volume relaxation allowing cell shape to change but with the symmetry fixed to obtain the equation of state.

The analysis of phonon modes for the monoclinic structure indicates a possible structural transition in the range of 25-30 GPa. To check this region more carefully we performed additional calculations at 25 GPa for structures with 20 and 40 atoms in the unit cell, and 30 GPa for structures with 10 atoms in the unit cell. As a result, we found a triclinic P$\bar{1}$ structure that is stable in the 20-28 GPa pressure region (Fig. 4.1c). As already mentioned, the evolutionary algorithm approach was able to find the structures that are the energetically most stable ones at high pressures (i.e. more stable than the best SA ones). These are triclinic (P$\bar{1}$), clustered (C12$\bar{m}$1^C) and distorted (P1). There are both metals and insulators present in the pool of all structures obtained by these structural search calculations, but the most energetically favorable are always insulating and strongly disordered.

The evolutionary algorithm calculations thus show that $BaBiO_3$ has a tendency to become more distorted when pressure is increased, destabilizing the perovskite environment without suppressing the charge disproportionation. In order to understand this tendency, we have performed an

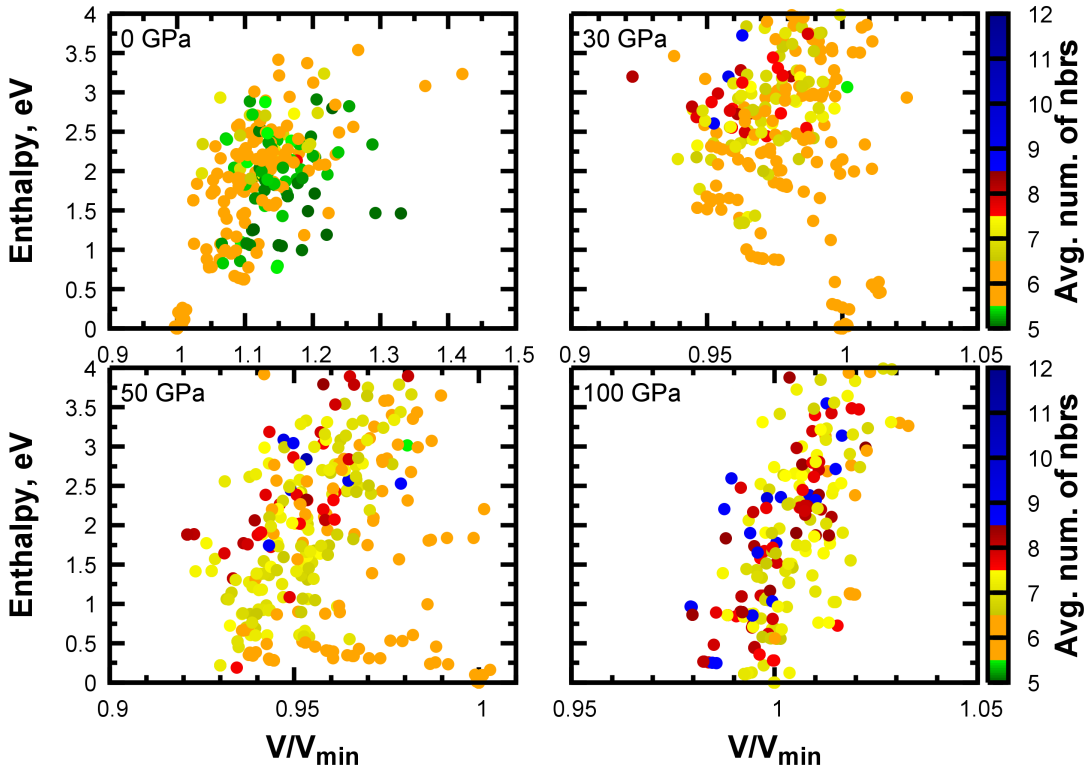

Figure 4.4.: (*color online*) Average number of O neighbors of Bi atoms for a pool of 2 f.u. $BaBiO_3$ structures obtained using the evolutionary algorithms approach. Each dot is associated with a specific structure and its color denotes the average number of neighbors. For the perovskite structure the average number of neighbors is 6 and the deviation from this value shows the amplitude of distortion presented in the system. Details on the neighbor analysis can be found in the Supplemental Material in subsection "D. Neighbors analysis".

additional analysis, measuring the change in the bonding environment of Bi in terms of its average number of neighbors [35, 36, 233, 234].

In an ideal perovskite this number is six; significant deviations from this value indicate strong distortions. The result of this analysis is presented in Fig. 4.4 (for details see the subsection "D. Neighbors analysis" of the Supplemental Material). In Fig. 4.4 each structure at the corresponding pressure is represented by a dot, with the color indicating the average number of neighbors of Bi and the coordinates describing the volume and enthalpy of the structure. The volume is rescaled to the volume of the ground-state structure for a given pressure (V_{min}) and the enthalpy is given with respect to the enthalpy of the ground-state structure. As expected, at ambient pressure for the low-enthalpy structures there are six O atoms in the Bi environment, while with increasing pressures structures with seven or more neighbors become competitive and finally become the ground-state ones. The plot thus shows that there is a general trend for $BaBiO_3$ to break the

perovskite structure and become more distorted.

Note that in order to maintain a reasonable computational cost, we performed this analysis using the results of the structural search for 2 f.u. structures, under the assumption that the tendency to distortion should be so general to show up already for smaller structures. In order to check the validity of this assumption, we cross-checked our results for a single pressure (100 GPa) for 8 f.u. structures, and found that, indeed, our assumption is correct, as also in this case low-lying structures have an average number of neighbors significantly larger than six.

Electronic properties

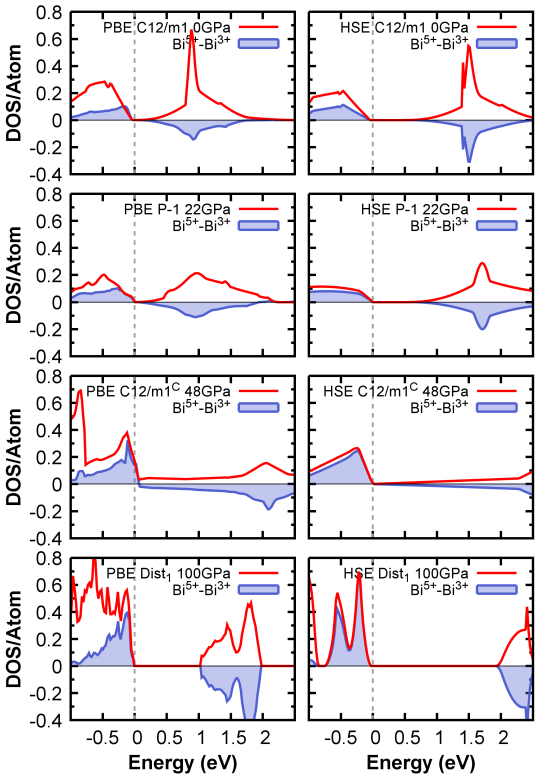

Figure 4.5.: (*color online*) DOS/atom and the difference of average PDOS for Bi^{5+} and Bi^{3+} atoms [235] for stable structures at the pressure of its stability. Left panel shows results obtained with PBE functional for structural relations and DOS calculations. Right panel shows results for structures at the left panel but DOS calculations were performed using the HSE functional using the structures from PBE calculations.

We analyzed the electronic properties of all four ground-state structures using both PBE and HSE functionals. Our calculations show that all structures are insulating (see Fig. 4.5); the tendency is to become more insulating with increasing pressure. Only the $C12\bar{m}1^C$ structure is metallic

at the PBE level but on the the HSE level opens a gap [3]. Here the use of HSE functional is important as PBE underestimates the band gap or predicts the structure to be a metal while actually it is an insulator [203]. Analyzing the partial DOS for Bi atoms it may be seen that all the structures have two inequivalent Bi atoms with different formal valence state, and the insulating behavior is associated with the CDW.

We determine the magnitude of the charge disproportionation by calculating the charge difference $\Delta\rho$ for the two types of bismuth, Bi^{3+} and Bi^{5+}, from the partial *spd* charge of the site-projected ground-state wave function; see Fig. 4.6. Note that although we name these atoms Bi^{3+} and Bi^{5+}, the actual difference in charge is much smaller than two [203].

For the C12$\bar{m}$1, P$\bar{1}$ and C12$\bar{m}1^C$ structures the charge disproportionation increases when the pressure is increased. The change of charge disproportionation for the distorted structure in the pressure range from 20 GPa to 100 GPa is small.

The only possible way to suppress the CDW and have a metallic $BaBiO_3$ phase is to have a highly symmetric structure with no inequivalent Bi atoms as electronic properties of $BaBiO_3$ are highly coupled to the structural ones. Our calculations show that for $BaBiO_3$ all energetically favorable structures are distorted in such a way that they are forced to be insulators, and metallic (symmetric) structures are strongly unfavorable in energy, and thus very unlikely to occur.

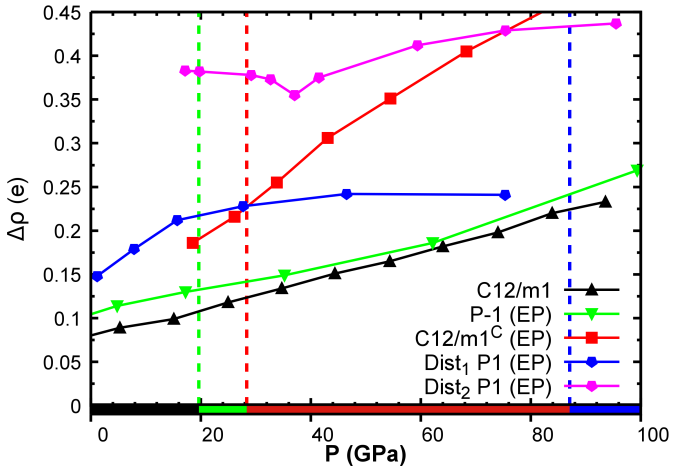

Figure 4.6.: (*color online*) Charge difference $\Delta\rho$ between two different Bi atoms for all stable structures in the phase diagram: the one with the maximal charge (represented by the Bi^{3+} atom) and the one with the minimal (represented by the Bi^{5+}); the HSE functional was used. The color scale at the bottom indicates the stability range of the various structures.

[3] Using the HSE functional on top of the C12$\bar{m}1^C$ obtained at PBE level leads to a semimetal solution. We investigated this case further and performed structure optimization at HSE level for this structure: as a result the gap is opened. To be consistent with the data for other structures on the plot, we left PBE+HSE data for C12$\bar{m}1^C$ on Fig. 4.5.

4.1.3. Conclusions

In this work we performed a theoretical study of the $BaBiO_3$ phase diagram under pressure to analyze the possibility of suppressing the CDW distortion, caused by charge disproportionation. We used two different structural search approaches to construct our *ab-initio* predicted high-pressure phase diagram: evolutionary algorithms and phonon mode analysis. The resulting phase diagram shows three structural phase transitions. The group-theoretical structure prediction method alone, which has been successfully applied to describe the structure of many transition-metal perovskites, is not able to find the best structures at high pressure as it is constrained only to structures with symmetry. By using evolutionary algorithms we found that $BaBiO_3$ becomes more distorted with increasing pressure. In fact, our calculations show that high pressure favors complicated structures with clustering and shearing distortions, which cannot be described as symmetry distortions of the single perovskite structures. The analysis of the electronic properties show that all ground-state structures remain insulating up to 100 GPa and the charge disproportionation is preserved at high pressure. This hinders the transition towards a metallic regime.

4.1.4. Computational details

For total energies and structural optimization we used GGA and HSE DFT calculations, as implemented in the `VASP` package [236–239] using PAW pseudopotentials [240, 241]. We used the hybrid HSE functional to improve the description of the electronic properties. The energy cutoff value was set to 500 eV and Γ-centered Monkhorst-Pack grid [242, 243] with 4x4x4 k-points was used for the GGA [244, 245] and HSE functional for the structural relaxation. To do the relaxation at a specific pressure we performed fixed-volume calculation. For DOS calculations we used an 8x8x8 grid for the GGA functional and a 2x2x2 for HSE which was sufficient to converge the value of the semiconducting gap (note that all structures at the HSE level are semiconducting). Phonon calculations were done with a 20x20x20 k-points grid at the PBE level with a 2x2x2 supercell.

We have used two approaches to predict possible structures at high pressure: evolutionary algorithms as implemented in the `USPEX` package [42] and the group-theoretical analysis using the `ISOTROPY` software suite [180]. Determination of dispersion relations was done with the `Phonopy` package [231]. The setup for `USPEX` calculations was the following: 20 structures in population, 40 structures in the initial population, maximal number of generations is 25, and we stopped the search when the best structure did not change for 8 generations.

The analysis of the Bi environment for the pool of structures obtain in the `USPEX` calculations was performed using the `Chemenv` module from the `Pymatgen` package [35, 36, 233]. The main goal of the `Chemenv` module is to determine the chemical environment of each atom in a structure finding the best polyhedron that can represent atomic positions using *continuous symmetry measure* as a parameter to determine the optimal polyhedron (more details can be found in the Supplemental

Material). The pool of structures consists of around 300 structures for each pressure with 10 atoms in the unit cell.

Note added Recently we became aware of a joint theoretical and experimental study by Martoňák et al. [6] on the high-pressure phase diagram of $BaBiO_3$. The resistivity data confirm our prediction that $BaBiO_3$ remains insulating up to at least 80 GPa. The authors also report a theoretical phase diagram in excellent agreement with ours, confirming our main conclusion that $BaBiO_3$ remains a charge-ordered insulator up to high pressures, forming more and more distorted structures.

Acknowledgments We thank Jiangang He for useful discussions and helpful instructions on symmetry analysis and David Waroquiers and Geoffroy Hautiers for the development of the `chemenv` package and very helpful technical support on its use. We acknowledge funding from the Austrian Science Fund FWF through SFB ViCoM, Project F41-P15, and computational resources from the VSC3 of the Vienna University of Technology. We are also grateful to Erio Tosatti for pointing out us Ref. [6].

4.2. *Ab initio* study of $ABiO_3$ (A=Ba, Sr, Ca) under high pressure

PHYSICAL REVIEW B **98**, 115158 (2018)

***Ab initio* study of $ABiO_3$ (A = Ba, Sr, Ca) under high pressure**

Andriy Smolyanyuk,[1,*] Cesare Franchini,[2] and Lilia Boeri[3,4]
[1]*Institute of Theoretical and Computational Physics, Graz University of Technology, NAWI Graz, 8010 Graz, Austria*
[2]*Faculty of Physics, University of Vienna, 1090 Vienna, Austria*
[3]*Department of Physics, Sapienza Universita di Roma, 00185 Rome, Italy*
[4]*Istituto dei Sistemi Complessi (ISC)-CNR, 00185 Rome, Italy*

(Received 16 July 2018; published 27 September 2018)

Abstract

Using *ab initio* crystal structure prediction we study the high-pressure phase diagram of $ABiO_3$ bismuthates (A=Ba, Sr, Ca) in a pressure range up to 100 GPa. All compounds show a transition from the low-pressure perovskite structure to highly distorted, low-symmetry phases at high pressures (PD transition), and remain charge-disproportionated and insulating up to the highest pressure studied. The PD transition at high pressures in bismuthates can be understood as a combined effect of steric arguments and of the strong tendency of bismuth to charge-disproportionation. In fact, distorted structures permit to achieve a very efficient atomic packing, and at the same time, to have Bi-O bonds of different lengths. The shift of the PD transition to higher pressures with increasing cation size within the $ABiO_3$ series can be explained in terms of chemical pressure.

4.2.1. Introduction

The study of the competition between superconductivity and charge-ordering phenomena has received a strong impulse from recent experiments on high-T_c cuprates [246] and transition metal dichalcogenides [247], raising questions on their interplay and, more in general, on the role of critical fluctuations in quasi-two-dimensional systems [248, 249].

However, the competition between superconductivity and charge density wave (CDW) ordering is not limited to two-dimensional systems, but has been observed in other systems with different dimensionality. A classical example is that of bismuthates with chemical formula $ABiO_3$, where A is an alkaline earth (Ba, Sr, or Ca). These compounds are charge-ordered insulators, but undergo an insulator-to-metal transition upon doping, reaching superconducting T_c's as high as 34 K [3–5, 193].

The CDW is associated to the mixed-valence behavior of bismuth, which can acquire two formal

oxidation states — Bi^{3+} and Bi^{5+} — which alternate on a perovskite lattice, giving rise to tilting and breathing distortions. The charge difference is significantly lower than 2 e^- due to the strong hybridization between Bi(s) and O(p) states. Based on this consideration an alternative picture has been proposed invoking the condensation of holes in lowest O band, resulting in the formation of $Bi^{3+}L^{2-}$ + Bi^{3+}, where L identifies the ligand hole [199, 250]. These two pictures are not mutually exclusive and it is likely that both processes (charge ordering and ligand hole) contributes to the opening of the CDW gap. Upon doping, the distortion is gradually suppressed and the lattice returns to the ideal perovskite structure [198], which is metallic and superconducting.

One might expect that extreme pressures could be used to suppress the lattice distortion also in the undoped samples, and hence achieve a metallic, possibly superconducting state without the complications introduced by doping. However, as shown in our previous work on $BaBiO_3$ [1] and independently confirmed by a combined theoretical and experimental work [6], high pressures do not stabilize an ideal perovskite structure, but a strongly distorted, amorphous-like structure, characterized by strong charge disorder and insulating behavior.

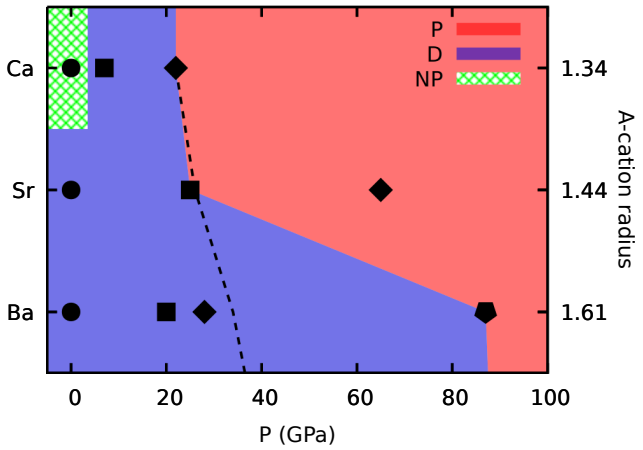

Figure 4.7.: (*color online*) Phase diagram of the structural phase transitions in $ABiO_3$ compounds. Each transition is labeled by a symbol which represents the rank of the structure in the sequence of transitions: *filled circle* for Structure I, *square* for Structure II, *diamond* for Structure III and *pentagon* for Structure IV. "Dark-gray" ("blue") region contains perovskite-like (P) structures, "light-gray" ("red") are distorted (D) structures and "stroked" ("green") non-perovskite (NP) structures. The thick dashed line indicates the transition line for the perovskite-to-distorted transition (PD transition) estimated from chemical pressure considerations, as explained in Sec. 4.2.3.

In this work, we investigate this phenomenon further, and address the effect of *chemical* pressure, studying the high-pressure phase diagram of the whole family of $ABiO_3$ compounds (A=Ca, Sr, Ba) with methods for evolutionary *ab initio* crystal structure prediction [42, 251]. The electronic spectra of all predicted phases are computed with a hybrid Hartree-Fock/density functional theory

(DFT) functional with the HSE (Heyd-Scuseria-Ernzerhof) exchange-correlation functional [26], which has been demonstrated to accurately describe the CDW insulating state of $BaBiO_3$ [198, 203, 204, 206], while ordinary DFT describes $BaBiO_3$ as a metal.

Our results show that the ordered CDW at low pressures and the increase charge disproportionation at high pressure, accompanied by larger structural distortions, are general features of the bismuthate phase diagram: in fact, as shown in Fig. 4.7, all compounds undergo a transition from a perovskite (P) to a strongly distorted (D) structure, and remain insulating up to 100 GPa. The occurrence of distorted structures is a consequence of a steric argument, combined with the tendency of bismuth to charge disproportionation.

This paper is organized as follows. In Sec. 4.2.2 we describe the results of our *ab initio* calculations starting with our prediction for the high-pressure phase diagram in Sec. 4.2.2, followed by the description of electronic properties of the most stable structures in Sec. 4.2.2. The discussion on the perovskite-to-distorted transition (PD transition) follows in Sec. 4.2.3. The main conclusions of this work are summarized in Sec. 4.2.4. Computational details are described at the end of the paper in Sec. 4.2.5.

4.2.2. Results

Phase Diagram

In Fig. 4.7 we show the phase diagram of $ABiO_3$ in the pressure range from 0 to 100 GPa, predicted using *ab initio* evolutionary crystal structure prediction methods. For Bismuthates, the use of an unbiased crystal structure prediction method is crucial, since the group-subgroup approach [181, 228–230] which is routinely used to predict structural transitions in perovskites is not able to capture the transition to the distorted structure — see Ref. [1] for details.

To generate the phase diagram in Fig. 4.7, a set of reference crystal structures was first obtained from evolutionary crystal structure prediction runs at 0, 50, and 100 GPa. The most promising structures from the pool of crystal structures obtained at these pressures were further relaxed at intermediate pressures at constant volume intervals, and interpolated with an analytical equation of state, which allowed us to determine the transition pressures accurately (see Sec. 4.2.5 for more details). The lowest-enthalpy structures at each pressure were then used to construct the final phase diagram.

We plot all $ABiO_3$ compounds on the same figure (Fig. 4.7), with a common pressure axis; the compounds are equispaced along the vertical axis; starting with Ca, which has the smallest ionic radius, the size of the A cation increases along the y axis from Ca to Ba exerting an effective *chemical pressure* on the perovskite lattice (see Table 4.3 for corresponding ionic radii and unit cell volumes). Assuming that the most important parameter governing the structural transitions is the volume of the unit cell, and that this is mainly determined by the size of the A cation, this

means that the sequence of structural transitions seen in $BaBiO_3$ should occur at lower pressures in $SrBiO_3$ and even lower in $CaBiO_3$.

In the figure, each transition is labeled by a symbol representing the rank of the structure in the transition series. The diagram is also divided into three regions, denoted with the letters P (perovskites), D (distorted) and NP (non-perovskite). The thick dashed line indicates the shift of perovskite-to-distorted transition pressure (PD transition), estimated from the simple cubic perovskite model, as explained in Sec. 4.2.3.

We start from the low-pressure region. An empirical guess of the ambient pressure structure for each compound can be obtained from the Goldschmidt tolerance factor, which is based on the size mismatch between the cations. The tolerance factor for double perovskites is defined as: $t = \frac{r_A + r_O}{\sqrt{2}(\langle r_{Bi} \rangle + r_O)}$, where r_A is the radius of the A cation, r_{Bi} is the averaged ionic radius of bismuth and r_{O} is the radius of oxygen. The ideal value $t = 1$ corresponds to a cubic perovskite structure; deviations from this ideal value indicate the amount of distortion needed to stabilize the atomic arrangement: the higher the deviation, the higher the distortion. Based on the value of t, one would expect that at ambient pressure all $ABiO_3$ compounds should be either monoclinic or orthorhombic perovskites with tilted oxygen octahedra, because $t < 0.97$ [252] for all A cations (see Table 4.3). Indeed, the tolerance factor correctly predicts the structure at ambient pressure for $BaBiO_3$ and $SrBiO_3$, which are known experimentally [4, 11]. However, the structure obtained by our evolutionary algorithm predictions for $CaBiO_3$ is trigonal, which apparently contradicts the argument based on the tolerance factor. Note, however, that in this case the value of t is extremely small, and several exceptions to the tolerance factor argument are known [253].

Table 4.3.: Ion Shanon radii (R) for the A cation in coordination XII; corresponding tolerance factors (t) for $ABiO_3$ compounds in the double perovskite structure; calculated volume per formula unit (V), average Bi-O distance ($\overline{BiO}$) and breathing distortion δ for $ABiO_3$ at P=0 GPa. $\delta = \frac{1}{2}(\overline{Bi_1O} - \overline{Bi_2O})$, where $\overline{Bi_1O}$ and $\overline{Bi_2O}$ are average Bi_1-O and Bi_2-O bond distances respectively.

	R(A) (Å)	V (Å^3/f.u.)	t	$\overline{BiO}$ (Å)	δ (Å)
$CaBiO_3$	1.34	76.91	0.85	2.29	0.122
$SrBiO_3$	1.44	80.00	0.88	2.25	0.089
$BaBiO_3$	1.61	85.87	0.93	2.24	0.074

At ambient pressure $BaBiO_3$ and $SrBiO_3$ structures exhibit different monoclinic symmetries: $C12\bar{m}1$ and $P2_1/c$, respectively [see Fig. 4.8c and 4.8b]. Both structures contain the characteristic perovskite building block formed by BiO_6 octahedra and share a common parent structure — an ideal cubic perovskite with $P3\bar{m}3$ symmetry. The two monoclinic structures can be obtained applying two different types of distortions to the parent structure: *breathing* (alternating the size of Bi-O octahedral environment) and *tilting* (rigid rotations of Bi-O octahedra). The difference between the two compounds is the different tilting pattern ($a^0b^-b^-$ and $a^+b^-b^-$ for $BaBiO_3$ and $SrBiO_3$ in Glazer notation [53], respectively) and the amount of breathing distortion (0.074 Å and 0.089 Å, see Table 4.3).

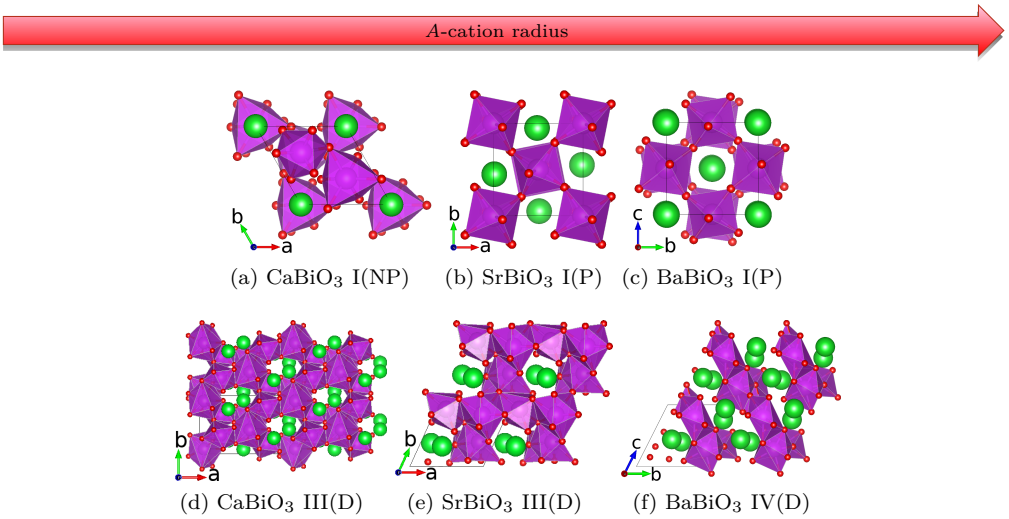

(a) $CaBiO_3$ I(NP) (b) $SrBiO_3$ I(P) (c) $BaBiO_3$ I(P)

(d) $CaBiO_3$ III(D) (e) $SrBiO_3$ III(D) (f) $BaBiO_3$ IV(D)

Figure 4.8.: (*color online*) Structures of $ABiO_3$ compounds used in this work: (a) non-perovskite $CaBiO_3$, (b) perovskite $SrBiO_3$, (c) $BaBiO_3$, and distorted (d) $CaBiO_3$, (e) $SrBiO_3$, and (f) $BaBiO_3$. *A* cations (Ba, Sr, Ca) are shown as light-gray (light-green) spheres, Bi — (gray) purple spheres inside dark-gray (purple) polyhedron, O — small gray (red) spheres.

Upon increasing pressure we observe that all compounds undergo a series of structural transitions. The common feature is that all $ABiO_3$ compounds undergo a transition to a highly distorted phase (D) beyond some critical pressure. By "highly distorted phase" we mean a structure that does not belong to the perovskite family, in the sense that a transition from the perovskite structure requires large atomic displacements and strong distortions of the original structural motifs, which cannot be decomposed into breathing and tilting distortions. It is worth noting that such drastic distortions may be an indicator of some critical phenomena that happens at high pressure for $ABiO_3$ compounds, such as a transition to an amorphous-like state or chemical decomposition, that cannot be explained by the *ab initio* methods used in our work [4] Even though they do not exhibit the regular arrangement seen at ambient pressures, the Bi sites in the high-pressure distorted structures exhibit charge disproportionation and insulating behavior, as discussed in Sec. 4.2.2.

Distorted structures in the bismuthates were predicted for the first time by us in $BaBiO_3$ [1], and later confirmed by the authors of Ref. [6].

We now describe the phase diagrams of the individual compounds in detail; the corresponding structural files are provided in the Supplementary Materials.

[4] We did a test calculation of the formation enthalpies (dF) of low-pressure monoclinic $BaBiO_3$ at 0 GPa and high-pressure distorted $BaBiO_3$ at 100 GPa using the PBE functional and using an evolutionary algorithm to find the crystal structures of Ba, Bi, and O at 100 GPa. For Ba and Bi we allow variable unit cell size with four to eight atoms in the cell, for O we keep 16 atoms in the unit cell. The resulting formation enthalpies are as follows: dF(monoclinic) = –9.900 eV/f.u. and dF(distorted) = –13.625 eV/f.u., which indicates that $BaBiO_3$ stochiometry should exist at high pressure.

$BaBiO_3$: The data for $BaBiO_3$ presented in this work are taken from our previous work [1]. We find that a first transition from the monoclinic I(P) [space group C12$\bar{m}$1; see Fig. 4.8c] to triclinic II(P) structure occurs at 20 GPa. The II(P) structure is another form of perovskite structure with an additional octahedral tilting axis compared to the I(P) structure. The next transition is from the triclinic II(P) to a *clustered* monoclinic III(P) structure at about 28 GPa. This structure can be described as a perovskite with the stacking fault resulting in only half of the Bi atoms exhibiting an octahedral environment. Although it strongly deviates from the perovskite structure, we still assign it to the perovskite family (P). The last transition is from a *clustered* monoclinic to a distorted IV(D) [see Fig. 4.8f] structure at 87 GPa, which has no symmetry.

$SrBiO_3$: The first transition is from a perovskite-like monoclinic I(P) [space group P121n1; see Fig. 4.8b] to a *distorted* II(D) structure at about 25 GPa [see Fig. 4.8e] and the second is from a distorted II(D) to another distorted structure III(D) at 65 GPa. These are two different *distorted* structures, but is difficult to give a clear description of the structural differences as the structures are too distorted to identify a clear pattern.

$CaBiO_3$: There are no experimental crystal structure data for $CaBiO_3$ at ambient pressure, but only a computational study suggesting a polar $R3$ structure [181]. Indeed, $CaBiO_3$ is unstable at ambient conditions but it is possible to stabilize it at high pressures [254] (about 6 GPa), or upon K doping, $Ca_xK_{1-x}O_3$, with $0.15 \leq x \leq 0.25$ [5]. According to our evolutionary predictions the structure at ambient pressure is trigonal (R3) and consists of "paired" distorted octahedra that share a common edge. We find that the Bi-Bi and Ca-Ca environment is no longer octahedral, as in perovskites, but tetrahedral. Therefore, in Fig. 4.7 this structure is classified as a non-perovskite structure (NP). Our structure is 12 meV/atom (17 meV/atom in HSE) lower in enthalpy than the perovskite structure proposed by He *et al.* in Ref. [181] and based on the traditional group-subgroup symmetry analysis [228].

The first structural transition is from the trigonal I(NP) [see Fig. 4.8a] to monoclinic II(P) structure at 7 GPa. In this case the Bi-Bi and Ca-Ca environment is distorted octahedral and the Bi-O octahedra are also distorted, with additional tilting. We therefore classify this structure as perovskite (P). The second transition is from the II(P) to a distorted III(D) [see Fig. 4.8d] structure with $C1c1$ symmetry at 22 GPa.

In summary, our study of the phase diagram of $ABiO_3$ compounds shows that pressure does not stabilize more symmetric structures, as in other transition metals perovskites, but highly distorted ones, as we originally observed for $BaBiO_3$ [1]. Furthermore, reducing the size of the A cation shifts the transition from perovskite-like to distorted structures to a lower pressure, in agreement with considerations based on *chemical pressure*, i.e., with the idea that substituting a cation with a smaller one is equivalent to applying an external pressure. In the next sections, we will study in more detail the nature and origin of the PD transition and the electronic properties of the most relevant structures.

Electronic Structure

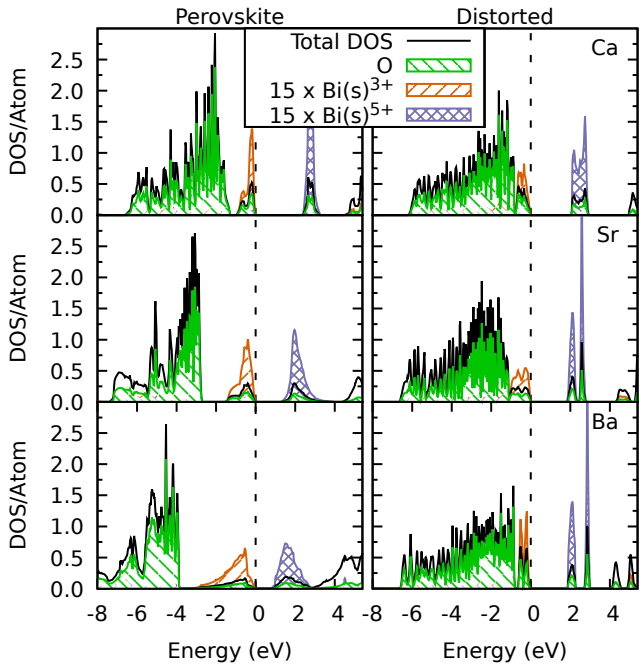

Figure 4.9.: (*color online*) Total and atom-projected DOS for $ABiO_3$ compounds before and after the PD transition: 22 GPa for $CaBiO_3$, 25 GPa for $SrBiO_3$ and 45 GPa for $BaBiO_3$, calculated with the HSE functional; the structures were optimized at the PBE level. Bi atoms are divided into formal Bi^{3+} and $Bi^{5}+$ valences. For the sake of clarity the Bi-DOS is multiplied by a factor of 15.

Figure 4.9 shows the total and atom-projected density of states (DOS) for all $ABiO_3$ compounds, at the transition pressure between the perovskite (P) and the distorted (D) structures, obtained with the HSE functional. For consistency, also for $BaBiO_3$ we show the DOS for the perovskite and the distorted structures, at the transition pressure between the two, but we remind that in this region the stable structure is the *clustered* one. The aim of the figure is, in fact, to trace the origin of the PD transition, which is common to all $ABiO_3$ compounds, while the *clustered* region is found only in $BaBiO_3$.

As it can be clearly seen, all structures are insulating, with a gap at ambient pressure: 0.6 eV for $BaBiO_3$ (experimental measurements vary from 0.2 eV [10] to 1.1 eV [93]), 1.1 eV for $SrBiO_3$, and 2.6 eV for $CaBiO_3$. The increase of the gap with decreasing cation size is consistent with the larger breathing distortions predicted for the $CaBiO_3$ structure (see Table 4.3). The behavior of the gap as a function of pressure is shown in Fig. 4.10 [255].

The mechanism leading to the opening of a gap in the perovskite structure has been discussed by several authors: charge disproportionation at the Bi site causes alternating breathing distortion of the ideal perovskite lattice, further stabilized by tilting distortion, and this opens a gap in

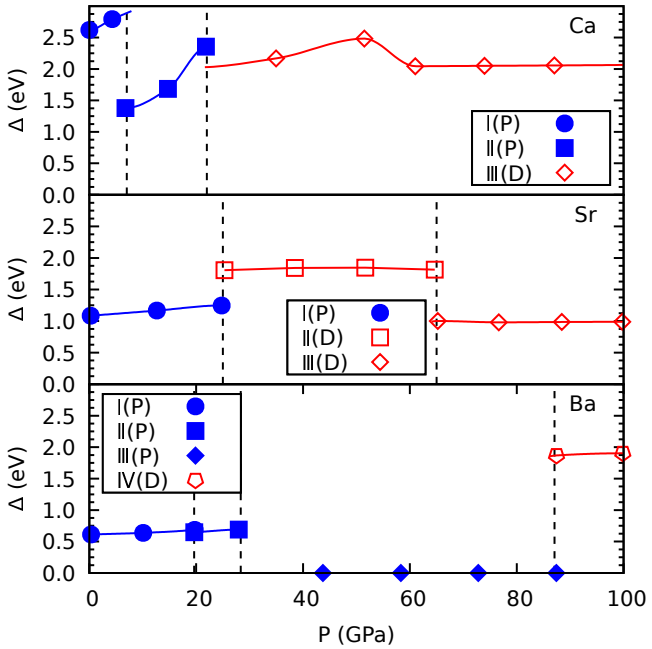

Figure 4.10.: (*color online*) Band gaps for the most stable structures of $ABiO_3$ compounds as a function of pressure [255]. Each symbol represents a specific structure, as defined in the caption of Fig. 4.7; the filling indicates whether the structure is perovskite-like (filled symbol) or distorted (empty symbol). Lines are meant as a guide to the eye.

the strongly hybridized Bi(s)-O(p) antibonding band [199, 203]. This is evidenced by the partial DOS plots, which show a clear splitting and charge redistribution between Bi^{3+} and Bi^{5+} states, localized below and above the semiconducting gap. A similar situation is found in distorted phases, where it is still possible to identify inequivalent Bi^{3+}– and Bi^{5+}–like ions. One clearly sees that the two contributions to the DOS are well separated, with Bi^{5+} and Bi^{3+} states giving the dominant contribution to the electronic DOS above and below the gaps, respectively. In distorted $SrBiO_3$ and $BaBiO_3$ the two main peaks are further split into several sub-peaks, indicating a more complex pattern of charge disproportionation.

In typical transition metal perovskites the application of pressure leads to a continuous closing of the gap [109]. However, for bismuthates the situation is different: increasing pressure by chemical substitution makes the gap larger, due to the gradual narrowing of the Bi^{3+} and Bi^{5+} peaks associated with the upward shift and broadening of the occupied oxygen band. Despite the larger degree of Bi-O hybridization the narrowing of the Bi^{3+} and Bi^{5+} peaks increases the bonding-antibonding repulsion, increases the bond- (see Table 4.3) and charge-disproportiation (see Fig. 4.11) and ultimately leads to a substantial increase of the gap size.

As already mentioned, the classification into Bi^{3+} and Bi^{5+} is clearly only indicative: due to the strong hybridization with oxygen the actual charge disproportionation between Bi sites is much

smaller than two. To obtain a quantitative estimate, we performed a Bader charge analysis [256–259], which is more accurate than the estimation based on the integration of the DOS, that we used in our previous works [1, 198]. Remarkably, we found that Bader charge analysis deliver charge differences between Bi^{3+} and Bi^{5+} ions three to four times larger. The results are shown in Fig. 4.11, where $\Delta\rho$ is a difference between the maximum and minimum charge located on bismuth atoms obtained in the Bader analysis. Each symbol in the figure represents a specific structure and its filling shows if the structure is perovskite-like (filled symbol) or distorted (empty symbol). The figure shows that the average charge difference is of $\sim 0.5\ e^-$/f.u., and slightly increases with pressure; apart from $BaBiO_3$, where the presence of the clustered structure complicates the phase diagram, the transition from the perovskite to the distorted structure is relatively smooth, similarly to what we observed for the DOS.

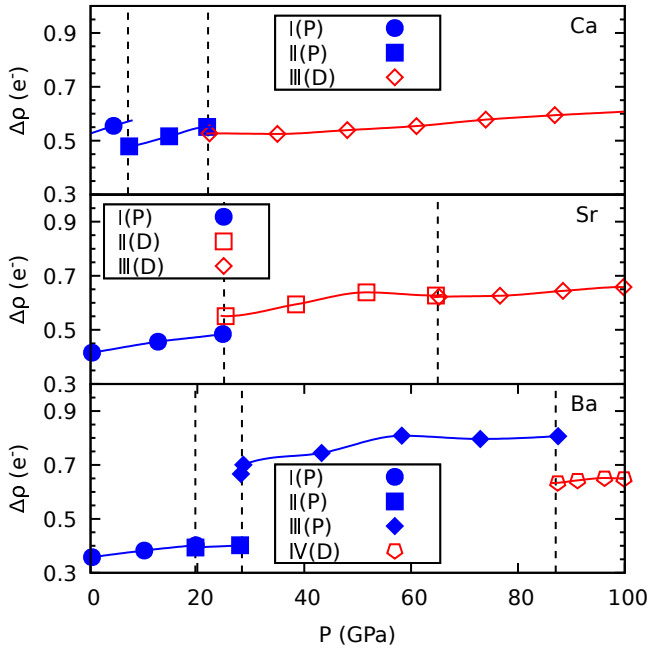

Figure 4.11.: (*color online*) Difference between maximum and minimum charge ($\Delta\rho$) located on bismuth atoms w.r.t pressure, obtained using Bader analysis. Note that the Bader charge analysis yields sensibly higher values than the estimate based on the partial DOS estimate used in our previous paper [1]. The meaning of the symbols is the same as in Fig. 4.10.

Having clarified the reasons behind the robustness of the CDW gap upon pressure we move now to the analysis of the PD structural transition, which is done in the following section.

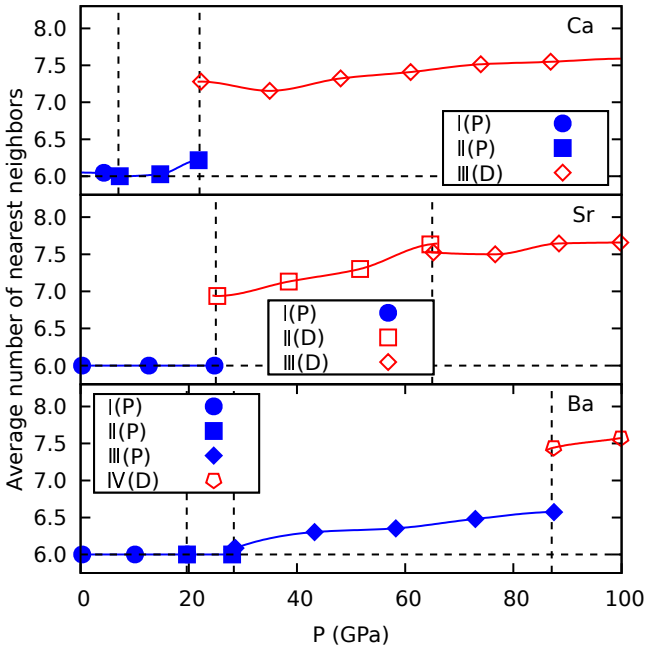

Figure 4.12.: (*color online*) Average number of Bi nearest neighbors as a function of pressure. The meaning of the symbols is the same as in Fig. 4.10.

4.2.3. Perovskite-to-Distorted Transition

The first obvious argument to explain the PD transition is a *steric* one, i.e., distorted structures, which are very compact, become favorable at high pressures, where the pV term becomes the dominant part of the total enthalpy. In fact, at the transition pressures between perovskite and distorted structures, the volumes of the distorted structures are on average $\sim 7.5\%$ smaller than those of the perovskite ones.

The lower specific volume of the distorted structures is achieved by a more efficient packing of the atoms with an increasing coordination number. To visualize this, in Fig. 4.12 we plot the average number of oxygens in bismuth environment as a function of pressure. Values close to six represent perovskite or perovskite-like structures. The higher the difference from this value, the higher the amount of distortion in the structure.

Clearly, all $ABiO_3$ compounds undergo a discontinuous jump from perovskite-like structures to distorted ones at different critical pressures: $CaBiO_3$ and $SrBiO_3$ at 22 to 25 GPa; and $BaBiO_3$ at 87 GPa (45 GPa if the *clustered* structure is neglected). Thus, the increase of coordination number is the general mechanism that stabilizes distorted structures at extremely high pressures in agreement with what we found for $BaBiO_3$ in the previous paper [1].

The origin of this effect can be understood as follows. Initially, pressure causes a compression of the Bi-O bonds. However, the compressibility of Bi-O bonds decreases with increasing pressure,

until it reaches a critical value, where it becomes energetically more favorable to introduce new chemical bonds and rearrange bond distances than to continue to compress bonds.

This can be easily seen from Fig. 4.13, showing the pressure-dependence of the average Bi-O length; for all $ABiO_3$ compounds there is a clear jump to larger Bi-O length at the pressures corresponding to the transition from perovskite-like to distorted structure. The increase in coordination number, and the tendency to form disordered structures, is also favored by the intrinsic tendency of bismuth to charge disproportionation, which leads to forming two (or even more) types of bonds with different lengths. The tendency to charge disproportionation increases with increasing pressure, as shown by the Bader charge analysis in Fig. 4.11, and hence the arrangement in high-symmetry structures becomes progressively less favorable.

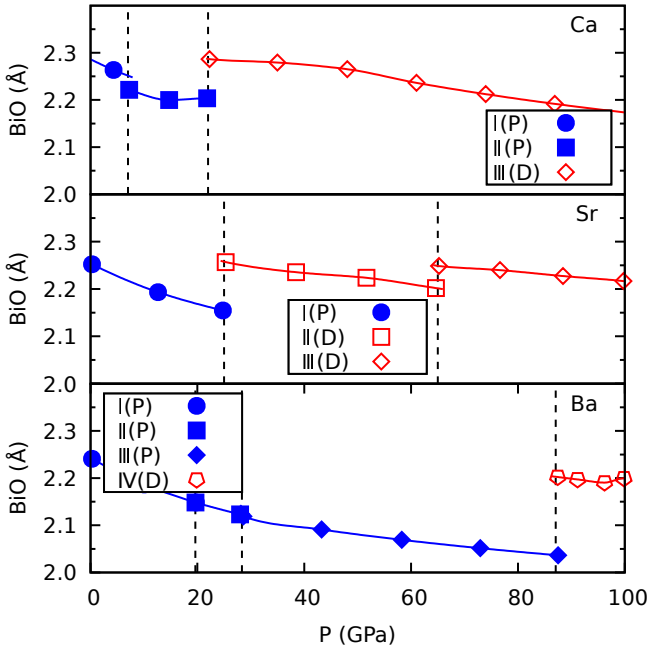

Figure 4.13.: (*color online*) Average BiO bond length as a function of pressure. The meaning of the symbols is the same as in Fig. 4.10.

Indeed, forming *distorted* structures, which have a very low symmetry, is an efficient way to increase the number of bonds in a very closely-packed structure. Let us consider first the Bi-O octahedral environment: the Bi-O coordination geometry is restricted by the chemical composition and crystallographic restriction theorem, which forbids Bi-O to form a regular polyhedron with coordination number larger than six. For example, the 7-coordinated pentagonal dipyramid has a 5-fold rotational symmetry and the 8-coordinated square antiprism has an 8-fold symmetry, which are both forbidden due to the crystal periodicity. Cubic coordination is not allowed by chemical composition as it requires a composition with the same number of Bi and O. As a result, when the coordination number increases due to the formation of new bonds under increasing

pressure, pronounced distortions of the local environment occur, that lead to highly-distorted structures at high pressure.

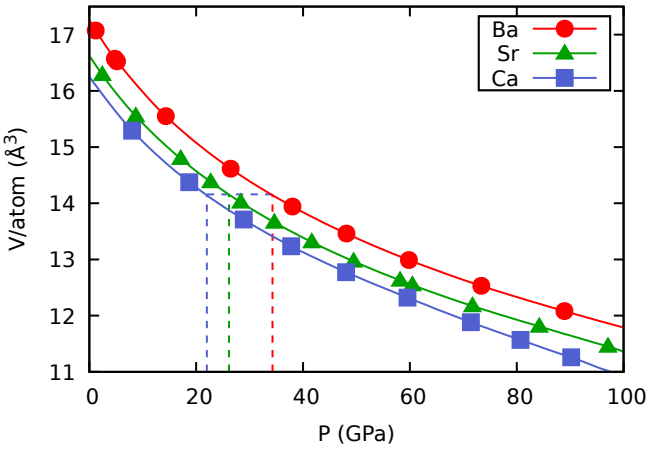

Figure 4.14.: (*color online*) Equation of state for $ABiO_3$ compounds in the ideal cubic perovskite structure, used as a model to estimate the shift of the PD transition line due to the chemical pressure, showed by dashed lines in Fig. 4.7. The PD transition at 22 GPa for $CaBiO_3$ is taken as a reference point to estimate a common volume for the transition (see text). Lines are meant as a guidance for the eye.

The perovskite-to-distorted transition pressure increases with increasing cation radius (see Fig. 4.7). This effect, sometimes referred to as *chemical pressure*, is based on the idea that replacing a cation with a larger one, keeping the volume fixed, increases the effective pressure on the BiO_3 sublattice. This effect is easily illustrated by a simple numerical experiment, based on the ideal cubic perovskite structure.

Figure 4.14 shows the equation of state (EOS) for $ABiO_3$ compounds in cubic structure. The influence of *chemical* pressure may be estimated calculating the pressures, corresponding to the intersection of a $V = const$ line with the EOS curve for a given compound. For example, according to Fig. 4.7, the PD transition pressure for $CaBiO_3$ is at around 22 GPa. We can use this value and the EOS for our cubic model to estimate the PD transition pressures in $SrBiO_3$ and $BaBiO_3$. First, we find the volume, which corresponds to 22 GPa on the EOS for cubic $CaBiO_3$ (V_{PD}). If we assume that the main driving force of the PD transition is the unit cell volume, we can estimate the PD transition pressure for $SrBiO_3$ and $BaBiO_3$ from the intersection of the $V = V_{PD}$ line with the relative EOS curves. The two values are shown as dashed lines in Fig. 4.14. Our crude estimate gives 26 GPa for $SrBiO_3$ and 34 GPa for $BaBiO_3$; the agreement with the transition pressure is remarkable for $SrBiO_3$ (25 GPa), but apparently quite bad for $BaBiO_3$ (87 GPa). However, we recall that in $BaBiO_3$ a *clustered* phase, in which only half of the Bi atoms are arranged in a regular octahedral environment, is predicted to occur in-between the perovskite and the distorted structure, shifting the transition to fully distorted structures to 87 GPa. If one disregards the *clustered* phase, the transition from perovskite to distorted structure

occurs at around 45 GPa, which is in fair agreement to the 34 GPa value, predicted from the ideal cubic model.

4.2.4. Conclusions

In conclusion, in this work we study the pressure behaviour of three rare-earth bismutathes $ABiO_3$ (A=Ba, Sr, Ca), using *ab-initio* crystal structure prediction and hybrid functional calculations. Similarly, to what was previously observed in $BaBiO_3$, we find that charge disproportionation is robust and not suppressed by pressure in all $ABiO_3$ compounds, which also all remain insulators up to 100 GPa. The charge disproportionation between Bi^{3+} and Bi^{5+}, estimated by Bader charge analysis, is much higher than what was predicted by the usual methods based on the DOS, starting from around 0.5 e^- at ambient pressure and going up to 0.7 e^- for the highly distorted high-pressure structures.

Indeed, the tendency to charge disproportionation becomes stronger with increasing pressure and has a big influence on the crystal structure; in fact, all compounds undergo a transition from perovskite structure to a highly distorted structure (PD transition); in $BaBiO_3$, this happens through a transition to an intermediate *clustered* phase, whose presence shifts the PD transition to higher pressures, with respect to the value estimated on the basis of chemical pressure.

The formation of distorted structures is explained by a steric effect, combined with the mixed-valence behavior of bismuth; distorted structures have a higher density (more efficient packing) than any variant of the perovskite structure, and this permits to reduce the pV contribution to the enthalpy which is dominant at high pressures. In the distorted structures, a more efficient packing is achieved by allowing the coordination number to increase beyond the value of 6 for the characteristic of the perovskite structure; this tendency, combined with that of the charge disproportionation, means that it is not possible to form any symmetric structure under these circumstances.

4.2.5. Computational Details

To construct the high-pressure phase diagram, candidate structures with 10, 20 and 40 atoms per unit cell at 0, 50 and, 100 GPa were generated using the `USPEX` code for evolutionary crystal structure prediction [42–44]. To have a higher probability to reach the global minimum, several USPEX runs were performed. We want to note that calculations with a larger number of atoms per unit cell are very computationally demanding. As a compromise, 40 atoms/cell is a reasonably large number. Low pressure structures of $BaBiO_3$ and $CaBiO_3$ require 10 atoms/cell, and $SrBiO_3$ requires 20 atoms/cell.

Usually, the higher the symmetry, the less the number of atoms/cell needed. This means, that if some structure with higher symmetry would appear, it would be sampled by calculations with units cells of 20 atom/cell. Even if it is possible that the unit cell of the actual structure contains

more than 40 atoms/cell, it should be distorted too or have a low symmetry, and it will definitely not be a cubic perovskite or related structure.

On the other hand, although we report different distorted structures for different $ABiO_3$ compounds, this does not necessarily imply that they are different in experiment: it might be that due to the too small size of the unit cell, we reproduce different parts of some more complex and bigger distorted structural motif.

There is always a possibility, that the precise global minimum of the energy surface is not reached, since the method is stochastic and does not ensure this. But the tendency for distorted structures to appear is robust, giving a reasonable confidence that the global minimum should be a distorted structure too.

For each group of structures, generated by a separate `USPEX` run, we chose five lowest in enthalpy to perform a final accurate structure relaxation. The structure relaxations were performed allowing for the atoms' relaxations and change of the cell shape, but the volume was fixed. Each structure was than relaxed on a grid of at least nine volumes, chosen between the average volumes corresponding to 0 and 100 GPa. The pressures of the relaxed structures were estimated from the stress tensor. The resulting pressure versus volume relation were then interpolated analytically; from the interpolation curves, we obtained the transition pressures used to derive the final phase diagram shown in Fig. 4.7.

We used density functional theory (DFT) in the generalized gradient approximation (GGA) with Perdew-Burke-Ernzerhof functional[244, 245] to calculate the total energies and perform structural optimization, as implemented in the `VASP` package [236–239] using projector augmented wave method (PAW) pseudopotentials [240, 241]. The hybrid HSE functional (Heyd-Scuseria-Ernzerhof) was used only to compute electronic spectra, in particular for the DOS calculations (Fig. 4.9) and for calculation of band gaps (Fig. 4.10)[255]. The energy cutoff value was set to 500 eV and Γ-centered Monkhorst-Pack grid [242, 243] with the reciprocal-space resolution 0.04 $2\pi\text{Å}^{-1}$ was used for the GGA for structural relaxation and 0.01 $2\pi\text{Å}^{-1}$ for total energy calculation. For calculations where HSE functional was used the reciprocal-space resolution was 0.04 $2\pi\text{Å}^{-1}$.

The neighbors analysis was performed with the help of the `CHEMENV`[35, 177] module from the `PYMATGEN`[36, 234] package. `CHEMENV` provides routines to obtain the best fit of the coordination environment polyhedron for a specific atom and this information was used to estimate the number of oxygen neighbors for each bismuth atom in Fig. 4.12.

Acknowledgments We acknowledge funding from the Austrian Science Fund FWF through SFB ViCoM, Project No. F04115 and computational resources from the VSC3 of the Vienna University of Technology and from the HPC TU Graz.

5. *Ab initio* prediction of novel iridates

In this chapter we present preliminary results of two ongoing projects on iridates. The interest in iridates is relatively recent, which means that only a few of possible compounds have been synthesized experimentally. Using state-of-the-art methods for crystal structure prediction generalized to a search over the full composition space, we aim to predict novel compounds which may actually be synthesized in experiments. For this task we use evolutionary crystal structure prediction method as implemented in the `USPEX` *package [42–44]. This method is employed to study the Na-Ir-O ternary diagram and our preliminary results of this study are discussed in Sec. 5.1.*

A search for a possible binary Ir_xO_{1-x} chemical compositions was carried out as a part of the ternary phase diagram refinement procedure. During this search an unexpected group of metastable 2D phases of IrO_2 started to emerge. So far, for IrO_2 only two bulk phases are known: rutile [260] and spinel [261]. Being interested in this discovery, we decided to have a closer look at this metastable phases and the preliminary results of IrO_2 study are presented in Sec. 5.2.

5.1. *Ab initio* prediction of the Na-Ir-O ternary diagram

In Sec. 2.2 we listed several prominent Ir-based compounds showing interesting properties: from relativistic $J_{eff} = \frac{1}{2}$ insulators to candidates for quantum spin liquids.

Up to now, only five ternary $Na_xIr_yO_{1-x-y}$ compounds were reported: the postperovskite [32] and hexagonal $NaIrO_3$ [33] depicted in Fig. 5.1a and 5.1b, the honeycomb-layered Na_2IrO_3 [262] depicted in Fig. 5.1c, Na_4IrO_4 [263] with square-planar coordinated Ir as depicted in Fig. 5.1d, the hyperkagome $Na_4Ir_3O_8$ [46] (Fig. 5.1e) and the B-site ordered spinel $Na_3Ir_3O_8$ [264] (Fig. 5.1f).

However, it is likely that many other stable or metastable phases exist in the phase diagram, which, given the strong interplay between CFS, SOC and electronic correlations, most likely host interesting physical properties. For this reason, we performed a broad scan of the Na-Ir-O ternary phase diagram using variable-composition evolutionary crystal structure prediction methods.

Our current database contains results from evolutionary search over the entire ternary compositional space ($Na_xIr_yO_{1-x-y}$) for structures with 6-12, 12-24 and 24-36 atoms in the unit cell. It contains 1736 compositions represented by 6513 final structures. The total number of structures sampled by the evolutionary search is larger, but we retained in the final database only up to 10 structures of each composition, which are the lowest in energy within the sampled structures at a

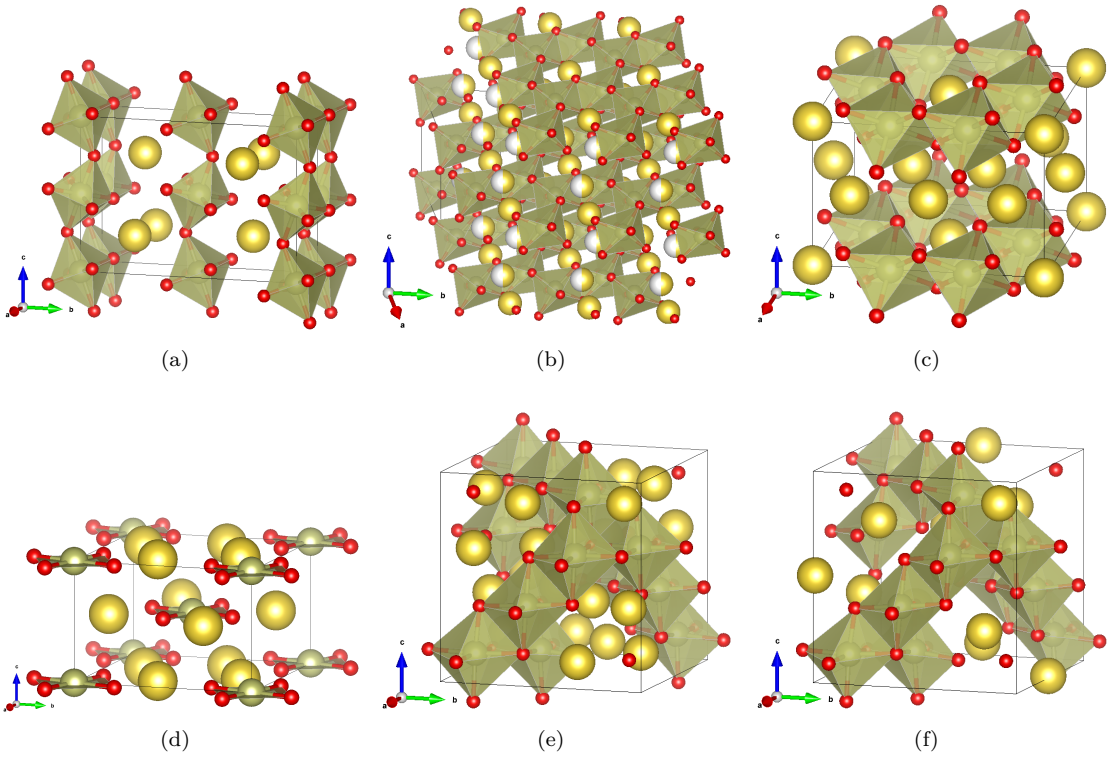

Figure 5.1.: The crystal structure of (a) postperovskite and (b) hexagonal $NaIrO_3$, (c) Na_2IrO_3, (c) Na_4IrO_4, (d) $Na_4Ir_3O_8$ and (e) $Na_3Ir_3O_8$. Golden spheres are Na, small red spheres are O and green spheres are Ir. For hexagonal $NaIrO_3$ some Na position were reported having 0.5 site occupation: this is denoted by half golden/half white spheres.

specific composition. The reason to retain not only the lowest-enthalpy (ground) structure is that the other structures may be needed for post-processing and for the determination of metastable structures. According to our previous experience with structural searches, the best procedure to identify the best structure is to first perform a search with a loose force threshold for structural optimization, and later re-optimize the best structures with tighter converge parameters. This may change the ranking of the structures, and, sometimes, the hull of stability of compounds. Thus, it is highly possible, that the current ranking of structures may be improved by a later post-processing of the data with a tighter threshold.

The computational details of the calculations used to construct the ternary phase diagram are described in Sec. 5.3.

The obtained ternary phase diagram is depicted in Fig. 5.2, where the formation enthalpy for the best structure of each sampled composition is assigned a color; the darker the color, the lower the value of the formation enthalpy (only structures with negative formation enthalpy are reported in

the plot). We denote the known experimental structures by green empty circles and our predicted structures, that belong to the convex hull, as white empty circles. The convex hull determines the set of all thermodynamically stable compositions, if the compositional space was fully sampled.

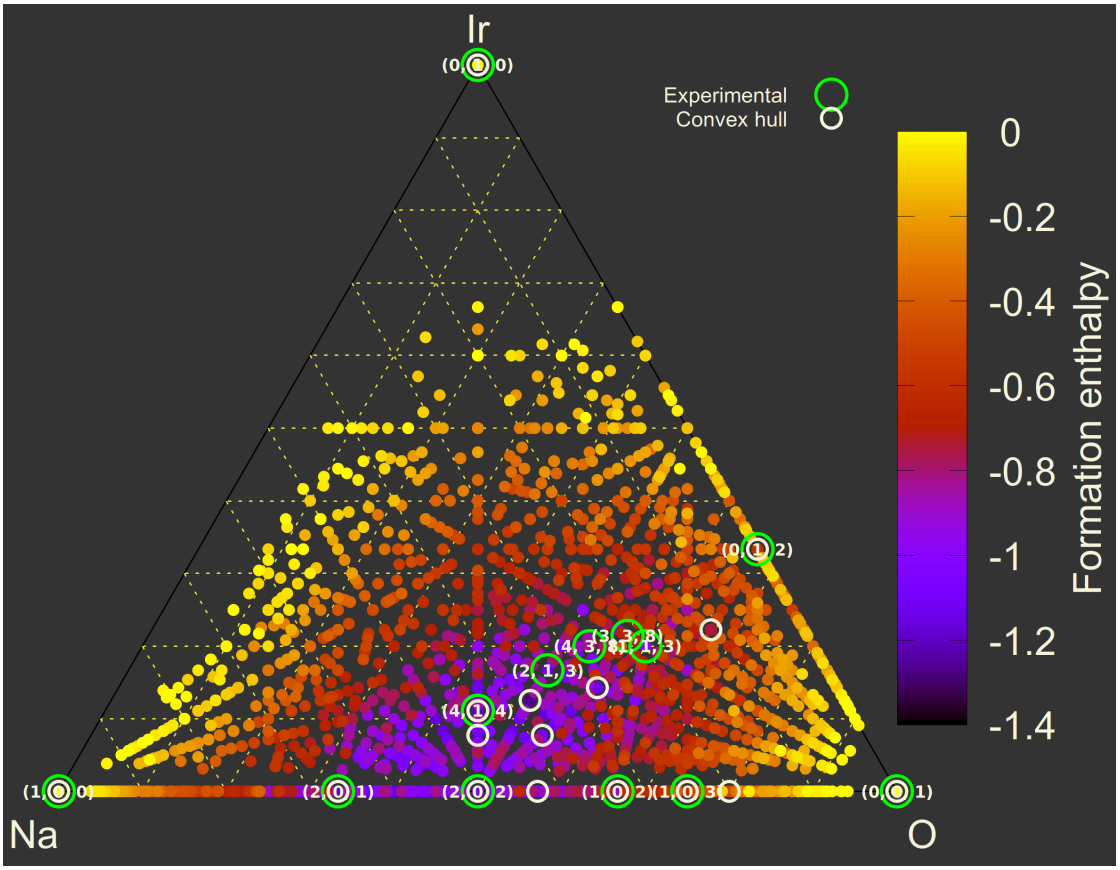

Figure 5.2.: Calculated ternary phase diagram for $Na_xIr_yO_{1-x-y}$. Green empty circles are available experimental compositions, white empty circles are predicted compositions, that belong to the convex hull. Formation enthalpy is color coded in the following way: the darker the color, the lower the value of the formation enthalpy.

At first, we want to compare our prediction with the known experimental data. We see that for ternary compounds full agreement with experiments is only for the Na_4IrO_4 composition. By full agreement we mean that the predicted structure is the same as the experimental one and it is found on the convex hull.

In the case of $NaIrO_3$ the best structure of our search does not belong to the convex hull. It has a similar structural motif as the experimental postperovskite $NaIrO_3$, however the tilting of the octahedra observed in experiments is not reproduced by our calculations. A possible explanation is that the convergence threshold for our preliminary exploration is too loose to capture these details, or that the evolutionary search was trapped in a local minimum.

The best predicted structure of Na_2IrO_3 does not belong to the convex hull too. It is layered, similarly to the experimental crystal structure, but Ir atoms form a square lattice instead of a honeycomb lattice. It is possible that this is a metastable structure of Na_2IrO_3 and its dynamical stability should be checked.

On the other hand, it is not surprising that we are not able to detect the structures for $Na_3Ir_3O_8$ and $Na_4Ir_3O_8$, since the experimental structures contain 56 and 64 atoms in the primitive unit cell respectively, and the largest unit cell sampled in our search contains 36 atoms.

Considering the complexity of the problem and the fact that we have not carried out a detailed post-processing of the data, including runs at specific compositions and further relaxations, we conclude that our prediction is in relatively good agreement with experiments. In total, we identified six ternary compounds that belong to the convex hull: Na_4IrO_4, Na_6IrO_6, Na_3IrO_4, Na_5IrO_7, Na_2IrO_4 and $NaIr_2O_6$. The work is in progress and more accurate relaxations and check of the dynamical stability of each structure should be done.

However, we can briefly describe the structure of the best candidates at these compositions:

- Na_6IrO_6 consists of unconnected IrO_6 octahedra intercalated in Na surrounding (IrO_6 can be imagined as periodically arranged impurities of a triclinic Na crystal);
- in Na_3IrO_4 the edge-shared IrO_6 octahedra form columns, forming a quasi-1D structure;
- Na_5IrO_7 structure is similar to the Na_6IrO_6 one, but it contains additional oxygens, which are bonded to 5 neighboring Na atoms. We have doubts about the stability of this structure and it is likely that this is a case of false positive prediction;
- Na_2IrO_4 consists of columns of edge-shared IrO_6 octahedra;
- $NaIr_2O_6$ contains layers of Ir atoms arranged in a honeycomb lattice with distorted IrO_6 octahedra.

It is important to have an automated way to estimate the dimensionality of the Ir network in a given structure in order to have a first insight into the properties of a given ternary phase. We used a simple algorithm to do this: first the set of the second nearest Ir-Ir neighbors is estimated. This set gives a set of vectors with the origin on the central Ir site and the end on each of the second nearest Ir-Ir neighbors. The dimensionality of the Ir network is then estimated as the number of linearly independent vectors from this set.

The result of the application of this algorithm[1] to the best structures for each composition is presented in Fig. 5.3.

Dots mark quasi-1D structures, squares mark layered Ir-Ir arrangement and triangles mark 3D Ir-Ir arrangement. We see that all the possible Ir arrangements are present in the region where

[1] The Ir network is not a well-defined concept for the compositions that contain less than 10% of Ir atoms, since Ir atoms are situated far apart from each other in this case. Our algorithm uses a fixed radius cut off to determine the nearest neighbors of a given site (4 Å), which is however too small for the structures at compositions with concentration of Ir atoms less than 10%.

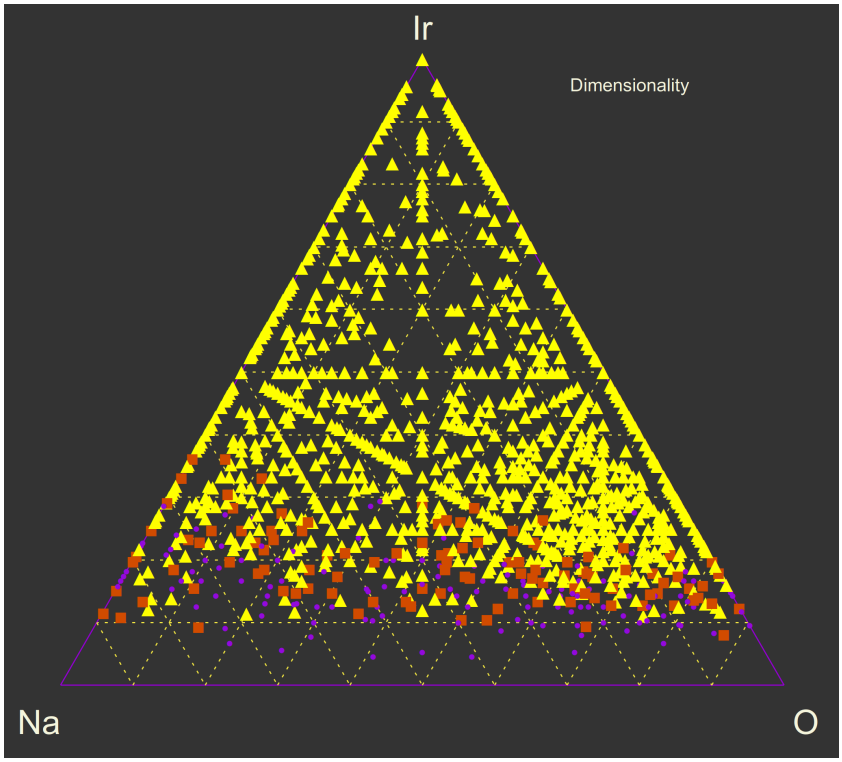

Figure 5.3.: Dimensionality of the Ir network for the best structure at each $Na_xIr_yO_{1-x-y}$. Triangles — 3D Ir network, squares — 2D Ir network, dot — semi-1D Ir network (containing Ir chains).

the structures with the lowest formation enthalpies are situated (pink/dark blue circles in Fig. 5.2 clustering in the middle bottom part of the ternary diagram).

Although the search over the full ternary phase diagram of $Na_xIr_yO_{1-x-y}$ is a very complicated problem, our preliminary results give a first, important insight into the possible compositions to study in more detail. We hope that a further post-processing of the obtained data will allow us to identify a few new structures that could be discovered experimentally.

5.2. *Ab initio* prediction of a new triangular Kitaev system: IrO_2

5.2.1. Motivation

The initial motivation for this study was to perform a search for possible novel binary phases with Ir_xO_{1-x} chemical compositions to characterize the edges of the ternary phase diagram in

Fig. 5.2; during this search, 2D phases of IrO_2 started to emerge. So far, for IrO_2 only two bulk phases are known: rutile [260] and spinel [261].

A novel phase of IrO_2 should have rich physics due to the interplay between strong spin-orbit interaction, electronic correlations and crystal field splitting. Being interested in this discovery, we decided to investigate these 2D IrO_2 phases further. In particular, we identified a particular phase, belonging to the 1T polytype, which may be a practical realization of a triangular Kitaev magnet.

A current hot topic in condensed matter physics research is the investigation of a *quantum spin liquid* [265] (QSL) state (disordered magnetic state). QSL has possible applications in memory devices, quantum computers and can be used to describe the high T_c superconductivity [138]. One of the specific models, that hosts QSL as a ground state, is the Kitaev model [17] (see the discussion in Secs. 1.3 and 1.4). The basic ingredient for a practical realization of the Kitaev model in a material is the presence of Kitaev exchange interaction, i.e. bond-directional spin-spin interactions, which are anisotropic between bonds and also depend on the orientation of a bond. Recently, a mechanism to "engineer" Kitaev exchange interactions in real materials was proposed by Jackeli and Khaliullin [19] (see Sec. 1.3.1 for a detailed description): Kitaev interaction can emerge in 4d or 5d transition metal (TM) oxides with strong spin orbit coupling, in which a TM ion is incarcerated within edge-shared oxygen octahedra, forming 90° TM-O-TM bonds. These requirements are realized in the proposed 2D phase of IrO_2, making it a prominent candidate for a novel Kitaev material.

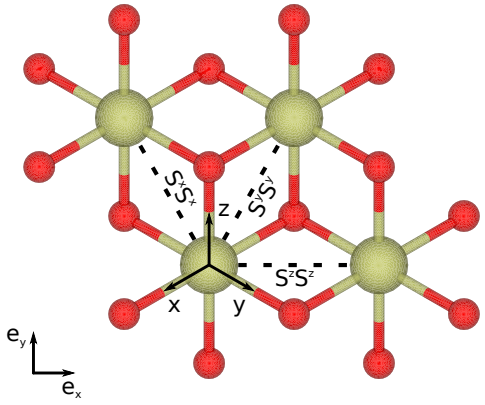

Figure 5.4.: 1T-IrO_2 polytype crystal structure: dark-gray (red) are oxygen atoms, light-gray (green) are iridium atoms. Three flavors of oxygen-assisted Ir-Ir bonds are indicated by dashed lines; the $\{\mathbf{x}, \mathbf{y}, \mathbf{z}\}$ axes label coordinate system in the local octahedral framework, the $\{\mathbf{e_x}, \mathbf{e_y}\}$ axes label the global coordinate system, $\mathbf{e_z}$ is perpendicular to the thesis plane.

Table 5.1.: Energies of various 2D IrO_2 structures (nonmagnetic calculations including SOC).

Name	**Energy/Atom (meV)**	**Energy/f.u. (meV)**
Rutile	0	0
1T	237	710
Rutile (001)	326	979
Rutile (110)	385	1154
1H	621	1867

5.2.2. Structural properties

In order to find the most favorable 2D-phase of IrO_2 we used the evolutionary crystal structure prediction method for 2D-crystals, as implemented in the `USPEX` [42–44] package, and also checked possible cuts of rutile structure (001 and 110). As a result, the most energetically favorable 2D structure is the 1T polytype [266] (see Table 5.1 for energy values of investigated structures).

This structure exhibits a triangular arrangement of iridium atoms, with oxygens in the middle of the triangles, forming two oppositely directed triangles above and below Ir plane as illustrated in Fig. 5.4. The structure exhibits the $P\bar{3}2/m1$ space group symmetry with the following unit cell parameters: $a = b = 3.16$ Å, $c = 12.30$ Å, $\alpha = \beta = 90°$, $\gamma = 120°$. The Ir atom is situated at Wyckoff position (a) (0,0,0) and two O atoms are situated at Wyckoff position (d) ($\frac{1}{3}$ $\frac{2}{3}$ 0.073). The oxygen environment of Ir atoms is formed by trigonally distorted (contracted) octahedra.

The proposed 2D phase of IrO_2 is very likely a van der Waals crystal, meaning that it should be possible to obtain a monolayer by exfoliation of the bulk layered phase. To prove that this is indeed true we performed a simple numerical experiment: the geometry of a fictitious bulk version of the 1T-structure was optimized allowing the cell volume to change in two separate calculations: with and without van der Waals interactions (employed by Tkatchenko-Scheffler method [267]). The results show a strong impact of the van der Waals interactions: the unit cell volume with the van der Waals interactions is 178.4 $Å^3$ (a=3.286 Å, c=19.079 Å) and without 249.97 $Å^3$ (a=3.158 Å, c=28.949 Å).

The next step was to check the dynamical stability of the structure calculating the phonon dispersion relations. For this task we performed calculations using a finite displacement method as implemented in `PHONOPY` package [231] using a 2x2x1 supercell. Under real conditions, i.e. including spin orbit coupling, strong correlations and magnetism, 1T-IrO_2 is dynamically stable.

5.2.3. Magnetic properties

In order to properly characterize our novel 2D IrO_2 phase, which has Ir^{4+} with one unpaired electron, we explored its magnetic phase diagram. Our calculations comparing different magnetic states find two semi-degenerate magnetic configurations, that are energetically favorable (the energy difference between the two is less than 1 meV/f.u.). These configurations are the *120°*

Neel configuration and the *inplane stripe* (shown in Fig. 5.5). The *120° Neel* configuration is a configuration where spins on the same Ir triangle are directed at a 120 degree angle with respect to each other and the *inplane stripe* configuration is formed by antiferromagnetically coupled rows of spins, pointing inplane. We notice that our calculations show an inplane anisotropy between different spin orientations with the most favorable direction perpendicular to the Ir-Ir bond, for which spins are pointing into the same direction: this is an indication of Kitaev interactions.

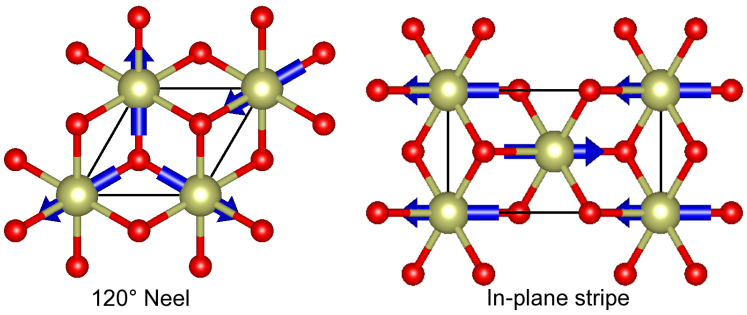

Figure 5.5.: Two lowest in energy semi-degenerate 1T-IrO_2 magnetic configurations. The arrows show directions of the spin magnetic moments on the Ir atoms.

5.2.4. Electronic structure

One of the key ingredients to realize a Kitaev material is 2D IrO_2 being insulating. Indeed, according to our calculations, the system is insulating in the two ground-state magnetic configurations: the bandgap for the *120° Neel* ordering is 0.42 eV and for the *inplane stripe* ordering is 0.24 eV.

The occurrence of an insulating state can be understood as follows. The Ir environment exhibits a D_{3d} point symmetry which means that the Ir d-bands are split into doubly degenerate e_g, single a_{1g} and doubly degenerate e_g' bands. When the electronic bands are projected onto the orbitals defined in the octahedral coordinate system as shown in Fig. 5.4, then a_{1g} and e_g' bands are formed by linear combinations of t_{2g} bands. Ir^{4+} has 5 electrons and thus the a_{1g} band is half-occupied and hence is prone to undergo an insulator-to-metal transition due to strong electronic correlations. A clearer picture of the transition can be obtained, inspecting the band structure plots in Fig. 5.6. Character bands projected on t_{2g} and e_g manifold with axes taken in octahedral coordinate system are plotted in the top left panel of Fig. 5.6. When SOC is included in the calculations, several band degeneracies are lifted as depicted in the top right panel of the figure (keeping projections onto t_{2g} and e_g manifold). A single half-filled band, which is now the only one crossing the Fermi level, is formed with a bandwidth of 0.95 eV. The spin degeneracy is lifted by the magnetic interactions and the splitting of the band is easily increased by increasing U, opening a gap as shown in the bottom panel of Fig. 5.6.

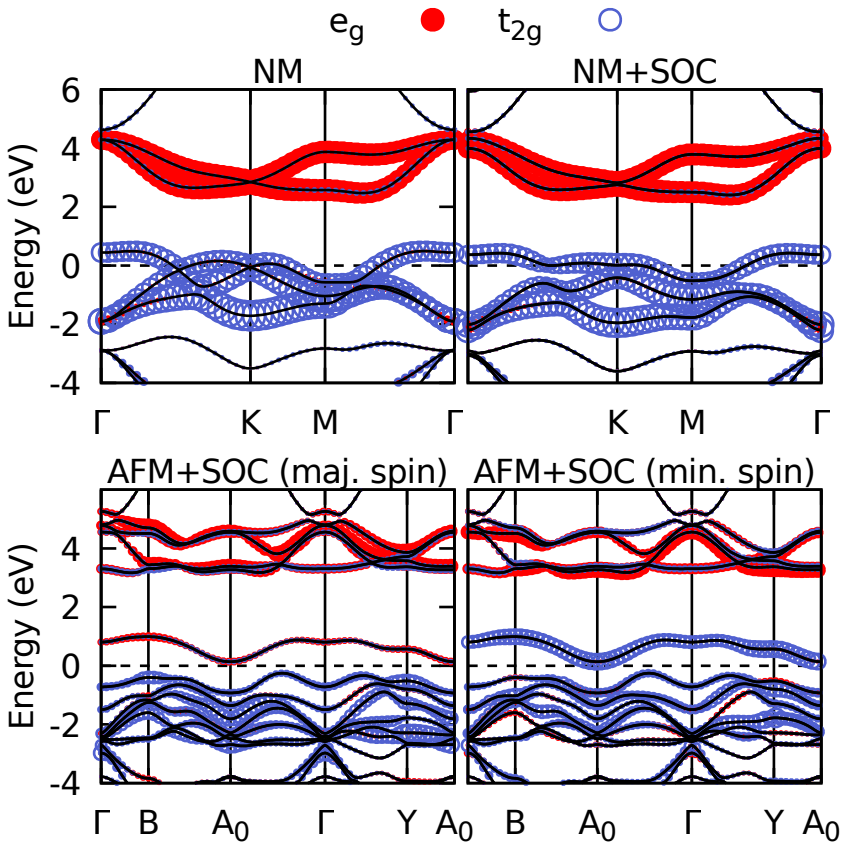

Figure 5.6.: Bandstructure of 1T-IrO_2 with projections on t_{2g}/e_g states for: nonmagnetic IrO_2 (top left panel), nonmagnetic IrO_2 with account of spin-orbit coupling (top right panel), stripe AFM configuration with SOC and U=2.7 eV (bottom left panel corresponding to the projection on up-spin and bottom right panel on down-spin).

5.2.5. Are there Kitaev Interactions?

To motivate the existence of a Kitaev exchange mechanism in 2D IrO_2 we need to inspect its local geometry and electronic structure more closely. As shown in Fig. 5.4, in this system Ir atoms are surrounded by an octahedral oxygen environment, in which neighboring octahedra share the edge, giving rise to an oxygen-assisted superexchange interaction between the Ir atoms with a "90 degrees"-type Ir-O-Ir bond, which is the first important ingredient for the realization of a Kitaev exchange interaction [19]. Due to the trigonal distortion of the octahedra, our structure does not match the ideal case and the Ir-O-Ir bond angle is ∼102 degrees instead of 90 degrees. This means that there will be a contribution from the direct overlap of *d*-orbitals, that can give rise to anisotropic interactions between spins.

Kitaev interaction tend to align the neighboring spins parallel to each other and perpendicular to

the Ir-O-Ir plaquette, formed by two neighboring Ir atoms and by the corresponding connecting oxygens. In general, there are three different bonds, which can be labeled according to the spatial orientation of the p-orbital of the connecting oxygens: X-bond, Y-bond and Z-bond (see Fig 5.4). Each of these bonds favors the corresponding spin interaction.

The interaction between the Ir-Ir γ-bond ($\gamma = \{X, Y, Z\}$) can be described by a model Hamiltonian [268] (similar to eq. (1.58) introduced in Sec. 1.3.2, but with one extra term, Γ'):

$$\begin{aligned} H_{ij|\gamma} =& J\vec{S}_i\vec{S}_j + KS_i^\gamma S_j^\gamma + \Gamma\left(S_i^\alpha S_j^\beta + S_i^\beta S_j^\alpha\right) + \\ & \Gamma'\left(S_i^\gamma S_j^\alpha + S_i^\alpha S_j^\gamma + S_i^\gamma S_j^\beta + S_i^\beta S_j^\gamma\right) \end{aligned} \tag{5.1}$$

where J is the Heisenberg interaction parameter, K is the Kitaev interaction parameter, the Γ term describes the further anisotropy among the diagonal components of the interaction, and the Γ' term determines the only symmetry-allowed nondiagonal element in the exchange interaction tensor. The value of the parameter Γ' is controlled by the trigonal field; the trigonal field also suppresses the parameter K [268].

We estimated the parameter J using the following equation:

$$E_{FM}(\hat{z}) - E_{Stripe}(\hat{z}) = 8J, \tag{5.2}$$

where $\hat{z}$ is direction toward local octahedral z-axis (see Fig. 5.4). The estimate gives $J = 4.7$ meV. However, the estimation of the parameters K, Γ and Γ' is still in progress.

5.3. Computational Details

We employed the variable-composition evolutionary search as implemented in `USPEX` package for the calculation of the ternary diagram. The geometry optimization was carried in four steps. In the final step the energy cutoff value was set to 350 eV, Methfessel-Paxton smearing scheme with σ=0.2 eV and Γ-centered Monkhorst-Pack grid [242, 243] with the reciprocal-space resolution 0.09 $2\pi\text{Å}^{-1}$ was used.

To calculate the total energies and perform structural optimization we used density functional theory (DFT) in the generalized gradient approximation (GGA) with Perdew-Burke-Ernzerhof functional[244, 245] as implemented in the `VASP` package [236–239] using projector augmented wave method (PAW) pseudopotentials [240, 241].

For the crystal structure prediction of 2D IrO_2 we used evolutionary structure prediction method as implemented in `USPEX` employing four-step structural relaxation using `VASP`. For the post-processing of the results from the evolutionary search and calculation of properties the energy cutoff was set to 600 eV and Γ-centered Monkhorst-Pack grid [242, 243] with the reciprocal-space resolution of 0.023 $2\pi\text{Å}^{-1}$ was used. The phonon dispersion was obtained using `PHONOPY`

package [231] using 2x2x1 supercell with total energy calculations made by `VASP`.

To get a correct description of the electronic structure we consider electronic correlations using GGA+U method with the value of U=2 eV as a reasonable estimate, since the exact value in this system is unknown. This choice was justified by the fact that U in other iridates is usually taken in the region 1.5-2.4 eV [269–271] and our calculations show no qualitative changes in the physics of 1T-IrO_2 for $1.3 < U < 4.0$ eV.

The band structure calculation was held by `Wien2k` [272], but the value of U was set to 2.7 eV (0.2 Ry) since the higher U is needed to open the gap when calculations are employed by `Wien2k` due to the difference between implementations (value of U is not transferable between `VASP` and `Wienk2` software). The 16x16x1 k-mesh was used defined on a special point grid [273].

6. Conclusions

The aim of this thesis is to describe the results of the *ab initio* investigation of several compounds that belong to two different oxide families: bismuthates and iridates.

The general thread that unifies the research highlighted in this thesis is the idea of combining state-of-the-art methods for crystal structure prediction with post-DFT (hybrid) approaches to study electronic structure. This approach is novel, because it combines two classes of methods which are intrinsically complicated: crystal structure prediction in fact requires sampling a large phase space, where several structures have comparable energetics; on the other hand, bismuthates and iridates are particularly sensitive systems, since the description of their physical properties require methods beyond the standard LDA and GGA semilocal functionals. Each of the four specific examples discussed in the thesis demonstrates the power of our approach.

In the first part of **Chapter 4** (Ref. [1]), we studied the high pressure phase diagram of $BaBiO_3$. The original motivation was to explore the possibility of suppressing CDW and inducing superconductivity using high pressures. To do this, we constructed the phase diagram using both the group-theoretical structure prediction method by employing *isotropy* subgroups theory and evolutionary algorithms. These two approaches were used to predict the possible high-pressure crystal structures, since no experimental data on crystal structures at high pressures are available. The first method was not able to find the best structures at high pressure, since the structures predicted by evolutionary algorithms were considerably lower in enthalpies for P>30 GPa. The reason of the failure of the group-subgroup analysis is the occurrence of a transition from the low-pressure perovskite to a high-pressure highly distorted structure, which have a very low symmetry and cannot be described by simple distortions of the perovskite structure. To our knowledge, it is the first time that it was demonstrated that the widely popular group-subgroup analysis fails for compounds that crystallize in perovskite structures. Our analysis shows that $BaBiO_3$ remains insulating up to 100 GPa and the charge disproportionation is robust and cannot be suppressed by pressure. These findings were confirmed by a joint theoretical and experimental work [6], where the resistivity of $BaBiO_3$ sample was measured up to 80 GPa and it was experimentally confirmed that $BaBiO_3$ remains insulating in this pressure region.

This work was generalized to study $SrBiO_3$ and $CaBiO_3$ compounds in a later publication [2]. Similarly to what was observed in $BaBiO_3$, we found that the charge disproportionation is robust and not suppressed by pressure for all $ABiO_3$ compounds (A=Ba, Sr, Ca). All compounds remain insulating up to 100 GPa and the tendency to charge disproportion becomes stronger with increasing pressure. Charge disproportionation also has a big influence on the crystal

structure. In addition to showing that the occurrence of distorted structure is a general trend of alkaline-earth bismuthates, we also tried to find a physical explanation for this phenomenon. First we showed that distorted structures are favored by a steric argument: they have a higher density than any variant of the perovskite structure, that permits to reduce the pV contribution to the enthalpy which is dominant at high pressures. In the distorted structures the coordination number is increased that gives rise to a more efficient packing. Taking into account the tendency to charge disproportionation, it is not possible to form any highly-symmetric structure under these circumstances. Our prediction for the occurrence of distorted structures in $BaBiO_3$ was confirmed by experiment [6], but so far there are no confirmations in other alkaline-earth bismuthates; we are in contact with experimental groups that are able to perform such experiments and would likely confirm our predictions.

In **Chapter 5** we have shown some preliminary results of our ongoing research on novel iridates. The first part describes a preliminary calculation of the ternary phase diagram for the ternary $Na_xIr_yO_{1-x-y}$ compound. A few exotic phases have been already discovered by experiments and the broad search of the possible new compositions could lead to interesting results. For this we have used an evolutionary algorithm extended to be able to perform a variable-composition structural search.

In our preliminary search we can access only three compounds that were determined in experiments due to the restriction on the unit cell size. Among them, Na_4IrO_4 is found to belong to the convex hull and our calculations reproduce the experimental crystal structure, while $NaIrO_3$ and Na_2IrO_3 stoichiometries are more problematic. However, since the results are very preliminary, it is possible that these discrepancies may be improved using tighter convergence criteria or further relaxations at specific compositions. We are confident that, in the next future, the refinement of our preliminary results will allow us to identify new exciting ternary Na-Ir-O compounds.

During the refinement of the binary Ir_xO_{1-x} phase diagram, we discovered a group of metastable layered IrO_2 structures. Up to now, IrO_2 is known only in two bulk phases, and a new 2D IrO_2 phase would be a quite interesting platform for novel 2D physics. Thus, we decided to examine this metastable phase further, computing its electronic structure in more detail. Employing the structural search for possible 2D phases, we find that the lowest structure for this composition is the 1T-polytype. The fact that two neighboring octahedra in this structure share its edge rises a possibility of Kitaev interactions to be realized in this system. We are currently performing calculations to estimate the strength of the different magnetic interactions. This information is needed to find out how promising the 2D IrO_2 is as a candidate of Kitaev materials.

Bibliography

1. A. Smolyanyuk, L. Boeri, and C. Franchini. "Ab initio prediction of the high-pressure phase diagram of $BaBiO_3$". *Phys. Rev. B* **96,** 035103 (2017). → pp. v, vii, 5, 9, 87, 102, 103, 105, 106, 109, 110, 127.
2. A. Smolyanyuk, C. Franchini, and L. Boeri. "Ab initio study of $ABiO_3$ (A = Ba, Sr, Ca) under high pressure". *Phys. Rev. B* **98,** 115158 (2018). → pp. v, vii, 5, 9, 87, 127.
3. R. J. Cava, B. Batlogg, J. J. Krajewski, R. Farrow, L. W. Rupp, A. E. White, K. Short, W. F. Peck, and T. Kometani. "Superconductivity near 30 K without copper: the $Ba_{0.6}K_{0.4}BiO_3$ perovskite". *Nature* **332,** 814 (1988). → pp. v, vii, 5, 7, 8, 45, 49, 88, 89, 101.
4. S. M. Kazakov, C. Chaillout, P. Bordet, J. J. Capponi, M. Nunez-Regueiro, A. Rysak, J. L. Tholence, P. G. Radaelli, S. N. Putilin, and E. V. Antipov. "Discovery of a second family of bismuth-oxide-based superconductors". *Nature* **390,** 148 (1997). → pp. v, vii, 45, 101, 104.
5. N. Khasanova, K. Yoshida, A. Yamamoto, and S. Tajima. "Extended range of superconducting bismuthates $K_{1-x}A_xBiO_3$ (A=La, Bi, and Ca)". *Physica C: Superconductivity* **356,** 12 (2001). → pp. v, vii, 45, 101, 106.
6. R. Martoňák, D. Ceresoli, T. Kagayama, Y. Matsuda, Y. Yamada, and E. Tosatti. "High-pressure phase diagram, structural transitions, and persistent nonmetallicity of $BaBiO_3$: Theory and experiment". *Phys. Rev. Materials* **1,** 023601 (2017). → pp. v, viii, 10, 52, 100, 102, 105, 127, 128.
7. J. Maddox. "Crystals from first principles". *Nature* **335,** 201 (1988). → p. 3.
8. *Modern methods of crystal structure prediction* (ed A. R. Oganov) (Wiley VCH, Weinheim, 2011). → p. 4.
9. S. M. Woodley and R. Catlow. "Crystal structure prediction from first principles". *Nature Materials* **7,** 937 (2008). → p. 4.
10. A. Sleight, J. Gillson, and P. Bierstedt. "High-temperature superconductivity in the $BaPb_{1-x}Bi_xO_3$ systems". *Solid State Communications* **17,** 27 (1975). → pp. 5, 7, 48, 107.
11. D. Cox and A. Sleight. "Crystal structure of $Ba_2Bi^{3+}Bi^{5+}O_6$". *Solid State Communications* **19,** 969 (1976). → pp. 5, 7, 48, 88, 91, 94, 104.
12. D. E. Cox and A. W. Sleight. "Mixed-valent $Ba_2Bi^{3+}Bi^{5+}O_6$: structure and properties vs temperature". *Acta Crystallographica Section B* **35,** 1 (1979). → p. 5.
13. L. Pauling. "The Principles Determining The Structure of Complex Ionic Crystals". *Journal of the American Chemical Society* **51,** 1010 (1929). → p. 6.

14. "Electron correlations in narrow energy bands". *Proceedings of the Royal Society of London A: Mathematical, Physical and Engineering Sciences* **276,** 238 (1963). → pp. 7, 25.
15. L. D. Landau and E. M. Lifshits. *Quantum mechanics: non-relativistic theory* (Butterworth-Heinemann, Amsterdam; London, 2004). → pp. 7, 30.
16. B. J. Kim, H. Jin, S. J. Moon, J.-Y. Kim, B.-G. Park, C. S. Leem, J. Yu, T. W. Noh, C. Kim, S.-J. Oh, J.-H. Park, V. Durairaj, G. Cao, and E. Rotenberg. "Novel $J_{\text{eff}} = 1/2$ Mott State Induced by Relativistic Spin-Orbit Coupling in Sr_2IrO_4". *Phys. Rev. Lett.* **101,** 076402 (2008). → pp. 7, 8, 53–55.
17. A. Kitaev. "Anyons in an exactly solved model and beyond". *Annals of Physics* **321.** January Special Issue, 2 (2006). → pp. 7, 37, 38, 57, 120.
18. G. Khaliullin. "Orbital Order and Fluctuations in Mott Insulators". *Progress of Theoretical Physics Supplement* **160,** 155 (2005). → pp. 7, 38, 39.
19. G. Jackeli and G. Khaliullin. "Mott Insulators in the Strong Spin-Orbit Coupling Limit: From Heisenberg to a Quantum Compass and Kitaev Models". *Phys. Rev. Lett.* **102,** 017205 (2009). → pp. 7, 38–40, 55, 57, 120, 123.
20. R. Scholder, K.-W. Ganter, H. Gläser, and G. Merz. "Über Alkali- und Erdalkalioxobismutate(V)". *Zeitschrift für anorganische und allgemeine Chemie* **319,** 375 (1963). → pp. 7, 45, 91.
21. J. Nagamatsu, N. Nakagawa, T. Muranaka, Y. Zenitani, and J. Akimitsu. "Superconductivity at 39 K in magnesium diboride". *Nature* **410,** 63 (2001). → p. 8.
22. J. G. Bednorz and K. A. Müller. "Possible highTc superconductivity in the Ba–La–Cu–O system". *Zeitschrift für Physik B Condensed Matter* **64,** 189 (1986). → p. 8.
23. R. O. Jones and O. Gunnarsson. "The density functional formalism, its applications and prospects". *Rev. Mod. Phys.* **61,** 689 (1989). → pp. 8, 48, 51.
24. A. I. Liechtenstein, V. I. Anisimov, and J. Zaanen. "Density-functional theory and strong interactions: Orbital ordering in Mott-Hubbard insulators". *Phys. Rev. B* **52,** R5467 (1995). → pp. 8, 48, 51.
25. C. Franchini, G. Kresse, and R. Podloucky. "Polaronic Hole Trapping in Doped $BaBiO_3$". *Phys. Rev. Lett.* **102,** 256402 (2009). → pp. 8, 47–51, 61.
26. J. Heyd, G. E. Scuseria, and M. Ernzerhof. "Hybrid functionals based on a screened Coulomb potential". *The Journal of Chemical Physics* **118,** 8207 (2003). → pp. 8, 9, 61, 69, 90, 103.
27. V. Meregalli and S. Y. Savrasov. "Electron-phonon coupling and properties of doped $BaBiO_3$". *Phys. Rev. B* **57,** 14453 (1998). → pp. 8, 51, 89.
28. A. I. Liechtenstein, I. I. Mazin, C. O. Rodriguez, O. Jepsen, O. K. Andersen, and M. Methfessel. "Structural phase diagram and electron-phonon interaction in $Ba_{1-x}K_xBiO_3$". *Phys. Rev. B* **44,** 5388 (1991). → pp. 8, 48, 51.
29. T. Bazhirov, S. Coh, S. G. Louie, and M. L. Cohen. "Importance of oxygen octahedra tilts for the electron-phonon coupling in K-doped $BaBiO_3$". *Phys. Rev. B* **88,** 224509 (2013). → pp. 8, 51.

30. P. W. Anderson. "Model for the Electronic Structure of Amorphous Semiconductors". *Phys. Rev. Lett.* **34,** 953 (1975). → pp. 8, 52.
31. T. M. Rice and L. Sneddon. "Real-Space and $\vec{k}$-Space Electron Pairing in $BaPb_{1-x}Bi_xO_3$". *Phys. Rev. Lett.* **47,** 689 (1981). → pp. 8, 52.
32. M. Bremholm, S. Dutton, P. Stephens, and R. Cava. "NaIrO3 — A pentavalent post-perovskite". *Journal of Solid State Chemistry* **184,** 601 (2011). → pp. 8, 56, 115.
33. D. C. Wallace and T. M. McQueen. "New honeycomb iridium(V) oxides: $NaIrO_3$ and $Sr_3CaIr_2O_9$". *Dalton Trans.* **44,** 20344 (2015). → pp. 8, 57, 115.
34. G. Cao and P. Schlottmann. "The challenge of spin–orbit-tuned ground states in iridates: a key issues review". *Reports on Progress in Physics* **81,** 042502 (2018). → p. 8.
35. `CHEMENV` is a module inside `PYMATGEN` package and is developed by David Waroquiers and Geoffroy Hautier. Website: `http://pymatgen.org/`. → pp. 9, 71, 96, 99, 114.
36. S. P. Ong, W. D. Richards, A. Jain, G. Hautier, M. Kocher, S. Cholia, D. Gunter, V. L. Chevrier, K. A. Persson, and G. Ceder. "Python Materials Genomics (pymatgen): A robust, open-source python library for materials analysis". *Computational Materials Science* **68,** 314 (2013). → pp. 9, 71, 96, 99, 114.
37. F. Aurenhammer, R. Klein, and D.-T. Lee. *Voronoi Diagrams and Delaunay Triangulations.* eprint: `https://www.worldscientific.com/doi/pdf/10.1142/8685` (WORLD SCIENTIFIC, 2013). → pp. 9, 71.
38. M. Pinsky and D. Avnir. "Continuous Symmetry Measures. 5. The Classical Polyhedra". *Inorganic Chemistry* **37,** 5575 (1998). → pp. 9, 71.
39. H. T. Stokes and D. M. Hatch. *Introduction to Isotropy Subgroups and Displacive Phase Transitions.* 2006. → pp. 9, 73, 90.
40. C. J. Howard and H. T. Stokes. "Group-Theoretical Analysis of Octahedral Tilting in Perovskites". *Acta Crystallographica Section B* **54,** 782 (1998). → pp. 9, 73.
41. C. J. Howard and H. T. Stokes. "Structures and phase transitions in perovskites – a group-theoretical approach". *Acta Crystallographica Section A* **61,** 93 (2005). → pp. 9, 73.
42. A. R. Oganov and C. W. Glass. "Crystal structure prediction using ab initio evolutionary techniques: Principles and applications". *The Journal of Chemical Physics* **124** (2006). → pp. 9, 77, 78, 90, 99, 102, 113, 115, 121.
43. A. O. Lyakhov, A. R. Oganov, H. T. Stokes, and Q. Zhu. "New developments in evolutionary structure prediction algorithm USPEX". *Computer Physics Communications* **184,** 1172 (2013). → pp. 9, 77, 113, 115, 121.
44. A. R. Oganov, A. O. Lyakhov, and M. Valle. "How Evolutionary Crystal Structure Prediction Works—and Why". *Accounts of Chemical Research* **44,** 227 (2011). → pp. 9, 77, 113, 115, 121.
45. S. M. Winter, A. A. Tsirlin, M. Daghofer, J. van den Brink, Y. Singh, P. Gegenwart, and R. Valentí. "Models and materials for generalized Kitaev magnetism". *Journal of Physics: Condensed Matter* **29,** 493002 (2017). → pp. 10, 58.

46. Y. Okamoto, M. Nohara, H. Aruga-Katori, and H. Takagi. "Spin-Liquid State in the S = 1/2 Hyperkagome Antiferromagnet $Na_4Ir_3O_8$". *Physical Review Letters* **99.** (2007). → pp. 10, 60, 115.
47. D. Khomskii. *Transition metal compounds* 1. publ. (Cambridge Univ. Press, Cambridge, 2014). → pp. 11, 12, 16, 19, 23, 34–36, 43.
48. R. D. Shannon. "Revised effective ionic radii and systematic studies of interatomic distances in halides and chalcogenides". *Acta Crystallographica Section A* **32,** 751 (1976). → p. 11.
49. F. Galasso, N. Kurti, and R. Smoluchowski. *Structure and Properties of Inorganic Solids: International Series of Monographs in Solid State Physics.* (Elsevier Science, 2016). → p. 15.
50. P. M. Woodward. "Octahedral Tilting in Perovskites. I. Geometrical Considerations". *Acta Crystallographica Section B* **53,** 32 (1997). → p. 14.
51. A. Okazaki, Y. Suemune, and T. Fuchikami. "The Crystal Structures of $KMnF_3$, $KFeF_3$, $KCoF_3$, $KNiF_3$ and $KCuF_3$". *Journal of the Physical Society of Japan* **14,** 1823 (1959). → p. 14.
52. V. M. Goldschmidt. "Die Gesetze der Krystallochemie". *Naturwissenschaften* **14,** 477 (1926). → p. 14.
53. A. M. Glazer. "Simple ways of determining perovskite structures". *Acta Crystallographica Section A* **31,** 756 (1975). → pp. 15, 94, 95, 104.
54. E. Pavarini. *Crystal-Field Theory, Tight-Binding Method, and Jahn-Teller Effect.* in *Correlated Electrons: From Models to Materials* (eds E. Pavarini, E. Koch, F. Anders, and M. Jarell) 21 (Forschungszentrum Jülich GmbH Institute for Advanced Simulation, 2012). → p. 21.
55. H. Bethe. "Zur Theorie der Metalle". *Zeitschrift für Physik* **71,** 205 (1931). → p. 25.
56. A. Georges, G. Kotliar, W. Krauth, and M. J. Rozenberg. "Dynamical mean-field theory of strongly correlated fermion systems and the limit of infinite dimensions". *Rev. Mod. Phys.* **68,** 13 (1996). → pp. 25–27.
57. "Electron correlations in narrow energy bands III. An improved solution". *Proceedings of the Royal Society of London A: Mathematical, Physical and Engineering Sciences* **281,** 401 (1964). → p. 25.
58. P. Fazekas. *Lecture Notes on Electron Correlation and Magnetism.* (World Scientific, 1999). → pp. 25, 26.
59. M. C. Gutzwiller. "Correlation of Electrons in a Narrow *s* Band". *Phys. Rev.* **137,** A1726 (1965). → p. 26.
60. W. F. Brinkman and T. M. Rice. "Application of Gutzwiller's Variational Method to the Metal-Insulator Transition". *Phys. Rev. B* **2,** 4302 (1970). → p. 26.
61. T. Pruschke, M. Jarrell, and J. Freericks. "Anomalous normal-state properties of high-T_c superconductors: intrinsic properties of strongly correlated electron systems?" *Advances in Physics* **44,** 187 (1995). → p. 26.

62. A. Georges. *Strongly Correlated Electron Materials: Dynamical Mean-Field Theory and Electronic Structure*. in *American Institute of Physics Conference Series* (eds A. Avella and F. Mancini) **715** (2004), 3. eprint: `cond-mat/0403123`. → p. 26.
63. K. Held. "Electronic structure calculations using dynamical mean field theory". *Advances in Physics* **56,** 829 (2007). → pp. 26, 27.
64. J. P. Lu. "Metal-insulator transitions in degenerate Hubbard models and A_xC_{60}". *Phys. Rev. B* **49,** 5687 (1994). → p. 27.
65. M. J. Rozenberg. "Integer-filling metal-insulator transitions in the degenerate Hubbard model". *Phys. Rev. B* **55,** R4855 (1997). → p. 27.
66. J. E. Han, M. Jarrell, and D. L. Cox. "Multiorbital Hubbard model in infinite dimensions: Quantum Monte Carlo calculation". *Phys. Rev. B* **58,** R4199 (1998). → p. 27.
67. A. Koga, Y. Imai, and N. Kawakami. "Stability of a metallic state in the two-orbital Hubbard model". *Phys. Rev. B* **66,** 165107 (2002). → p. 27.
68. T. Pruschke and R. Bulla. "Hund's coupling and the metal-insulator transition in the two-band Hubbard model". *The European Physical Journal B - Condensed Matter and Complex Systems* **44,** 217 (2005). → p. 27.
69. L. de'Medici. "Hund's coupling and its key role in tuning multiorbital correlations". *Phys. Rev. B* **83,** 205112 (2011). → pp. 27, 28.
70. L. de'Medici, J. Mravlje, and A. Georges. "Janus-Faced Influence of Hund's Rule Coupling in Strongly Correlated Materials". *Phys. Rev. Lett.* **107,** 256401 (2011). → pp. 27, 28.
71. Z. Y. Meng, Y. B. Kim, and H.-Y. Kee. "Odd-Parity Triplet Superconducting Phase in Multiorbital Materials with a Strong Spin-Orbit Coupling: Application to Doped Sr_2IrO_4". *Phys. Rev. Lett.* **113,** 177003 (2014). → p. 28.
72. G. Zhang, E. Gorelov, E. Sarvestani, and E. Pavarini. "Fermi Surface of Sr_2RuO_4: Spin-Orbit and Anisotropic Coulomb Interaction Effects". *Phys. Rev. Lett.* **116,** 106402 (2016). → p. 28.
73. M. Kim, J. Mravlje, M. Ferrero, O. Parcollet, and A. Georges. "Spin-Orbit Coupling and Electronic Correlations in Sr_2RuO_4". *Phys. Rev. Lett.* **120,** 126401 (2018). → p. 28.
74. R. Triebl, G. J. Kraberger, J. Mravlje, and M. Aichhorn. "Spin-orbit coupling and correlations in three-orbital systems". Version 1. arXiv: `http://arxiv.org/abs/1807.05106v1 [cond-mat.str-el]`. (13, 2018). → pp. 28–30.
75. L. de'Medici. "Hund's metals, explained". eprint: `arXiv:1707.03282` (2017). → p. 29.
76. S. V. Streltsov and D. I. Khomskii. "Orbital physics in transition metal compounds: new trends". *Physics-Uspekhi* **60,** 1121 (2017). → pp. 30, 35, 36.
77. S. Sugano. *Multiplets of Transition-Metal Ions in Crystals*. (Elsevier Science, 2012). → p. 35.
78. S. Trebst. "Kitaev Materials". Version 1. arXiv: `http://arxiv.org/abs/1701.07056v1 [cond-mat.str-el]`. (24, 2017). → pp. 36, 37, 40.
79. I. Kimchi and A. Vishwanath. "Kitaev-Heisenberg models for iridates on the triangular, hyperkagome, kagome, fcc, and pyrochlore lattices". *Phys. Rev. B* **89,** 014414 (2014). → pp. 41, 42.

80. H. T. Diep and H. Giacomini. in *Frustrated spin systems* (ed H. T. Diep) 2nd edition, 1 (World Scientific, [Hackensack] New Jersey, 2013). → p. 42.
81. J. T. Chalker. in *Introduction to Frustrated Magnetism* (eds C. Lacroix, P. Mendels, and F. Mila) chap. 1 (Springer Berlin Heidelberg, Berlin, Heidelberg, 2011). → p. 43.
82. A. P. Ramirez. "Strongly Geometrically Frustrated Magnets". *Annual Review of Materials Science* **24,** 453 (1994). → p. 43.
83. C. Lhuillier and G. Misguich. in *Introduction to Frustrated Magnetism* (eds C. Lacroix, P. Mendels, and F. Mila) chap. 2 (Springer Berlin Heidelberg, Berlin, Heidelberg, 2011). → p. 43.
84. C. M. Varma. "Missing valence states, diamagnetic insulators, and superconductors". *Phys. Rev. Lett.* **61,** 2713 (1988). → pp. 45, 52.
85. A. Walsh, G. W. Watson, D. J. Payne, R. G. Edgell, J. Guo, P.-A. Glans, T. Learmonth, and K. E. Smith. "Electronic structure of the α and δ phases of Bi_2O_3: A combined ab initio and x-ray spectroscopy study". *Phys. Rev. B* **73,** 235104 (2006). → p. 47.
86. C. Franchini, A. Sanna, M. Marsman, and G. Kresse. "Structural, vibrational, and quasiparticle properties of the Peierls semiconductor $BaBiO_3$: A hybrid functional and self-consistent GW + vertex-corrections study". *Phys. Rev. B* **81,** 085213 (2010). → pp. 47, 61.
87. S. Pei, J. D. Jorgensen, B. Dabrowski, D. G. Hinks, D. R. Richards, A. W. Mitchell, J. M. Newsam, S. K. Sinha, D. Vaknin, and A. J. Jacobson. "Structural phase diagram of the $Ba_{1-x}K_xBiO_3$ system". *Phys. Rev. B* **41,** 4126 (1990). → pp. 46, 47, 49.
88. K. Inumaru, H. Miyata, and S. Yamanaka. "Partial suppression of structural distortion in epitaxially grown $BaBiO_3$ thin films". *Phys. Rev. B* **78,** 132507 (2008). → p. 46.
89. G. Kim, M. Neumann, M. Kim, M. D. Le, T. D. Kang, and T. W. Noh. "Suppression of Three-Dimensional Charge Density Wave Ordering via Thickness Control". *Phys. Rev. Lett.* **115,** 226402 (2015). → p. 46.
90. B. Meir, S. Gorol, T. Kopp, and G. Hammerl. "Observation of two-dimensional superconductivity in bilayers of $BaBiO_3$ and $BaPbO_3$". *Phys. Rev. B* **96,** 100507 (2017). → p. 47.
91. L. F. Mattheiss and D. R. Hamann. "Electronic structure of $BaPb_{1-x}Bi_xO_3$". *Phys. Rev. B* **28,** 4227 (1983). → p. 48.
92. T. Thonhauser and K. M. Rabe. "Fcc breathing instability in $BaBiO_3$ from first principles". *Phys. Rev. B* **73,** 212106 (2006). → p. 48.
93. K. Kunc, R. Zeyher, A. Liechtenstein, M. Methfessel, and O. Andersen. "Ab-initio calculation of the charge and lattice modulation in $BaBiO_3$". *Solid State Communications* **80,** 325 (1991). → pp. 48, 89, 91, 107.
94. A. W. Sleight. "Bismuthates: $BaBiO_3$ and related superconducting phases". *Physica C: Superconductivity and its Applications* **514.** Superconducting Materials: Conventional, Unconventional and Undetermined, 152 (2015). → pp. 48, 88.

95. D. Korotin, V. Kukolev, A. V. Kozhevnikov, D. Novoselov, and V. I. Anisimov. "Electronic correlations and crystal structure distortions in $BaBiO_3$". *Journal of Physics: Condensed Matter* **24,** 415603 (2012). → p. 48.
96. K. Foyevtsova, A. Khazraie, I. Elfimov, and G. A. Sawatzky. "Hybridization effects and bond disproportionation in the bismuth perovskites". *Phys. Rev. B* **91,** 121114 (2015). → p. 49.
97. A. Khazraie, K. Foyevtsova, I. Elfimov, and G. A. Sawatzky. "Oxygen holes and hybridization in the bismuthates". *Phys. Rev. B* **97,** 075103 (2018). → p. 49.
98. T. Nishio, J. Ahmad, and H. Uwe. "Spectroscopic Observation of Bipolaronic Point Defects in $Ba_{1-x}K_xBiO_3$". *Phys. Rev. Lett.* **95,** 176403 (2005). → p. 49.
99. J. Ahmad and H. Uwe. "Small-polaron excitations in $Ba_{1-x}K_xBiO_3$ studied by optical reflectivity measurements". *Phys. Rev. B* **72,** 125103 (2005). → p. 49.
100. M. A. Karlow, S. L. Cooper, A. L. Kotz, M. V. Klein, P. D. Han, and D. A. Payne. "Optical conductivity of $Ba_{1-x}K_xBiO_3$ through the metal-semiconductor transition". *Phys. Rev. B* **48,** 6499 (1993). → p. 50.
101. I. B. Bischofs, V. N. Kostur, and P. B. Allen. "Polaron and bipolaron defects in a charge density wave: A model for lightly doped $BaBiO_3$". *Phys. Rev. B* **65,** 115112 (2002). → p. 49.
102. N. Tralshawala, J. F. Zasadzinski, L. Coffey, W. Gai, M. Romalis, Q. Huang, R. Vaglio, and K. E. Gray. "Tunneling, $\alpha^2F(\omega)$, and transport in superconductors: Nb, V, VN, $Ba_{1-x}K_xBiO_3$, and $Nd_{1.85}Ce_{0.15}CuO_4$". *Phys. Rev. B* **51,** 3812 (1995). → p. 51.
103. Q. Huang, J. F. Zasadzinski, N. Tralshawala, K. E. Gray, D. G. Hinks, J. L. Peng, and R. L. Greene. "Tunnelling evidence for predominantly electron-phonon coupling in superconducting $Ba_{1-x}K_xBiO_3$ and $Nd_{2-x}Ce_xCuO_{4-y}$". *Nature* **347,** 369 (1990). → p. 51.
104. R. Kuentzler, C. Hornick, Y. Dossman, S. Wegner, R. E. Farsi, and M. Drillon. "Superconductivity of Pb, K and Rb-doped $BaBiO_3$". *Physica C: Superconductivity* **184,** 316 (1991). → p. 51.
105. Z. P. Yin, A. Kutepov, and G. Kotliar. "Correlation-Enhanced Electron-Phonon Coupling: Applications of *GW* and Screened Hybrid Functional to Bismuthates, Chloronitrides, and Other High-T_c Superconductors". *Phys. Rev. X* **3,** 021011 (2013). → p. 51.
106. G. Vielsack and W. Weber. "Search for negative U in the $Ba_{1-x}K_xBi_{1-y}Pb_yO_3$ system using constrained density-functional theory". *Phys. Rev. B* **54,** 6614 (1996). → p. 52.
107. P. Prelovsek, T. Rice, F. Zhang, and A. Klostermann. in *Proceedings of the Yamada Conference XVIII on Superconductivity in Highly Correlated Fermion Systems* (eds M. Tachiki, Y. Muto, and S. Maekawa) 268 (Elsevier, 1987). → p. 52.
108. B. K. Chakraverty and J. Ranninger. "Bipolarons and superconductivity". *Philosophical Magazine B* **52,** 669 (1985). → p. 52.
109. J. He, M.-X. Chen, X.-Q. Chen, and C. Franchini. "Structural transitions and transport-half-metallic ferromagnetism in $LaMnO_3$ at elevated pressure". *Phys. Rev. B* **85,** 195135 (2012). → pp. 52, 108.

110. H. Sugiura and T. Yamadaya. "Compression curve of $BaBiO_3$". *Solid state communications* **49,** 499 (1984). → pp. 52, 92.
111. H. Sugiura and T. Yamadaya. "High pressure studies on the perovskite-type compound $BaBiO_3$". *Physica B+ C* **139,** 349 (1986). → pp. 52, 92.
112. G. A. Samara, T. Sakudo, and K. Yoshimitsu. "Important Generalization Concerning the Role of Competing Forces in Displacive Phase Transitions". *Phys. Rev. Lett.* **35,** 1767 (1975). → p. 52.
113. R. J. Angel, J. Zhao, and N. L. Ross. "General Rules for Predicting Phase Transitions in Perovskites due to Octahedral Tilting". *Phys. Rev. Lett.* **95,** 025503 (2005). → p. 52.
114. H. J. Xiang, M. Guennou, J. Íñiguez, J. Kreisel, and L. Bellaiche. "Rules and mechanisms governing octahedral tilts in perovskites under pressure". *Phys. Rev. B* **96,** 054102 (2017). → p. 52.
115. J. J. Randall, L. Katz, and R. Ward. "The Preparation of a Strontium-Iridium Oxide $Sr_2IrO_4^{1,2}$". *Journal of the American Chemical Society* **79,** 266 (1957). → p. 53.
116. M. K. Crawford, M. A. Subramanian, R. L. Harlow, J. A. Fernandez-Baca, Z. R. Wang, and D. C. Johnston. "Structural and magnetic studies of Sr_2IrO_4". *Phys. Rev. B* **49,** 9198 (1994). → p. 53.
117. G. Cao, J. Bolivar, S. McCall, J. E. Crow, and R. P. Guertin. "Weak ferromagnetism, metal-to-nonmetal transition, and negative differential resistivity in single-crystal Sr_2IrO_4". *Phys. Rev. B* **57,** R11039 (1998). → p. 53.
118. H. Watanabe, T. Shirakawa, and S. Yunoki. "Microscopic Study of a Spin-Orbit-Induced Mott Insulator in Ir Oxides". *Phys. Rev. Lett.* **105,** 216410 (2010). → p. 54.
119. S. J. Moon, H. Jin, K. W. Kim, W. S. Choi, Y. S. Lee, J. Yu, G. Cao, A. Sumi, H. Funakubo, C. Bernhard, and T. W. Noh. "Dimensionality-Controlled Insulator-Metal Transition and Correlated Metallic State in 5*d* Transition Metal Oxides $Sr_{n+1}Ir_nO_{3n+1}$ ($n = 1$, 2, and ∞)". *Phys. Rev. Lett.* **101,** 226402 (2008). → p. 55.
120. S. Fujiyama, K. Ohashi, H. Ohsumi, K. Sugimoto, T. Takayama, T. Komesu, M. Takata, T. Arima, and H. Takagi. "Weak antiferromagnetism of $J_{\text{eff}} = \frac{1}{2}$ band in bilayer iridate $Sr_3Ir_2O_7$". *Phys. Rev. B* **86,** 174414 (2012). → p. 55.
121. G. Cao, V. Durairaj, S. Chikara, L. E. DeLong, S. Parkin, and P. Schlottmann. "Non-Fermi-liquid behavior in nearly ferromagnetic $SrIrO_3$ single crystals". *Phys. Rev. B* **76,** 100402 (2007). → p. 55.
122. H. Zhang, K. Haule, and D. Vanderbilt. "Effective J=1/2 Insulating State in Ruddlesden-Popper Iridates: An LDA+DMFT Study". *Phys. Rev. Lett.* **111,** 246402 (2013). → p. 55.
123. B. Kim, P. Liu, and C. Franchini. "Dimensionality-strain phase diagram of strontium iridates". *Phys. Rev. B* **95,** 115111 (2017). → p. 55.
124. K. Ohgushi, H. Gotou, T. Yagi, Y. Kiuchi, F. Sakai, and Y. Ueda. "Metal-insulator transition in $Ca_{1-x}Na_xIrO_3$ with post-perovskite structure". *Phys. Rev. B* **74,** 241104 (2006). → p. 55.

125. K. Ohgushi, J.-i. Yamaura, H. Ohsumi, K. Sugimoto, S. Takeshita, A. Tokuda, H. Takagi, M. Takata, and T.-h. Arima. "Resonant X-ray Diffraction Study of the Strongly Spin-Orbit-Coupled Mott Insulator $CaIrO_3$". *Phys. Rev. Lett.* **110,** 217212 (2013). → p. 55.
126. J. Gunasekera, L. Harriger, A. Dahal, T. Heitmann, G. Vignale, and D. K. Singh. "Magnetic fluctuations driven insulator-to-metal transition in $Ca(Ir_{1-x}Ru_x)O_3$". *Scientific Reports* **5,** 18047 (2015). → p. 55.
127. A. Subedi. "First-principles study of the electronic structure and magnetism of $CaIrO_3$". *Physical Review B* **85,** 020408 (2012). → p. 55.
128. N. A. Bogdanov, V. M. Katukuri, H. Stoll, J. van den Brink, and L. Hozoi. "Post-perovskite $CaIrO_3$: A $\mathbf{j = 1/2}$ quasi-one-dimensional antiferromagnet". *Phys. Rev. B* **85,** 235147 (2012). → p. 55.
129. S.-W. Kim, C. Liu, H.-J. Kim, J.-H. Lee, Y. Yao, K.-M. Ho, and J.-H. Cho. "Nature of the Insulating Ground State of the 5*d* Postperovskite $CaIrO_3$". *Physical Review Letters* **115,** 096401 (2015). → p. 55.
130. M. M. Sala, K. Ohgushi, A. Al-Zein, Y. Hirata, G. Monaco, and M. Krisch. "$CaIrO_3$: A Spin-Orbit Mott Insulator Beyond the $j_{\text{eff}} = 1/2$ Ground State". *Physical Review Letters* **112,** 176402 (2014). → p. 55.
131. S. Chikara, D. Haskel, J.-H. Sim, H.-S. Kim, C.-C. Chen, G. Fabbris, L. S. I. Veiga, N. M. Souza-Neto, J. Terzic, K. Butrouna, G. Cao, M. J. Han, and M. van Veenendaal. "$Sr_2Ir_{1-x}Rh_xO_4(x\ 0.5)$: An inhomogeneous $j_{\text{eff}} = \frac{1}{2}$ Hubbard system". *Physical Review B* **92,** 081114 (2015). → p. 56.
132. T. F. Qi, O. B. Korneta, L. Li, K. Butrouna, V. S. Cao, X. Wan, P. Schlottmann, R. K. Kaul, and G. Cao. "Spin-orbit tuned metal-insulator transitions in single-crystal $Sr_2Ir_{1-x}Rh_xO_4$ $(0 \leq x \leq 1)$". *Physical Review B* **86,** 125105 (2012). → p. 56.
133. P. Liu, M. Reticcioli, B. Kim, A. Continenza, G. Kresse, D. D. Sarma, X.-Q. Chen, and C. Franchini. "Electron and hole doping in the relativistic Mott insulator $\mathbf{Sr_2IrO_4}$: A first-principles study using band unfolding technique". *Phys. Rev. B* **94,** 195145 (2016). → p. 56.
134. S. Calder, J. W. Kim, G.-X. Cao, C. Cantoni, A. F. May, H. B. Cao, A. A. Aczel, M. Matsuda, Y. Choi, D. Haskel, B. C. Sales, D. Mandrus, M. D. Lumsden, and A. D. Christianson. "Evolution of competing magnetic order in the $J_{\text{eff}} = 1/2$ insulating state of $Sr_2Ir_{1-x}Ru_xO_4$". *Physical Review B* **92,** 165128 (2015). → p. 56.
135. T. Hogan, Z. Yamani, D. Walkup, X. Chen, R. Dally, T. Z. Ward, M. P. M. Dean, J. Hill, Z. Islam, V. Madhavan, and S. D. Wilson. "First-Order Melting of a Weak Spin-Orbit Mott Insulator into a Correlated Metal". *Physical Review Letters* **114,** 257203 (2015). → p. 56.
136. S. Bhowal, S. Baidya, I. Dasgupta, and T. Saha-Dasgupta. "Breakdown of $J = 0$ nonmagnetic state in d^4 iridate double perovskites: A first-principles study". *Phys. Rev. B* **92,** 121113 (2015). → p. 56.
137. L. Du, X. Sheng, H. Weng, and X. Dai. "The electronic structure of $NaIrO_3$, Mott insulator or band insulator?" *EPL (Europhysics Letters)* **101,** 27003 (2013). → p. 57.

138. P. W. Anderson. "The Resonating Valence Bond State in La_2CuO_4 and Superconductivity". *Science* **235,** 1196 (1987). → pp. 57, 120.
139. L. Balents. "Spin liquids in frustrated magnets". *Nature* **464,** 199 (2010). → p. 57.
140. R. Comin, G. Levy, B. Ludbrook, Z.-H. Zhu, C. N. Veenstra, J. A. Rosen, Y. Singh, P. Gegenwart, D. Stricker, J. N. Hancock, D. van der Marel, I. S. Elfimov, and A. Damascelli. "Na_2IrO_3 as a Novel Relativistic Mott Insulator with a 340-meV Gap". *Physical Review Letters* **109,** 266406 (2012). → p. 58.
141. S. C. Williams, R. D. Johnson, F. Freund, S. Choi, A. Jesche, I. Kimchi, S. Manni, A. Bombardi, P. Manuel, P. Gegenwart, and R. Coldea. "Incommensurate counterrotating magnetic order stabilized by Kitaev interactions in the layered honeycomb $\alpha-Li_2IrO_3$". *Phys. Rev. B* **93,** 195158 (2016). → p. 58.
142. G. Cao, T. F. Qi, L. Li, J. Terzic, V. S. Cao, S. J. Yuan, M. Tovar, G. Murthy, and R. K. Kaul. "Evolution of magnetism in the single-crystal honeycomb iridates $(Na_{1-x}Li_x)_2IrO_3$". *Phys. Rev. B* **88,** 220414 (2013). → p. 58.
143. M. Abramchuk, C. Ozsoy-Keskinbora, J. W. Krizan, K. R. Metz, D. C. Bell, and F. Tafti. "Cu_2IrO_3: A New Magnetically Frustrated Honeycomb Iridate". *Journal of the American Chemical Society* **139,** 15371 (2017). → p. 58.
144. J. Chaloupka, G. Jackeli, and G. Khaliullin. "Kitaev-Heisenberg Model on a Honeycomb Lattice: Possible Exotic Phases in Iridium Oxides A_2IrO_3". *Phys. Rev. Lett.* **105,** 027204 (2010). → p. 58.
145. J. Reuther, R. Thomale, and S. Trebst. "Finite-temperature phase diagram of the Heisenberg-Kitaev model". *Phys. Rev. B* **84,** 100406 (2011). → p. 58.
146. I. I. Mazin, H. O. Jeschke, K. Foyevtsova, R. Valentí, and D. I. Khomskii. "Na_2IrO_3 as a Molecular Orbital Crystal". *Phys. Rev. Lett.* **109,** 197201 (2012). → pp. 59, 60.
147. C. Martins, M. Aichhorn, and S. Biermann. "Coulomb correlations in 4d and 5d oxides from first principles—or how spin–orbit materials choose their effective orbital degeneracies". *Journal of Physics: Condensed Matter* **29,** 263001 (2017). → p. 58.
148. V. M. Katukuri, S. Nishimoto, V. Yushankhai, A. Stoyanova, H. Kandpal, S. Choi, R. Coldea, I. Rousochatzakis, L. Hozoi, and J. van den Brink. "Kitaev interactions between j = 1/2 moments in honeycomb Na_2IrO_3 are large and ferromagnetic: insights from ab initio quantum chemistry calculations". *New Journal of Physics* **16,** 013056 (2014). → pp. 58, 59.
149. S. Nishimoto, V. M. Katukuri, V. Yushankhai, H. Stoll, U. K. Rößler, L. Hozoi, I. Rousochatzakis, and J. van den Brink. "Strongly frustrated triangular spin lattice emerging from triplet dimer formation in honeycomb Li_2IrO_3". *Nature Communications* **7.** Article, 10273 (2016). → pp. 58, 59.
150. I. Kimchi and Y.-Z. You. "Kitaev-Heisenberg-J_2-J_3 model for the iridates A_2IrO_3". *Phys. Rev. B* **84,** 180407 (2011). → p. 58.
151. Y. Singh, S. Manni, J. Reuther, T. Berlijn, R. Thomale, W. Ku, S. Trebst, and P. Gegenwart. "Relevance of the Heisenberg-Kitaev Model for the Honeycomb Lattice Iridates A_2IrO_3". *Phys. Rev. Lett.* **108,** 127203 (2012). → p. 59.

152. S. K. Choi, R. Coldea, A. N. Kolmogorov, T. Lancaster, I. I. Mazin, S. J. Blundell, P. G. Radaelli, Y. Singh, P. Gegenwart, K. R. Choi, S.-W. Cheong, P. J. Baker, C. Stock, and J. Taylor. "Spin Waves and Revised Crystal Structure of Honeycomb Iridate Na_2IrO_3". *Phys. Rev. Lett.* **108,** 127204 (2012). → p. 59.
153. Y. Sizyuk, C. Price, P. Wölfle, and N. B. Perkins. "Importance of anisotropic exchange interactions in honeycomb iridates: Minimal model for zigzag antiferromagnetic order in Na_2IrO_3". *Phys. Rev. B* **90,** 155126 (2014). → p. 59.
154. I. Rousochatzakis, J. Reuther, R. Thomale, S. Rachel, and N. B. Perkins. "Phase Diagram and Quantum Order by Disorder in the Kitaev $K_1 - K_2$ Honeycomb Magnet". *Phys. Rev. X* **5,** 041035 (2015). → p. 59.
155. L. Janssen, E. C. Andrade, and M. Vojta. "Magnetization processes of zigzag states on the honeycomb lattice: Identifying spin models for $\alpha-RuCl_3$ and Na_2IrO_3". *Phys. Rev. B* **96,** 064430 (2017). → p. 60.
156. K. Foyevtsova, H. O. Jeschke, I. I. Mazin, D. I. Khomskii, and R. Valentí. "Ab initio analysis of the tight-binding parameters and magnetic interactions in Na_2IrO_3". *Phys. Rev. B* **88,** 035107 (2013). → p. 60.
157. J. P. Clancy, H. Gretarsson, J. A. Sears, Y. Singh, S. Desgreniers, K. Mehlawat, S. Layek, G. K. Rozenberg, Y. Ding, M. H. Upton, D. Casa, N. Chen, J. Im, Y. Lee, R. Yadav, L. Hozoi, D. Efremov, J. van den Brink, and Y.-J. Kim. "Pressure-driven collapse of the relativistic electronic ground state in a honeycomb iridate". *npj Quantum Materials* **3,** 35 (2018). → p. 60.
158. T. Takayama, A. Kato, R. Dinnebier, J. Nuss, H. Kono, L. S. I. Veiga, G. Fabbris, D. Haskel, and H. Takagi. "Hyperhoneycomb Iridate $\beta-Li_2IrO_3$ as a Platform for Kitaev Magnetism". *Phys. Rev. Lett.* **114,** 077202 (2015). → p. 60.
159. K. A. Modic, T. E. Smidt, I. Kimchi, N. P. Breznay, A. Biffin, S. Choi, R. D. Johnson, R. Coldea, P. Watkins-Curry, G. T. McCandless, J. Y. Chan, F. Gandara, Z. Islam, A. Vishwanath, A. Shekhter, R. D. McDonald, and J. G. Analytis. "Realization of a three-dimensional spin–anisotropic harmonic honeycomb iridate". *Nature Communications* **5.** Article, 4203 (2014). → p. 60.
160. A. Biffin, R. D. Johnson, S. Choi, F. Freund, S. Manni, A. Bombardi, P. Manuel, P. Gegenwart, and R. Coldea. "Unconventional magnetic order on the hyperhoneycomb Kitaev lattice in $\beta - Li_2IrO_3$: Full solution via magnetic resonant x-ray diffraction". *Physical Review B* **90.** (2014). → p. 60.
161. A. Biffin, R. D. Johnson, I. Kimchi, R. Morris, A. Bombardi, J. G. Analytis, A. Vishwanath, and R. Coldea. "Noncoplanar and Counterrotating Incommensurate Magnetic Order Stabilized by Kitaev Interactions in $\gamma-Li_2IrO_3$". *Phys. Rev. Lett.* **113,** 197201 (2014). → p. 60.
162. Y. Singh, Y. Tokiwa, J. Dong, and P. Gegenwart. "Spin liquid close to a quantum critical point in $Na_4Ir_3O_8$". *Physical Review B* **88,** 220413 (2013). → p. 60.

163. R. Dally, T. Hogan, A. Amato, H. Luetkens, C. Baines, J. Rodriguez-Rivera, M. J. Graf, and S. D. Wilson. "Short-Range Correlations in the Magnetic Ground State of $Na_4Ir_3O_8$". *Physical Review Letters* **113,** 247601 (2014). → p. 60.
164. A. Balodhi, A. Thamizhavel, and Y. Singh. "Evolution of magnetic, transport, and thermal properties in $Na_{4-x}Ir_3O_8$". *Physical Review B* **91,** 224409 (2015). → p. 60.
165. O. Szabo. *Modern quantum chemistry* (Attila Szabo & Neil S. Ostl, Estados Unidos, 1982). → p. 61.
166. W. Koch and M. Holthausen. *A Chemist's Guide to Density Functional Theory.* (Wiley, 2015). → pp. 61, 65, 66, 68, 69.
167. R. M. Martin. *Electronic Structure: Basic Theory and Practical Methods* (Cambridge University Press, 2004). → p. 61.
168. P. Hohenberg and W. Kohn. "Inhomogeneous Electron Gas". *Phys. Rev.* **136,** B864 (1964). → p. 66.
169. W. Kohn and L. J. Sham. "Self-Consistent Equations Including Exchange and Correlation Effects". *Phys. Rev.* **140,** A1133 (1965). → p. 67.
170. J. P. Perdew and Y. Wang. "Accurate and simple analytic representation of the electron-gas correlation energy". *Phys. Rev. B* **45,** 13244 (1992). → p. 68.
171. P. J. Stephens, F. J. Devlin, C. F. Chabalowski, and M. J. Frisch. "Ab Initio Calculation of Vibrational Absorption and Circular Dichroism Spectra Using Density Functional Force Fields". *The Journal of Physical Chemistry* **98,** 11623 (1994). → p. 69.
172. S. H. Vosko, L. Wilk, and M. Nusair. "Accurate spin-dependent electron liquid correlation energies for local spin density calculations: a critical analysis". *Canadian Journal of Physics* **58,** 1200 (1980). → p. 69.
173. A. D. Becke. "Density-functional thermochemistry. III. The role of exact exchange". *The Journal of Chemical Physics* **98,** 5648 (1993). → p. 69.
174. C. Lee, W. Yang, and R. G. Parr. "Development of the Colle-Salvetti correlation-energy formula into a functional of the electron density". *Phys. Rev. B* **37,** 785 (1988). → p. 69.
175. W. Kohn. "Density functional theory for systems of very many atoms". *International Journal of Quantum Chemistry* **56,** 229. → p. 69.
176. M. Tinkham. *Group Theory and Quantum Mechanics.* (Dover Publications, 2003). → p. 70.
177. D. Waroquiers, X. Gonze, G.-M. Rignanese, C. Welker-Nieuwoudt, F. Rosowski, M. Göbel, S. Schenk, P. Degelmann, R. André, R. Glaum, and G. Hautier. "Statistical Analysis of Coordination Environments in Oxides". *Chemistry of Materials* **29,** 8346 (2017). → pp. 70–72, 114.
178. J. Lima-de-Faria, E. Hellner, F. Liebau, E. Makovicky, and E. Parthé. "Nomenclature of inorganic structure types. Report of the International Union of Crystallography Commission on Crystallographic Nomenclature Subcommittee on the Nomenclature of Inorganic Structure Types". *Acta Crystallographica Section A* **46,** 1 (1990). → p. 71.
179. M. R. Hartshorn, H.-H. Evamarie, K. René, and L. G. Jeffery. *Pure and Applied Chemistry.* in. 10, 1779 (2007). → p. 71.

180. H. T. Stokes, D. M. Hatch, and J. D. Wells. "Group-theoretical methods for obtaining distortions in crystals: Applications to vibrational modes and phase transitions". *Phys. Rev. B* **43,** 11010 (1991). → pp. 73, 90, 99.
181. J. He, C. Franchini, and J. M. Rondinelli. "Ferroelectric Oxides with Strong Visible-Light Absorption from Charge Ordering". *Chemistry of Materials* **29,** 2445 (2017). → pp. 74, 103, 106.
182. A. R. Oganov and S. Ono. "Theoretical and experimental evidence for a post-perovskite phase of $MgSiO_3$ in Earth's D″ layer". *Nature* **430,** 445 (2004). → pp. 77, 92.
183. D. Duan, Y. Liu, F. Tian, D. Li, X. Huang, Z. Zhao, H. Yu, B. Liu, W. Tian, and T. Cui. "Pressure-induced metallization of dense $(H_2S)_2H_2$ with high-T_c superconductivity". *Scientific Reports* **4.** Article, 6968 (2014). → pp. 77, 89.
184. A. P. Drozdov, M. I. Eremets, I. A. Troyan, V. Ksenofontov, and S. I. Shylin. "Conventional superconductivity at 203 Kelvin at high pressures in the sulfur hydride system". *Nature* **525,** 73 (2015). → p. 77.
185. X. Dong, A. R. Oganov, A. F. Goncharov, E. Stavrou, S. Lobanov, G. Saleh, G.-R. Qian, Q. Zhu, C. Gatti, V. L. Deringer, R. Dronskowski, X.-F. Zhou, V. B. Prakapenka, Z. Konôpková, I. A. Popov, A. I. Boldyrev, and H.-T. Wang. "A stable compound of helium and sodium at high pressure". *Nature Chemistry* **9.** Article, 440 (2017). → p. 77.
186. C. W. Glass, A. R. Oganov, and N. Hansen. "USPEX—Evolutionary crystal structure prediction". *Computer Physics Communications* **175,** 713 (2006). → pp. 77, 78.
187. A. R. Oganov, Y. Ma, A. O. Lyakhov, M. Valle, and C. Gatti. *Evolutionary Crystal Structure Prediction and Novel High-Pressure Phases.* in *High-Pressure Crystallography* (eds E. Boldyreva and P. Dera) (Springer Netherlands, Dordrecht, 2010), 293. → pp. 78, 79.
188. A. R. Oganov, Y. Ma, C. W. Glass, and M. Valle. "Evolutionary crystal structure prediction: overview of the USPEX method and some of its applications". *Psi-K Highlights* (2007). → p. 78.
189. A. R. Oganov and M. Valle. "How to quantify energy landscapes of solids". *The Journal of Chemical Physics* **130,** 104504 (2009). → p. 79.
190. A. Oganov. *Modern Methods of Crystal Structure Prediction.* (Wiley, 2011). → p. 81.
191. R. E. Cohen. "Origin of ferroelectricity in perovskite oxides". *Nature* **358,** 136 (1992). → p. 88.
192. B. Raveau, A. Maignan, C. Martin, and M. Hervieu. "Colossal Magnetoresistance Manganite Perovskites: Relations between Crystal Chemistry and Properties". *Chemistry of Materials* **10,** 2641 (1998). → p. 88.
193. S. Uchida, K. Kitazawa, and S. Tanaka. "Superconductivity and metal-semiconductor transition in $BaPb_{1-x}Bi_xO_3$". *Phase Transitions* **8,** 95 (1987). → pp. 88, 89, 101.
194. K. Inumaru, H. Miyata, and S. Yamanaka. "Partial suppression of structural distortion in epitaxially grown $BaBiO_3$ thin films". *Phys. Rev. B* **78,** 132507 (2008). → p. 88.
195. G. Kim, M. Neumann, M. Kim, M. D. Le, T. D. Kang, and T. W. Noh. "Suppression of Three-Dimensional Charge Density Wave Ordering via Thickness Control". *Phys. Rev. Lett.* **115,** 226402 (2015). → p. 89.

196. B. Yan, M. Jansen, and C. Felser. "A large-energy-gap oxide topological insulator based on the superconductor $BaBiO_3$". *Nat Phys* **9,** 709 (2013). → p. 89.
197. V. Vildosola, F. Güller, and A. M. Llois. "Mechanism to Generate a Two-Dimensional Electron Gas at the Surface of the Charge-Ordered Semiconductor $BaBiO_3$". *Phys. Rev. Lett.* **110,** 206805 (2013). → p. 89.
198. C. Franchini, G. Kresse, and R. Podloucky. "Polaronic Hole Trapping in Doped $BaBiO_3$". *Phys. Rev. Lett.* **102,** 256402 (2009). → pp. 89–91, 102, 103, 109.
199. K. Foyevtsova, A. Khazraie, I. Elfimov, and G. A. Sawatzky. *Hybridization effects and bond disproportionation in the bismuth perovskites.* 2015. → pp. 89, 102, 108.
200. R. Zeyher and K. Kunc. "Instabilities in cubic BaBiO3 from total-energy calculations". *Solid State Communications* **74,** 805 (1990). → pp. 89, 91.
201. P. Blaha, K. Schwarz, P. Dufek, G. Vielsack, and W. Weber. "The Breathing Mode of $BaBiO_3$: Electric Field Gradient and Total Energy Calculations". *Zeitschrift für Naturforschung A.* **49,** 129 (1994). → pp. 89, 91.
202. A. I. Liechtenstein, I. I. Mazin, C. O. Rodriguez, O. Jepsen, O. K. Andersen, and M. Methfessel. "Structural phase diagram and electron-phonon interaction in $Ba_{1-x}K_xBiO_3$". *Phys. Rev. B* **44,** 5388 (1991). → pp. 89, 91.
203. C. Franchini, A. Sanna, M. Marsman, and G. Kresse. "Structural, vibrational, and quasiparticle properties of the Peierls semiconductor $BaBiO_3$: A hybrid functional and self-consistent GW + vertex-corrections study". *Phys. Rev. B* **81,** 085213 (2010). → pp. 89–91, 94, 98, 103, 108.
204. D. Korotin, V. Kukolev, A. V. Kozhevnikov, D. Novoselov, and V. I. Anisimov. "Electronic correlations and crystal structure distortions in $BaBiO_3$". *Journal of Physics: Condensed Matter* **24,** 415603 (2012). → pp. 89–91, 103.
205. T. Bazhirov, S. Coh, S. G. Louie, and M. L. Cohen. "Importance of oxygen octahedra tilts for the electron-phonon coupling in K-doped $BaBiO_3$". *Phys. Rev. B* **88,** 224509 (2013). → p. 89.
206. Z. P. Yin, A. Kutepov, and G. Kotliar. "Correlation-Enhanced Electron-Phonon Coupling: Applications of *GW* and Screened Hybrid Functional to Bismuthates, Chloronitrides, and Other High-T_c Superconductors". *Phys. Rev. X* **3,** 021011 (2013). → pp. 89, 90, 103.
207. A. F. Kusmartseva, B. Sipos, H. Berger, L. Forró, and E. Tutiš. "Pressure Induced Superconductivity in Pristine $1T-TiSe_2$". *Phys. Rev. Lett.* **103,** 236401 (2009). → p. 89.
208. M. Leroux, I. Errea, M. Le Tacon, S.-M. Souliou, G. Garbarino, L. Cario, A. Bosak, F. Mauri, M. Calandra, and P. Rodière. "Strong anharmonicity induces quantum melting of charge density wave in $2H - NbSe_2$ under pressure". *Phys. Rev. B* **92,** 140303 (2015). → p. 89.
209. M. Hanfland, K. Syassen, N. Christensen, and D. Novikov. "New high-pressure phases of lithium". *Nature* **408,** 174 (2000). → p. 89.
210. Ma Yanming, Eremets Mikhail, Oganov Artem R., Xie Yu, Trojan Ivan, Medvedev Sergey, Lyakhov Andriy O., Valle Mario, and Prakapenka Vitali. "Transparent dense sodium". *Nature* **458,** 182 (2009). → p. 89.

211. A. P. Drozdov, M. I. Eremets, I. A. Troyan, V. Ksenofontov, and S. I. Shylin. "Conventional superconductivity at 203 Kelvin at high pressures in the sulfur hydride system". *Nature* **000,** 2015/08/17/online (2015). → p. 89.
212. A. Drozdov, M. I. Eremets, and I. A. Troyan. "Superconductivity above 100 K in PH_3 at high pressures". *ArXiv e-prints.* arXiv: `1508.06224 [cond-mat.supr-con]` (2015). → p. 89.
213. C. Heil and L. Boeri. "Influence of bonding on superconductivity in high-pressure hydrides". *Phys. Rev. B* **92,** 060508 (2015). → p. 89.
214. Flores-Livas, José, Sanna, Antonio, and Gross, E. K.U. "High temperature superconductivity in sulfur and selenium hydrides at high pressure*". *Eur. Phys. J. B* **89,** 63 (2016). → p. 89.
215. N. Bernstein, C. S. Hellberg, M. D. Johannes, I. I. Mazin, and M. J. Mehl. "What superconducts in sulfur hydrides under pressure and why". *Phys. Rev. B* **91,** 060511 (2015). → p. 89.
216. I. Errea, M. Calandra, C. J. Pickard, J. Nelson, R. J. Needs, Y. Li, H. Liu, Y. Zhang, Y. Ma, and F. Mauri. "High-Pressure Hydrogen Sulfide from First Principles: A Strongly Anharmonic Phonon-Mediated Superconductor". *Phys. Rev. Lett.* **114,** 157004 (2015). → p. 89.
217. J. A. Flores-Livas, M. Amsler, C. Heil, A. Sanna, L. Boeri, G. Profeta, C. Wolverton, S. Goedecker, and E. K. U. Gross. "Superconductivity in metastable phases of phosphorus-hydride compounds under high pressure". *Phys. Rev. B* **93,** 020508 (2016). → p. 89.
218. A. Shamp, T. Terpstra, T. Bi, Z. Falls, P. Avery, and E. Zurek. "Decomposition Products of Phosphine Under Pressure: PH_2 Stable and Superconducting?" *Journal of the American Chemical Society* **138.** PMID: 26777416, 1884 (2016). → p. 89.
219. Y. Fu, X. Du, L. Zhang, F. Peng, M. Zhang, C. J. Pickard, R. J. Needs, D. J. Singh, W. Zheng, and Y. Ma. "High-Pressure Phase Stability and Superconductivity of Pnictogen Hydrides and Chemical Trends for Compressed Hydrides". *Chemistry of Materials* **28,** 1746 (2016). → p. 89.
220. C. Kokail, C. Heil, and L. Boeri. "Search for high-T_c conventional superconductivity at megabar pressures in the lithium-sulfur system". *Phys. Rev. B* **94,** 060502 (2016). → p. 89.
221. E. Wigner and H. Huntington. "On the possibility of a metallic modification of hydrogen". *J. Chem. Phys.* **3,** 764 (1935). → p. 89.
222. P. Cudazzo, G. Profeta, A. Sanna, A. Floris, A. Continenza, S. Massidda, and E. K. U. Gross. "Ab Initio Description of High-Temperature Superconductivity in Dense Molecular Hydrogen". *Phys. Rev. Lett.* **100,** 257001 (2008). → p. 89.
223. M. Borinaga, I. Errea, M. Calandra, F. Mauri, and A. Bergara. "Anharmonic effects in atomic hydrogen: Superconductivity and lattice dynamical stability". *Phys. Rev. B* **93,** 174308 (2016). → p. 89.
224. R. Dias and I. Silvera. "Observation of the Wigner-Huntington transition to metallic hydrogen". *Science* **355,** 715 (2017). → p. 89.

225. The `ISOTROPY` software suite is a collection of software which applies group-theoretical methods to the analysis of phase transitions in crystalline solids; see `http://stokes.byu.edu/iso/isotropy.php`. → p. 90.
226. T. Nakamura, S. Kose, and T. Sata. "Paramagnetism and Semiconductivity in a Triclinic Perovskite $BaBiO_3$". *Journal of the Physical Society of Japan* **31,** 1284 (1971). → p. 91.
227. R. Arpe and H. Müller-Buschbaum. "Ein Beitrag zur Kristallchemie von $BaBiO_3$". *Zeitschrift für anorganische und allgemeine Chemie* **434,** 73 (1977). → p. 91.
228. C. J. Howard and H. T. Stokes. "Structures and phase transitions in perovskites – a group-theoretical approach". *Acta Crystallographica Section A* **61,** 93 (2005). → pp. 92, 103, 106.
229. P. V. Balachandran and J. M. Rondinelli. "Interplay of octahedral rotations and breathing distortions in charge-ordering perovskite oxides". *Phys. Rev. B* **88,** 054101 (2013). → pp. 92, 103.
230. J. He and C. Franchini. "Structural determination and electronic properties of the 4*d* perovskite $SrPdO_3$". *Phys. Rev. B* **89,** 045104 (2014). → pp. 92, 103.
231. A. Togo and I. Tanaka. "First principles phonon calculations in materials science". *Scripta Materialia* **108,** 1 (2015). → pp. 94, 99, 121, 125.
232. Phonopy website: `https://atztogo.github.io/phonopy/`. Phonopy is a package for phonon calculations at harmonic and quasiharmonic levels and uses the supercell approach with the finite displacements method. It finds the corresponding force constants, builds the dynamical matrix, diagonalizes it and then calculate the phonon dispersion relaxations. → p. 94.
233. *Local environments statistics in oxides from an automatic and robust detection algorithm. (To be published).* → pp. 96, 99.
234. `PYMATGEN` is a `Python` programming language library for materials analysis that has capabilities of generation of phase diagrams, Pourbaix diagrams, diffusion analysis, reactions, electronic structure analysis, and so on. Also it provides tools to construct, manipulate, and analyze structures. One of them is the `CHEMENV` module that is developed for chemical environment analysis. → pp. 96, 114.
235. It is possible to precisely determine the difference of partial DOS only for monoclinic C12$\bar{m}$1 $BaBiO_3$ as it has only two Bi atoms which are inequivalent. For the other structures we have separated Bi atoms into two formal groups representing Bi^{5+} and Bi^{3+} case. After averaging partial DOS in each group the difference was taken. → p. 97.
236. G. Kresse and J. Hafner. "*Ab initio* molecular dynamics for liquid metals". *Phys. Rev. B* **47,** 558 (1993). → pp. 99, 114, 124.
237. G. Kresse and J. Hafner. "*Ab initio* molecular-dynamics simulation of the liquid-metal–amorphous-semiconductor transition in germanium". *Phys. Rev. B* **49,** 14251 (1994). → pp. 99, 114, 124.
238. G. Kresse and J. Furthmüller. "Efficiency of ab-initio total energy calculations for metals and semiconductors using a plane-wave basis set". *Computational Materials Science* **6,** 15 (1996). → pp. 99, 114, 124.

239. G. Kresse and J. Furthmüller. “Efficient iterative schemes for *ab initio* total-energy calculations using a plane-wave basis set”. *Phys. Rev. B* **54,** 11169 (1996). → pp. 99, 114, 124.
240. G. Kresse and D. Joubert. “From ultrasoft pseudopotentials to the projector augmented-wave method”. *Phys. Rev. B* **59,** 1758 (1999). → pp. 99, 114, 124.
241. P. E. Blöchl. “Projector augmented-wave method”. *Phys. Rev. B* **50,** 17953 (1994). → pp. 99, 114, 124.
242. H. J. Monkhorst and J. D. Pack. “Special points for Brillouin-zone integrations”. *Phys. Rev. B* **13,** 5188 (1976). → pp. 99, 114, 124.
243. J. D. Pack and H. J. Monkhorst. “"Special points for Brillouin-zone integrations" — a reply”. *Phys. Rev. B* **16,** 1748 (1977). → pp. 99, 114, 124.
244. J. P. Perdew, K. Burke, and M. Ernzerhof. “Generalized Gradient Approximation Made Simple”. *Phys. Rev. Lett.* **77,** 3865 (1996). → pp. 99, 114, 124.
245. J. P. Perdew, K. Burke, and M. Ernzerhof. “Generalized Gradient Approximation Made Simple [Phys. Rev. Lett. 77, 3865 (1996)]”. *Phys. Rev. Lett.* **78,** 1396 (1997). → pp. 99, 114, 124.
246. J. Chang, E. Blackburn, A. T. Holmes, N. B. Christensen, J. Larsen, J. Mesot, R. Liang, D. A. Bonn, W. N. Hardy, A. Watenphul, M. V. Zimmermann, E. M. Forgan, and S. M. Hayden. “Direct observation of competition between superconductivity and charge density wave order in $YBa_2Cu_3O_{6.67}$”. *Nature Physics* **8,** 871 (2012). → p. 101.
247. A. F. Kusmartseva, B. Sipos, H. Berger, L. Forró, and E. Tutiš. “Pressure Induced Superconductivity in Pristine $1T-TiSe_2$”. *Phys. Rev. Lett.* **103,** 236401 (2009). → p. 101.
248. C. S. Snow, J. F. Karpus, S. L. Cooper, T. E. Kidd, and T.-C. Chiang. “Quantum Melting of the Charge-Density-Wave State in $1T-TiSe_2$”. *Phys. Rev. Lett.* **91,** 136402 (2003). → p. 101.
249. A. H. Castro Neto. “Charge Density Wave, Superconductivity, and Anomalous Metallic Behavior in 2D Transition Metal Dichalcogenides”. *Phys. Rev. Lett.* **86,** 4382 (2001). → p. 101.
250. A. Khazraie, K. Foyevtsova, I. Elfimov, and G. A. Sawatzky. “Oxygen holes and hybridization in the bismuthates”. *Phys. Rev. B* **97,** 075103 (2018). → p. 102.
251. `USPEX` is based on an evolutionary algorithm approach and its main idea is to form a population of crystal structures which are evolved under various evolutionary operators imitating biological ideas of mutation, reproduction, recombination, and selection. Algorithm minimizes the fitness function represented by an enthalpy of the system, calculated using ab intio methods. This allows `USPEX` to predict the crystal structure of a given composition and at a given pressure without any prior knowledge. → p. 102.
252. D. Serrate, J. M. D. Teresa, and M. R. Ibarra. “Double perovskites with ferromagnetism above room temperature”. *Journal of Physics: Condensed Matter* **19,** 023201 (2007). → p. 104.
253. S. Vasala and M. Karppinen. “$A_2B'B''O_6$ perovskites: A review”. *Progress in Solid State Chemistry* **43,** 1 (2015). → p. 104.

254. Personal communication with Minu Kim. → p. 106.
255. HSE on top of PBE structure describes clustered $BaBiO_3$ as a semimetal. However, if a proper geometry optimization on the HSE level is performed, the structure is insulator. Due to the computational cost and for consistency reasons we did not perform this optimization for the whole pressure range, but only checked the behavior at a specific pressure. → pp. 107, 108, 114.
256. R. Bader. *Atoms in Molecules: A Quantum Theory*. (Clarendon Press, 1994). → p. 109.
257. Code for the Bader charge analysis is available on the website: `http://theory.cm.utexas.edu/henkelman/code/bader/`. → p. 109.
258. W. Tang, E. Sanville, and G. Henkelman. "A grid-based Bader analysis algorithm without lattice bias". *Journal of Physics: Condensed Matter* **21,** 084204 (2009). → p. 109.
259. In Bader analysis atomic charges are separated by "zero-flux" surfaces: these are surfaces where there is no flux in the gradient vector field of charge density. → p. 109.
260. V. Goldschmidt, T. Barth, G. Lunde, and W. Zachariasen. "Geochemische Verteilungsgesetze VII. Die Gesetze der Krystallochemie". *Skrifter utgitt av det Norske Videnskaps-Akademi i Oslo 1: Matematisk-Naturvidenskapelig Klasse (1926), (*) p1-p17.* → pp. 115, 120.
261. H. Kuriyama, J. Matsuno, S. Niitaka, M. Uchida, D. Hashizume, A. Nakao, K. Sugimoto, H. Ohsumi, M. Takata, and H. Takagi. "Epitaxially stabilized iridium spinel oxide without cations in the tetrahedral site". *Applied Physics Letters* **96,** 182103 (2010). → pp. 115, 120.
262. Y. Singh and P. Gegenwart. "Antiferromagnetic Mott insulating state in single crystals of the honeycomb lattice material Na_2IrO_3". *Phys. Rev. B* **82,** 064412 (2010). → p. 115.
263. K. Mader and R. Hoppe. "Zu Oxoiridaten mit quadratisch-planaren $[IrO4]^{4-}$-Gruppen: Na_4IrO_4, eine MgO-Ersetzungsvariante mit geordneten Lücken im Anionenteilgitter". *Zeitschrift für anorganische und allgemeine Chemie* **619,** 1647 (1993). → p. 115.
264. T. Takayama, A. Yaresko, A. Matsumoto, J. Nuss, K. Ishii, M. Yoshida, J. Mizuki, and H. Takagi. "Spin-orbit coupling induced semi-metallic state in the 1/3 hole-doped hyper-kagome $Na_3Ir_3O_8$". *Scientific Reports* **4,** 6818 (2014). → p. 115.
265. P. Anderson. "Resonating valence bonds: A new kind of insulator?" *Materials Research Bulletin* **8,** 153 (1973). → p. 120.
266. A. Guinier (Chairman), G. B. Bokij, K. Boll-Dornberger, J. M. Cowley, S. Ďurovič, H. Jagodzinski, P. Krishna, P. M. de Wolff, B. B. Zvyagin, D. E. Cox, P. Goodman, T. Hahn, K. Kuchitsu, and S. C. Abrahams. "Nomenclature of polytype structures. Report of the International Union of Crystallography *Ad hoc* Committee on the Nomenclature of Disordered, Modulated and Polytype Structures". *Acta Crystallographica Section A* **40,** 399 (1984). → p. 121.
267. A. Tkatchenko and M. Scheffler. "Accurate Molecular Van Der Waals Interactions from Ground-State Electron Density and Free-Atom Reference Data". *Phys. Rev. Lett.* **102,** 073005 (2009). → p. 121.

268. J. Chaloupka and G. Khaliullin. "Hidden symmetries of the extended Kitaev-Heisenberg model: Implications for the honeycomb-lattice iridates A_2IrO_3". *Physical Review B* **92,** 024413 (2015). → p. 124.

269. S. M. Winter, Y. Li, H. O. Jeschke, and R. Valentí. "Challenges in design of Kitaev materials: Magnetic interactions from competing energy scales". *Phys. Rev. B* **93,** 214431 (2016). → p. 125.

270. P. Liu, S. Khmelevskyi, B. Kim, M. Marsman, D. Li, X.-Q. Chen, D. D. Sarma, G. Kresse, and C. Franchini. "Anisotropic magnetic couplings and structure-driven canted to collinear transitions in Sr_2IrO_4 by magnetically constrained noncollinear DFT". *Phys. Rev. B* **92,** 054428 (2015). → p. 125.

271. K. Li, S.-L. Yu, and J.-X. Li. "Global phase diagram, possible chiral spin liquid, and topological superconductivity in the triangular Kitaev–Heisenberg model". *New Journal of Physics* **17,** 043032 (2015). → p. 125.

272. P. Blaha, K. Schwarz, G. K. H. Madsen, D. Kvasnicka, and J. Luitz. *WIEN2K, An Augmented Plane Wave + Local Orbitals Program for Calculating Crystal Properties* (Karlheinz Schwarz, Techn. Universität Wien, Austria, Wien, Austria, 2001). → p. 125.

273. P. E. Blöchl, O. Jepsen, and O. K. Andersen. "Improved tetrahedron method for Brillouin-zone integrations". *Phys. Rev. B* **49,** 16223 (1994). → p. 125.